BLOOD FLOW SIMULATION IN STENTED VESSELS AND FLOW REVERSAL CONDITIONS

A Dissertation

Presented to

the Faculty of the Department of Mechanical Engineering

University of Houston

In Partial Fulfillment

of the Requirements for the Degree

Doctor of Philosophy

in Mechanical Engineering

by

Mircea Ionescu

May 2012

For my parents, Mihai and Irina

Acknowledgments

I am especially grateful to my advisor, Dr. Ralph Metcalfe, for his patience, guidance, support, and inspiration during my studies. I would also like to thank my defense committee members, Dr. Stanley Kleis, Dr. Matthew Franchek, Dr. Kirill Larin, Dr. Ioannis Kakadiaris, Dr. William Cohn, and Dr. Morteza Naghavi, for their valuable advice and suggestions. Many thanks to Dr. Goetz Benndorf and Dr. John Hipp for their time spent on stent deployment and imaging and to Dr. Craig Hartley for flow measurements.

In addition, I would like to offer my deepest thanks to my family for their support, encouragement, love, and infinite sacrifice. I am very grateful to Lori for inspiration and support.

I am also indebted to my colleagues and friends for many helpful discussions, Wasy Akhtar, Pranab Jha, Andrés Hernandez, Aishwarya Mantha, and Max Lingamfelter. Also, many thanks to Erik Engquist for his help as visualization lab administrator at the Texas Learning & Computation Center.

This work was supported in part by the Texas Learning and Computation Center, in part by the National Science Foundation Grant DGE-0840889 awarded to the University of Houston, and in part by Grant Number R01HL085054 awarded to the Texas Heart Institute by the National Heart, Lung, and Blood Institute (NHLBI).

BLOOD FLOW SIMULATION IN STENTED VESSELS AND FLOW REVERSAL CONDITIONS

An Abstract

of a

Dissertation

Presented to

the Faculty of the Department of Mechanical Engineering

University of Houston

In Partial Fulfillment

of the Requirements for the Degree

Doctor of Philosophy

in Mechanical Engineering

by

Mircea Ionescu

May 2012

Abstract

Hemodynamics is one of the major factors involved in the development of cardiovascular diseases and adverse events associated with endovascular stent implantation such as in-stent restenosis and thrombosis. The first part of this work is dedicated to the imaging of stent deployment in graft tubes and *ex vivo* arterial segments and the investigation of in-stent hemodynamics through computational hemodynamic simulations, i.e., CHD, based on realistic *in vitro* stent and wall geometries. The second part is concerned with the parameterization of flow rate waveforms resembling physiologic waveforms and the description of waveform properties that lead to the occurrence of wall flow reversal in straight, cylindrical pipes.

Stent reconstruction by high-resolution micro-computed tomography (microCT) is compared with reconstructions obtained from clinical CT: multislice CT (MS-CT), C-arm flat detector CT (C-arm CT), and flat panel CT (FP-CT). The spatial resolution of current clinical CT for stent imaging is insufficient to visualize fine geometrical details as stent struts appear over-sized. Deployment characteristics such as stent strut prolapse into the lumen, strut vertex misalignment, under-deployment, wall prolapse, and wall creases at strut vertices of intracranial and coronary stents with open- and closed-cell designs are demonstrated by microCT imaging. In-stent hemodynamics are significantly altered by non-uniform deployment characteristics (misaligned strut vertices, malapposed struts, or wall creases), important effects not realistically captured in previous, computer generated stent models.

Periodic waveforms with positive net flow rates can exhibit flow reversal. The physiological flow waveform is divided into acceleration and deceleration phases

described by sinusoids, and two non-dimensional parameters to quantify wall flow reversal conditions are proposed. For waveforms typical of arterial blood flow, the wall shear stress reversal during the second deceleration phase is strongly influenced by the amplitude ratio of the preceding acceleration and deceleration phases and less by the relative time period of the deceleration phase. The method presented here can identify the occurrence of wall flow reversal and indicate the possibility of oscillatory wall shear stress that may negatively affect endothelial cell function due to blood flow waveform characteristics.

Table of Contents

List of Figures

List of Tables

Chapter 1

Introduction

The cardiovascular and pulmonary systems have been one of the earliest studied systems since the advent of physiologic studies on the human body and have inspired physicians, as well as scientists, to think of both systems as pipe networks analogous to hydraulic systems. Both physiologic systems involve fluid transport in the form of gas (air, for the pulmonary system) or particle suspensions in a liquid (blood, which is a mixture of small cells, molecules, and plasma, for the cardiovascular system) through small, round tubes. In particular, the cardiovascular system is responsible for the active transport of essential nutrients and vital information (via signaling molecules) throughout the entire body. This is accomplished by a vast network of vessels through which blood, pumped by the heart, flows uninterrupted. As with any living system, the cardiovascular system is not immune from developing diseases which sometimes can result in abnormal blood flow with dangerous consequences such as the restriction of the normal supply of blood to important organs, thus, starving them of nutrients and oxygen. Most of the deaths in developing countries are attributed to arterial diseases such as atherosclerosis that result in heart attacks and strokes, therefore, providing a strong motivation for the study of the cardiovascular system and the development of its diseases. The physiological, biological, and fluid mechanics aspects of the cardiovascular system have resulted in an interdisciplinary research effort to understand and model the blood flow phenomenon. In general, the main purposes for studying the cardiovascular system under normal and diseased physiologic conditions can be reduced

to:

- understanding how the cardiovascular system works;
- determining the factors or the exact combination of factors that lead to various cardiovascular diseases;
- identifying the effects of diseases and how to efficiently treat them to restore normal cardiovascular function.

The analogy between the cardiovascular system consisting of the heart (the pump) and arteries and veins (the pipes) and hydraulic systems represents the first step in studying and modeling blood flow through arteries. Therefore, a large number of scientific studies that employ fluid mechanics principles have been performed in order to understand the complex interaction between arteries and blood flow conditions (hemodynamics) that lead to arterial diseases. Particularly, computational hemodynamics, in which computer simulations are used to model blood flow, has been a very active research area since advancements in imaging techniques have allowed the reconstruction of real arterial geometries. Also, another area where the modeling of arterial flow conditions plays an important role is the development of devices and treatment methods for cardiovascular diseases.

In this work, the first part is dedicated to the visualization and modeling of blood flow through arterial graft tubes and an *ex vivo* arterial segment that have been implanted with a stent—a wire mesh that acts as scaffold for weak arterial walls and is used for treatment of diseased arteries in order to restore normal blood to flow. The second part is dedicated to the investigation of temporal effects that arise from the blood flow waveform specific to large human arteries. The flow waveform is parameterized in an effort to identify which waveform characteristics induce abnormal blood flow that potentially results in the development of arterial

diseases. This chapter provides an overview of the arterial hemodynamics and the interactions with the arterial wall, the different mathematical models used to describe blood flow and the role of abnormal flow patterns in the development of arterial diseases such as atherosclerosis and aneurysm formation.

1.1 Arterial hemodynamics

Blood flow is characterized by high pulsatility in arteries and arterioles (diameter > 0.5 mm) while in small arterioles and capillaries the flow becomes continuous [1]. The pulsatile nature of blood flow originates from the cardiac cycle defined by the heart contractions in which blood fills the heart and is then ejected in alternating cycles known as diastole and systole. During diastole, the heart relaxes and the left ventricle fills with oxygenated blood coming from the lungs. Then, during systole, the strong contraction of the left ventricle pushes the blood into the aorta which distributes blood to other major arteries so that oxygenated blood will reach every part of the body. Blood returns to the right atrium of the heart via the venous network, thus completing what is known as the systemic circulation. During diastole, blood from the right atrium flows into the right ventricle from which it is ejected, via the pulmonary arteries, toward the lungs from which it returns, via the pulmonary veins, to the left atrium at end diastole, completing the pulmonary circulation. As the heart pumping is intermittent there is no flow from the heart once the aortic valve closes and a minimum pressure would be expected in the aorta. The aortic wall is elastic, giving the aorta a radial dilation, $\Delta R/R \times 100$, of 12% during peak systolic flow making the aorta a compliance chamber that acts as a pressure reservoir during late systole and diastole ensuring the net blood flow rate is positive and the pressure in the systemic arteries does not fall to zero as

illustrated in Figure 1.1 which is adapted from Nichols and O'Rourke [1]. The pressure and flow waveforms change downstream of the ascending aorta with the amplitude of flow velocity decreasing and that of the pressure pulse increasing. The shape of the flow and pressure waveforms also suffers alterations along the vascular tree. This is the result of arterial compliance, which decreases with the arterial diameter, and of reflected pressure waves. When the aortic valve closes and the pressure decreases, the aortic wall, which distended locally in response to increased systolic blood pressure, will begin to contract, thus, accelerating the flow. This effect, combined with the inertia of the blood gives rise to a pressure wave that propagates along the aorta and the downstream arteries. This pressure wave will suffer wave reflections at arterial bifurcations that alter the shape of the pressure and flow rate waveforms as indicated in Figure 1.1. Other changes of the waveform shape are due, to a lesser degree, to arterial tapering and an increase in arterial wall stiffness of the downstream arteries and the dissipative action of the blood viscosity [2].

In general, the blood flow rate is positive during diastole with some exceptions such as the brachial and femoral arteries that have high downstream resistance and usually exhibit brief flow reversal. During systole, the flow is zero or reversed in the coronary arteries as these arteries are attached to the wall of the left ventricle and are squeezed during the ventricular contraction that takes place during systole but flow in these arteries is positive during diastole. The pulsatile flow conditions found in healthy systemic arteries are laminar with no disturbances or reversal (with few exceptions in diseased arteries). The typical Reynolds number for systemic arteries, defined as $\mathrm{Re} = \rho \bar{U} D/\mu$, where ρ is the blood density, $\bar{U}$ is the mean velocity, D is the arterial diameter, and μ is the absolute blood viscosity, is about 800 during systole with a time-average value of 300. The peak Reynolds number in

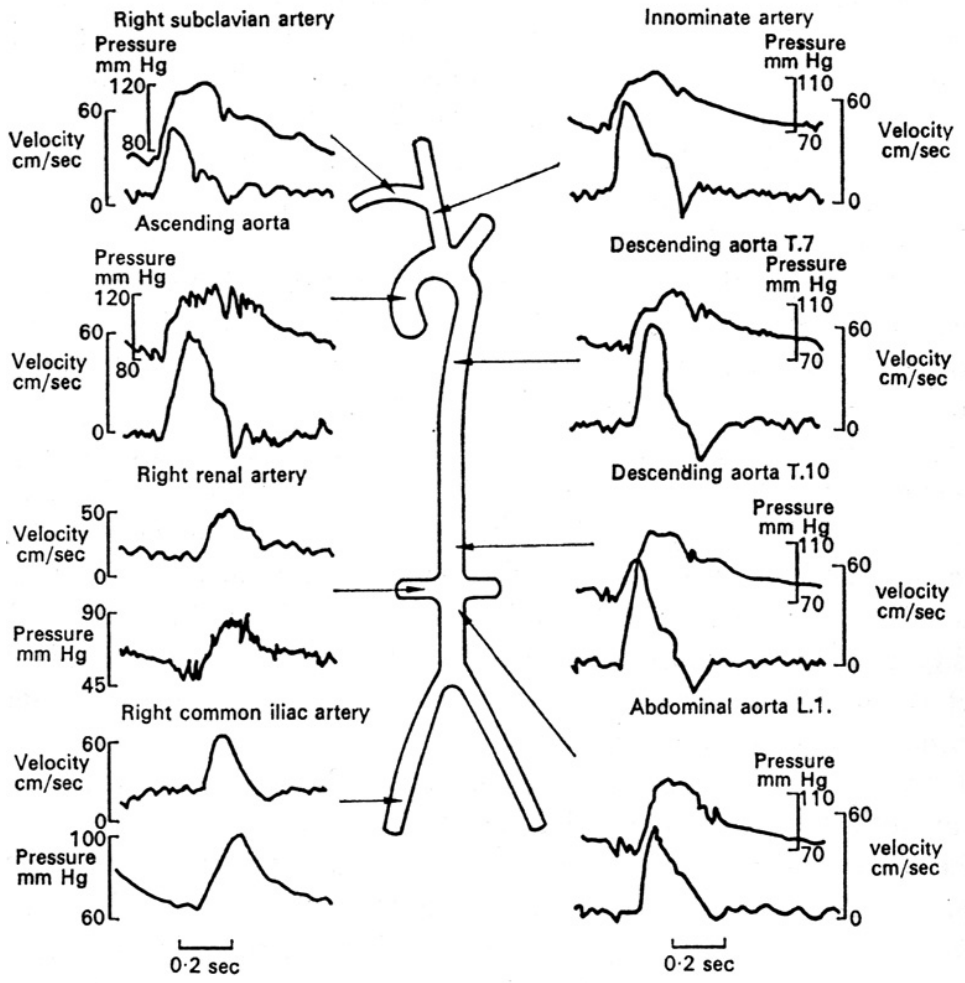

Figure 1.1. Arterial pressure and flow velocity at various locations along the systemic arterial tree

the aorta is about 2000. This range of Reynolds numbers indicates that both the viscous and inertial effects are important and neither can be neglected from the equations governing the fluid motion, also known as the Navier-Stokes equations, when modeling blood flow in arteries.

For periodic pulsatile flows, a dimensional analysis of the Navier-Stokes equations yields another non-dimensional parameter that quantifies the flow pulsatility, the Womersley number,

$$\alpha = R\sqrt{\frac{\omega\rho}{\mu}} = R\sqrt{\frac{2\pi\rho}{T\mu}}, \tag{1.1}$$

where R is the arterial radius, $\omega = 2\pi k f$, $f = 1/T$, with k being the k^{th} harmonic, and T being the time period of the fundamental harmonic for a periodic waveform. This new parameter can be thought of as the ratio of the unsteady forces to viscous forces. For $\alpha \leq 1$, the unsteady effects are negligible and the flow exhibits a parabolic velocity profile typical of steady pipe flows, or Poiseuille flows. As α increases and becomes larger than 5, unsteady inertial forces begin to dominate and the velocity profile departs from the parabolic shape. For arterial blood flow under resting conditions, typical values for α range from 1 in arterioles to about 8 in the aorta and the major arteries such the carotid, renal, and femoral. For upper body circulation the typical value of α is about 5. Therefore, the pulsatile nature of the blood flow cannot be neglected as transient effects play a major role in arterial hemodynamics.

Blood is a complex mixture of particles such as cells, platelets, proteins, lipoproteins, ions, and other macromolecules and liquid, represented by plasma. A typical unit volume of blood contains approximately 40% red blood cells, 5% white blood cells and platelets and about 55% plasma. This composition results in a variable blood viscosity that depends on the shear rate, the red blood cells concentration (hæmatocrit), and blood vessel diameter. For hæmatocrit values of 40%, the blood has a density of 1060 $\mathrm{kg/m^3}$ and a viscosity of about 4×10^{-3} $\mathrm{kg/(m{\cdot}s)}$ that does not change as long as the shear rate is greater than 100 $\mathrm{s^{-1}}$. For shear rates less than this value, the viscosity increases and blood starts to behave as a non-Newtonian fluid. Also, as the hæmatocrit value increases, the viscosity increases rapidly even for higher shear rates and the non-Newtonian behavior is present over a wider range of shear rates. For pulsatile blood flow in human arteries, the shear rate is well above 300 $\mathrm{s^{-1}}$ during systolic flow and at normal hæmatocrit values of 40% the non-Newtonian behavior is negligible [1]. The assumption of blood as a

fluid with uniform viscosity and homogeneity (i.e., a Newtonian fluid) is considered to be reasonable in major arteries with diameters larger than 500 μm [2–4]. As the blood vessel diameter decreases below 300 μm, the effective viscosity begins to decrease due to red blood cells aggregation toward the center of the vessel and the formation of cell-free layer adjacent to the wall—also know as the Fåhræus-Lindqvist effect. The thickness of this layer is about 10–12 μm and consists of low viscosity plasma, hence, increased shear rate at the wall [4]. This effect is more apparent for small arterioles and capillaries with diameters less than 20 μm in which the red blood cells (10 μm in diameter) are aligned in a linked chains structure.

Arteries are not simple, inert tubes but actively respond to changes in hemodynamic conditions and the health of the arterial wall is affected by abnormal blood flow. As mentioned earlier, arteries are elastic tubes whose diameter will change as a pulsating pressure wave passes through and undergo dilation or contraction to regulate blood flow and body temperature. The arterial wall, shown in Figure 1.2 (adapted from [5]), is composed of three layers: the adventitia, media, and intima, the inner-most layer. Each layer is made of different tissue with adventitia consisting of collagen, elastin, and connective tissue, media consisting of fibers, elastin, and smooth muscle cells, and intima consisting of vascular endothelium which is directly exposed to the lumen and blood flow.

The endothelial cells that line the inner or luminal face of the artery are able to sense changes in blood flow velocity and pressure and activate signal pathways that result in arterial adaptation. As one of the fundamental assumptions from fluid mechanics states that the flow velocity at a non-porous surface is zero, the endothelial cells do not directly sense the flow velocity. Instead, they respond to the friction force exerted by the moving flow which is directly proportional to the

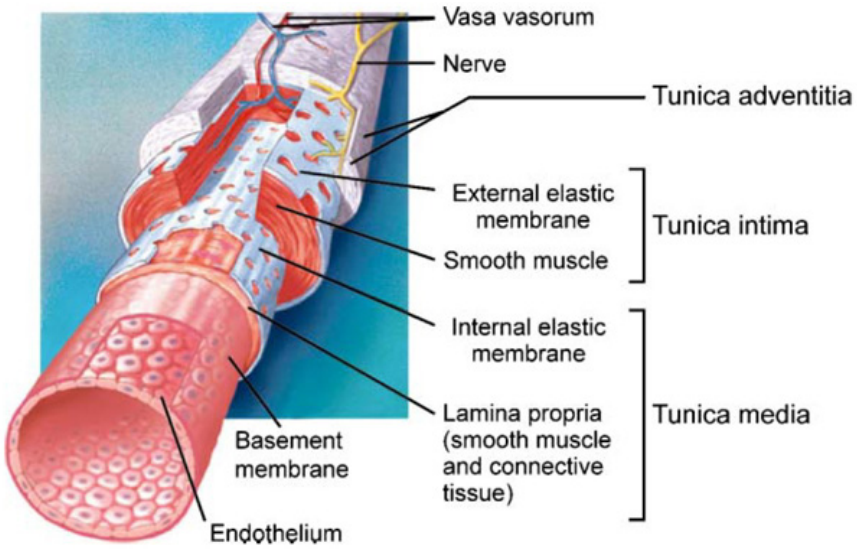

Figure 1.2. Schematic of the wall structure typical of systemic arteries with three major layers: adventitia, media and intima [5]

velocity gradient at the arterial wall. This friction force, also known as the wall shear stress (WSS), has been shown to regulate the activity and signaling processes of the endothelium that result in arterial remodeling and angiogenesis [6–9].

The typical arterial response to increases in blood flow and consequently shear stress is an expansion of the luminal radius such that the shear stress is maintained at a baseline value which has been determined experimentally to be about 1.5–2 Pa (15–20 dyne/cm^2) [8, 9]. Conversely, a decrease in WSS as a direct result of decreased blood flow leads to a reduction in the luminal radius. These compensatory responses are also active and tend to restore baseline flow by vessel dilation when stenosed arterial segments (arteries that have developed plaque) result in decreased blood flow in vascular districts distal of the stenosis. This is also one of the reasons why the majority of early arterial disease stages are asymptomatic and hard to diagnose. A schematic of the blood flow in a vessel showing the WSS and the typical range of shear stress magnitude encountered in the cardiovascular system is shown in Figure 1.3 as adapted from Malek *et al.* [10].

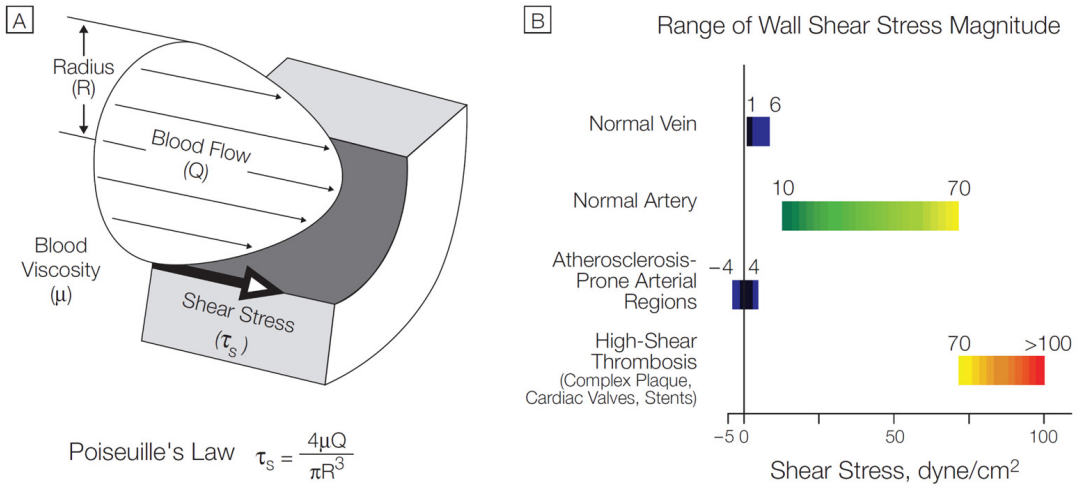

Figure 1.3. Schematic of blood flow and wall shear stress (WSS) in a cylindrical pipe. Typical WSS values found in arteries and veins range from 10 to 70 dyne/cm^2 [10]

The response of endothelial cells to changes in the flow environment, namely WSS, is complex and not yet fully understood [11]. Morphological changes as well as gene expression, release of growth regulators, inflammatory response, expression of adhesion molecules, recruitment and accumulation of monocytes and macrophages, and thrombogenic responses are just a few of the endothelial cell processes that are regulated by hemodynamic WSS [12]. Exposure to unidirectional flow transforms the polygonal shaped endothelial cells into fusiform cells aligned in the direction of flow [13, 14]. As shown in Figure 1.4, adapted from Malek *et al.* [10], bovine endothelial cells exposed to shear stress ($>$ 15 dyne/cm^2 or 1.5 Pa) align in the direction of blood flow while cells exposed to low and oscillatory shear stress ($\pm$4 dyne/cm^2 or $\pm$0.4 Pa) are not aligned and exhibit a polygonal shape. The hemodynamic conditions resulting in fusiform endothelial cells are also associated with decreased endothelial cell proliferation and apoptosis, increased production of vasodilators, growth inhibitors, and antioxidants as well as inhibition of inflammatory mediators, thus, providing atheroprotective functions.

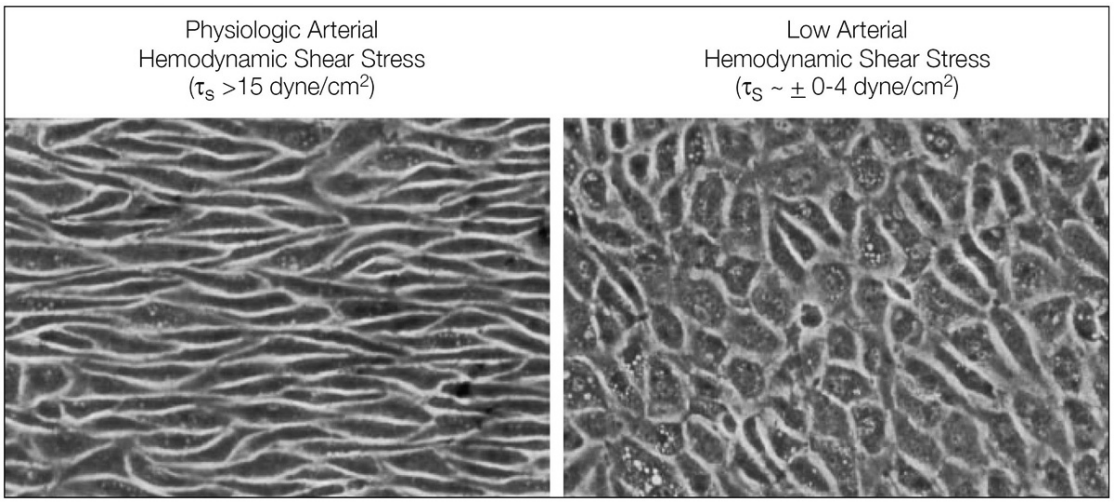

Figure 1.4. Morphology of bovine endothelial cells exposed to normal shear stress (left) and low shear stress (right)

Under low or disturbed hemodynamic flow, the endothelial cells exhibit a polygonal shape and smooth muscle cell proliferation while endothelial desquamation, higher levels of growth factors and monocyte attachment to and migration into the endothelial layer occur within hours of exposure to these flow conditions [12].

The large evidence showing the wealth of interactions between endothelial cells and hemodynamic factors such as WSS has been summarized in extensive reviews [10–12, 15] and has led to the conclusion that arterial hemodynamic factors play a major role in cardiovascular pathology especially in regard to arterial diseases such as atherosclerosis, aneurysms, and restenosis. These findings have motivated numerous hemodynamic studies—experimental as well as computational—that attempt to identify and classify flow conditions and arterial locations favorable for the initiation and/or progression of arterial disease. Predicting arterial diseases and finding the best treatment options by studying the hemodynamic conditions specific to the cardiovascular system is a complex task that requires the use of mathematical as well as fluid dynamics modeling and accurate blood flow measurements.

1.2 The role of flow in arterial diseases

Blood flow modulates the activity of endothelial cells and cardiovascular pathology as discussed in the previous section. Abnormal blood flow patterns and WSS can damage or initiate inflammatory responses in endothelial cells. Early experimental work hypothesized that high WSS magnitude damages endothelial cells resulting in the onset of arterial diseases so that regions of the arterial wall with elevated WSS are prone to lesions [16]. However, this view was later contradicted by findings indicating that arterial lesions occur at sites of low mean WSS values [17]. As time-dependent flow effects have been recognized to play an important role as well, the current general consensus is that regions of low and oscillatory WSS are susceptible to arterial diseases [18]. The most investigated arterial diseases include atherosclerosis or the build up of plaque on the arterial wall and aneurysms. An aneurysm is an abnormal widening and subsequent development of a balloon like structure in the arterial wall due to a weakening of the wall. The role of blood flow in the pathology of these two types of arterial disease is discussed below.

1.2.1 Atherosclerosis

Laminar, undisturbed blood flow results in hemodynamic forces that have beneficial effects on the endothelium, modulating essential physiologic functions of endothelial cells [11]. Arterial bifurcations, highly curved arterial segments and sites of multiple arterial branching are regions where the flow, still laminar, becomes disturbed due to the arterial geometry and time-dependent variations. These regions are characterized by rapidly changing WSS distribution, flow recirculation zones, and oscillating flow velocity. Typical locations of these regions associated

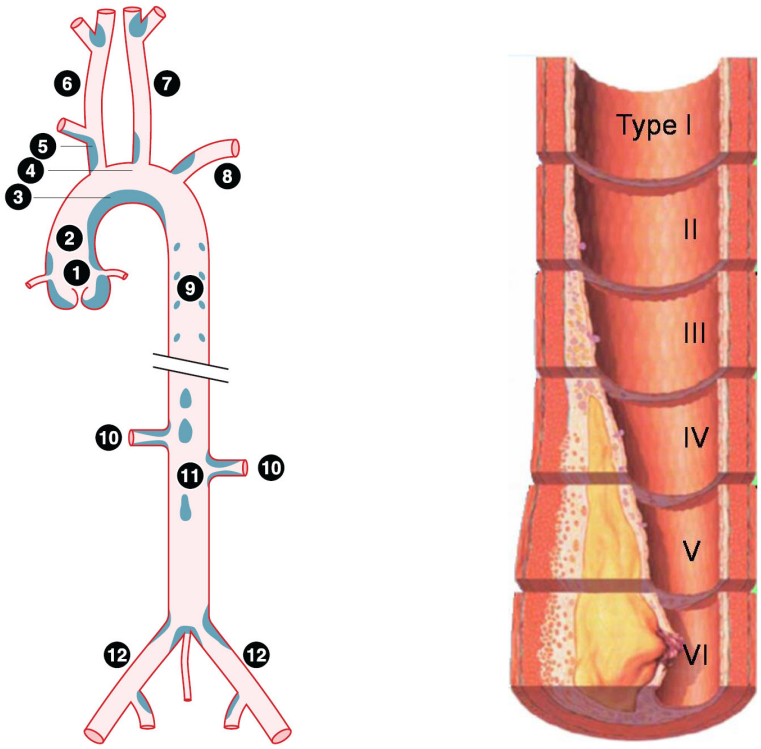

(a) (b)

Figure 1.5. Arterial regions prone to atherosclerotic plaque development (a) and plaque formation stages (b)

with atherosclerotic plaque development in the vascular network are depicted in Figure 1.5a (adapted from [12]). They include: the aortic sinus, 1, ascending aorta, 2, aortic arch, 3 and 4, innominate artery, 5, left and right common carotid arteries, 6 and 7 respectively, left subclavian artery, 8, thoracic artery, 9, renal artery, 10, abdominal aorta, 11, and the iliac arteries, 12. Other regions with high incidence of atherosclerosis include cerebral (mostly the carotid) and coronary arteries.

The development of atherosclerotic plaque, depicted in Figure 1.5b (the National Institutes of Health) for the most common type at different stages, is not completely understood but inflammation responses from endothelial cells are one of the initial events involved in plaque formation as summarized in the work by

Libby [19] and Chiu and Chien [12]. Low and oscillatory WSS induces the activation of monocytes, platelet derived growth factors, and infiltration of monocytes into the arterial wall. Low density lipoproteins also infiltrate the intima and cause the endothelial cells to express adhesion molecules which act as recruiters for immune system cells such as cytokines and T cells. This particle migration toward the arterial wall may be enhanced by favorable hemodynamics conditions such as low blood flow velocity, flow recirculation, and oscillatory WSS [3, 18]. Mounting evidence associating these hemodynamic conditions and arterial WSS with the initation and progression of atherosclerotic plaque has been published [20–24].

The accumulation of low density lipoproteins and monocytes in the intima triggers further inflammatory reactions and the formation of macrophages and fatty molecules beneath the endothelium layer. As the macromolecules continue to accumulate, the plaque begins to grow and a fibrous cap consisting of smooth muscle cells that have migrated from the media forms underneath the endothelium and over a fatty core that makes up the bulk of the plaque. Some atherosclerotic arterial segments exhibit initial positive remodeling, i.e., the arterial wall expands to preserve the luminal area. As the plaque grows, it begins to protrude into the lumen, thus restricting normal blood flow and resulting in higher flow velocity and consequently higher WSS over the plaque and the occurrence of perturbed flow with recirculation regions distal to the plaque site [25]. In particular, the investigation by Samady *et al.* [24] consisting of intravascular ultrasound analysis and computational fluid dynamics studies on patients with coronary artery diseases concludes that low WSS arterial regions promote plaque progression while high WSS, present over the atherosclerotic regions, promotes the regression of fibrous tissue that develops over the fatty core, thereby increasing the risk of plaque rupture.

The arterial segment where an atherosclerotic plaque develops is usually called a stenosed artery. Although the fibrous cap acts as a shield that prevents the soft, fatty core of the plaque from breaking away from the endothelium, inflammatory substances released by the cytokines trapped inside the plaque also degrade the fibrous cap resulting in either thrombus formation due to inflammatory responses or plaque rupture due to high hemodynamic forces [19, 26, 27]. This is the most common type of vulnerable plaque along with several other types that are being considered for a cumulative vulnerability index assessing the risk of adverse cardiac events as proposed by Naghavi *et al.* [27]. Plaque rupture can have very serious consequences as debris and/or thrombus originating from the plaque can disrupt or completely block the blood flow in distal vascular districts especially in the case of the coronary arteries that feed the heart muscle. If the blood flow is interrupted (ischemia), the heart muscle cells begin to die and the heart is not able to pump blood at normal levels resulting in what is known as myocardial infraction or a heart attack. Therefore, there is a strong incentive to investigate the hemodynamic conditions that lead to atherosclerotic plaque development and rupture and to predict the potential of such occurrences.

Stenosed arteries can be treated by a procedure known as angioplasty, or widening of a narrowed vessel, in which a catheter is inserted into the artery and a balloon is inflated to reopen the artery and reestablish normal blood flow [25]. However, this method only provides a temporary fix as the plaque continues to grow and further reduce the arterial lumen. Another angioplasty method for treating stenosed arteries consists of a stent being deployed over the atherosclerotic plaque to act as a scaffold for the arterial wall and to reopen the arterial lumen; however, negative outcomes such as in-stent restenosis (regrowth of the plaque) and thrombus formation are shown to occur in $\sim 30\%$ of the cases [28–30]. Stenting and the vas-

cular complications associated with this procedure are discussed in greater detail in chapter 3.

1.2.2 Aneurysms

The aneurysm lesions that develop on the arterial wall are different from those involving stenosed arteries. As the pressure pulse wave generated by the heart travels through a network of elastic arteries, the arterial wall undergoes constant dilation and contraction depending of the degree of elasticity or compliance of each artery. A complex feedback control system regulated by hemodynamic forces acting on the endothelium is responsible for the adaption of the arterial wall to changes in cardiac output. As discussed earlier, the aorta is the most elastic artery of the vascular system and as the diameter of the arteries decreases so does the degree of elasticity. While the mechanisms of aneurysm formation are not well known it is believed that a combination of biological as well as hemodynamic factors are responsible for the weakening of the arterial wall which, coupled with the high arterial pressure associated with the traveling pressure pulse wave, results in the permanent distention and local widening of the arterial wall that leads to the formation of an aneurysm [5].

The development of aneurysms is typically asymptomatic and they are detected in the late stages when the aneurysm sac is large enough to affect normal blood flow or the surrounding tissue [31]. Arterial locations where aneurysms tend to preferentially occur include the thoracic and abdominal aorta, intracranial arteries, and the circle of Willis. In some cases, as the aneurysm grows, the wall may eventually be unable to sustain the stresses exerted by the blood flow and ruptures, thus, leading to internal bleeding (subarachnoid hemorrhage for intracranial aneurysms) that, in severe cases, cause death. Treatment of diagnosed aneurysms

include coiling and/or stent placement that attempt to minimize the blood flow into the aneurysm sac fostering thrombus formation inside the sac. This may stabilize the aneurysm and reduce the risk of rupture [5]. Typical hemodynamic studies of flow in aneurysms involves investigation of complex flow patterns that may influence rupture and the effectiveness of stent implants in reducing the flow into the aneurysm sac [32–36]. Indicators of abnormal WSS distribution have been proposed to predict arterial locations susceptible to aneurysm development [37, 38].

1.3 Blood flow modeling

There are two major approaches taken with fluid dynamics studies of blood flow in arteries. One is concerned with the propagation of the pressure pulse and the pressure-flow relationship along the arterial network with the aim of measuring and interpreting blood flow and pressure waveforms. The other approach is focused on the flow patterns and the WSS distribution in arteries with the goal of understanding the relationship between WSS and the initiation of arterial diseases. The propagation of pulse waves is modeled using one-dimensional linear or weakly non-linear theory while the time-dependent flow patterns in complex three-dimensional arterial geometries are investigated with computational tools capable of solving the full Navier-Stokes non-linear equations and the fluid-structure interaction models for flows where the arterial wall compliance has a significant effect on the blood flow. In this section, a brief overview of current mathematical and computational models on blood flow—which includes lumped parameter models (for pressure pulse propagation) and three-dimensional hemodynamics simulations—is given.

1.3.1 Lumped parameter models

At the larger scale, blood flow exhibits wave-like behavior with pulse waves traveling from the heart into arteries. Alterations in the arterial network structure (e.g., by bypass surgery) and vessel wall properties can lead to changes in wave reflections, which, in turn, will alter the flow waveforms in distal vascular districts. A change in the local waveform affects the velocity distribution across the lumen, which, in turn, alters the WSS distribution and can result in pathological responses in the endothelium. To understand the function and the wave-like behavior of the arterial system, simplified models based on lumped parameter models described below have been developed and studied [39]. The basic concept underlying simple lumped parameter models assumes that distributed properties of the arterial system such as the resistance and compliance of individual arteries can be grouped into one lumped term, the total (peripheral) systemic resistance and the total systemic compliance, respectively. The purpose of the lumped parameters models is to estimate the total hydraulic load of the heart and the volumetric outflow from pressure measurements in the aorta.

The first lumped parameter model of the arterial system, consisting of two elements that account for the arterial resistance and compliance, was developed from the observation that the variations in pressure are related to the elasticity of the large arteries and it was proposed as an analogy to the Windkessel used in fire engines and depicted in Figure 1.6 (adapted from [39]). The resistance to flow is found in resistance vessels such as small arteries and arterioles whereas the compliance element is determined by the elasticity of the large arteries. Either the aortic pressure waveform or the aortic volumetric waveform is provided as input while the flow or pressure, respectively, is obtained as output. The analogy

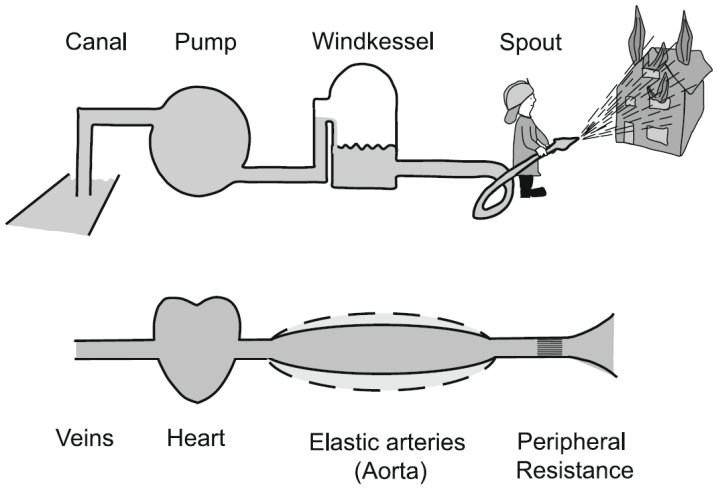

Figure 1.6. Simplified model of the cardiovascular system as a Windkessel system

between hydraulic networks and electrical circuits has led to the use of electrical circuit analysis in defining and solving lumped parameter models. In Figure 1.7, adapted from [39], the electric circuit representing the two-element lumped parameter model is shown where R is the peripheral or terminal resistance and C is the capacitance element representing the total arterial compliance. Other lumped parameter models include the three- and four-element Windkessel models (Figure 1.7), consisting of resistive, compliant, and characteristic impedance elements were proposed to improve the behavior of the model at medium to high frequencies [40].

Simple Windkessel models with their physiologically relevant parameters (the peripheral resistance, the total arterial compliance, and the aortic characteristic impedance) have been extensively used to describe and study various aspects and functions of the circulatory system. Clinically relevant uses of the Windkessel model include derivation of the ambulatory arterial stiffness index and of cardiac output [41–43], estimation of the total load on the heart [40], modeling of peripheral beds in distributed models, calculation of load in an artificial heart and valve

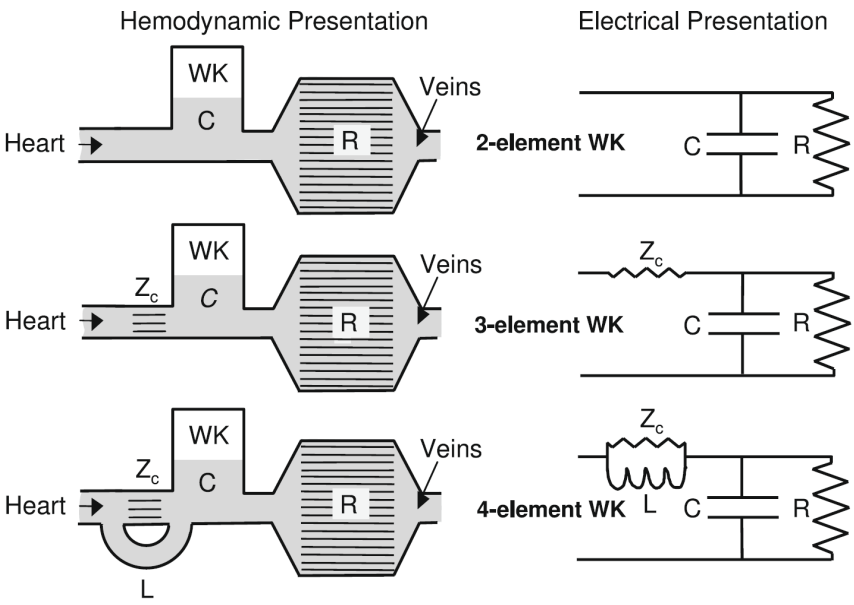

Figure 1.7. Two-, three-, and four-element lumped models shown in hydraulic and electrical circuit equivalent forms

studies [44–46], assessment of right ventricular afterload, etc.

1.3.2 Multiscale models

The distributed lumped parameter model offers insight into large scale behavior of the blood flow and can provide useful information on blood volume distribution in the arterial system. On the other hand, at the small scale, local flow features that can have a global effect on the circulation depend strongly on the particular topology of a specific arterial segment or bifurcation. To investigate the local behavior of blood flow, more detailed three-dimensional models that capture the vessel geometry and involve equations describing the motion of the blood and its interaction with the compliant vessel wall are needed. In order to capture both the systemic and local effects of the blood flow, lumped models coupled with one- or three-dimensional models have been developed. These multiscale models can provide greater flexibility in terms of model complexity and computational

requirements. For instance, using the aortic flow as input, the flow and pressure waveforms in a particular vascular district can be estimated by using lumped models. This information can then be used as a boundary condition for higher dimensional models.

One of the early studies that investigated the multiscale modeling of the circulatory system employed a distributed lumped model coupled with a one-dimensional models representing a straight arterial segment [47]. A schematic of the multiscale model is presented in Figure 1.8. The electrical network equivalent of the lumped model was solved to determine the pressure and flow values upstream and downstream, respectively, of the one-dimensional tube section and then the one-dimensional model equations are solved to find the pressure and flow distribution inside the segment. It was found that the computed flow waveform upstream of the one-dimensional segment was unperturbed while the downstream waveform exhibited wave reflections which cannot be captured with simple lumped models. The model showed promising results by combining the simplicity of the lumped model with the improved accuracy of the one-dimensional model and led the authors to propose the coupling of the lumped parameter and one-dimensional models to more complex, three-dimensional models to provide accurate boundary conditions for the latter model.

In a subsequent study, a coupled one-dimensional and three-dimensional model was employed [48]. The study sets the mathematical and numerical basis for formulating and solving the coupled multiscale model. A finite element solver is used to estimate the pulse wave propagation and the flow and pressure waveforms (one-dimensional model) which are used as boundary conditions to the three-dimensional model of a straight arterial segment. The results showed good predictions for traveling pulse wave phenomena and the effects of spurious reflec-

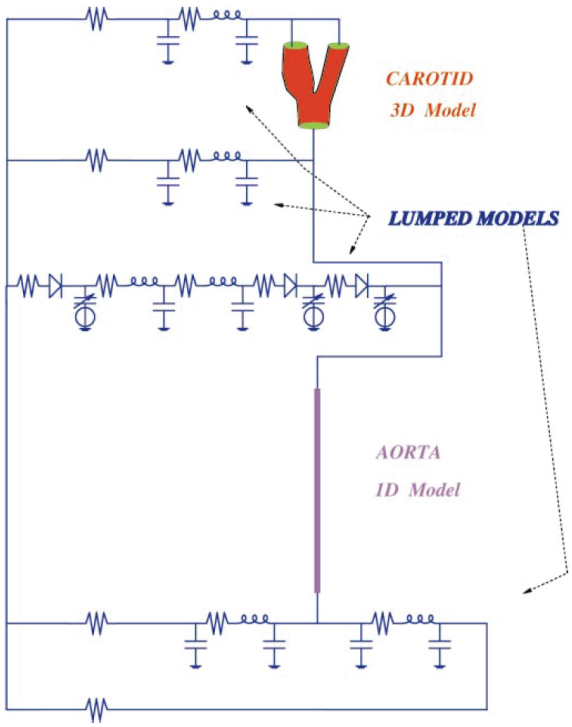

Figure 1.8. Multiscale blood flow modeling showing the coupling of lumped parameter models with one- and three-dimensional models

tions were significantly reduced. A similar multiscale coupled model was used to investigate blood flow through a realistic carotid bifurcation [49–51], the cerebral arteries [52, 53], and the pulmonary arteries [54].

1.3.3 Three-dimensional models

The mathematical models discussed so far do not account for the complex flow patterns and geometric shapes of the cardiovascular system and treat arteries as straight, round pipes. For a complete description of the blood flow through arteries the geometrical effects on the flow must be included as well, especially since hemodynamic factors such as WSS have a direct influence on the arterial wall and the development of arterial diseases. Therefore, a large number of fluid dynamics and bioengineering studies employing physical experiments, numerical

simulations, and mathematical analysis of the arterial hemodynamics continue to be performed to understand the complex flow patterns and the WSS distribution that occur in complex, three-dimensional arterial geometries. These studies have evolved from simple, steady flows in rigid straight tubes, bifurcations, and asymmetric branches to flows that include compliant walls, real arterial geometries (bifurcations, aneurysms, circle of Willis), and time dependent effects as well as non-Newtonian blood models.

Arterial geometries, first approximated by idealized models in which generic geometrical features are used to provide general estimates about WSS distribution, are increasingly based on real physiologic data acquired from patients as advancements in medical imaging technologies have allowed for the imaging of any part of the cardiovascular system. Magnetic resonance imaging (MRI) and x-ray computed tomography (CT) are widely used to capture the geometry of real arterial segments. From the MRI or CT data the contour of the arterial segment of interest is extracted and a surface representing the arterial wall is generated. Typically some degree of image processing such as segmentation, image artifact removal, edge detection, and smoothing is involved and this might introduce additional uncertainties regarding the true topology of the arterial wall. Then, the surface representing the arterial wall is converted into a computational mesh for use in either finite element or finite volume solvers which can yield detailed flow solutions. The flow rate at the inlet or the pressure at the inlet and outlet of the computational domain are provided as boundary conditions for these three-dimensional models. These boundary conditions represent either physiologic data published in the literature or directly measured in patient-specific cases or is indirectly derived by using lumped parameter or one-dimensional models as discussed in the previous sections. For physiologic flow data, Doppler ultrasound (US) and

MRI are the methods of choice for measuring *in vivo* blood flow velocity (US) or volumetric flow rates (MRI).

The wall shear stress distribution is sensitive to small geometrical perturbations and flow transients in pulsatile flow conditions. Three-dimensional CHD models are capable of capturing the great complexity of blood flow in physiological arterial topologies and can provide valuable information about cardiovascular flow and function especially in patient-specific cases. Vascular imaging and blood flow measurement techniques allow the acquisition of both the unique patient's vascular geometry and blood flow waveform which can be incorporated into CHD models. Various aspects of the cardiovascular flow such as flow in healthy and diseased arteries or flow variability due to diurnal cycle or amount of physical activity can be modeled. Also, the design of surgical implants such as stents, ventricular assist devices, total artificial hearts, arterial grafts, flow diverters, and others as well as surgical procedures are benefiting from the use of three-dimensional models. The general trend in this research area is toward specialized, patient-specific modeling of blood flow using realistic arterial and flow data [55].

Early three-dimensional studies of blood flow through arteries involved experimental work with glass or plastic cast models of idealized or real arterial segments involving both healthy or atherosclerotic cases. The carotid bifurcation, pictured in Figure 1.9, and in particular the carotid sinus are prone to atherosclerotic plaque development and hence have been the subject of numerous experimental as well as computational hemodynamics studies. One of the first such studies that has been widely cited for correlating disturbed flow patterns and the development of atherosclerotic plaques involves the visualization of flow patterns in a glass cast of a human carotid bifurcation as pictured in Figure 1.9a (adapted from [56]). Hydrogen bubble visualization indicates complex helical flow patterns and flow

separation—under steady flow at Re = 800—in the region of the carotid sinus (the region between B and C, Figure 1.9a) which is associated with atheroclerotic plaque development. As the flow enters the internal carotid, the flow perturbations decrease distal to the carotid sinus (region D) [56].

Numerical hemodynamics studies, taking advantage of newer and more accurate CT and MRI imaging techniques, are able to simulate blood flow in real carotid bifurcation geometries as exemplified in Figure 1.9b in which time-averaged WSS contours are plotted from the work by Hoskins and Hardman [57]. The computation of numerical solutions of flows in such complex geometries provides unprecedented details about flow patterns, velocity profiles, and WSS and pressure distributions especially when visualized with immersive three-dimensional technology. These in-depth details are not readily available from experimental models or from idealized computational models and have the potential of providing valuable information for the clinician when treatment options for diseased arteries or the heart are explored. Also, one has to bear in mind the assumptions and simplifications associated with numerical solutions and interpret the results within the limitations of the blood model.

Computational hemodynamics studies have been performed on almost every part of the cardiovascular system from aortic, coronary, cerebral, and pulmonary arteries to ventricular and heart motion. Attempts to quantify changes in WSS distributions that correlate with the development of atherosclerotic plaque or aneurysm formation have also used computational hemodynamics [37, 38, 58]. Indices based on WSS gradients such as the oscillatory shear index (OSI) proposed in [58], the aneurysm formation indicator (AFI) proposed in [37] and the gradient oscillatory number (GON) proposed in [38] are being used to identify potential sites along the arterial wall where atherosclerotic plaque and aneurysm might de-

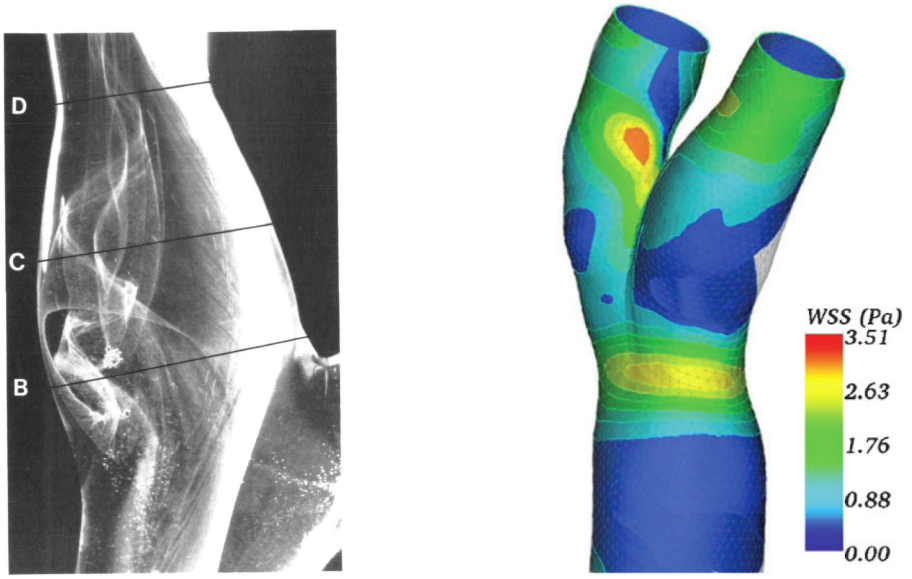

(a) **(b)**

Figure 1.9. Flow in the carotid bifurcation obtained from an experimental model (a) and from a three-dimensional computational hemodynamics model (b)

velop. A detailed discussion about computational hemodynamics results is beyond the scope of this work but excellent reviews on the current state of research in this highly active field can be consulted [3, 25, 55].

1.4 Purpose and overview

The role of hemodynamics in the development of arterial diseases and the clinical complications associated with arterial stenting have motivated much of the present work. The unsteady flow over real deployed stents acquired from high-resolution microCT data is investigated with a focus on WSS reversal occurrence for both intracranial and coronary stents. The occurrence of wall flow reversal during the deceleration phase of flow waveforms observed from flow simulations in stented tubes motivated the investigations of the waveform influence on flow

reversal. The time-dependent aspects of blood flow that result in flow reversal and oscillatory WSS are explored by parameterizing the relevant features of the volumetric flow rate waveform specific to systemic arteries.

The present work consists of two major parts. The first one regards the acquisition of real deployed stent geometry and computational hemodynamics simulations of unsteady blood flow. High-resolution imaging of real stents is compared with current clinical CT imaging (chapter 2). Computational hemodynamics simulations are performed to identify regions of flow reversal and oscillatory WSS in arterial graft tubes and arterial segments implanted with different types of stents and under various unsteady flow conditions (chapter 3). The second part of this work is concerned with flow waveform parameterization (chapter 4) and investigation of the flow conditions that determine flow reversal at the wall and hence oscillatory WSS (chapter 5). The analysis is applied to both sinusoidal and physiologic flow waveforms. An overview of the results and future directions of research are discussed at the end (chapter 6).

Chapter 2

Stent deployment and imaging

The development of atherosclerotic plaques in systemic arteries usually leads to blood flow reduction and to increased risk of plaque rupture and blood flow blockage during the late stages of atherosclerosis. Angioplasty, as discussed in chapter 1, section 1.2, is a preferred treatment method for atherosclerosis with vascular interventions consisting of stent implantation being performed in greater numbers than balloon angioplasty, the first interventional method developed for atherosclerosis treatment. Evaluation of stent placement inside arteries and subsequent follow-up to assess the effectiveness of stenting and any negative outcomes such as restenosis or thrombosis are performed with computed tomography (CT) imaging. This medical imaging method is also used to acquire the complex geometric shape of arterial segments for use in computational hemodynamics simulations. However, limitations in both spatial and temporal resolution of clinical CT modalities pose challenges in imaging stented arteries in which relatively small structures such as stent struts need to be resolved at a high enough resolution to permit the accurate reconstruction of the arterial wall and stent struts.

In this chapter, four CT modalities (two clinical and two pre-clinical) are used to visualize the deployment of a coronary stent in a straight tube and assess the quality of three-dimensional stent surface reconstructions as previously published in [59]. Also, the deployment characteristics of intracranial and coronary stents are assessed with high-resolution microCT with the goal of demonstrating the capability of microCT in imaging real stent deployment anomalies such as strut

prolapse, misalignment, and impingement.

2.1 Introduction

Stents are small wire meshes made of stainless steel or alloys (nitinol) that are implanted in arterial regions where atherosclerotic plaque or aneurysms have developed. In the former type of intervention, the purpose of the stent implant is to act as a scaffold for the arterial wall such that normal flow is restored while also providing support for the atherosclerotic plaque to prevent its detachment from the wall. An example of a stenosed coronary artery imaged pre- and post-stenting with CT is shown in Figure 2.1 (adapted from [60]). Contrast agent (light gray) is used to indicate blood flow. In the left panel, a three-dimensional CT reconstruction of the heart shows the stenosed main coronary artery in the vicinity of the aortic tube graft while in the middle and right panels a two-dimensional plane shows the coronary lumen pre- and post-stent implantation, respectively. In the latter type of intervention, the stent is deployed at the aneurysm neck to reduce the flow of blood inside the aneurysm sac therefore reducing the flow velocity and hence the shear rate. This can produce a thrombus or blood clot inside the aneurysm sac that will stabilize the aneurysm and greatly decrease the risk of rupture. Also, it is common practice to perform multiple stent deployment for a single intracranial aneurysm in order to increase flow blockage inside the sac [61–64].

During the stent deployment procedure, a catheter is introduced through the iliac artery and guided toward the deployment site with the help of fluoroscopic CT imaging mode. Post-stenting and follow-up evaluation of stent deployment are performed with CT imaging modalities such as 64-multislice CT (MS-CT), C-arm cone beam CT (C-arm CT, or angiographic computed tomography (ACT),

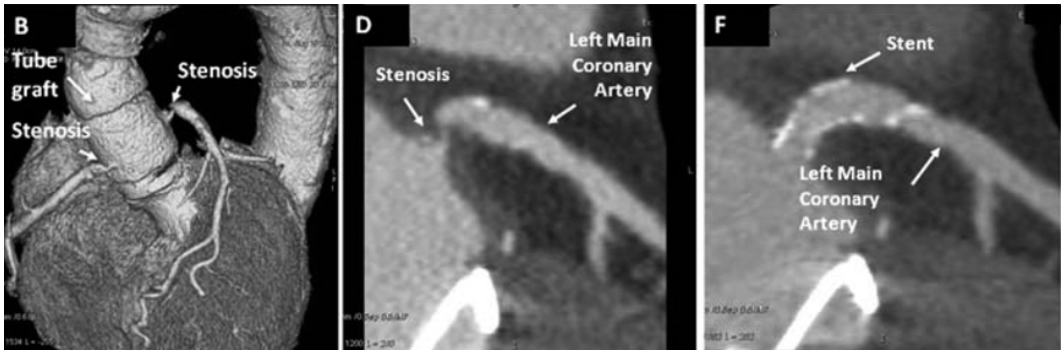

Figure 2.1. Computed tomography visualization of a stenosed coronary artery before and after stent implantation

DynaCT, XperCT) or flat panel CT (FP-CT). With a relatively short scanning time and reasonable spatial resolution, cardiac motion-gated MS-CT are used for coronary stent evaluation while C-arm CT and FP-CT, with longer scanning times, are mainly used for intracranial stent evaluation.

Increased temporal and spatial resolution of newer MS-CT systems have made these imaging systems capable of providing more accurate visualization of stented lesions with a sensitivity of 99% in detecting significant coronary artery disease [65, 66]. However, the specificity remains at 68%, still relatively low, due to blooming effects and other imaging artifacts especially in stented arteries with diameter less than 3 mm [67]. Blooming effects occur because of beam hardening, causing the struts to appear thicker and resulting in underestimation of the inner stent lumen [68]. Partial volume effects can occur when an object lying off-center protrudes partially into the x-ray beam [69]. Partial volume averaging is based on limited spatial resolution yielding a CT number (i.e., density in Hounsfield unit) that represents the average attenuation with a given voxel.

Spatial resolution for most 64-slice MS-CT scanners is in the range of $0.3 \times 0.3 \times 0.625$ mm whereas strut dimensions of most coronary artery and intracranial stents are 0.150 mm or less [68]. Because of these limitations inherent to cross-sectional

imaging tools, major efforts are being made to improve the visualization quality of small stents using invasive imaging techniques such as intravascular ultrasound (IVUS) or optical coherence tomography (OCT) [70, 71]. Imaging of stent deployment as well as stent-induced thrombosis by OCT has been performed *in vivo* and has shown promising visualization of stent patency, strut malapposition, and in-stent thrombosis [72]. Stent strut fracture was detected by *in vivo* OCT imaging during a follow-up study performed by Okamura and Matsuzaki [73]. The stent structure inside the artery was visible but small gaps in the reconstructed stent image are present and the reconstruction quality of the stent surface appears to be less than that of the microCT, thus, warranting the need for further studies that directly compare three-dimensional OCT and microCT stent reconstructions.

Stent placement in cerebral arteries for aneurysm treatment or intracranial stenosis is relatively new and the number of stent interventions has increased due to the development of small self-expanding intracranial stents made of compliant alloys such as nitinol that can be safely deployed in tortuous cerebral arteries. With relatively high in-stent restenosis rate of up to 30% for stenosed cerebral arteries [74], reliable assessment of stent patency, deployment characteristics, and the detection of adverse mechanics is of interest. The importance of stent deployment anomalies and their potentially adverse hemodynamic effects has been investigated by Benndorf *et al.* [75]. C-arm CT, although offering lower temporal resolution compared to MS-CT, is less prone to metallic artifacts and also provides higher spatial resolution (approximately 0.17 mm isotropic), thus improving the visualization of small metallic stent implants [76, 77]. A newer preclinical imaging modality, FP-CT consists of a flat detector mounted into a conventional CT gantry and also provides higher spatial resolution than MS-CT but comparable to C-arm CT with potential future application for imaging of small vessels and stents [78].

Computational hemodynamics studies on patient-specific data use CT angiography images of arterial segments of interest to reconstruct the arterial lumen. The spatial resolution of clinical CT angiography, in the range of 0.1 mm, is acceptable for arterial wall imaging and reconstruction as discussed by Steinman [79]. However, clinical CT resolution is similar to or even larger than the dimension of stent struts—in the range of 0.06–0.15 mm—that are used for atherosclerotic plaque and aneurysm interventions. MicroCT is a high-resolution imaging cone beam CT technique that plays an increasing role in vascular imaging of small animals or *ex vivo* specimens [75, 80, 81]. With a spatial resolution of approximately 4 μm, microCT can provide sufficient resolution for stent imaging and stent geometry reconstruction for computational hemodynamics as shown by Benndorf *et al.* [75, 82], and Ionescu *et al.* [59].

The first part of this chapter is concerned with the evaluation of the image quality of a small metallic coronary stent as determined by the spatial resolution of two clinical and one preclinical CT systems in comparison to high-resolution microCT. In the second part of this chapter, the deployment characteristics of both intracranial and coronary stents are evaluated from geometric reconstructions—stent and wall—based on high-resolution microCT imaging.

2.2 Previous work

2.2.1 MS-CT stent imaging

Stent visualization performed with MS-CT scanners, including 64-slice scanners that are commonly used for noninvasive coronary imaging, provide stent reconstructions that are often compromised by partial volume averaging artifacts.

Maintz *et al.* [83] used a 4-slice MS-CT to *in vitro* evaluate 19 stents deployed in straight polymer tubes and found that the size of the imaging artifacts depends on the stent material, the metal content, and strut diameter. The study also concluded that stent lumen can only be partially visualized and evaluation of in-stent restenosis is not reliable.

Suzuki *et al.* [84], using a 16-slice MS-CT device, visualized the *in vitro* deployment of a coronary stent in a straight tube with and without simulated stenosis. The investigation found that the quality of lumen imaging is affected by the vessel diameter, convolution kernel, and orientation of the vessel with respect to the x-ray beam axis of rotation. Otsuka *et al.* [66] compared the visibility of a metallic stent and a polymer stent in the same coronary artery. Although the vessel segment stented with the bioabsorbable stent was clearly visualized, the in-stent lumen evaluation in the adjacent segment stented with the metallic stent was clearly hampered by the blooming struts. Accurate assessment of stent apposition to the arterial wall is important as both stent oversizing and undersizing have adverse effects. It was found that undersizing of the stents is one of the main predictors for coronary stent thrombosis that was seen in 2.1% of cases studied [85].

In an effort to minimize partial volume averaging artifacts, more recently dual energy CT (DECT) systems with optimized x-ray tube voltage have been used. Boll *et al.* [86] have obtained slightly better stent imaging and in-stent lumen assessment in comparison with single-energy CT by reducing image noise and enhancing contrast. By lowering the x-ray tube voltage of the high energy beam the lumen depiction was enhanced in smaller stents, whereas for larger stents, composed of more mesh material, a higher tube voltage provided better visualization. However, significant improvement of stent deployment assessment and in-stent lumen measurement cannot not be achieved with DECT [87]. Although the use of

dedicated post-processing software with edge-enhancing convolution kernels may improve image quality for better evaluation of stent patency mainly in cardiac CT [83, 88], the resolution is insufficient to resolve critical details of strut apposition to the wall and to generate accurate stent and vessel wall geometries for use in computational hemodynamics studies since the stent-wall boundary is not well imaged.

2.2.2 C-arm CT and FP-CT stent imaging

It has been shown that C-arm CT is capable of providing high-resolution data sets that allow *in vitro* and *in vivo* visualization of fine structural stent details that are not obtainable by MS-CT imaging methods [76, 77, 89, 90]. The use of this technology for evaluation of small stents in the intracranial circulation is currently expanding and plays an increasing role for post-stenting evaluation and follow-up studies. Buhk *et al.* [89] have demonstrated the superiority of intravenous angiography using C-arm CT versus conventional CT angiography using an MS-CT scanner.

C-arm CT, with the size of one detector element being 154 mm and an isotropic resolution 0.17 mm, can be obtained when an unbinned acquisition mode is used. This mode, while experimental, is used in this work and in Ionescu *et al.* [59] and provides so-called 2K images (2480×1920) versus conventional 1K imaging (1024×1024) in digital subtraction angiography systems. This increased C-arm CT spatial resolution has provided new insights into stent geometry that allow detection of adverse mechanical phenomena such as strut prolapse and stent kinking, when stents are placed in curved or irregular vessels [77]. Thus, C-arm CT improves the understanding of the deployment mechanics of intracranial stents over that obtained from MS-CT imaging.

2.2.3 MicroCT stent imaging

The use of microCT in stent imaging is relatively new and few studies have been performed to assess stent deployment in polymer tubes or *ex vivo* arterial segments. Connolley *et al.* [91] investigated the shape of a stainless steel, balloon-expandable coronary stent at different deployment stages with a simulated stenosis inside a latex tube. The high-resolution (5.3 μm isotropic) microCT image set provided highly detailed stent strut configurations. Some attenuation artifacts were present due to the metallic struts which have high attenuation values. These artifacts affected the regions surrounding the struts by masking them.

The results on microCT stent imaging presented in this work have been published previously in [59, 75, 82]. In a more recent study by Morlacchi *et al.* [92], a balloon-expandable stent deployed *in vivo* inside the coronary artery (which was subsequently excised) was imaged with microCT at a 12 μm isotropic resolution. Overexpansion and asymmetric stent deployment were noticed and the authors correlated these non-uniformities with the amount and distribution of neointimal hyperplasia covering the stent struts.

2.3 Methods

The stent deployment, CT imaging techniques, and surface reconstructions are described in this section. A comparison between stent deployment visualization and geometry reconstruction obtained from different clinical and pre-clinical CT is performed on a single coronary stent deployed in a polymer tube while the study on stent deployment characteristics visualized by microCT is performed using a variety of intracranial and coronary stents.

2.3.1 Stent deployment

The stents used in this work are deployed in straight polytetrafluoroethylene tubes (PTFE; W. L. Gore and Associates, Newark, DE) that are commonly used as arterial grafts during cardiovascular interventions while one stent is deployed *ex vivo* in an excised canine artery segment. All stent deployments were performed by Goetz Benndorf, M. D., Ph. D., at The Methodist Hospital Research Institute, Houston, TX. The self-expanding intracranial stents used in this study are: a 4.5×30 mm open-cell design Neuroform Treo (NF3) manufactured by Boston Scientific, Freemont, CA, a 3.5×20 mm NF3 (deployed in the canine artery), a 4.5×28 mm closed-cell design Enterprise (Cordis Neurovascular, Miami Lakes, FL), a 3.0×19 mm braided wires design Leo (Balt Extrusion, Montmorency, France), and a 3.0×8.0 mm hybrid design (open-cell/closed-cell) Pharos (Micrus Endovascular, San Jose, CA). The balloon-expandable coronary stents deployed in PTFE tubes are: a 3.0×20 mm closed-cell design Cypher (Cordis, Miami Lakes, FL), 3.0×27 mm closed-cell design BxVelocity (Cordis, Miami Lakes, FL), and a 3.0×16 mm open-cell design Taxus Express (Boston Scientific, Freemont, CA). The Cypher stent has the same shape as the BxVelocity stent as it represents the DES version of BxVelocity BMS.

2.3.2 CT acquisition and image reconstruction

MS-CT reconstruction

Images roughly perpendicular to the long axis of the Cypher stent and PTFE tube phantom are acquired with a clinical MS-CT system (GE LightSpeed VCT Series, GE Healthcare, Nyskayuna, NY) with a 32×0.625 mm detector configuration, Circle of Willis protocol, and the following parameters: 120 kV tube voltage,

335 mA tube current, field of view (FOV) 40 mm, 0.4 s helical rotation time, 3.8 s exposure time, SFOV: Head, 5.0° gantry tilt. Image reconstructions are performed using a "detail" kernel. The detector spatial resolution and image voxel size are given in Table 2.1. The MS-CT stent imaging and reconstruction were performed by Goetz Benndorf, M.D., Ph.D., at The Methodist Hospital Research Institute.

C-arm CT reconstruction

The second imaging dataset of the Cypher stent as well as another dataset of the NF3 stent and tube phantom is obtained using a single flat detector C-arm CT angiographic system with a 30 × 40 cm CsI/amorphous Silicon detector (Axiom Artis dBA, Siemens Medical Solutions, Germany) with the following parameters: 70 kVp, 32 mA, 20 s rotation time, 0.4° increment, 543 projections, microfocus 0.3 mm, total angle: 219°, 2480 × 1920 matrix (2K matrix, DynaCT, Siemens Medical Solutions), and a dose of approximately 60 mGy computed tomography dose index (CTDI), comparable to the dose of a standard CT scan of the head (MS-CT).

Image reconstructions were performed by Goetz Benndorf, M.D., Ph.D., using a dedicated, commercially available workstation (Leonardo, Siemens) using a "bonesharp" kernel and a 512 × 512 reconstruction matrix. The voxel size is 0.096 mm isotropic (Table 2.1).

FP-CT reconstruction

The FP-CT imaging was performed by Dianna D. Cody, Ph.D., at The University of Texas M. D. Anderson Cancer Center, Houston, TX using a preclinical research flat-panel CT system manufactured by GE Global Research Center, Niskayuna, NY [81]. The Cypher stent and tube phantom was positioned near

gantry iso-center and a single volume of data ($\sim$ 40 mm long) was obtained using 140 kVp, 30 mA, 8 s rotation, and 1000 views. A standard reconstruction algorithm was used with a voxel size of 0.04 mm (Table 2.1).

The CTDI dose is estimated using a 160 mm acrylic CTDI phantom, a standard CT pencil ion chamber (Capintec, Ramsey, NJ), and a calibrated electrometer (Keithley 3505A, Cleveland, OH) as described by Ross *et al.* [81]. For the VCT (MS-CT), the dose is calculated to be 54 mGy, for the C-arm CT is 60 mGy, and for the FP-CT is 85 mGy.

MicroCT reconstruction

The microCT datasets were obtained by John A. Hipp, Ph.D., at Baylor College of Medicine, Houston, TX, using a preclinical microCT specimen scanner, eXplore Locus SP (GE Healthcare, Niskayuna, NY), with the following parameters: 80 kV, 3 s rotation time, 0.4° increment, and 500 projections. To save the dataset in DICOM format for further post-processing, the image reconstructions were performed using eFilm (MERGE Healthcare, Milwaukee, WI) with a standard reconstruction algorithm and a voxel size of 14 μm. The use of microCT for *in vivo* imaging is limited by the long scan time (e.g., 4 hours for a 30 mm long specimen) and high levels of x-ray radiation.

The low attenuation (radiopacity) of the PTFE tube is in the range of the background noise, causing poor differentiation between the wall lumen. This is not an issue when the sole purpose of CT visualization is stent imaging in which case the differentiation between stent struts and the wall is more than adequate. However, when the luminal face of the wall and the details of the stent strut apposition to the wall are needed, the surface representing the lumen must be reconstructed as well. To ensure a clear segregation between the tube wall and the

Table 2.1. Computed tomography (CT) detector resolution and reconstruction voxel size

Scanner	Application	Detector resolution (mm)	Image voxel size (mm)
MS-CT[1]	Clinical	0.74[3]	$0.180 \times 0.180 \times 0.625$
C-arm CT	Clinical	0.13[3]	$0.096 \times 0.096 \times 0.096$
FP-CT[2]	Pre-clinical	0.26[4]	$0.040 \times 0.040 \times 0.040$
MicroCT	Pre-clinical	0.04[3]	$0.014 \times 0.014 \times 0.014$

[1] multislice CT [2] flat panel CT [3] measured [4] vendor supplied

lumen during image segmentation the tube is filled with contrast agent such that the lumen would have attenuation values higher than the wall but lower than the struts. For MS-CT, C-arm CT, and FP-CT, a non-diluted iodine solution is used (Hypaque 76, Amersham Health, Princeton, NJ), while for the microCT a barium sulfate suspension solution (60% w/v, 41% w/w, E-Z-EM, Westbury, NY) is used.

2.3.3 Surface reconstructions

The reconstructed stent and PTFE tube image generated by each CT device is exported as DICOM format for image post-processing and analysis. For the comparative study on stent visualization with MS-CT, C-arm CT, FP-CT, and microCT no additional image post-processing is performed. The datasets are loaded on a Leonardo workstation (Siemens Healthcare) to generate maximum intensity projections (MIPs) of 4 mm plane thickness (approximate PTFE tube diameter) and of 0.07 mm plane thickness (half the diameter of the stent strut). First, MIPs are created using identical window and level settings and in a second step these settings are adjusted to obtain the best subjective rendering for each CT imaging method. To visualize and reconstruct the stent surface, the DICOM datasets, obtained using the four different CT methods, are loaded into an image

processing and visualization software package, Amira 4.1 (Zuse Institute Berlin, Germany). The datasets are subjected to an image intensity threshold to identify the stent struts boundary. These segmentation threshold values are chosen such that the resulting surface resembles as accurately as possible the stent shape and architectural detail and conforms to the stent's dimensions. Using these threshold values, the Amira segmentation editor is used to separate the voxels representing the stent struts. Image analysis of the attenuation values distribution is performed by defining a sample line two cross-sectional planes (passing through one regular strut region and one interstrut region) and recording the attenuation values (gray intensity values). The sample data are plotted using MATLAB 7.9 (MathWorks, Natick, MA).

For the stent datasets acquired from microCT and used in this work to investigate stent deployment characteristics, both the stent and wall surfaces are reconstructed using the Amira 4.1 segmentation editor as described above. A cross-sectional slice from the NF3 stent dataset acquired with microCT is shown in Figure 2.2. The high-intensity pixels (bright white) represent the stent struts while the lumen is represented by lower intensity pixels (gray). Based on the intensity of each pixel, the stent geometry can be reconstructed by selecting the pixels with a certain intensity range that define either the strut or the lumen as shown in Figure 2.2b. The metallic material of stent struts exhibits high x-ray attenuation values and therefore represents the highest intensity pixels. The attenuation values for the contrast agent are much higher than the values of the PTFE material or the arterial wall (for the canine artery stent deployment) providing adequate differentiation between lumen and the wall. The surface generator module implemented in Amira 4.1 is used to construct the stent surface and the wall surface separately or combined. The cylindrical surface of the stent and tube wall can be projected

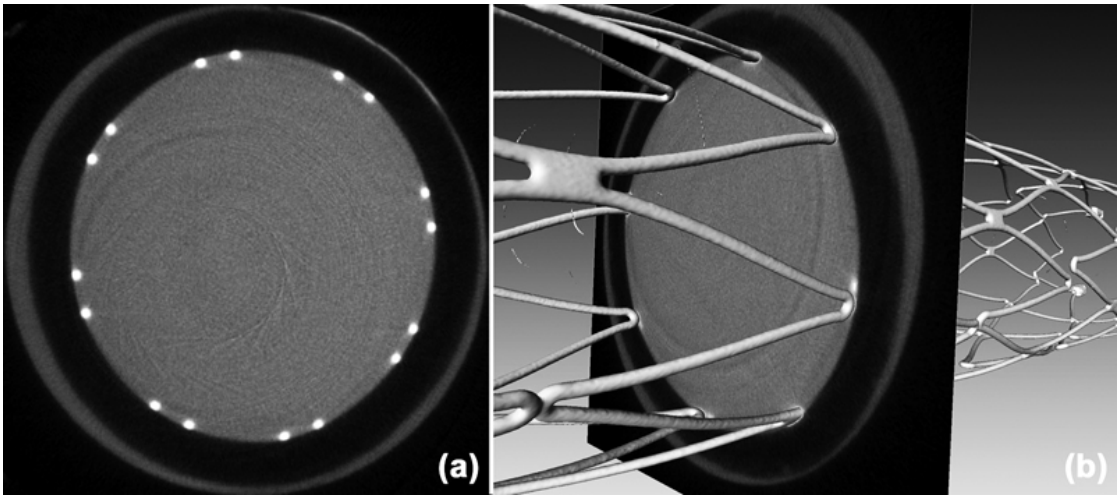

Figure 2.2. Micro computed tomography slice showing the lumen (gray) and stent struts (white) in (a) and the reconstructed stent surface in (b) based on attenuation values

on a planar surface for enhanced stent deployment visualization by remapping the nodes of the triangles defining the original surface. This is accomplished by an in-house algorithm developed by Max Lingamfelter in MATLAB [93].

The blooming and partial volume rendering artifacts present in the MS-CT imaging of stents do not allow for the reconstruction of the wall surface. The C-arm CT and FP-CT datasets also contain imaging artifacts that do not allow for the accurate reconstruction of the wall surface especially in the vicinity of the stent struts, vertices, and markers. Therefore, for the stent deployment study the wall surface is reconstructed from imaging data acquired with microCT.

The datasets obtained from microCT imaging also contain artifacts, mainly attenuation artifacts caused by the high attenuation values specific to metallic stent struts. Some examples of the artifacts observed for the NF3 stent deployment in the PTFE tube are shown in Figure 2.3. The region marked in red in Figure 2.3a represents the lumen in one cross-sectional slice. A boundary surface representing the luminal face of the wall and the stent struts is generated from the entire dataset

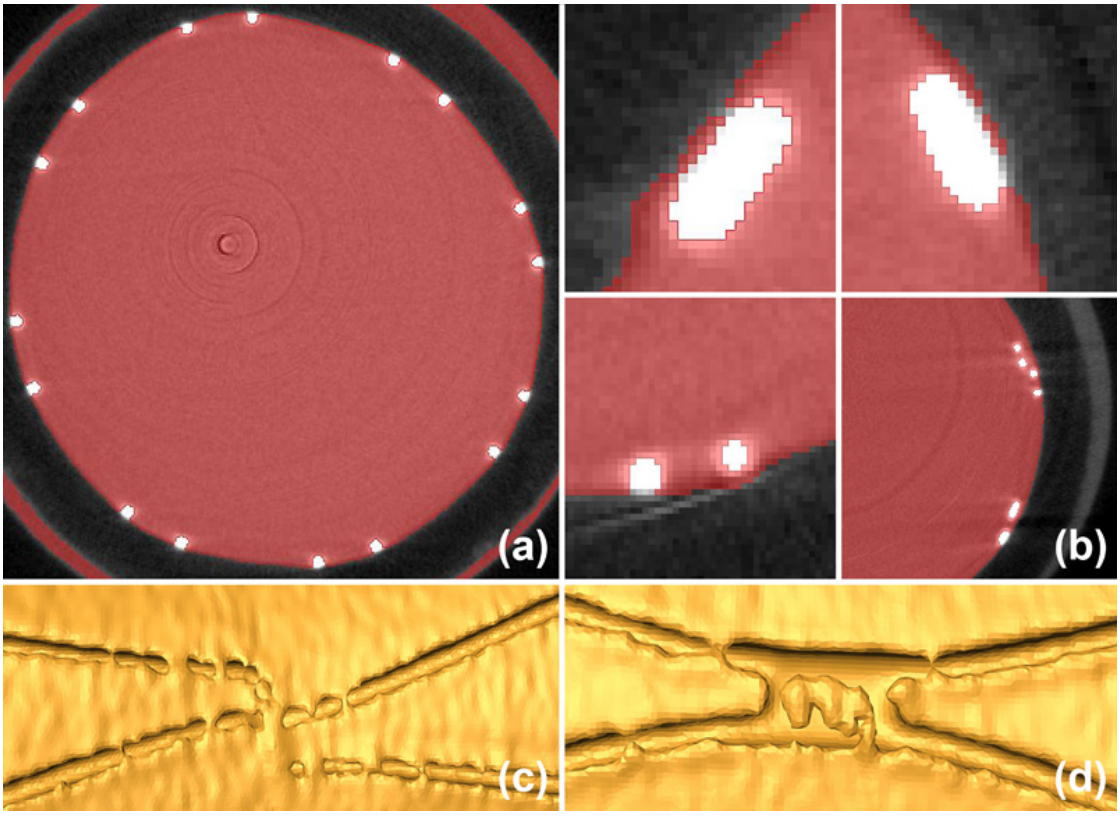

Figure 2.3. The lumen region is shown in red (a). Attenuation artifacts are present near the wall and strut regions in microCT images (b). These artifacts result in false strut prolapse (c) & (d)

of cross-sectional slices. Also, this boundary surface is exported as a faceted surface for later use in computational hemodynamic studies where it will be defined as a wall boundary.

Attenuation artifacts such as those depicted in the two upper images and the lower-left image of Figure 2.3b occur at different locations between the struts and the wall and can result in false lumen regions appearing under stent struts. These artifacts can be removed by defining threshold sizes for small pixel regions (also called islands) that are surrounded by larger regions of higher or lower pixel intensities. For example, if an island defined by 10 pixels or less and is surrounded by another region, then the island pixels are assigned to the larger region. However,

care must be taken as the size of the small strut regions can also be considered islands and can be wrongfully assigned to the lumen region. Also, real strut malapposition such as the one shown in the lower-right corner image of Figure 2.3b should not be confused with imaging artifacts. If these artifacts are not removed, they will result in false lumen surfaces that will be generated on the wall side of the stent struts as exemplified in Figure 2.3c & 2.3d—where the lumen boundary surface is visualized from the outside of the PTFE graft tube. Inspection of the boundary surface shown in Figure 2.3c at a misaligned strut vertex and in Figure 2.3d at a strut connector clearly demonstrates that the small surfaces generated between the strut and the wall do not represent strut prolapse and are the result of attenuation artifacts.

2.4 Stent imaging with clinical and pre-clinical CT

The resolution differences among MS-CT, C-arm CT, FP-CT, and microCT are apparent in the cross-sectional plane images shown in Figure 2.4. The axial plane cutting through the stent struts (indicated in Figure 2.4i), is shown in Figures 2.4a, 2.4b, 2.4c, and 2.4d which correspond to stent reconstructions obtained from the MS-CT, C-arm CT, FP-CT, and microCT, respectively. The MS-CT visualization could not provide a clear definition of the strut shape due to resolution limitations resulting in artifacts such as partial volume averaging that over-estimate strut dimensions and also significantly affect the inter-strut regions. The wall between the stent struts is not visible with MS-CT.

The stent reconstruction obtained from FP-CT exhibits partial volume averaging artifacts which are comparable to the artifacts from the C-arm CT. The strut

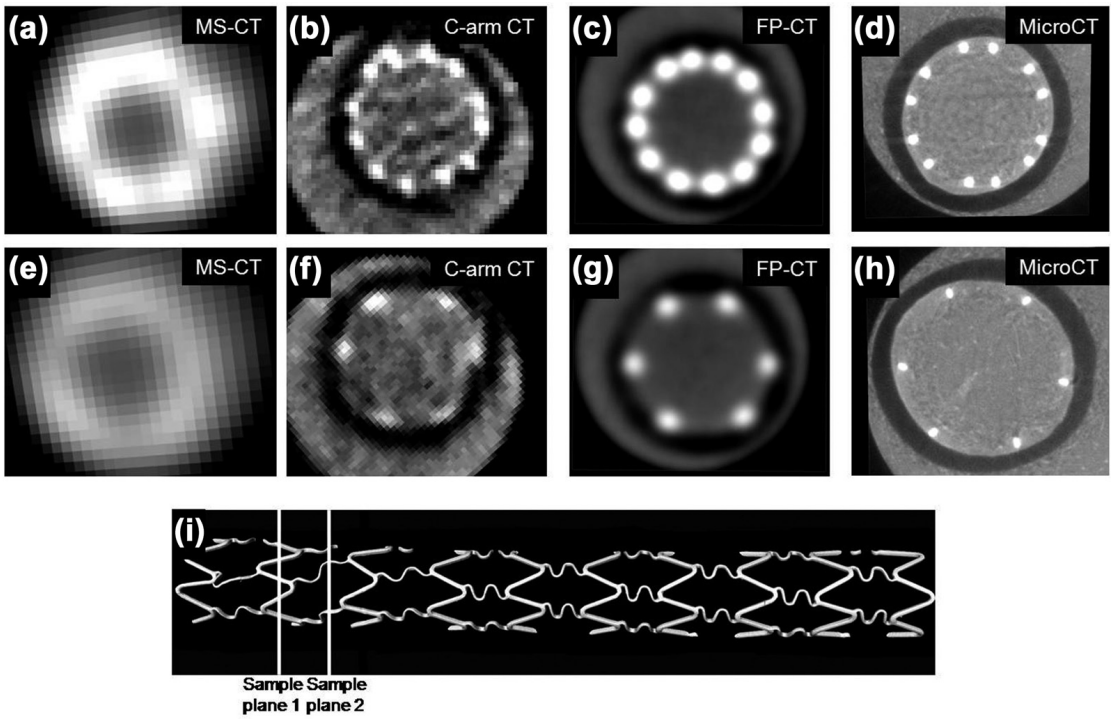

Figure 2.4. Cross-sectional planes cutting through regular struts (a, b, c, d) and ribbon-like connectors (e, f, g, h) from multislice CT, C-arm CT, flat panel CT, and microCT, respectively

shape is uniform with a cylindrical rather than a rectangular contour. The strut edges are better defined and the inter-strut gaps are visible although some of the struts appear to be fused, especially near the vertices. The wall surface between the stent struts is visible.

The microCT reconstruction provides the best stent and wall-lumen boundary visualization. The rectangular shape of the struts and ribbon-like connectors is clearly reconstructed with well defined edges and the wall-lumen boundary can be accurately identified as well. The high-resolution of the microCT reconstruction also allows for the visualization of the hemodynamically important gaps between the struts and wall (strut malapposition) that result from suboptimal stent deployment.

The axial plane shown in Figures 2.4e, 2.4f, 2.4g, and 2.4h from the MS-CT,

C-arm CT, FP-CT, and microCT, respectively, is located at one of the ribbon-like strut connectors (indicated in Figure 2.4i). These connectors are flexible metal ribbons that link thick struts and are designed to enhance stent flexibility and conformity in tortuous arteries. The MS-CT reconstruction is not able to capture these connectors due in part to their small size and to the volume averaging artifacts from the thick, regular struts. While the C-arm CT reconstruction can capture the ribbon-like connectors, the attenuation values in these regions are smaller than those of the regular struts although they are made from the same material. The FP-CT reconstruction provides slightly better visualization of the connectors as the attenuation value distribution is more uniform, although the width of the reconstructed connectors is oversized ($\sim$ 160 μm). At the same location, the microCT reconstruction can capture all six connectors with an approximate width of 80 μm. Partial volume averaging artifacts are insignificant and the shape and size of regular struts and connectors is accurately reconstructed.

A comparison of the voxel intensity distribution profile for the MS-CT, C-arm CT, FP-CT, and microCT data normalized by the peak strut intensity is shown in Figure 2.5. The signal intensity across the lumen is measured on a cross-sectional plane such as the one shown in Figure 2.4 along a sample line that passes through one strut, across the lumen, and then between two struts to capture the intensity of the wall region between two struts. The data is collected on two sample planes (shown in Figure 2.4i), one plane passing through a regular strut section and the second plane passing through a connectors section to demonstrate the signal noise and variability. The microCT data (Figure 2.5d) is used as reference due to its highly accurate stent reconstruction.

The strut region for the microCT non-dimensional intensity distribution, I^*, extends from $D^* = 0.07$ to $D^* = 0.13$ while the region between $0.16 \leq D^* \leq 0.9$

represents the lumen (Figure 2.5d), where D^* is the non-dimensional diameter, $D^* = d/D$. The secondary peak at $D^* \sim 0.85$ in Figures 2.5a, 2.5b, and 2.5c is due to the presence of partial volume averaging artifacts at the gap between the struts for the MS-CT, C-arm CT, and FP-CT datasets, respectively. The amplitude of the signal variation between the two sample planes shown in Figure 2.5 decreases between the MS-CT and C-arm CT and between C-arm CT and microCT. The strut thickness reconstructed using the mid-threshold value (the average between the maximum attenuation in the strut region and the attenuation in the lumen region) is represented by the vertical dashed lines while the vertical solid lines define the correct strut dimension. For the MS-CT reconstruction (Figure2.5a), using the mid-threshold value results in oversized strut dimensions which are very sensitive to changes in the threshold values. The FP-CT and C-arm CT reconstructions exhibit lower strut dimensions than MS-CT; however, the sensitivity to threshold values is still present.

The strut diameter measurements from the microCT images (140 μm) are equivalent to the manufacturer specifications—140 μm. The strut diameter obtained from the MS-CT is overestimated at approximately 600 μm. This dimension is based on the mid-threshold value discussed above. A higher threshold value would result in formation of gaps in the reconstructed stents due to non-uniform signal intensity across the strut region. Strut dimensions obtained from the FP-CT vary between 250 and 300 μm while those from C-arm CT images vary from 240 to about 350 μm. The FP-CT and C-arm CT datasets generate enlarged, irregular struts as compared with microCT reconstructions which have smooth struts. The partial volume averaging effects described above increase the diameter of the struts and also fuse the gaps between strut vertices.

Isosurfaces defined using the stent attenuation average values for each of the

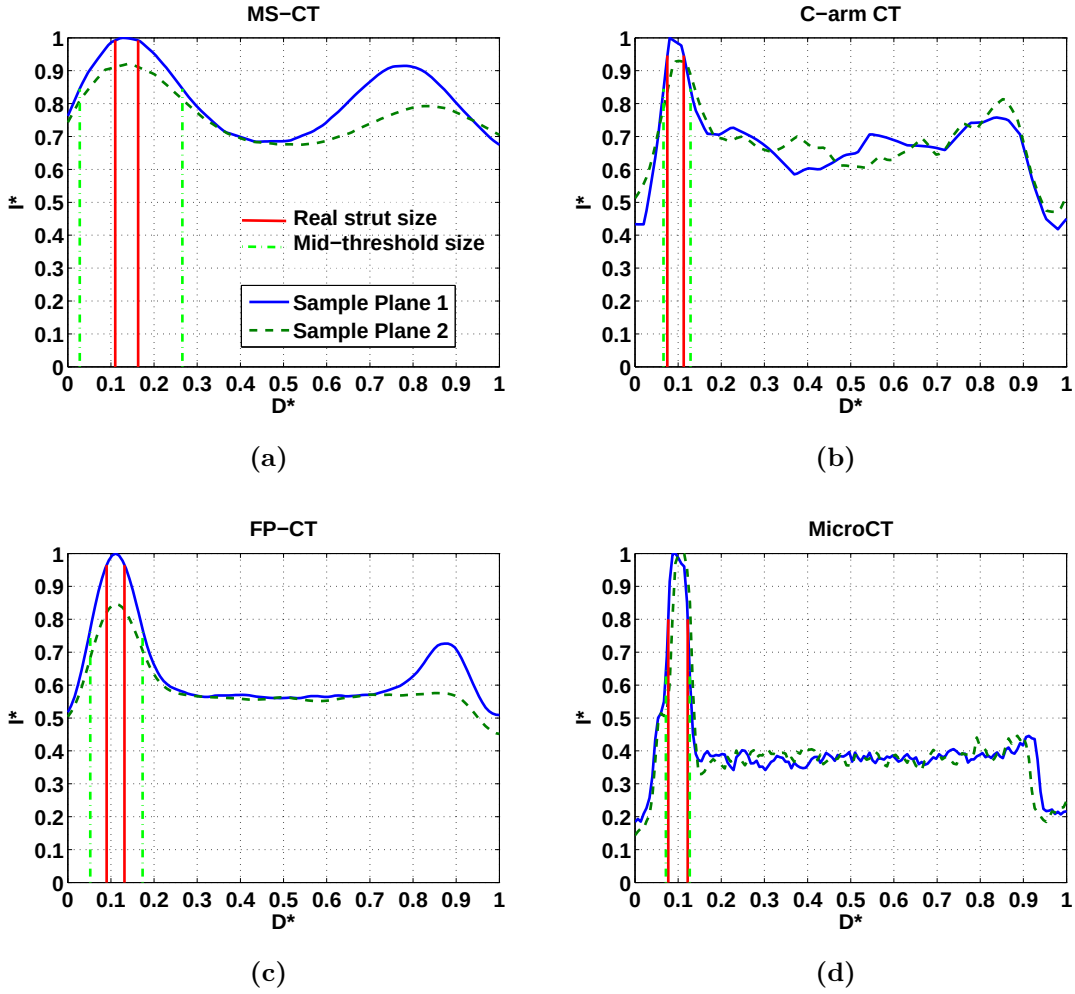

Figure 2.5. Distribution of attenuation values on a regular struts plane (plane 1) and on a connectors plane (plane 2)

datasets are compared in Figure 2.6. The MS-CT reconstruction of the stent surface exhibits oversized struts and fused cell vertices (arrow, Figure 2.6a) due to partial volume averaging effects. In the case of C-arm CT reconstruction (Figure 2.6b), the stent surface is better defined in terms of strut shape and dimensions. However, the connectors cannot be fully captured and some gaps are present at the connector regions (arrows, Figure 2.6c). The FP-CT reconstruction depicted in Figure 2.6c exhibits oversized struts as well as missing connectors (indicated

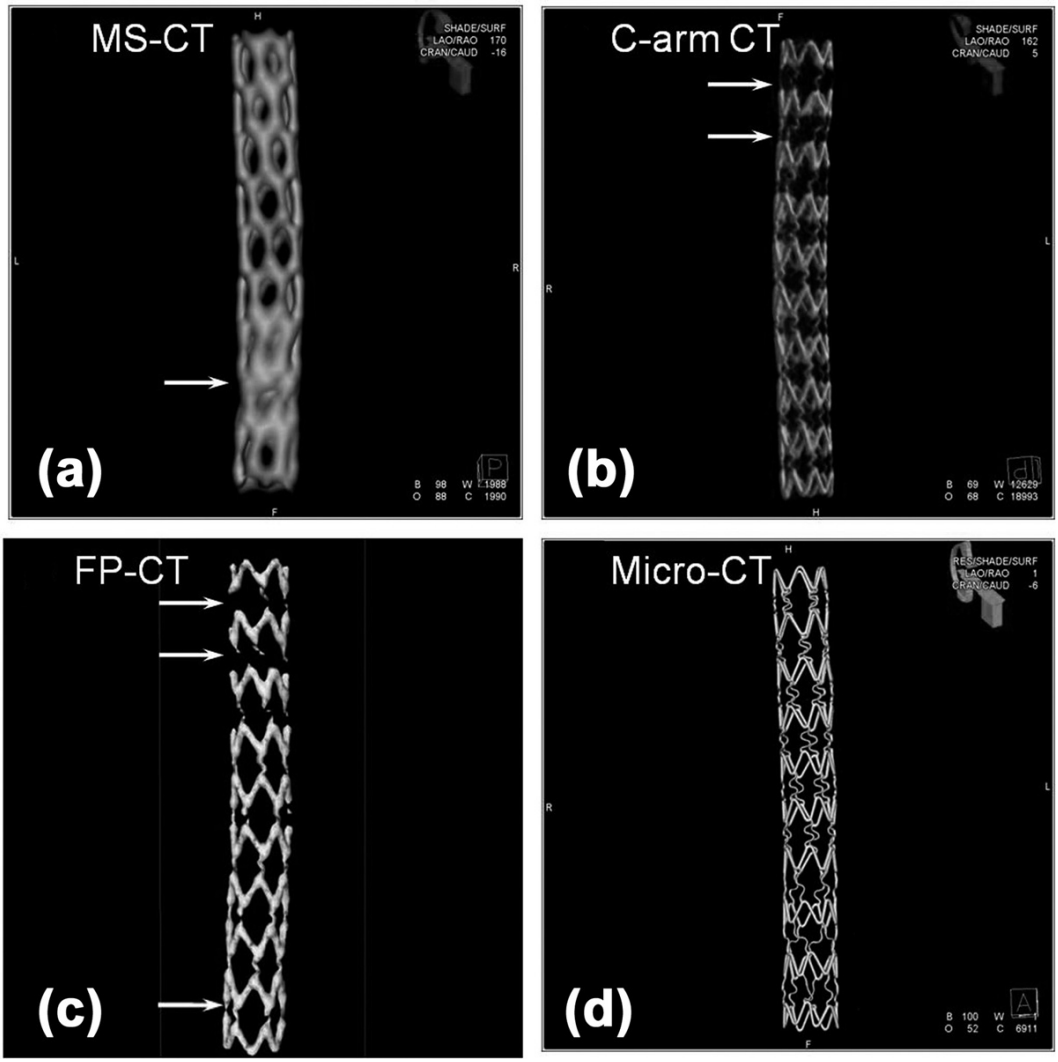

Figure 2.6. Stent strut surface reconstructions reveal over sized struts (a) and gaps at strut connectors (b) & (c). The most accurate stent reconstruction is provided by microCT (d)

by arrows, Figure 2.6c). The surface rendering appears smoother than those from C-arm CT due to the reconstruction algorithm. The microCT reconstruction (Figure 2.6d) provides the most accurate rendering of the stent geometry and thus is used as a reference in this work.

Lumen diameter measurements between the edges of the struts and between segments of bare wall are performed for all four CT methods and shown in Fig-

ure 2.7. The difficulty in evaluating the wall-to-wall lumen diameter from the MS-CT data is apparent from Figure 2.7a and results in a value much lower, 1.8 mm, than the reference value from the microCT measurement which is 2.9 mm. The C-arm CT and FP-CT values are closer to the microCT value, with the C-arm CT underestimating the wall-to-wall diameter values, while the FP-CT generated overestimates.

The in-stent lumen diameter is estimated in a similar way for the four CT images. The in-stent lumen is defined from the inner edge of one strut to the inner edge of the diametrically opposed strut. The location of the inner edge of the strut is determined based on the threshold value used for image segmentation (the mid-threshold values, also marked in Figure 2.5 by the dashed vertical lines). The C-arm CT and FP-CT show smaller lumen diameter than the microCT, while the lumen diameter obtained from the MS-CT is about 50% less than the diameter from the microCT.

The lower spatial resolution of MS-CT, C-arm CT, and FP-CT reconstructions poses two problems: first, the challenge of defining appropriate attenuation threshold values that capture the true dimensions of the struts, and second, the ability to differentiate between the lumen and vessel wall. The profile distribution presented in Figure 2.5 is useful in determining optimal threshold levels necessary for such differentiation. With the lower resolution MS-CT, C-arm CT, and FP-CT, the frequency of the attenuation noise decreases—the amplitude also decreases—making it more difficult to determine a threshold value that will accurately differentiate between the vessel wall and lumen. As evident from Figure 2.7, the in-stent lumen evaluation using MS-CT even under ideal (motionless) conditions is far from being accurate. It underlines the need for improved spatial resolution of MS-CT systems for stent imaging in both the coronary and intracranial circulation. While

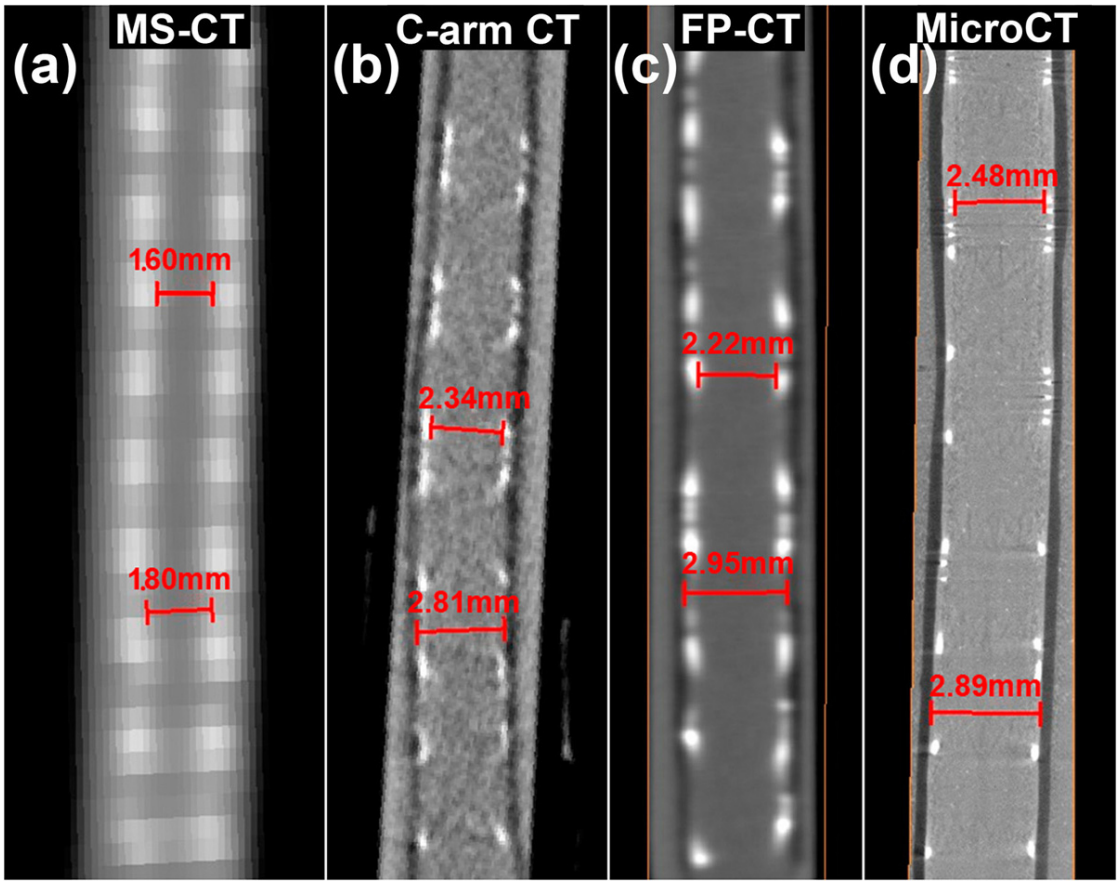

Figure 2.7. Lumen dimension measured between diametrically opposed struts and between bare wall regions

the spatial resolution of C-arm CT is currently higher, its low temporal resolution makes its use currently unfeasible for *in vivo* coronary vessel imaging.

To assess the spatial resolution of the different scanners, the stented tube phantom used in the study was fixed, therefore, any temporal motion artifacts due to breathing and cardiac activity that are usually present in clinical practice are excluded. The brain and its vasculature is subject to pulsations, although to a much lesser degree than elsewhere in the body, especially in cardiac vessels. It can be expected that motion artifacts can negatively affect the quality of stent imaging and reconstruction and result in imaging artifacts. Thus, improvement of clinical spatial resolution alone will only partially solve the problems in both coronary or

intracranial stent imaging. For assessment of temporal imaging accuracy, a different reference imaging standard would be required. Furthermore, microCT cannot presently be used for clinical practice nor is this likely in the foreseeable future due to long scanning time and small sample size constraints for high-resolution imaging. The PTFE tube used to emulate the vascular wall does not exhibit the morphological characteristics present in real arteries such as wall irregularities, tapering, and curvature. Also, there is no surrounding tissue that might induce additional artifacts and noise.

2.5 Stent deployment visualized by microCT

The high-resolution microCT imaging modality, as shown above, provides accurate stent geometry reconstructions that allow the visualization of minute stent deployment details such as strut-wall interaction, strut misalignemnt, and strut prolapse into the lumen and is therefore suited to study *in vitro* stent deployment in graft tubes and arteries. In this section, microCT is used to evaluate the deployment characteristics and the stent-wall interaction of four intracranial stents and two coronary stents. All stents are deployed in straight PTFE graft tubes with the exception of a NF3 stent deployed in an excised canine artery.

2.5.1 Intracranial stents

The intracranial stents used in this work for stent deployment evaluation include NF3, Enterprise, Leo, and Pharos as described earlier in section 2.3. The bare stent surface in the deployed configuration inside the PTFE tubes is shown in Figure 2.8 for all four intracranial stents. The images preserve the approximate stent dimensions relative to each other. The NF3 and Enterprise stents have similar

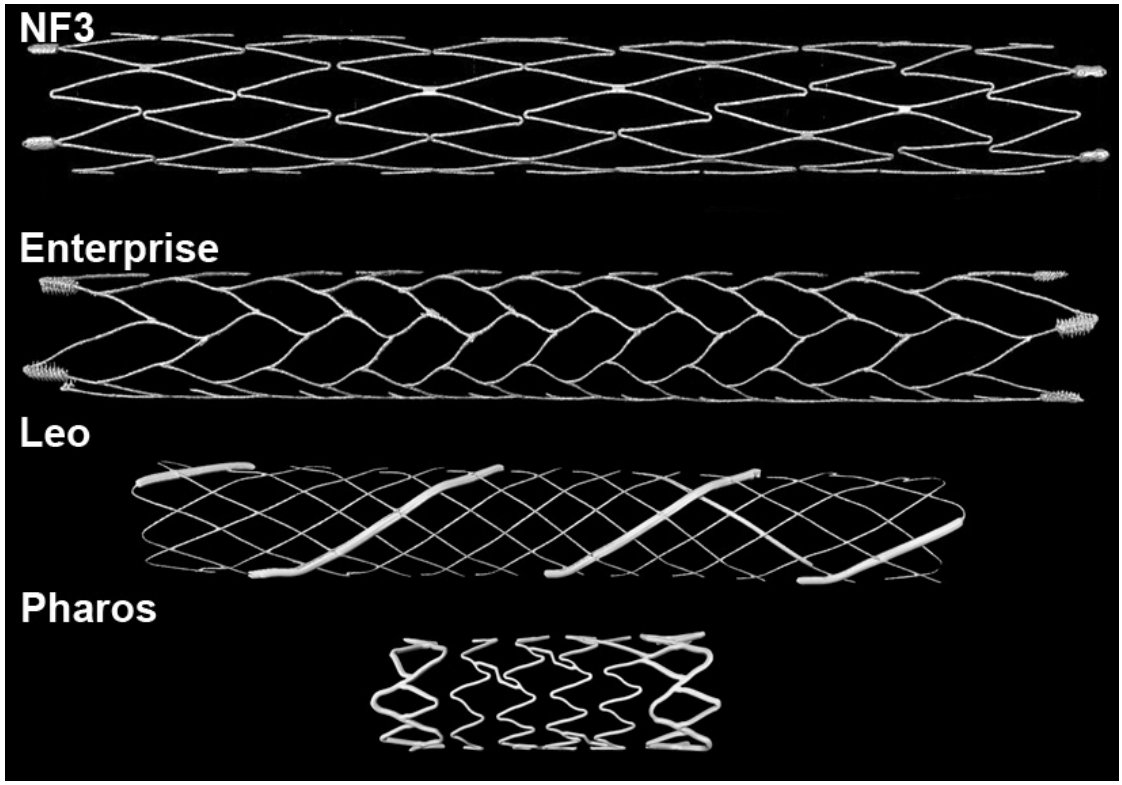

Figure 2.8. Surface reconstructions of four intracranial stents from microCT imaging

length and diameter while Leo and Pharos stents have slightly smaller diameters and are shorter than the first two stents. The relatively large metallic structures at both ends of the NF3 and Enterprise stents and the two relatively thick wires along the Leo stent represent radiopaque markers made usually of platinum or tantalum that enhance stent visualization under CT fluoroscopic mode during deployment for stents made of low radiopaque material such as nitinol. The Pharos stent, consisting of stainless steel struts, is sufficiently radiopaque and does not require the inclusion of stent markers.

The NF3 stent in this particular deployed configuration is 30 mm long and has a 4 mm diameter. The stent struts, made of nitinol, are approximately 70 μm thick and the stent platinum markers are 180 μm thick and 400 μm wide. The NF3

deployment in a straight PTFE tube is shown in Figure 2.9. The wall and stent surface are transformed from a cylindrical surface into a planar surface by using a projection subroutine developed in MATLAB to enhance the visualization of stent deployment characteristics (Figure 2.9a). The NF3 stent has an open-cell design for better compliance in tortuous arteries with trapezoidal shaped cells of uniform area (in ideal deployment) with four strut junctions per cell. The markers are parallel to the vessel axis while the strut orientation for this particular deployment is, on average, 20° with respect to the vessel axis.

The NF3 deployment exhibits aligned strut vertices (left-oriented arrows, Figure 2.9a) with vertex gaps of different length while at some locations the vertices are touching and no gap exists between stent cells (left-oriented arrow, middle of Figure 2.9a). The NF3 stent, due to its open-cell design, also exhibits strut vertex misalignment as indicated by right-oriented arrows in Figure 2.9a and 2.9b that allows the struts to slide parallel to each other. Strut vertex prolapse into the lumen, also called strut malapposition, is present at some locations indicated by upward-oriented arrows (Figure 2.9a). A close-up of the strut vertex prolapse is shown in Figure 2.9c which corresponds to the prolapse shown in one of the CT image slices shown in the lower-right image of Figure 2.3b. There are three such prolapses for this particular NF3 deployment. These strut vertex and strut prolapse into the lumen commonly occur in stent deployment inside curved vessels as shown in [94–96].

Another NF3 stent is deployed *ex vivo* in an excised canine arterial segment and its reconstructed surface geometry is shown in Figure 2.10. The NF3 stent used in this case is 20 mm long and is 3.5 mm in diameter with strut dimension as before. The NF3 is deployed in a tapered artery segment with inlet diameter of $\sim$ 3.3 mm and an outlet diameter of $\sim$ 2.2 mm. The arterial segment is not

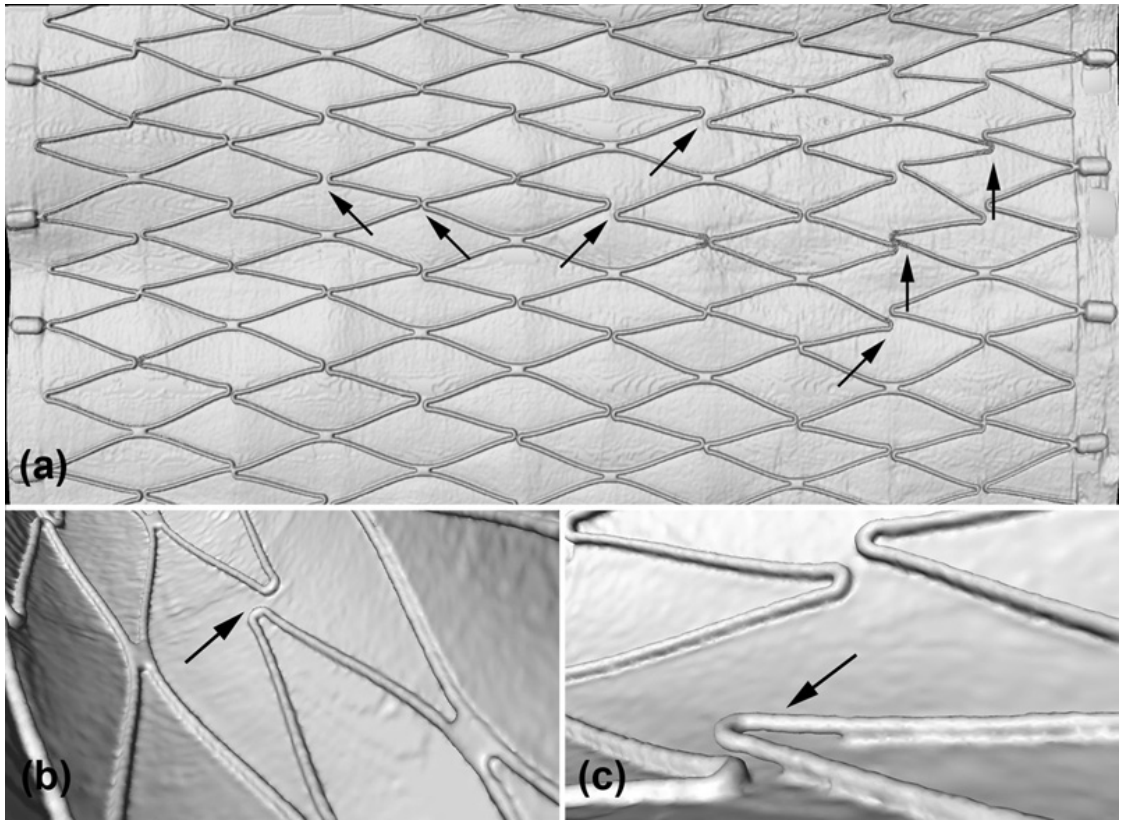

Figure 2.9. Neuroform Treo (NF3) stent deployment in a straight tube. Strut vertex misalignment (a) & (b) and strut prolapse into the lumen (c) are present

straight and exhibits curvature; however, the stented segment is relatively straight (Figure 2.10a). This may be due to the force exerted by the stent during deployment on the arterial wall and to shrinkage after the arterial segment was placed in a formalin solution for preservation.

The NF3 placed inside the canine artery also shows stent vertex misalignment (Figure 2.10b) while strut impingement on the wall and strut vertex embedding are present. This is indicated by the double arrows in Figure 2.10b at a location in the middle of the stent. Also noticeable is the wall prolapse into the lumen at the cell center as indicated by the arrowheads. Circumferential creases form at the wall due to strut vertex impingement on the wall (arrows, Figure 2.10b). Significant

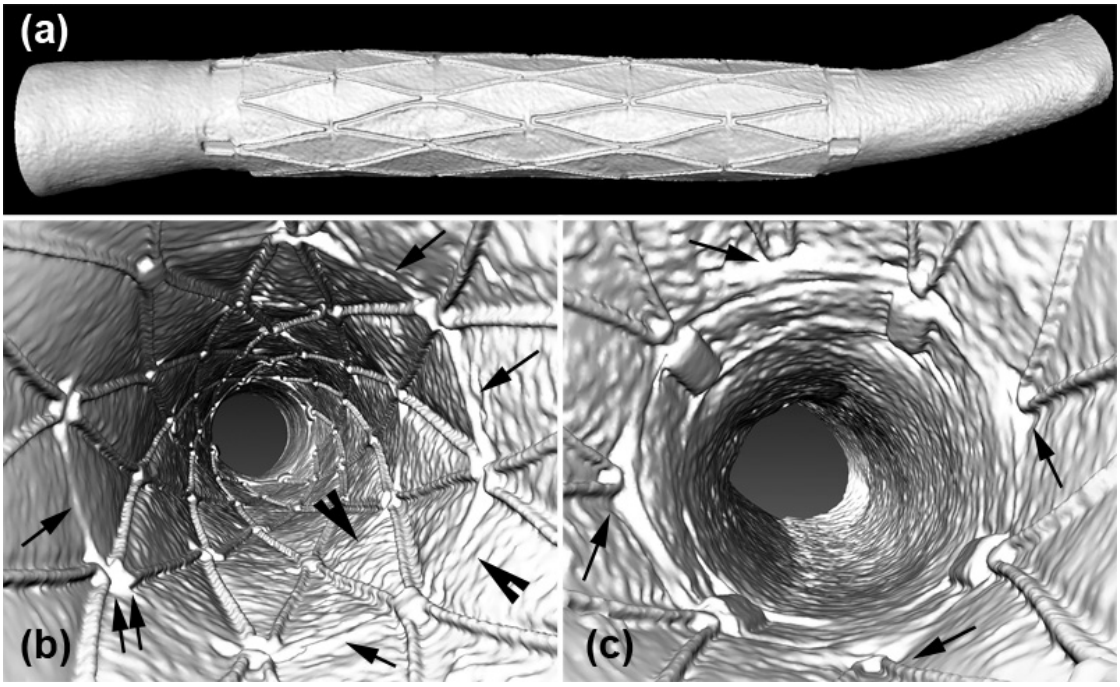

Figure 2.10. Neuroform Treo (NF3) stent deployed *ex vivo* in canine femoral artery (a). Strut embedding and wall creases at strut vertices form (b) & (c)

strut impingement and embedding into the wall is observed at the distal end of the stent where the arterial diameter is less than the proximal arterial diameter (indicated by arrows, Figure 2.10c).

The Enterprise stent deployed in the PTFE tube and shown in Figure 2.11 is also 30 mm long and has a 4 mm diameter as the NF3 stent. It is a closed-cell, self-expandable intracranial stent made of nitinol struts that are 60 μm thick and with tantalum markers that are 250 μm thick and 300 μm wide. The stent cells have a trapezoidal shape with larger cells at both ends of the stent. The stent cell arrangement is staggered with 6 strut junctions per cell (Figure 2.11a). The stent markers are obliquely oriented with respect to the vessel axis while the struts are oriented at 35° and 45°.

The Enterprise stent deployed in this PTFE tube does not exhibit any strut

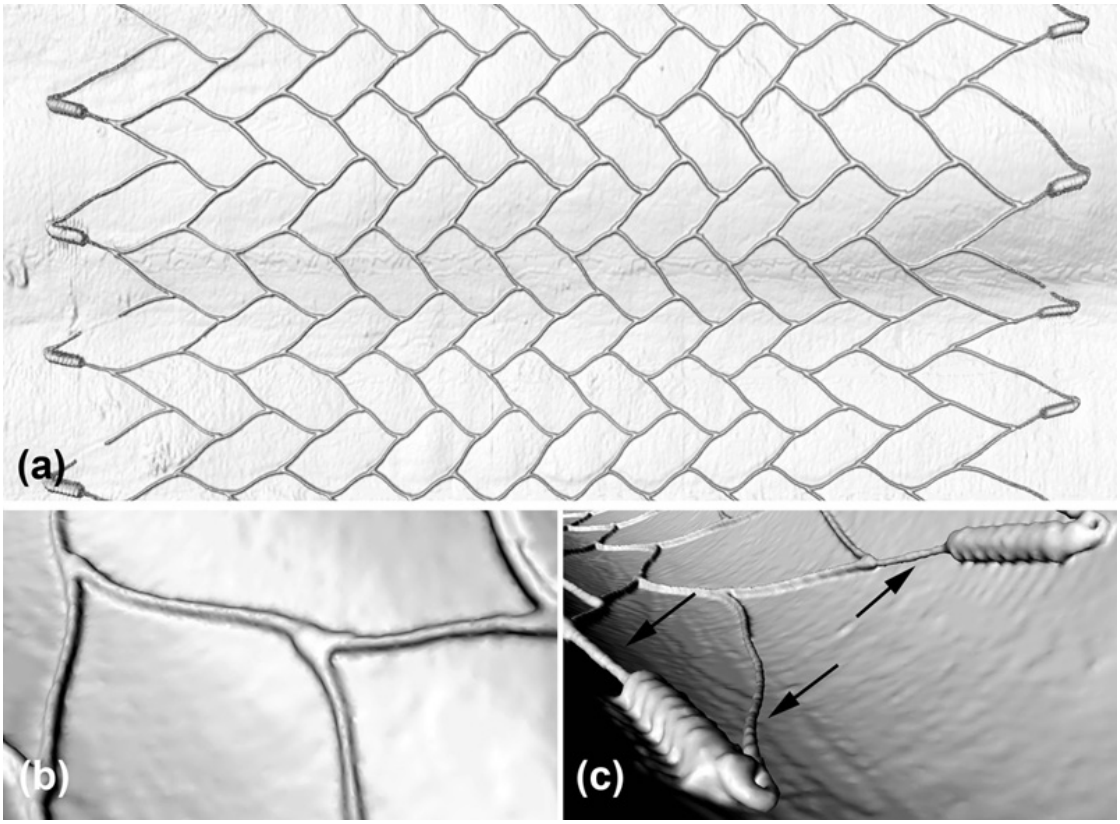

Figure 2.11. Enterprise stent deployment (a). No strut prolapse is present in the mid-section (b); only struts connected to markers show prolapse into the lumen (c)

prolapse into the lumen or strut misalignment due to the closed-cell design and good apposition to the wall (Figure 2.11b). The only exception is the strut prolapse that occurs near the stent markers as the regular struts connected to the larger stent markers are forced away from the wall. The strut prolapse is indicated by arrows in Figure 2.11c.

The planar projection of the Leo stent deployment is shown in Figure 2.12a. The self-expandable Leo is a braided wires design that can be described as a closed-cell design and is 19 mm in length and with a diameter of 3 mm. The struts or wires, made of nitinol and measuring 55 μm in diameter, are allowed to slide past each other while two parallel platinum marker threads are positioned along

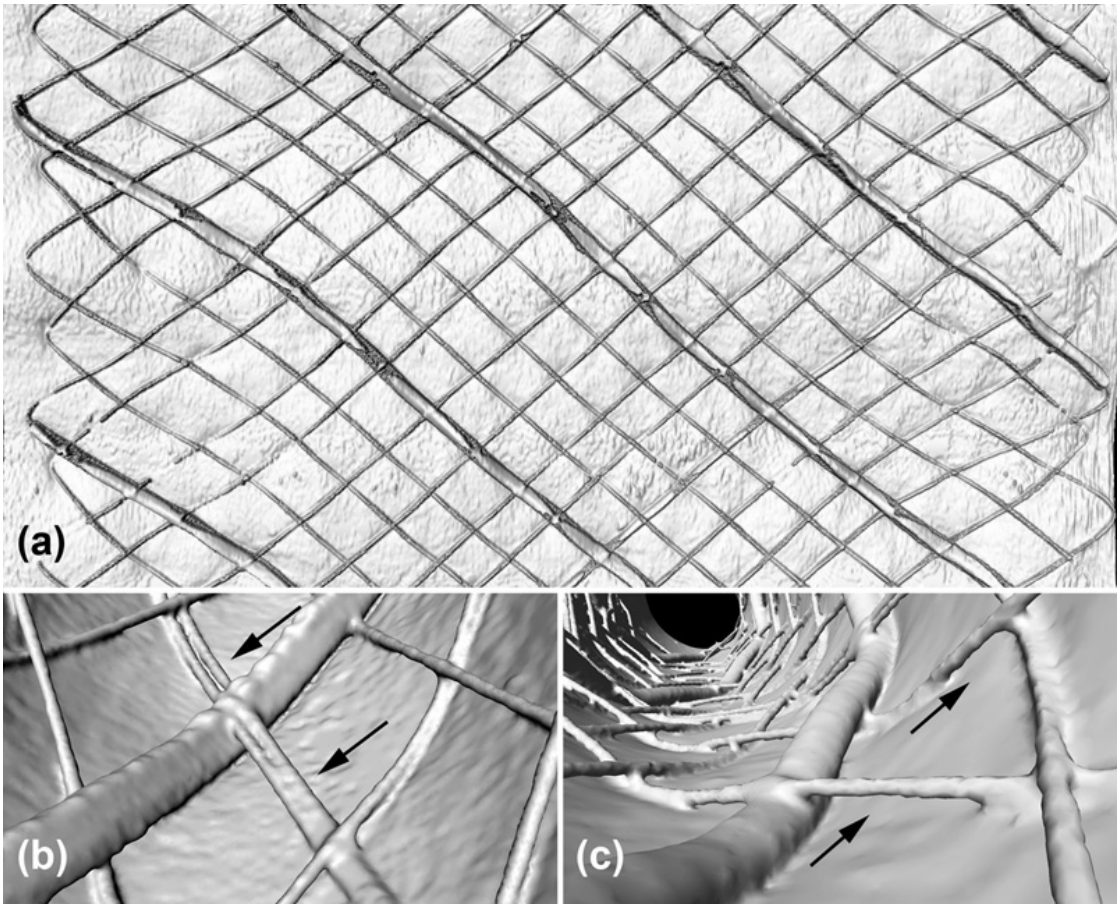

Figure 2.12. Planar projection of the Leo stent (a). Two parallel wires are observed along the stent (b). Strut prolapse occurs at wire-wire and wire-marker intersections as indicated by arrows(c)

the stent. The markers are 250 μm wide and are obliquely oriented to the vessel axis. The shape of the stent cells is rectangular (Figure 2.12a) and the struts are oriented at approximately 45° with respect to the vessel axis.

Stent deployment characteristics for the Leo stent include irregular cell size due to the movement of stent wires with most of the irregularities occurring at both ends of the stent while cells of uniform shape and area are present in the middle section. A double wire is observed, which, due to resolution limits and the small separation between the wires, appears at some locations as one thick wire as indicated by arrows in Figure 2.12b. Strut prolapse into the lumen occurs

at locations where wires or wires and markers are intertwined as illustrated in Figure 2.12c and indicated by arrows. Also, no significant strut impingement on the wall is present.

The planar projection of the Pharos stent deployed in a PTFE tube is shown in Figure 2.13. It is a short, balloon-expandable intracranial stent consisting of a combination of open-cell/closed-cell design and is 8 mm long and with a diameter of 3 mm. The stent struts are made of stainless steel—adequate radiopacity, hence, no markers required—and are thicker than the struts of other intracranial stents (strut diameter of 160 μm at both ends of the stent and strut diameter of 100 μm at mid section). The shape of the closed-cells at both ends of the stent is trapezoidal and the cell area varies. The strut orientation with respect to the vessel axis varies from $\sim 28^\circ$ to $\sim 60^\circ$.

Strut misalignment is present in the mid-section of the stent while good wall apposition results in no strut prolapse into the lumen (Figure 2.13). The size of gaps between strut vertices varies due to the non-uniform stent design. At both ends of the stent as well as in the mid-section there is slight strut impingement on the wall as indicated by small creases that form at the strut vertices. Also, the closed-cells at both ends of the stent exhibit non-uniform shapes due probably to the deployment method. The vertex gaps very in length with shorter gaps being present between thicker and thinner struts

2.5.2 Coronary stents

The coronary stents imaged with microCT for use in computational hemodynamics studies are the BxVelocity and Taxus Express (Taxus). These two stainless steel stents are used for arterial angioplasty as either bare-metal stents or coated with antibiotics and immunosuppressants and used as drug eluting stents under

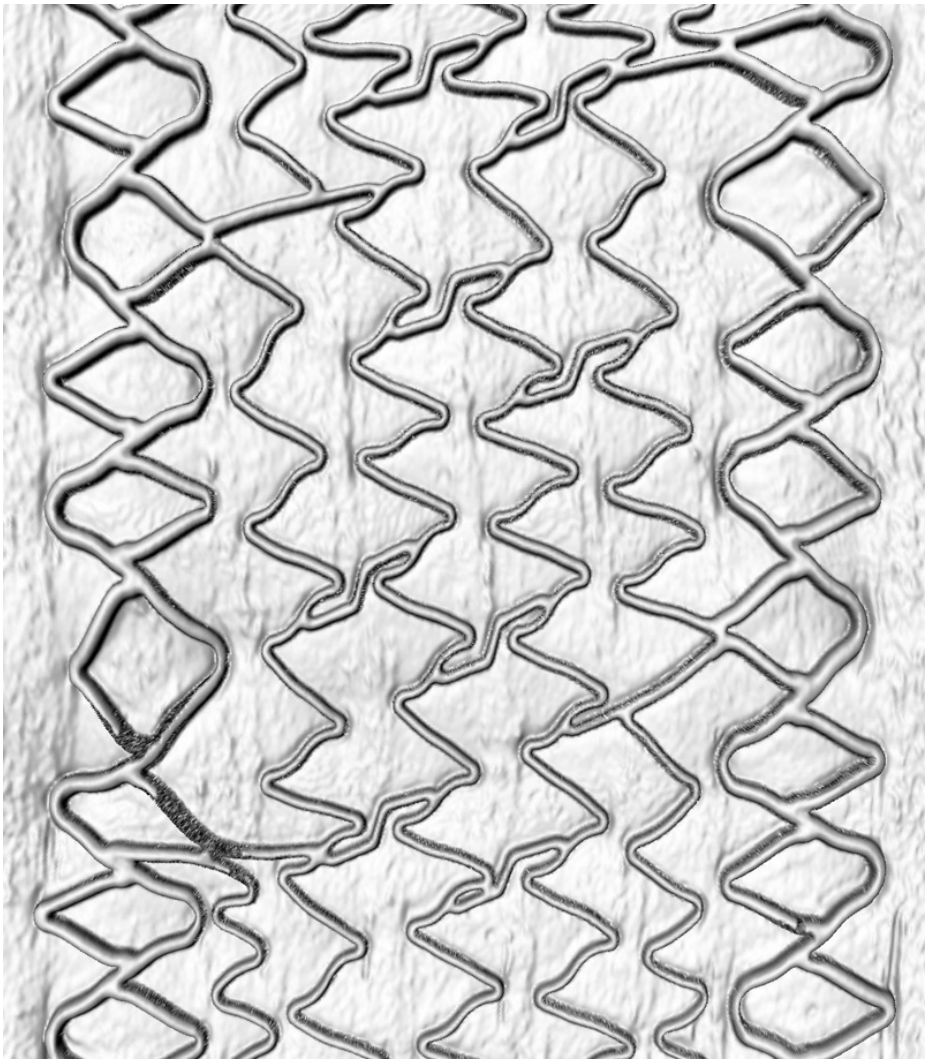

Figure 2.13. The deployment of Pharos in a straight tube shows strut vertex impingement on the wall, strut misalignment, and irregular cells at both ends of the stent

new marketing names, Cypher and Taxus Express2, respectively. Coronary stents usually have thicker struts, are stiffer, and, due to the high radiopacity of steel, require no imaging markers as compared with intracranial struts [97].

The BxVelocity, shown in Figure 2.4i as bare stent surface (by excluding the PTFE graft tube surface) and in planar projection in Figure 2.14, is a balloon-expandable stent with a length of 27 mm and a diameter of 3 mm. It is a closed-

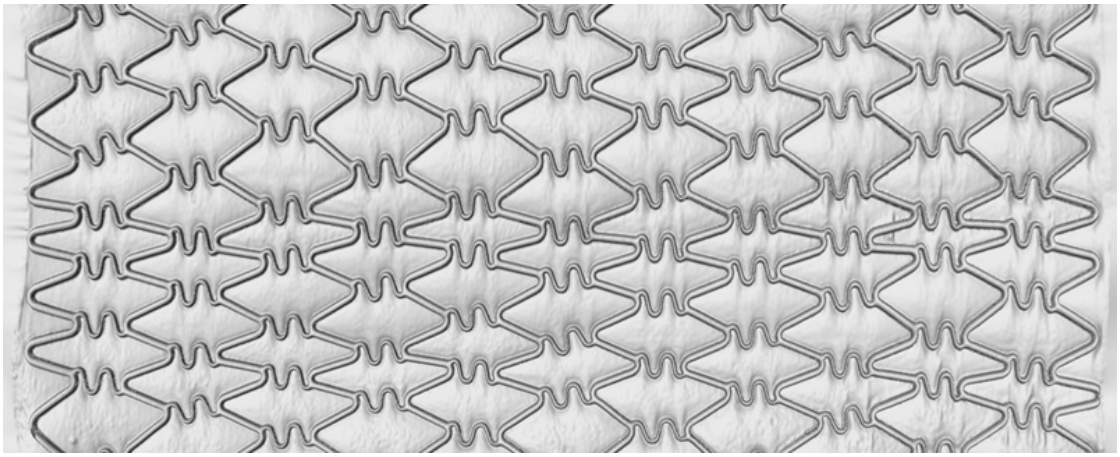

Figure 2.14. BxVelocity stent deployed in a straight tube shows strut vertex impingement on the wall, connector misalignment, and slight wall prolapse into the lumen at cell centers

cell design consisting of 14 circumferential struts with 140 μm thick struts that are linked by ribbon-like connectors for increased flexibility. There are seven ribbon-like connectors per circumference and each connector is about 60 μm wide and 140 μm thick.

The BxVelocity deployment is uniform in general with the exception of a cell row that is under-expanded along the entire length of the PTFE graft tube (Figure 2.14). Also, some of the ribbon-like connectors are misaligned when compared to the other connectors and the angle of struts with respect to the axis of the tube varies depending on the cell size—smaller size cells exhibit struts aligned with the tube axis. There is also slight wall prolapse into the lumen occurring at the cell centers and strut vertex impingement on the wall can be observed at each end of the BxVelocity stent.

A Taxus stent is also placed in a 3 mm PTFE tube resulting in a deployed configuration as shown in Figure 2.15 with a length of 16 mm and a diameter of 3 mm. It is an open-cell design, balloon-expandable stent consisting of 8 pairs of alternating strut sections with 105 μm width (12 per circumference) and 85 μm

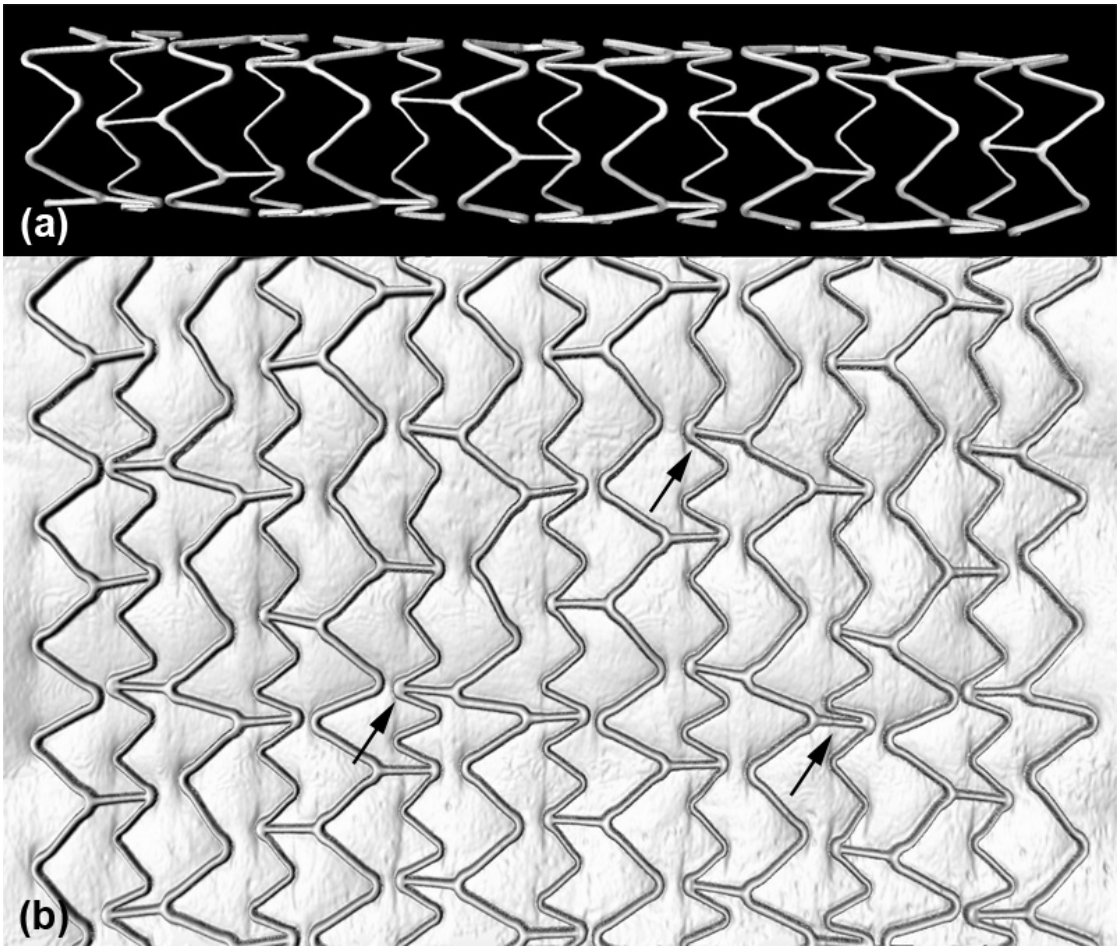

Figure 2.15. Taxus stent deployed in a straight tube shows strut vertex impingement on the wall and strut misalignment

width (18 per circumference) and 140 μm height. The pairs of struts are linked by connectors of 85 μm width and 140 μm height (three per circumference).

The deployment characteristics of this particular Taxus stent include vertex gaps of different lengths with some of the gaps exhibiting vertex and strut misalignment as indicated by arrows in Figure 2.15b. Some of the connectors are not aligned with the tube axis and the angle formed by the struts with the axis direction is not uniform for struts of similar position along the stent. Slight wall prolapse into the lumen occurs in the middle of the cells while strut vertex impingement on the wall is present as indicated by small wall creases at both ends of the

stented segment as well as inside the stent (Figure 2.15b). Good wall apposition is indicated by no strut prolapse into the lumen.

2.6 Summary

In this chapter, the quality of stent reconstructions obtained from clinical and pre-clinical CT modalities are evaluated and compared. Stent deployment characteristics in straight graft tubes and in a canine arterial segment are evaluated using high-resolution microCT.

The current spatial resolution limits of the MS-CT, C-arm CT, and FP-CT compromise significantly the quality of visualization detail in the imaging of a small coronary stent. MS-CT, C-arm CT, and FP-CT images may introduce false gaps in stent struts and incorrectly remove real strut gaps by merging adjacent strut vertices. When compared to high-resolution microCT, structural details of the stent and deployment characteristics are less precisely depicted in the MS-CT, C-arm CT, and FP-CT. Dominating blooming effects and partial volume averaging effects in these data sets lead to exaggerated strut dimensions and results in the inability to accurately resolve strut connectors and compromises the in-stent lumen evaluation. Higher spatial resolution in clinical CT imaging of small intravascular stents is thus required. Improved CT technology should enable a more accurate clinical assessment of coronary and intracranial artery stent patency and improved detection of in-stent pathology.

Stent deployment assessment by high-resolution microCT is performed *in vitro* for intracranial and coronary stents. This method allows for the visualization of minute stent details in the deployed configuration inside straight PTFE tubes and arterial specimens. Strut misalignment, strut prolapse into the lumen, and

non-uniform strut vertex gaps can occur in open-cell intracranial stents (NF3, Pharos). Strut prolapse can also occur for closed-cell stents such as Enterprise and Leo at locations where two struts intersect or where regular struts and markers are connected. Balloon-expandable stents (intracranial and coronary) can exhibit strut misalignment and non-uniform cell area as well as strut impingement on the wall and wall prolapse into the lumen at cell centers. Strut embedding, wall creases at strut vertices, and wall prolapse into the lumen at cell centers are present in NF3 stent deployment in an excised canine arterial segment.

As demonstrated in this chapter, the high-resolution microCT imaging modality is able to accurately capture the geometry of the stent and vessel wall and can be used in conjunction with computational fluid dynamics to perform simulations of blood flow through real deployed stents, thus, adding another level of reality.

Chapter 3

Pulsatile flow in stented vessels

Angioplasty of atherosclerotic arteries by stent implantation is performed to restore normal blood flow and to reduce the risk of potential plaque rupture. While this method provides long-term relief from atherosclerosis and keeps the implanted artery open, adverse vascular events such as neointimal hyperplasia that leads to restenosis (plaque regrowth) and in-stent thrombogenesis occur in about 30% of interventions [28–30]. Multiple factors, among which arterial hemodynamic conditions play an important role, determine these negative outcomes. Elucidating these deleterious conditions and designing stents that are bio-compatible and have lesser impact on arterial hemodynamics may improve the success rate of stent interventions [28, 98].

Blood flow modeling and computational fluid dynamics or computational hemodynamics (CHD) simulations, as discussed in chapter 1, represent powerful tools that are used to investigate the cardiovascular system. Their potential uses also include the analysis of various treatment options to determine which strategy is best suited for patient-specific cases and the investigation of different designs for medical implants [99]. In this chapter, the blood flow in real deployed stents imaged by high-resolution micro computed tomography (microCT)—discussed in chapter 2—is investigated under steady and time-dependent flow conditions by performing CHD simulations. Clinical and experimental studies that correlate neointimal hyperplasia and in-stent thrombosis with disturbed flow patterns and stent deployment anomalies are discussed first, followed by a review of the relevant

work on blood flow in stented arteries. Next, the CHD methods and the flow conditions are presented, then followed by the presentation of results on blood flow in intracranial and coronary stents under steady and physiologic flow conditions. The chapter ends with a discussion and a brief summary of the main findings.

3.1 Introduction

Implantation of metallic stents in atherosclerotic arteries as a treatment method for restoring normal blood flow and preventing acute arterial blockage has been performed since the late 1980s. Its first application was in atherosclerotic coronary arteries and the method was quickly adopted as an alternative to coronary artery bypass surgery. The first bare metal stent (BMS) implants proved to be plagued by subacute thrombosis which resulted in coronary occlusion a few weeks after arterial stenting [97]. Despite the initial setbacks, the advantages offered by stent deployment as well as subsequent improved stent designs have resulted in the widespread use of stents. Acute in-stent restenosis rates were significantly reduced to $\sim 10\%$—compared with ~ 30–50% for BMS—by the coating of metallic stents with immunosupressant and anti-proliferative drugs (sirolimus, paclitaxel, zotarolimus) that resulted in a new class of stents—drug eluting stents (DES) [29, 97]. Despite lower acute in-stent restenosis rates, the risk of in-stent thrombosis—with rates of $\sim 4\%$ that are similar to those of BMS—is still associated with DES deployments [97]. Evidence, as discussed below, suggests that stent strut dimensions, stent apposition to the arterial wall, strut prolapse into the lumen and stent design are among the main factors contributing to in-stent thombosis and early in-stent restenosis [29].

Wall shear stress (WSS) is cited in the review article by Farooq *et al.* [29]

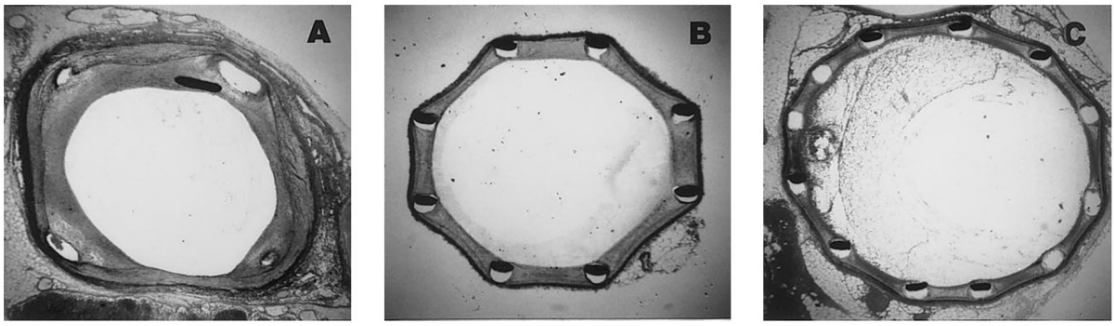

Figure 3.1. Cross-sectional slices of rabbit iliac arteries implanted with three different stent designs show acute non-uniform neointimal growth

as one of the factors directly influencing in-stent restenosis. Low and oscillatory WSS values are believed to promote the accumulation of cytokines, growth factors, and platelets inside injured endothelium regions leading to neointimal growth and atherosclerosis. In the study by Garasic *et al.* [28] it was found that acute neointimal thickening in stented rabbit iliac arteries was non-uniformly distributed and that increased neointima growth occurred in stents with a smaller number of struts per circumference. Histological analysis of excised arteries implanted with two different BMS (shown in Figure 3.1, adapted from [28]) indicates that more neoinitmal growth is present in the stent with eight struts per circumference (left and middle image) than in stents with 12 struts per circumference. Arterial wall polygonalization is present for both stents (Figure 3.1) with this effect being more exacerbated in stent regions with greater strut spacing. Thicker stent struts also correlated with increased neointima thickness while monocytes, platelets, and macrophages accumulated around the stent struts. The authors concluded that stent strut distribution, strut dimension as well as strut apposition to the arterial wall are factors that play a major role in neointimal growth and restenosis.

The results from a randomized, multicenter clinical trial on coronary stenting indicates that strut thickness influences in-stent restenosis [100]. The study

included 611 patients with symptomatic coronary artery disease that were implanted with either the ACS RX Multi-Link stent—strut thickness of 50 μm and width of 100 μm—or the BxVelocity stent—strut thickness of 140 μm. Angiographic data from the six-month follow-up indicated that in-stent restenosis was present in 17.9% of the patients implanted with the thin strut stent (Multi-Link) while restenosis occurred in 31.4% of patients implanted with the thick strut stent (BxVelocity). The one-year follow-up showed that 12.3% of the patients implanted with the thin strut stent and 21.9% of those with thick strut stent implant required percutaneous coronary angioplasty or bypass surgery indicating that less adverse effects are associated with thin strut stents. The study concluded that stent design and strut thickness influences the in-stent restenosis rate and that thinner strut stents have lower restenosis rates than thicker strut stents.

Compliance and apposition of stents to the arterial wall and its role in restenosis process was investigated by Rolland *et al.* [101]. Two types of BMS based on the nitinol SMART stent (with and without variable oversizing, compliance matching ends) were deployed in the carotid arteries of healthy adult Pietran swines. Post-stenting angiography, histological analysis as well as scanning electron microscopy imaging of the stented arteries were performed post-excision to assess stent compliance and neointimal growth. No prolapse of stent struts or mismatch between the arterial wall and stents was observed. Endothelial coverage of stent struts was observed three months post-stenting with slight lumen reduction and restenosis occurring outside non-compliance matching stents and proliferation of smooth muscle cells at both ends of the compliance matching stents where the vascular wall bulged radially outward. The correlation between neointimal growth and non-uniform strut distribution was observed by Takebayashi *et al.* [102] in patients with coronary DES implants at six month follow-up. Neointimal hyperplasia occurred

at sites of maximal interstrut angle in 82% of the cases and neointimal thickness was larger in stents with fewer struts, thus indicating the direct impact on intimal growth of stent deployment characteristics and the potential flow disturbances created by such non-uniformities in stented arterial segments.

The effect of shear stress on in-stent neointimal hyperplasia in both BMS and DES was investigated by Papafaklis *et al.* [103]. A six-month follow-up evaluation was preformed on 30 patients that underwent coronary stenting. The authors found neointimal thickness to be significantly correlated (inversely) with shear stress and that DES performed better (i.e., lower restenosis rates) than BMS. Another study investigating the influence of in-stent hemodynamics and stent deployment characteristics on intimal hyperplasia found that both flow disturbances and intramural stress concentration near stent struts correlate with intimal hyperplasia [104]. In the experimental study by Morlacchi *et al.* [92], stent deployment and in-stent restenosis were evaluated by histological analysis at different time intervals following stenting of coronary arteries in healthy swine. The findings indicate a direct correlation between neointimal hyperplasia and the amount of strut impingement on the wall leading the authors to suggest that a comibnation of recirculating flow near the stent struts and endothelial damage from strut impingement might be one of the factors involved in neointimal growth [92]. Similar findings were also presented in the study by [105] in which a computational model of smooth muscle cells proliferation was compared against *in vivo* data of swines implanted with stents.

Thrombosis, or the formation of blood clots, is another adverse cardiovascular outcome associated with stent implants. Visualization of in-stent thrombosis is typically achieved by intravascular ultrasound or optical coherence tomography as illustrated in Figure 3.2 which is adapted from Okamura *et al.* [72]. Stent

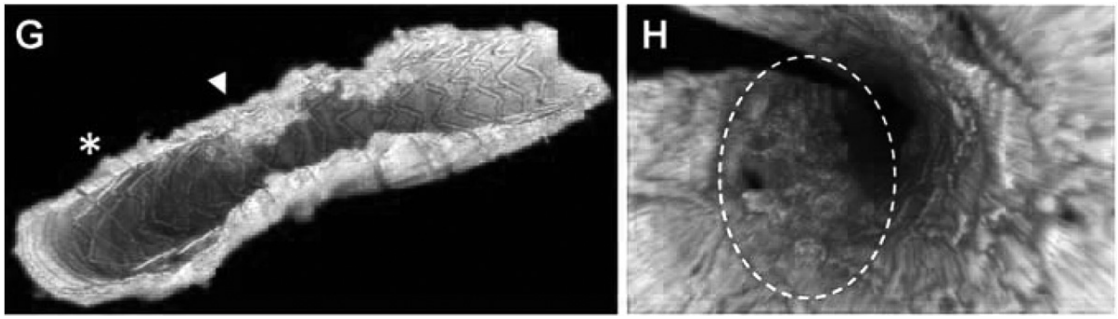

Figure 3.2. Optical coherence tomography of in-stent thrombosis indicated by arrowhead (left image) and circle (right image)

induced thrombosis is attributed in part to changes in arterial hemodynamics due to stent implantation and to stent strut prolapse into the lumen. This adverse outcome is prevalent even in DES as one of the studies on the subject shows [106]. Coronary stent deployment was evaluated by intravascular ultrasound in patients with DES implants more than one year following stent deployment. Incomplete stent apposition—i.e., strut prolapse into the lumen—was found to correlate with very late stent thrombosis in 77% of the cases [106]. Strut dimensions and stent apposition to the wall were found to be critical factors for in-stent thrombosis as suggested by Kolandaivelu *et al.* [30]. The thrombogenicity of both BMS and DES was compared during *in vitro* experiments. The strut dimension and position relative to the flow were found to be critical factors in development of in-stent thrombosis as stents with thicker struts were 1.5-fold more thrombogenic than thinner strut stents while thrombogenicity increased in malapposed or overlapping stent configurations.

The influence of blood flow in atherosclerotic carotid bifurcations on neointimal growth and in-stent thrombosis was investigated by Nakazawa *et al.* [98]. Two groups of patients, one with untreated atherosclerotic coronary bifurcation and another with stented bifurcation lesions were examined. For the unstented group, significantly greater intimal thickening was found on the lateral bifurcation

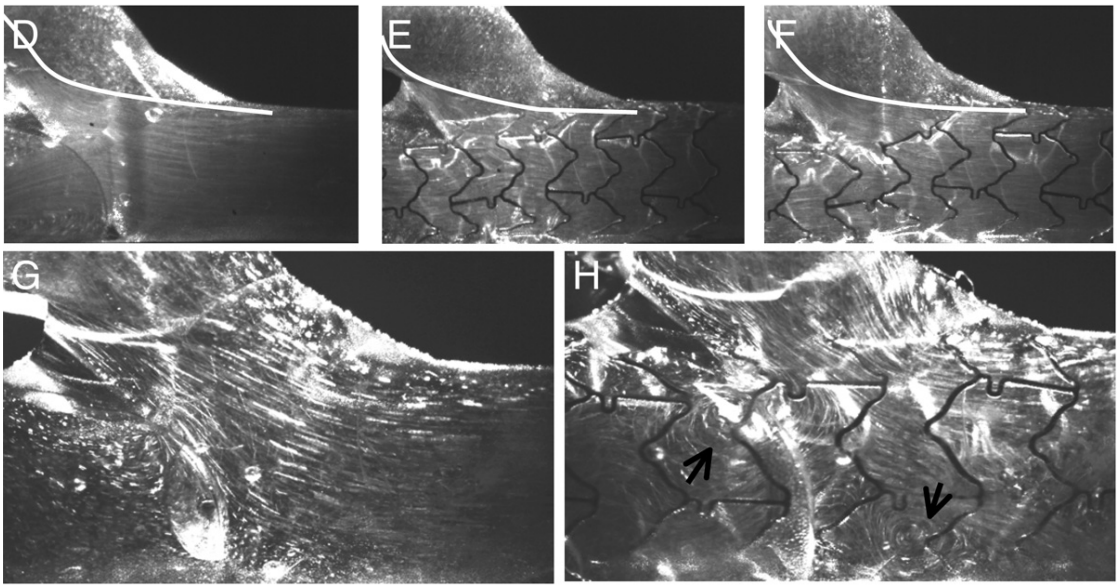

Figure 3.3. Flow recirculation is present at the lateral bifurcation wall (upper-left image) while flow disturbances develop near the wall due to stent placement (lower-right image)

wall than on the flow divider wall. This particular region is subject to recirculating flow during systole as found in the bifurcation model used in the study and shown in Figure 3.3. Late stent thrombosis and restenosis was found in patients with stented coronary bifurcation while neointimal growth was significantly less at the flow divider wall than at the lateral wall. The study also included flow experiments in stented bifurcation models obtained from arterial casts that showed flow disturbances near the stent struts (lower-right image, Figure 3.3).These disturbances may play a role in stent-induced thrombosis, fibrin, and platelet deposition as well as decreasing drug elution rates for DES, thus decreasing their effectiveness in healing the arterial wall.

The role of arterial hemodynamics in atherosclerosis development has been discussed in chapter 1, section 1.2 and most of the findings suggest that low mean and oscillating WSS are a promoter of intimal thickening. The studies discussed above suggest that stent design, stent strut dimension, deployment characteristics

such as malapposition, non-uniform strut distribution, and strut prolapse influence neointimal growth, in-stent restenosis, and thrombosis. These findings have motivated the use of CHD to analyze stent-induced alterations of blood flow and to estimate potentially deleterious effects caused by stent implants.

3.2 Previous work

Blood flow modeling in stented arteries using CHD simulations has been performed using two- and three-dimensional representations of stent and arteries with stent geometries being generated by computer aided design programs—which results in uniform virtual stent deployment. Two-dimensional studies, although limited, can provide useful insights into flow around stent struts and potential zones of flow reversal and recirculation. Investigation of strut size and inter-strut spacing in the study by Berry *et al.* [107] reveals the impact of stent geometry and configuration on flow hemodynamics. Thicker struts result in larger recirculation zones downstream of the struts while small strut spacing (less than six strut diameters) results in recirculation zones extending from one strut to another. Estimates of drug elution rates for DES have been obtained from simple two-dimensional models as well. The influence of DES strut distribution and single and overlapping stent configuration on drug delivery to the arterial wall has been studied by Balakrishnan *et al.* [108]. The findings indicate that drug deposition into the arterial wall occurs more as the result of flow-mediated transport than of contact between the stent and arterial wall.

Results from *in vitro* experiments on stent-induced thrombosis suggesting that flow disturbances due to stent placement are influencing thrombosis were interpreted using two-dimensional CHD simulations of flow over rectangular stent struts

[30]. The study concluded that in-stent thrombosis correlates with disturbed flow generated on the downstream side of struts. However, these two-dimensional models fail to capture the full flow field, especially secondary flow effects determined by the three-dimensionality of real stent struts. The majority of stent configurations have struts oriented at an angle with respect to flow direction or vessel axis. Secondary flow along the struts decreases the size of flow recirculation regions that form on the downstream side of struts indicating an overestimation of flow reversal region by two-dimensional studies [109].

A large number of CHD simulations of blood flow in stented vessels are performed using three-dimensional stent models. Some of the first studies on this subject have been performed by LaDisa and colleagues [110] using computer generated stent models seeking to investigate different aspects of stent configurations and their effect on hemodynamics. In the initial study, a stent model based on the Palmaz-Schatz—350 μm wide and 100 μm thick struts—deployed in a straight tube was generated using computer aided design software [110]. Simulations based on flow data from canine coronary artery were performed with results indicating stagnation zones developing adjacent to stent struts and significant decrease—by 77%—in minimum WSS inside the stented segment when compared with the unstented section of the vessel.

In a subsequent study the effect of stent overexpansion (i.e., the diameter of the stented segment is larger then the one of the unstented segment) and the number of struts per circumference on the in-stent flow was investigated [111]. The stent designs had four or eight struts per circumference and deployment ratios (stent-artery diameter ratios) of 1.1-1 and 1.2-1. Steady flow simulations indicated the dependence of WSS distribution on stent design and the amount of overexpansion as exemplified in Figure 3.4 (adapted from [111]). Regions of high WSS are

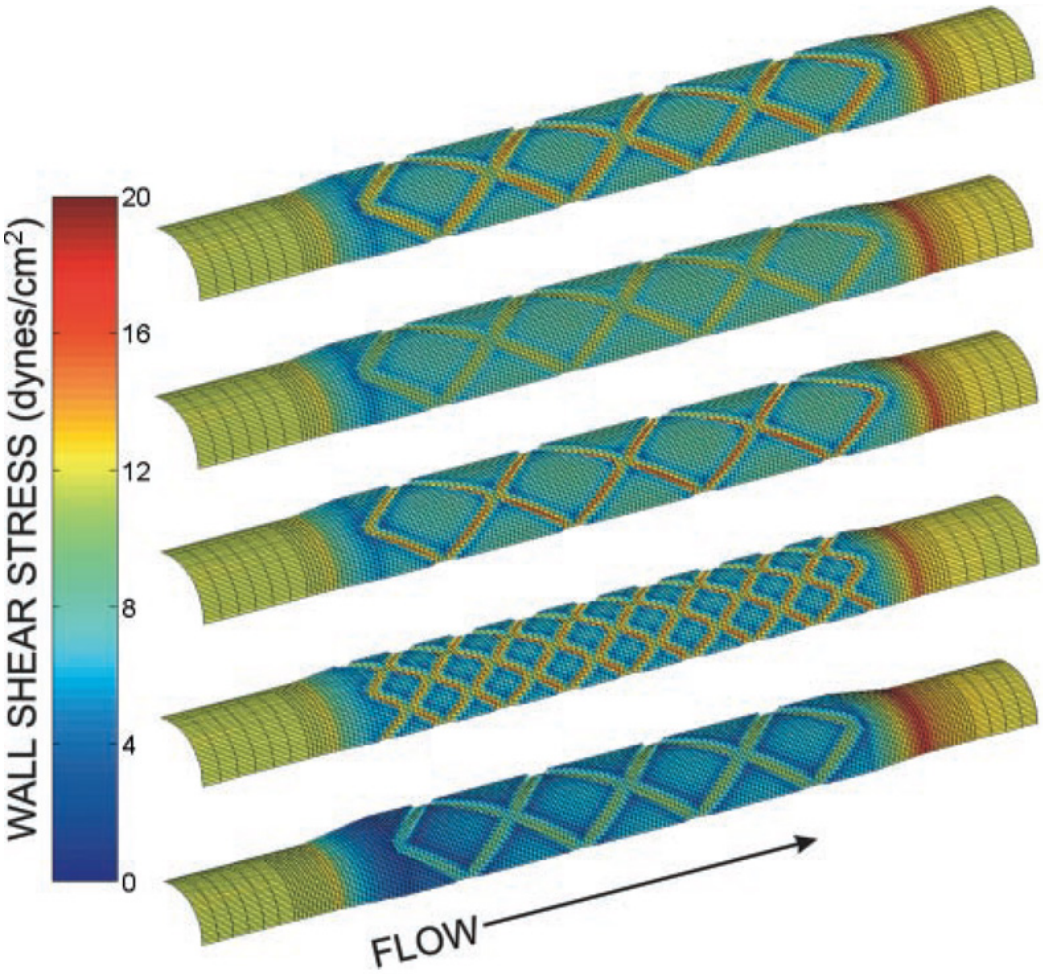

Figure 3.4. Wall shear stress distribution in stented segments with different over-expansion ratios and number of struts

present on the luminal side of struts and at the distal end of stents while low WSS is present at the proximal end of stents and downstream of struts. Other computational studies on stent hemodynamics showing similar findings regarding WSS distribution and stent design have been published [35, 112–114].

Stent strut orientation with respect to flow direction and vessel axis was found to influence the WSS distribution with larger strut angles resulting in increased low WSS area and elevated WSS spatial gradients [109]. A CHD study by He *et al.* [115] on strut shape and orientation concluded that in order to reduce the impact

of stent placement on flow, interstrut spacing should be larger, struts should be oriented to the flow direction, and strut connectors should be parallel to the vessel axis.

In a more complex study combining experimental and CHD simulations, LaDisa *et al.* [116] constructed a stented arterial segment model based on a plastic cast of a stented rabbit iliac artery and compared the flow conditions obtained from computational models with results from histological analysis on the stented iliac artery. It was found that the neointimal hyperplasia correlated with low WSS and high WSS spatial gradient regions. However, these conclusions should be treated with some degree of caution as the results from CHD simulations were obtained using a computer generated stent model and not from using the real stent and artery geometry.

Arterial wall prolapse at the stent cell center and the polygonalization of the wall contour due to stent deployment and their effect on blood flow was modeled in another study by LaDisa *et al.* [117]. Results indicate that elevated WSS values are present at stent cell centers and that stents with a lower number of struts in a cross-sectional plane and polygonal wall contours have larger areas exposed to low WSS than stents with a higher number of struts.

A more recent study involving the virtual deployment of a stent model in arterial segments acquired from CT images also investigated in-stent hemodynamics. The purpose was to demonstrate the feasibility of this method for investigation of patient-specific cases in which stent models are implanted in reconstructed arterial geometries [118]. A similar study was performed earlier in which teams from different research institutions were provided with the same arterial and stent geometries and were asked to perform virtual stenting and CHD simulations under the same flow conditions [36]. The results showed excellent agreement among the

flow solutions obtained with different numerical solvers by each team.

Real deployed stent geometry acquired from an excised arterial segment by microCT imaging was used in the study by Morlacchi *et al.* [92] on hemodynamics and in-stent restenosis. Stent coverage due to neointimal growth did not allow for the reconstruction of the arterial wall and a finite element analysis was used to virtually recreate the wall. Flow simulations were performed and correlations between WSS and neointimal hyperplasia distribution obtained from histological analysis were found. Although the geometry of a real stent adds more realism to CHD simulations and should provide better results, the use of an artificial arterial wall cannot fully capture the stent-arterial wall interaction and may raise doubts about estimating the true *in vivo* WSS distribution. As shown in chapter 2, section 2.5, the stent-wall interaction results in important stent deployment non-uniformities such as strut prolapse, strut vertex misalignment, wall creases, and wall prolapse at stent cell centers that influence in-stent hemodynamics.

3.3 Computational methods

The flow in stented tubes presented in this chapter is obtained from CHD simulations performed in stent and vessel wall geometries acquired through high-resolution microCT imaging with the exception of the NF3 stent for which the stent and wall geometry reconstructed from clinical C-arm CT is also used. The details of stent deployment, imaging, and stent and wall surface reconstructions are not discussed in this section as they have been already addressed in chapter 2. The stents used for flow simulations in this work are the Neuroform Treo (NF3), Enterprise, BxVelocity, and Taxus Express (Taxus). The dimensions of the stented segments and the stent properties are shown in Table 3.1. Another NF3 stent of

Table 3.1. Properties of stents used in computational hemodynamics simulations

Stent properties	**NF3**	**Enterprise**	**BxVelocity**	**Taxus**
Application	Intracranial	Intracranial	Coronary	Coronary
Stent length (mm)	30	28	27	16
Diameter (mm)	4.5	4.5	3.0	3.0
Strut thickness (μm)	70	60	140	140
Design	Open-cell	Closed-cell	Closed-cell	Open-cell

3.5 mm diameter and 20 mm length (not included in Table 3.1) deployed in an excised canine artery is also used for CHD simulations. While all the stents have similar diameters and approximately the same length, intracranial stents have thinner struts than coronary stents—almost half the thickness. This is typical of intracranial stents which need to be more flexible to provide enhanced compliance in tortuous cerebral arteries. The numerical method used to solve the flow, the meshing techniques, and spatial and temporal convergence tests are discussed in this section.

3.3.1 Numerical solver

The equations of motion for fluid flow are solved using FLUENT 6.3, a computational fluid dynamics software package developed by ANSYS, Inc. (Canonsburg, PA). The program is an advanced flow solver that can be used in a large array of applications for both compressible and incompressible flows, using laminar flow or a variety of turbulence models. The program also allows for simulating both single phase and multiphase flows. The major advantage of commercial codes such as FLUENT is their flexibility for solving flows in complex computational domains such as those generated from arterial geometries. FLUENT uses the finite volume method to numerically solve the governing flow equations—non-linear partial

differential equations. The entire computational domain is discretized into small volumes or grid cells that represent the computational mesh and each cell is considered as a control volume over which the Navier-Stokes equations are integrated. Increasing the number of grid cells—i.e., smaller discrete control volumes—results in a finer computational mesh that usually generates a more accurate solution but also increases the computational cost.

For the CHD studies performed in this work the segregated solver in FLUENT is chosen. In the segregated solver, the governing equations (continuity and balance of momentum) are solved sequentially in an iterative fashion until some convergence criteria are met. The solver is used with a QUICK [119] face value interpolation scheme, the SIMPLE pressure-velocity coupling algorithm [119], second-order upwind discretization for momentum, and a second-order implicit time discretization. The convergence criteria imposed on the residuals of the velocity field and of the continuity equation is 10^{-5}, where the residuals represent the difference between successive approximated values.

3.3.2 Blood flow model

Blood flow in arteries is too complex for CHD studies to accurately model every aspect of it and certain simplifying assumptions that ignore less significant aspects are therefore used. In this work, the most common and widely accepted assumptions in CHD simulations are also considered. These assumptions include:

- rigid, non-porous arterial walls;
- blood as a single-phase, Newtonian fluid;
- laminar, incompressible flow.

Arterial walls, as discussed in chapter 1, are elastic and expand and contract in response to pressure pulse and other stimuli. The arterial wall compliance effects are most significant for flows in the aorta and coronary arteries; however, for flows in the carotid and cerebral arteries the compliance effects are usually second order; their compliance is much smaller than that of the aorta [2, 3]. Also, stent deployment is shown to decrease arterial compliance [120]; therefore, a rigid arterial wall is considered a reasonable assumption for CHD studies in stented vessels.

Blood behavior as a single-phase fluid is an accepted assumption when modeling blood flow in arteries with diameters larger than 0.5 mm [2, 4]. It is only flow in small blood vessels such the arterioles and capillaries that two-phase flow behavior with a cell-free layer forming near the vessel wall occurs. This layer is about 10–12 μm in thickness and consists of blood plasma with a lower viscosity than that of whole blood [4]. The layer thickness is relatively small in larger arteries and the assumptions of uniform blood viscosity and single-phase flow are warranted [2, 4]. The non-Newtonian behavior of blood at low and high shear rates when modeling flow in stented vessels was shown to have a somewhat limited impact on the flow variables such as WSS [35].

Blood flow in healthy arteries is considered to be laminar as the Reynolds number (Re) at peak systolic flow is less than the critical Reynolds number for transition to turbulence in pipes [1, 3]. For special cases such as aortic valve flow or stenotic arteries, the flow might become turbulent due to increased blood flow velocity and local vascular topology and require the use of turbulence models in CHD studies [25]. The range of peak systole Reynolds numbers typical of the blood flow encountered in major systemic arteries other than the aorta is 100–1200 which is considered inside the laminar flow regime.

While the importance of arterial compliance and non-Newtonian blood behavior should not be neglected more complex and extensive CHD studies should incorporate these second order effects. The purpose of the current work is to investigate blood flow in stented vessels by adding another degree of realism through the use of stent and vessel wall geometry acquired from actual deployed stents. For all simulations in this work, flow is considered laminar and blood is modeled as a Newtonian fluid with viscosity $\mu = 4 \times 10^{-3}$ kg/(m·s) and a uniform density $\rho = 1060$ kg/m^3.

3.3.3 Computational mesh

The computational mesh based on each stent and vessel wall geometry is generated with GAMBIT 3.4 (ANSYS), the native meshing program associated with FLUENT. An example of the mesh used for the BxVelocity stent is shown in Figure 3.5 in which small tetrahedral elements are used on the surface representing the stent and the wall and larger elements are used in the middle of the domain. The choice of this meshing strategy is discussed below.

The stent and wall surfaces reconstructed from microCT data and generated in Amira, as discussed in chapter 2, subsection 2.3.3, are exported as one surface in stereolithography (STL) format in which the surface is represented by triangular faces. The only edges defined on this surface are the inlet and outlet contours. When the combined stent-wall surface—the STL faceted surface—is loaded into GAMBIT, the meshing algorithm builds the mesh from the inlet and outlet edges. This means that the mesh spacing is uniform on the entire stent-wall surface and is dependent on the mesh spacing defined on the existing two edges (at the inlet and outlet, in this case). As the stent strut dimensions are relatively small when compared with the diameter of the artery or vessel, a finer mesh spacing is required

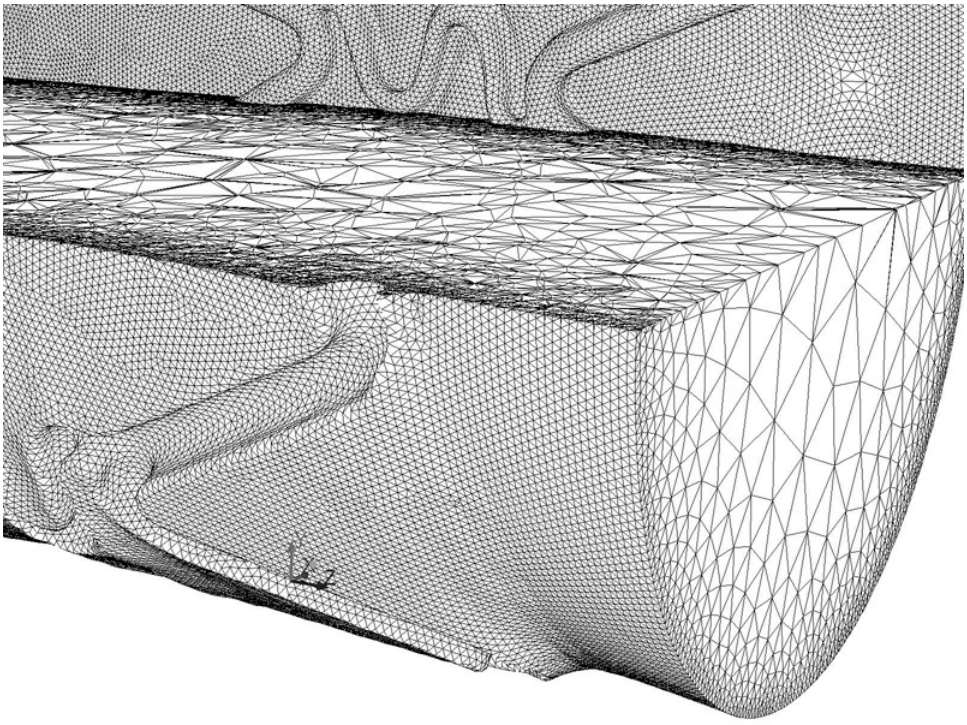

Figure 3.5. Tetrahedral mesh with finer mesh spacing on and near the stent and wall and coarser in the middle of the tube

on and near the stent struts in order to obtain more accurate flow solutions. This can result in a very large number of mesh cells that increase the computational cost (i.e., the time required to solve the flow over the entire computational domain).

To optimize the mesh size, larger mesh elements can be used in regions where spatial gradients of flow variables such as the velocity are small. In pipe flows, the central region does not experience high velocity gradients and, therefore, coarser mesh elements can be used as illustrated in Figure 3.5. Other optimization techniques for meshing can include the use of finer meshing only on the stent struts and in their vicinity while for the rest of the wall surface a coarser mesh can be used. This strategy is illustrated in Figure 3.6 where virtual edges are built along each side of the stent struts to define a finer mesh in these regions. This technique is time consuming as each of the virtual edges has to be manually built along both

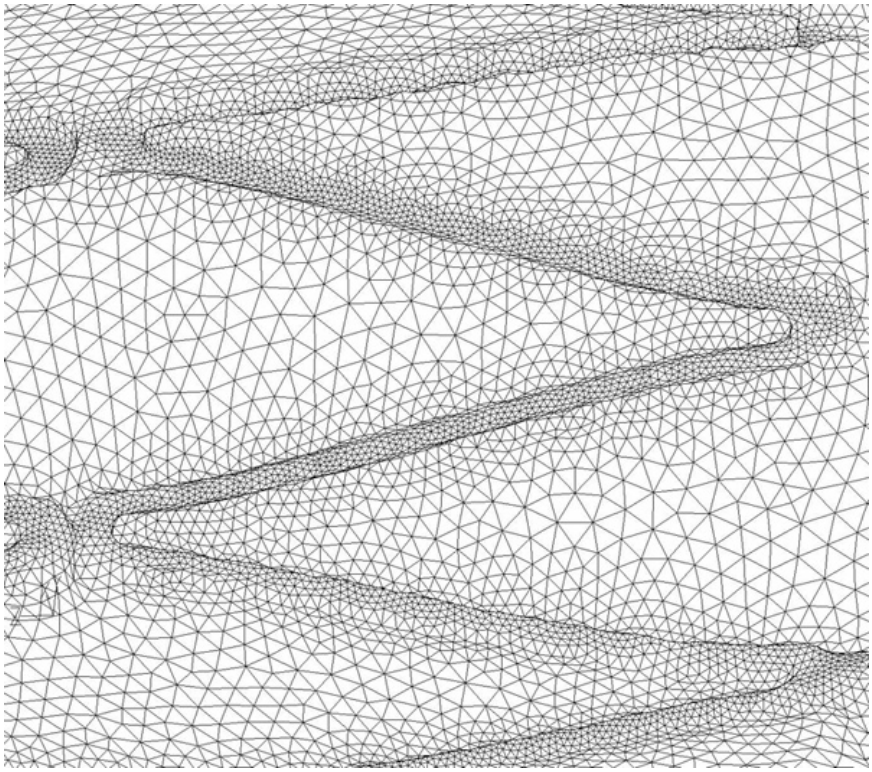

Figure 3.6. Tetrahedral mesh with finer mesh spacing on and near the struts and coarser meshing on the regular wall

sides of each strut. The use of non-parametric surfaces such as the faceted surface obtained for the stent-wall surface does not allow for the automatic generation of edges along the stent struts.

The mesh for all stents in this work is built using tetrahedral elements. The complex topology and the fact that the surface representing the stent and the wall is a faceted surface and not a parametric one does not directly allow for the use of hexahedral elements which provide better accuracy by reducing numerical diffusion and offering an overall volumetric mesh with a lower number of equivalent mesh elements. Numerical diffusion typically arises in solutions obtained from tetrahedral meshes due to small numerical errors generated when fluxes of flow variables are computed on mesh faces that are oriented at small angles with respect to the gradients of those variables.

3.3.4 Spatial and temporal convergence

A uniformly fine mesh is generated along the stent-wall surface. The spatial resolution is checked by computing the root mean square of the velocity field difference between two consecutively refined meshes. Spatial mesh convergence was considered satisfactory when the root mean square error in the velocity field between two consecutive mesh sizes was less than 5%. The ratio of the mesh size h to the strut diameter d—$h/d \leq 0.3$—is within the mesh resolution limits recommended by Stuhne and Steinman [121] in their simulations of flow over an idealized stent model.

The mesh size used for CHD simulations contains 8,600,000 mesh elements for the NF3, 9,800,000 for the Enterprise, 8,100,000 for BxVelocity, and 9,300,000 for Taxus. For the NF3 stent deployed in the canine artery, the meshing strategy described above with finer mesh elements generated on and near the struts and coarser on the rest of the regular wall resulted in a volumetric mesh with approximately 2,700,000 mesh elements. Considering that the canine artery stented section is also shorter than the other stented tube segments the total number of mesh elements can be reduced by roughly one half using the meshing strategy employed for the stented canine artery geometry. The NF3 geometry reconstructed from C-arm CT images and used in this part for CHD simulations is described by a tetrahedral mesh containing 1,700,000 mesh elements.

For time-dependent CHD simulations the temporal convergence is examined by comparing the velocity and WSS at two different locations in the stented segment and at the same moment in time for time steps of 10^{-2} s, 10^{-3} s, and 10^{-4} s. The 10^{-3} s time step is chosen as no significant difference in flow variables exist between solutions obtained with 10^{-3} s and 10^{-4} s time steps. Periodic time-dependent

volumetric flow rates that are described later in this chapter are used for unsteady CHD simulations. The periodic flow is initialized by obtaining the converged flow solution at the initial time from the steady flow simulation. Three consecutive time periods of the waveform are computed and the results between each time period are compared to ensure that transients associated with initializing an unsteady flow simulation from a steady solution are negligible. As the flow solution—in terms of velocity profiles—obtained from the second and third time periods are similar, the results from the second time period are used to represent the solution to periodic time-dependent flow.

3.3.5 Validation

For the flow simulations performed in this work there are no analytical solutions or flow results for similar stent geometries. A validation test that can be performed is the comparison between flow solutions obtained from FLUENT and the analytical solution to the time-dependent flow in a round pipe obtained by Womersley [122]. The velocity profiles obtained from three types of tetrahedral meshes and from one hexahedral mesh for sinusoidal flow in a straight pipe are compared with the profiles obtained from the analytical solution at different points in time along the waveform.

The four meshes used in this validation study are shown in Figure 3.7. The coarsest tetrahedral mesh contains 36 circumferential nodes and the mesh is uniform throughout the entire computational domain (Figure 3.7a). A slightly finer tetrahedral mesh with 56 circumferential nodes is shown in Figure 3.7b. To test the influence on the numerical solution of a non-uniformly distributed mesh with fine mesh at the wall, a tetrahedral mesh is built with 128 circumferential nodes and uniform mesh on the wall while the interior mesh is allowed to increase as

shown in Figure 3.7c. A hexahedral mesh is also built with 36 circumferential nodes with a fine mesh at the wall that is allowed to grow with increasing distance from the wall (Figure 3.7c). The hexahedral elements at and in the vicinity of the wall are arranged in a radial orientation in what is known as boundary layer meshing. This meshing strategy ensures that mesh elements are oriented along the normal of the local boundary to minimize numerical diffusion and that mesh spacing (or resolution) is small such that gradients of flow variables such as the velocity can be resolved near the wall boundary.

The meshes described above are used to obtain the velocity profiles for a periodic flow defined by a sinusoidal waveform shown in Figure 3.8a. Three points in time are analyzed: at the beginning of the flow acceleration, at peak flow, and near the end of deceleration when flow reverses. The Womersley number for the flow is 5 while peak Reynolds number is ~ 200. Due to the relatively high flow pulsatility the shape of the velocity profiles differs from the parabolic shape typical of steady or low pulsatility flows. The velocity profiles obtained with the hexahedral mesh closely match the analytical profiles at all points in time. The velocity profiles obtained with the tetrahedral meshes match the analytical solution well only during peak flow (Figure 3.8c) while at other points in time larger errors occur—especially at the center of the pipe. The tetrahedral mesh with fine mesh spacing at the wall provides a better velocity approximation than the other tetrahedral meshes; however, the error in velocity at the center of the pipe is larger than the error displayed by the other tetrahedral meshes used (Figure 3.8d).

It is clear from Figure 3.8 that the numerical solution obtained with the hexahedral mesh is more accurate than a solution obtained with any of the tetrahedral meshes. As discussed before, the numerical diffusion associated with tetrahedral elements introduces errors and the results obtained from such computational grids

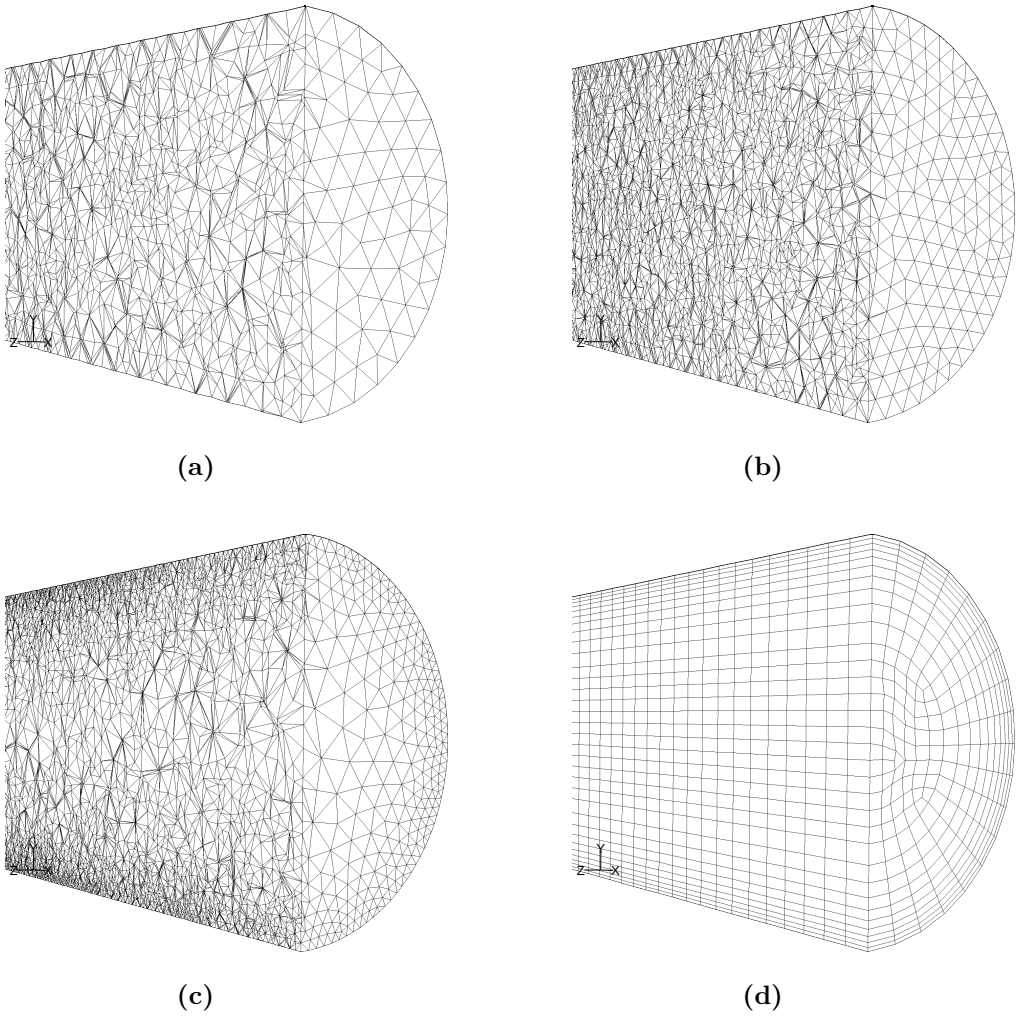

Figure 3.7. Tetrahedral meshes with 36, 56, and 128 circumferential nodes and a hexahedral mesh with 36 circumferential nodes are used for validation purpose

must be interpreted with this limitation in mind. The ease of tetrahedral mesh generation over highly complex computational domains makes the use of these type of elements very appealing for complex arterial geometries. Hexahedral mesh generation over highly convoluted arterial segments or bifurcations requires special techniques such as block meshing which consists of decomposing the grid into smaller rectangular blocks that span short sections. Although time consuming

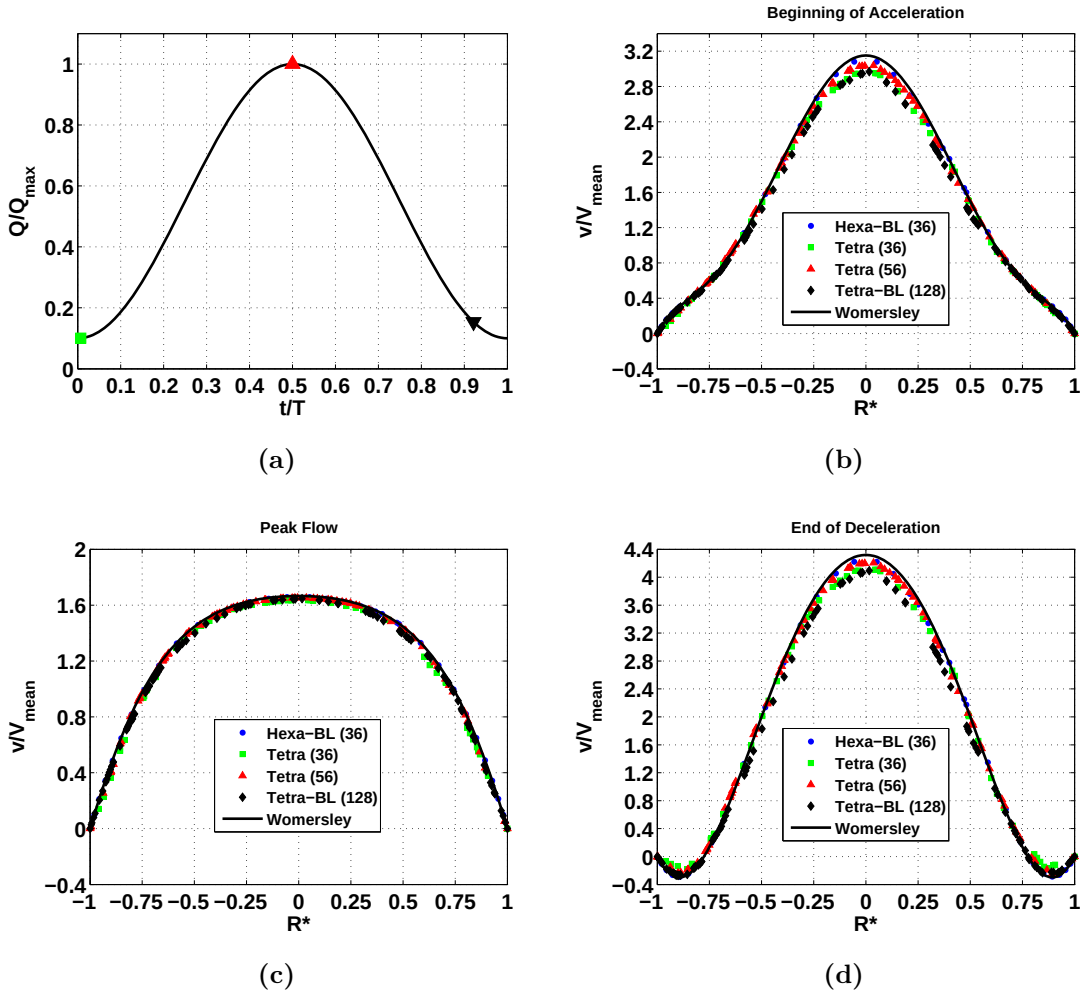

Figure 3.8. Velocity profiles for pulsatile flow (Womersley number = 5) at beginning acceleration (b), peak flow (c), and end of deceleration (d)

when compared with tetrahedral meshing, this block meshing technique can be performed in arterial segments with smooth walls. For realistic stent geometries acquired from CT or other imaging modalities this might not be feasible as meshing challenges are encoutered at regions where prolapsed struts intersect the vessel wall. Overall, the solution to the time-dependent flow in a round pipe is reasonably approximated by FLUENT when tetrahedral meshes are used; however, consistent under-estimation of the velocity magnitude associated with tetrahedral meshes due

to numerical diffusion must not be neglected.

3.4 Steady flow

The blood flow in stented vessels is modeled as described above using stent and vessel wall geometries acquired by high-resolution microCT imaging. The use of realistic stent deployment in CHD studies represents a step forward in modeling the interaction between stents and blood flow and its impact on neointimal hyperplasia, in-stent restenosis & thrombogenesis. This section is concerned with steady flow simulations at moderate Reynolds number in intracranial and coronary stents. Although blood flow is pulsatile in nature, valuable information can be gained from steady flow simulations which are less computationally costly to perform than unsteady simulations. First, the impact of accurate stent geometry reconstruction on CHD simulations is discussed by comparing flow results obtained with C-arm CT acquired stent geometry and flow results obtained with microCT. Then, the results from CHD simulations based on intracranial and coronary stents acquired by microCT imaging are presented.

3.4.1 Boundary conditions

The conditions imposed in FLUENT include incompressible, laminar flow with a no-slip boundary condition on the wall. A mass-flux rate boundary condition is defined at the inlet surface to generate steady flow corresponding to peak systolic conditions encountered in the common carotid artery. Inlet and outlet segments are added upstream and downstream of the stented segment to minimize any numerical errors from the boundaries. The inlet segment also serves as an entrance tube that allows the flow to become fully developed—i.e., to allow for viscous effects to be

present in the entire flow field and not only near the wall. For steady, laminar, fully developed flows in cylindrical pipes the velocity profile exhibits a parabolic shape while in the entrance region the velocity profile displays a blunt profile with uniform velocity in the center. To ensure the flow is fully developed, the length of the inlet tube is calculated using the empirical formula determined for flows in pipes, $L = 0.06 \cdot D \cdot \mathrm{Re}$, where D is the pipe diameter [123]. For the outlet surface, a zero pressure boundary condition is imposed. The Reynolds number, based on proximal vessel diameter and mean velocity, is 550—typical of human carotid arteries [3].

3.4.2 Flow obtained from C-arm CT and microCT stent reconstructions

The quality of stent surface reconstructions from clinical CT images has been discussed in chapter 2 where it was shown that spatial resolution limitations of current CT modalities such as 64-slice CT (MS-CT), flat panel CT (FP-CT), and C-arm CT result in an overestimation of stent strut dimension and inaccurate stent reconstructions. To assess the impact of stent reconstruction quality on in-stent hemodynamics, CHD simulations were performed using the C-arm CT reconstruction of the NF3 stent deployed in the PTFE graft tube. The results from steady flow conditions are compared with similar results obtained from CHD simulations performed on the same NF3 stent imaged by microCT. The overall WSS distribution inside the stented segment and depicted in Figure 3.9 shows that the enlarged C-arm CT strut reconstructions are generating much higher WSS than struts reconstructed with the microCT. The irregularities in the wall within the strut cells due to beam hardening artifacts are also apparent in the heterogeneous

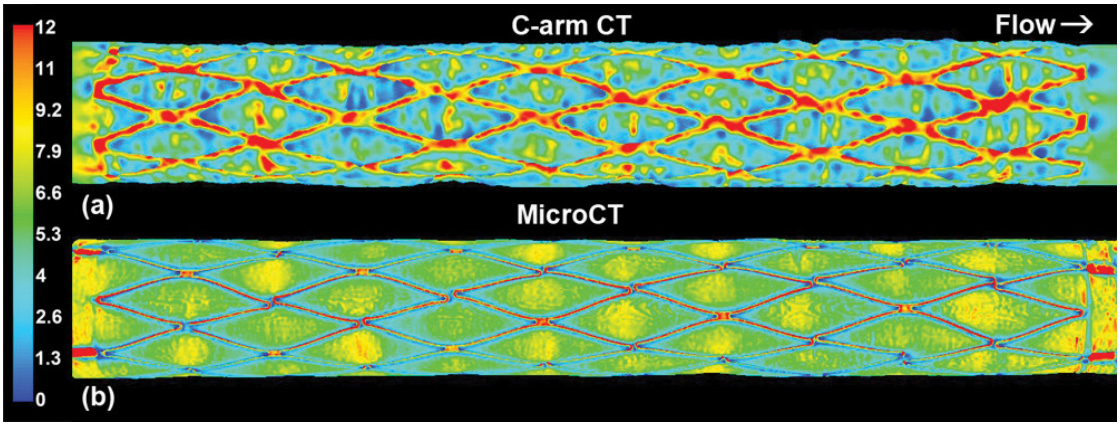

Figure 3.9. Wall shear stress contours (Pa) for the NF3 stent deployed in a straight graft tube acquired from C-arm CT (a) and from microCT (b)

WSS distribution shown in Figure 3.9a. Also noticeable is the absence of the stent markers for the C-arm CT reconstruction due to beam hardening artifacts present that made impossible the reconstruction of markers.

The impact of stent reconstruction quality on hemodynamics at locations of strut prolapse and strut vertex misalignment is illustrated in Figure 3.10. Three different stent cells are compared: a normal cell with vertex and strut connector, a cell with strut prolapse into the lumen, and a cell with two vertex gaps. The C-arm CT images cannot distinguish between the connector and the vertex gap (indicated by the arrow) in Figure 3.10a—the vertex gap is fused and resembles a strut connector with high WSS on the luminal face. The same stent cell reconstructed from microCT imaging shows the WSS distribution in the vicinity of the gap and the strut connector (Figure 3.10b).

The microCT simulations show a relatively uniform WSS near the cell center while the C-arm CT simulation shows a strongly varying WSS with due to wall non-uniformity. Relatively low WSS (< 0.2 Pa) is present adjacent to the struts, while the C-arm CT simulation suggests the existence of such zones near the center

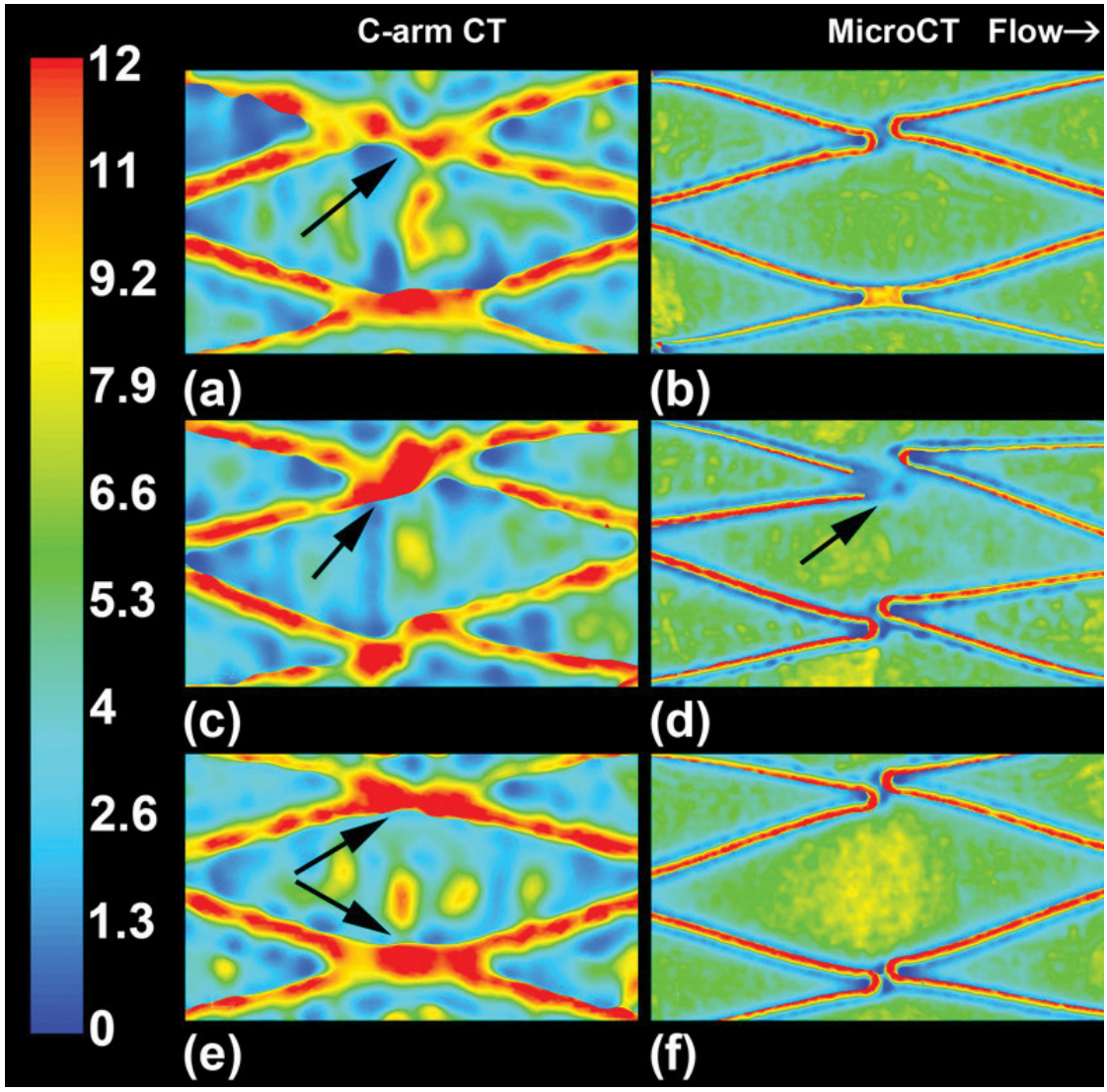

Figure 3.10. Wall shear stress contours (Pa)—comparison between C-arm CT and microCT reconstructions

of the stent cells. A cell with a strut prolapse into the lumen and away from the vessel wall (indicated by arrows) is shown in Figures 3.10c & 3.10d. The region of very low WSS is due to flow diversion by the elevated strut as captured by the microCT reconstruction. The comparable location with C-arm CT does not show this effect, but exhibits elevated WSS instead while the misaligned vertex gap immediately below it appears to be fused and also exhibits high WSS. In

Figure 3.10e & 3.10f a cell with two vertex gaps is shown. Again, high WSS is predicted by the C-arm CT due to the fused vertex gaps.

Potentially misleading results from CHD simulations based on stent and wall surface reconstructions from C-arm CT are due to the artifacts generated near strut vertex gaps where the vertices are artificially connected and the locations of strut prolapse into the lumen—which are not detected. It is here that the C-arm CT reconstruction fails to capture the real flow diversion effects of the struts and the consequent low WSS. Other significant reconstruction artifacts include strut oversizing with an average strut diameter of 190 μm—the real strut size is 60 μm, wall roughness, and the inability to capture stent markers.

3.4.3 Intracranial stents

The deployment of the NF3 and Enterprise stents in polytetrafluoroethylene (PTFE) arterial grafts has already been discussed in chapter 2, section 2.5 (Figures 2.9–2.11). The influence of stent deployment and its characteristics (e.g., strut misalignment and prolapse) on the flow in discussed in this part. The contour plots of the axial velocity magnitude on a cross-sectional plane are shown in Figure 3.11 along with the wall and stent surface (shown in gray). The NF3 stent is well apposed to the wall over most of the stented segment; however, it does exhibit small malapposition in several cells near the distal end of the stent. The prolapse of an open strut vertex into the lumen (single arrow, Figure 3.11a) permits low-velocity flow between the strut and the wall. In addition, misalignment of the vertices (double arrows, Figure 3.11a) also results in low velocity flow developing at strut vertices. Due to the closed-cell design—all vertices are physically connected—vertex misalignment or strut vertex prolapse into the lumen cannot occur with the Enterprise stent.

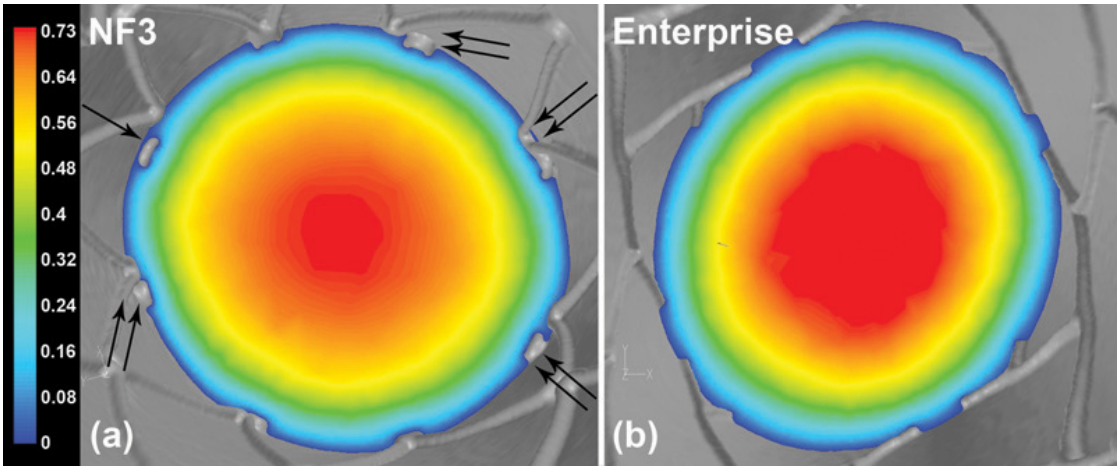

Figure 3.11. Down-the-barrel views of the wall surface (gray) and velocity contours (m/s). Single arrow indicated strut prolapse into the lumen while double arrows indicate strut vertex misalignment

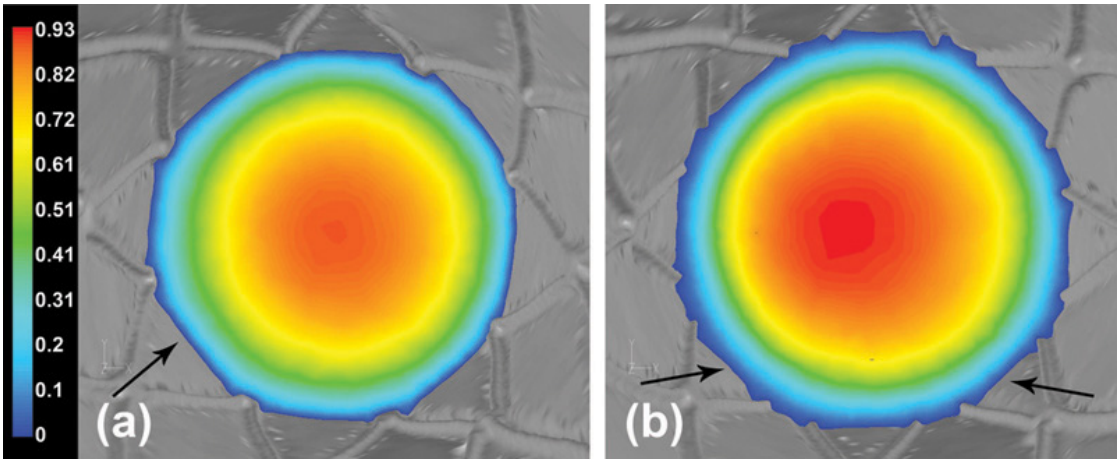

Figure 3.12. Velocity contours (m/s) on two cross-sectional planes. The NF3 deployed in canine artery exhibits wall polygonalization (arrow, (a)) and prolapse into the lumen (arrows, (b))

The NF3 deployed in the canine artery exhibits wall prolapse into the lumen which generates a polygonal wall contour as illustrated in Figure 3.12. The velocity magnitude contours are shown on two cross-sectional planes: one in the middle of the stent cells (Figure 3.12a) and another one near the strut vertices (Figure 3.12b). The wall prolapse and the polygonalization effects—indicated by arrows—cause higher velocity variation in the radial direction and thus, higher WSS.

The WSS distribution in the stented region is shown for the NF3 stent in Figure 3.13. For better visualization of WSS, the cylindrical stent and wall surface (Figure 3.13a) is projected on a planar surface shown in Figure 3.13b. Low WSS values (< 0.5 Pa) are observed around the stent struts while the values on the luminal face of the struts are about 12 Pa. Slightly larger regions exposed to low WSS are present near the strut prolapse into the lumen as indicated by arrows in Figure 3.13b. Non-uniform WSS distribution inside the stent cells is present—higher values at cell centers—due to slight wall prolapse at the cell centers. The peak WSS at the centers of some of the NF cells is 8.5 Pa, whereas the average WSS over the cells is 5.6 Pa. Relatively higher WSS is present near the markers at both stent ends due to the deployment characteristics of the NF3. One plausible explanation is less expansion force exerted against the wall at the end of the NF3 by the large markers than with the interior struts due to the the self-expandable nature of the NF3 stent. Across the top luminal surface of the stent markers—which are wider and thicker than regular struts—the WSS values reach 28 Pa. Downstream of the stent markers, small regions of low WSS develop.

The WSS distribution for the closed-cell design Enterprise stent is shown in Figure 3.14 on both the original and planar projection surface. The Enterprise stent is well apposed to the vessel wall and due to its design does not have prolapsing strut vertices and does not exhibit the non-uniform cells present in the case of the NF3 stent. Also, the WSS distribution inside stent cells is more uniform compared with the NF3 stent with peak values of 6.8 Pa at cell centers and average WSS values of 5.5 Pa. Low WSS similar in magnitude with the one from the NF3 stent is present around the struts, downstream of imaging markers, and in regions where the struts connecting the larger markers with the regular struts are protruding into the lumen (Figure 3.14b). WSS on the luminal face of markers

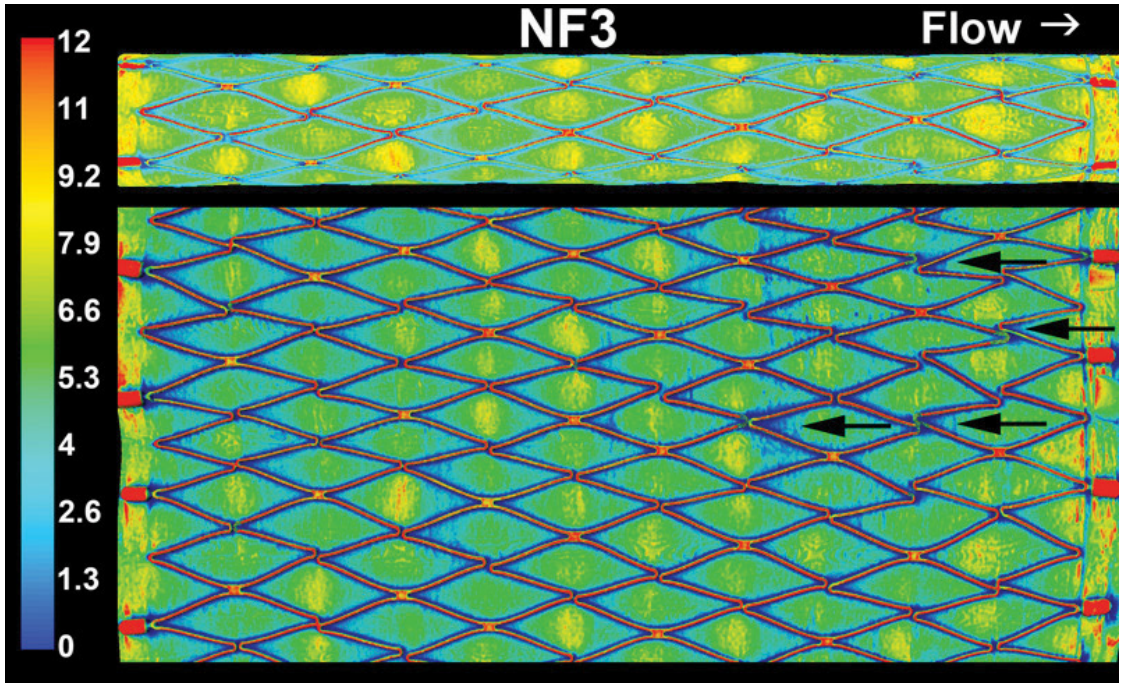

Figure 3.13. Wall shear stress contours (Pa) for the NF3 stent deployed in a straight arterial graft

is about 20 Pa for the Enterprise stent.

The NF3 stent deployed in the canine artery exhibits greater WSS variation (shown in Figure 3.15) than the NF3 stent deployed in the PTFE tube due to the arterial geometry that is characterized by proximal and distal curvatures and arterial tapering toward the distal end of the stented section. As with the NF3 deployed in the straight tube, low WSS occurs along the struts and at strut vertices. The highest WSS values, reaching a peak of 28 Pa, occur at the curved inlet and outlet section due to local arterial radius reduction, while inside the stented region high WSS of about 17 Pa occurs at the cell centers near the distal end of the stent due to arterial tapering. The circumferential creases (polygonalization effect) formed by the struts impinging on the wall at some of the strut vertices also affect the WSS distribution inside stent cells as discussed below in greater detail.

Local WSS distribution in interior, regularly apposed stent cells for the NF3

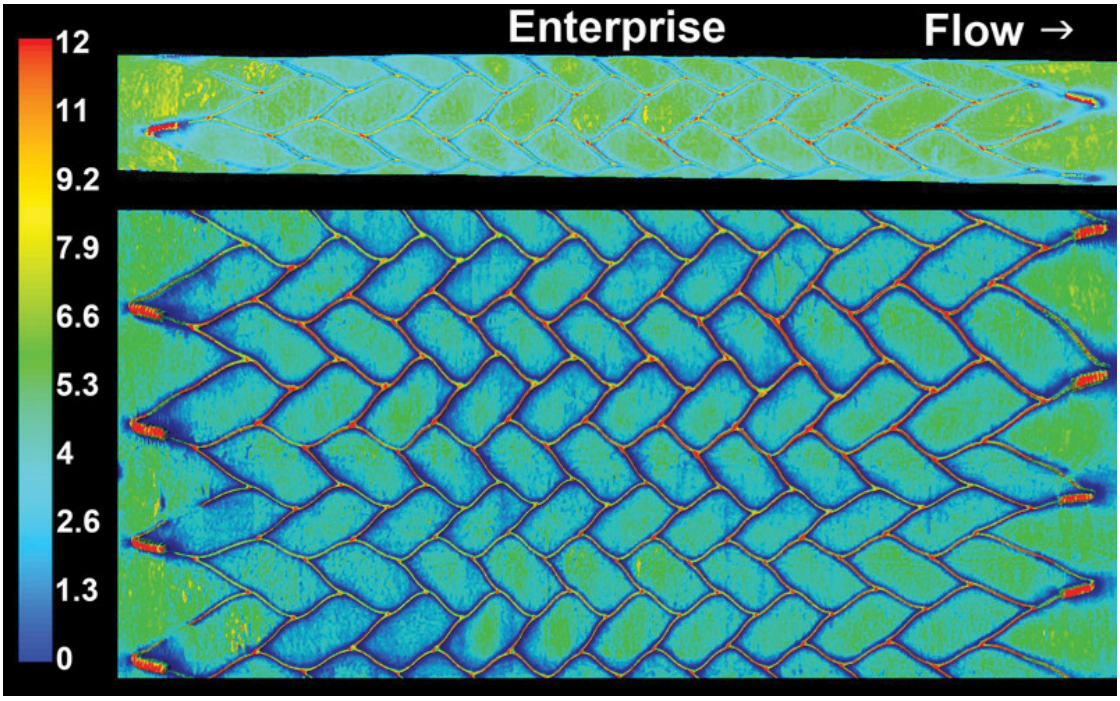

Figure 3.14. Wall shear stress contours (Pa) for the Enterprise stent

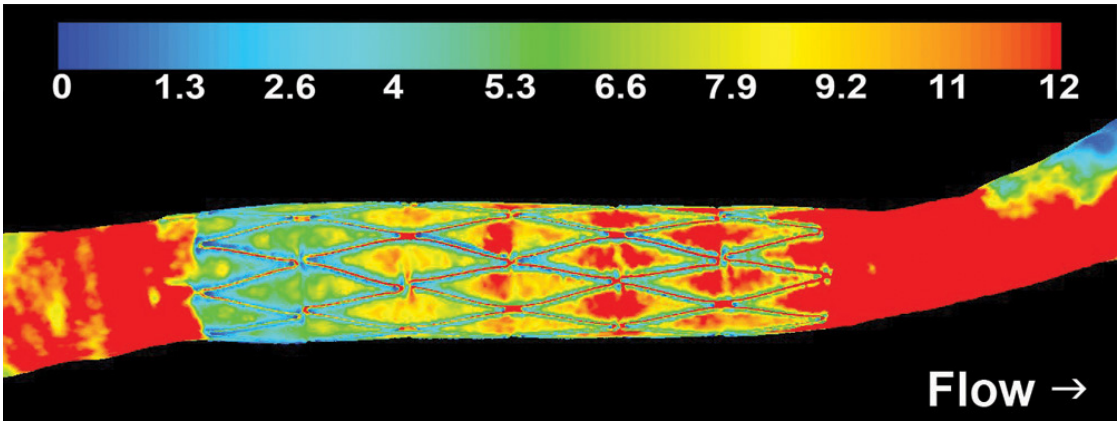

Figure 3.15. Wall shear stress contours (Pa) for the NF3 stent deployed in a canine artery

and Enterprise is shown in Figure 3.16 while for the NF3 stent deployed in the canine artery is shown in Figure 3.17. Relatively higher WSS values ($\sim$ 8.5 Pa) occur at the center of the NF3 stent cells when compared with Enterprise stent cells ($\sim$ 5.5 Pa) due to slight wall prolapse at the cell center of the NF3 stent while for the Enterprise the prolapse is minimized and the WSS is more uniformly

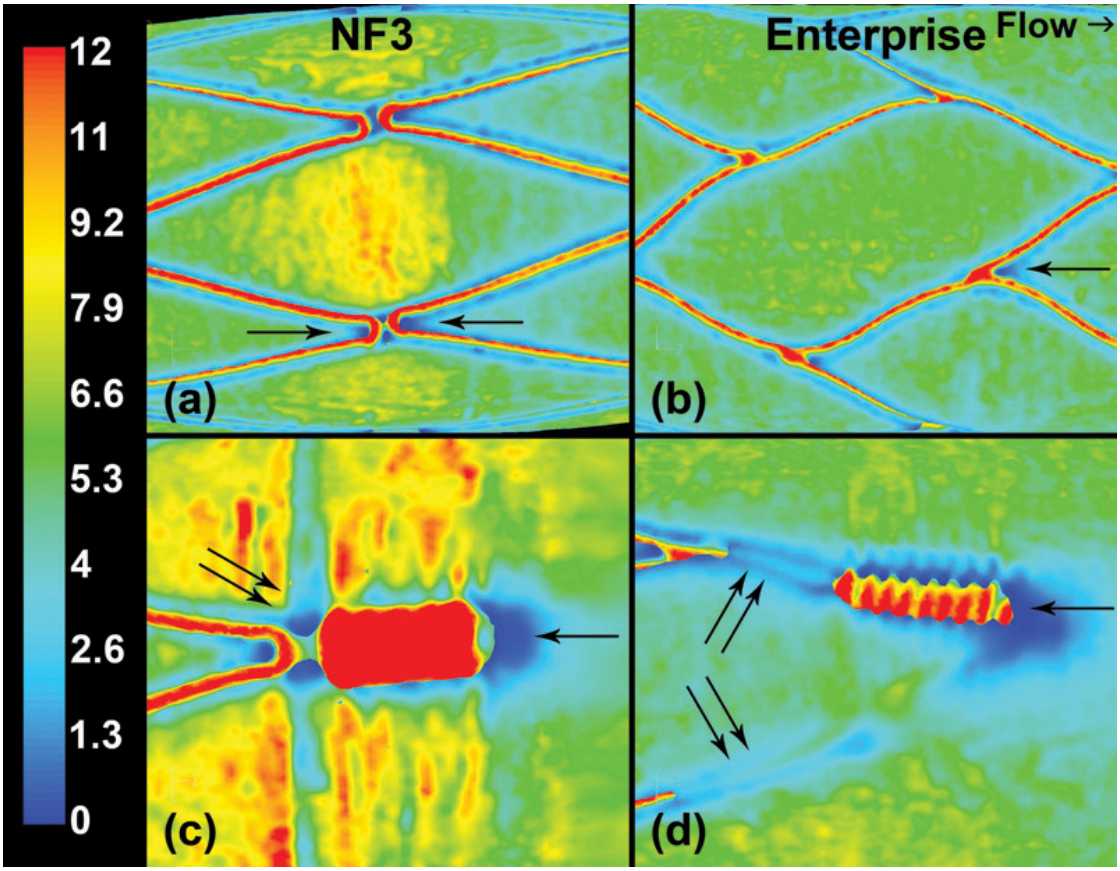

Figure 3.16. Local wall shear stress (WSS) contours (Pa) for the NF3 (a) and Enterprise (b) showing regions of low WSS developing near strut vertices, stent markers, and prolapsed struts

distributed. Low, but not necessarily reverse WSS zones develop near the strut vertices (on both the upstream and downstream sides) and stent markers in both stents as indicated by single arrows (Figure 3.16a and 3.16b). These zones also occur along the stent struts where the struts come in contact with the wall but no negative WSS values are present.

Regions of low WSS also occur downstream of the relatively large imaging markers as shown in Figure 3.16c and 3.16d. Relatively larger zones of low WSS are generated proximal to the markers of both NF3 and Enterprise stents and under struts that connect regular, smaller size struts with larger markers in the

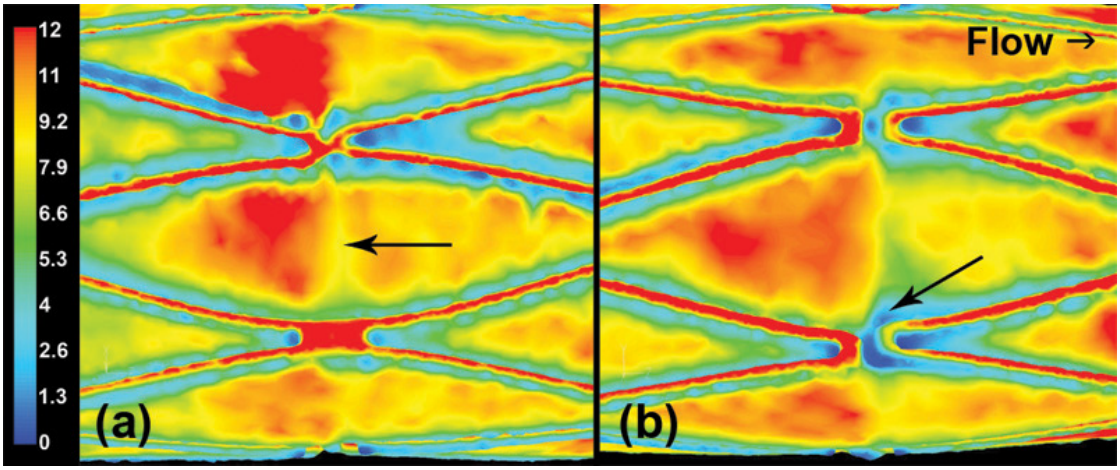

Figure 3.17. Local wall shear stress contours (Pa) for the NF3 deployed in a canine artery

case of the latter stent. Higher WSS near the markers of the NF3 stent is present due to wall roughness and slight local decrease of the PTFE tube diameter.

Similar images of local WSS distribution in stent cells for the NF3 stent deployed in the canine artery are shown in Figure 3.17. The effects of the circumferential crease at the vertex junctions on the WSS distribution for the NF3 stent deployed in the canine artery are most apparent at the cell centers. High WSS values occur on the upstream half of the stent cell while lower values tend to occur downstream of the crease (indicated by arrow, Figure 3.17a). This effect is more accentuated by strut vertices that impinge on the wall in stent cells that consist of strut vertices as exemplified in Figure 3.17b. The strut vertex indicated by the arrow appears to be partially embedded into the wall. This results in low WSS near and around the vertex and in slightly lower WSS downstream of the crease—the WSS jumps from high to low values as the flow passes over the crease which is aligned with the vertices. Low and positive WSS values also occur along the struts.

The contours of WSS magnitude presented so far do not indicate the presence

of flow reversal at the wall. However, plotting the WSS component that is aligned with the mean flow direction can indicate where negative WSS occurs and therefore flow reversal at the wall. In all stent cases investigated in this work the stented segment is conveniently aligned with the z-axis which the same as the direction of the flow. Thus, the z-component WSS is plotted to identify flow reversal.

To investigate the regions of flow reversal at different Reynolds numbers, two steady flow CHD simulations are performed at Re = 160 and at Re = 1600. The Reynolds value of 160 is typical of the mean flow encountered during diastole in the common carotid artery [3, 58]. The high value of Re = 1600 is chosen to investigate the effect of increasing the Reynolds number by one order of magnitude on flow reversal due to stent deployment.

For the NF3 stent, the z-component WSS is shown in Figure 3.18. The WSS values have been clipped to show only negative values, therefore regions experiencing positive axial-component WSS—and positive flow at the wall—are shown in red. Small regions of flow reversal develop at the wall on the downstream side of strut vertices and at gaps of aligned vertices. There is no significant difference in the size of these flow reversal regions as the Reynolds number increases 10-fold—illustrated by the zoom-in images in Figure 3.18a and 3.18b. Misaligned vertex gaps exhibit smaller flow reversal regions than aligned gaps (zoom-in, Figure 3.18b). The Enterprise stent shows no flow reversal at low as well as at high Reynolds numbers while for the NF3 stent deployed in the canine artery the size of flow reversal does not increase with Reynolds number—similar to the NF3 deployed in the straight PTFE tube graft. The low strut profile—60 μm for intracranial stents such as the NF3 and Enterprise—relative to a typical cerebral artery diameter (3–6 mm) may be insufficient to generate large flow recirculation zones and negative WSS at high Reynolds number.

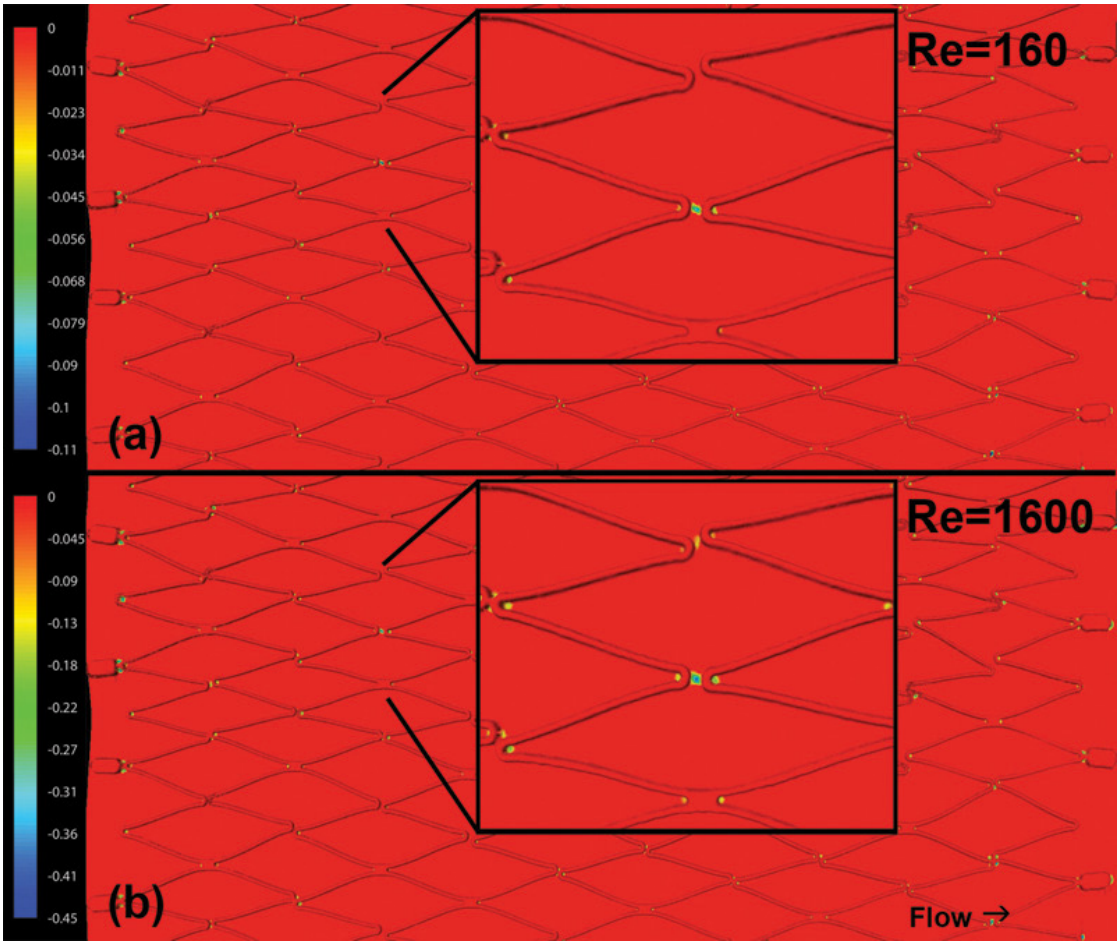

Figure 3.18. Wall shear stress (axial-component) contours (Pa) for the NF3 stent at Re = 160 (a) and at Re = 1600 (b)

3.4.4 Coronary stents

The coronary stents used in this study, as mentioned before, are the BxVelocity and Taxus. The steady flow simulations for these stents are performed at a Reynolds number of 500. The WSS distribution for the Taxus is shown in Figure 3.19 with the results being presented in a similar fashion to the results obtained for the intracranial stents. The cylindrical (Figure 3.19a) and planar projection (Figure 3.19b) of the stent and wall surface are used to visualize the WSS distribution.

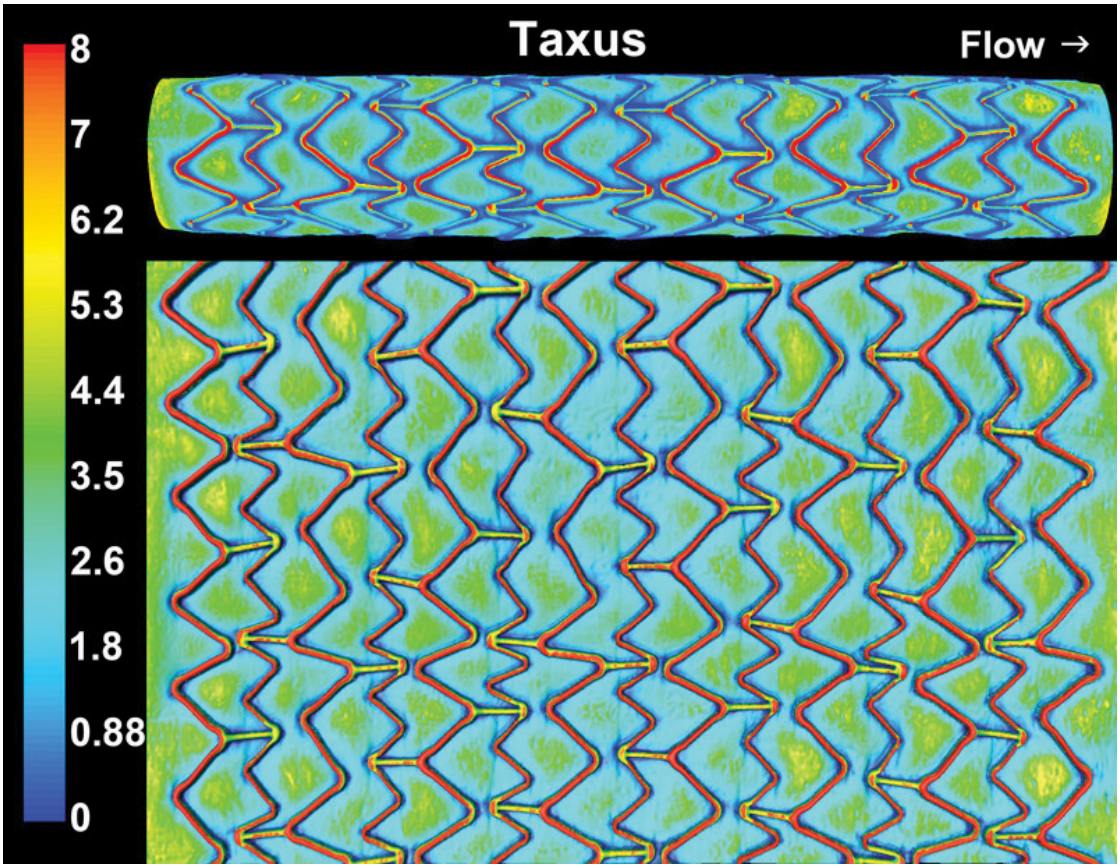

Figure 3.19. Distribution of wall shear stress contours (Pa) for the Taxus stent deployed in a straight arterial graft. Contours are clipped to show negative WSS regions

High magnitude WSS (12 Pa) is present on the luminal face of struts with an average of 8 Pa while the WSS is non-uniformly distributed inside the stent cells with values in the range of 4.5 Pa at the cell centers where wall prolapse is present and in the range of 0.7 Pa near vertex gaps and along the struts and connectors. Low WSS also occurs at small gaps of aligned strut vertices and at most vertex gaps where slight strut impingement on the wall forms short, local creases unlike the NF3 stent deployed in the canine artery that exhibits long creases spanning the entire stent cell width which also affect WSS inside stent cells.

The contours of WSS magnitude obtained for the closed-cell design BxVeloc-

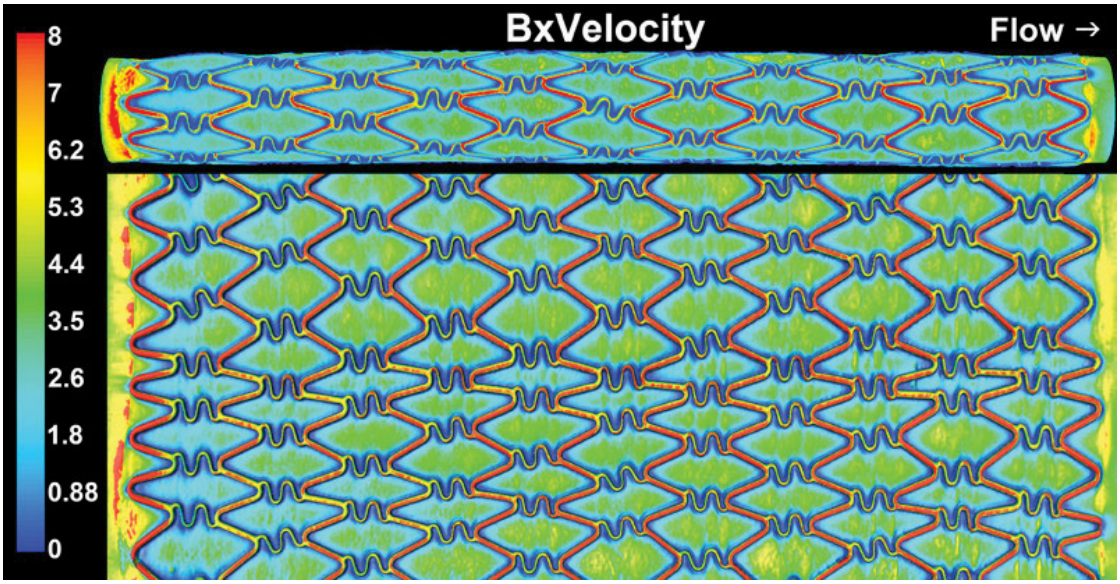

Figure 3.20. Wall shear stress contours (Pa) for the BxVelocity stent deployed in a straight arterial graft

ity stent deployment are shown in Figure 3.20. Again higher WSS is present at the center of stent cells with most of the low WSS occurring at and around the ribbon-like connectors and downstream of strut vertices. Relatively higher WSS is present at the proximal and distal end of the BxVelocity possibly due to slight stent overexpansion inside the PTFE tube. As discussed in the previous chapter, this particular BxVelocity deployment exhibits an under-deployed row of stent cells (middle section of Figure 3.20b) which results in lower WSS values when compared with larger cells.

Regions of flow reversal are identified by plotting the mean-flow component of the WSS vector as discussed above. Plots of the clipped axial-component WSS values are shown in Figure 3.21. The overall WSS distribution on the entire stent and wall surface is not shown as the zoom-in images on stent details provide better visualization of the effects of realistic stent deployment on the flow. For the Taxus stent, reversal zones are located downstream of the strut vertices with

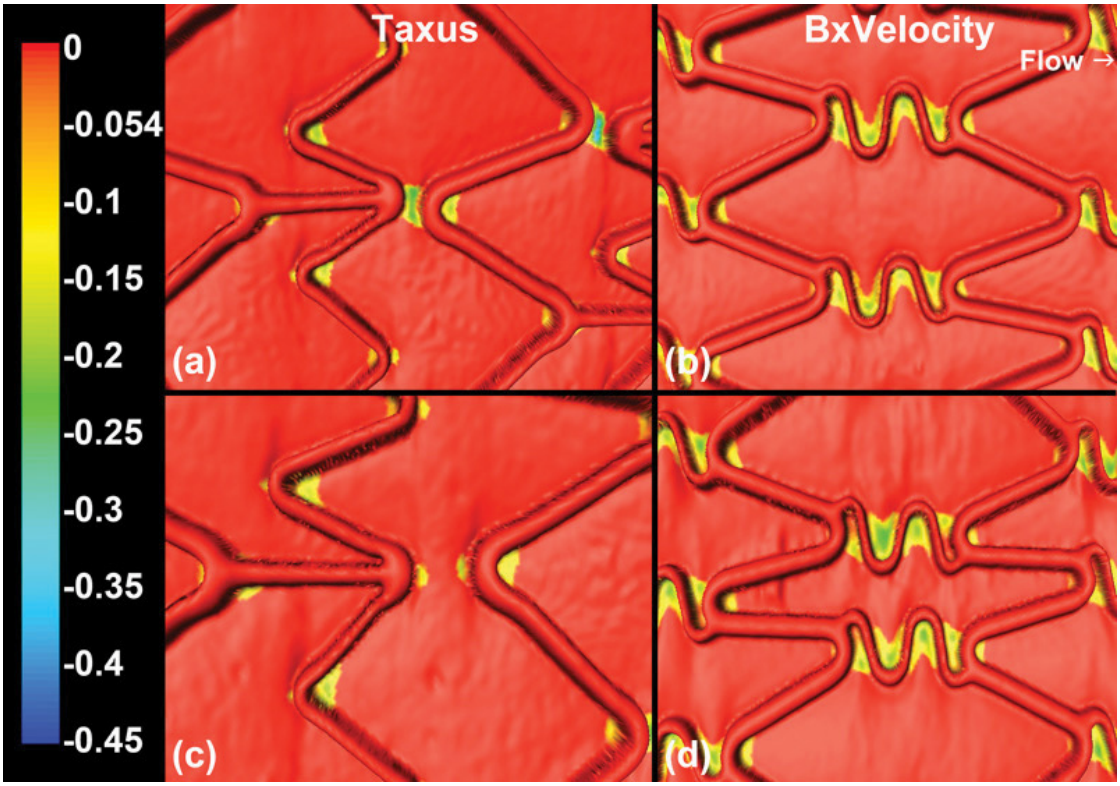

Figure 3.21. Local axial-component of wall shear stress (WSS) contours (Pa) for the Taxus (a) and BxVelocity (b) showing regions of reversed WSS

larger zones being present at the vertices for struts oriented in a diverging pattern (Figure 3.21a and 3.21c). Significant reversal zones are also present at vertex gaps of length less than 0.2 mm (Figure 3.21a). Larger vertex gaps do not exhibit flow reversal as exemplified in Figure 3.21c. The reversal regions inside the BxVelocity stent develop between the ribbon-like connectors and on the downstream side of the strut vertices (Figure 3.21b and Figure 3.21d). Although the WSS is lower in under-deployed cells than in regularly deployed cells as shown above, there is only slight difference in the size of negative axial-component WSS regions and in WSS magnitude.

The effect of the Reynolds number on the reversal flow regions generated by the struts of Taxus and BxVelocity stents is investigated in the same manner as

it was done for the NF3 stent—steady flow at Re = 160 and Re = 1600. The flow reversal regions occurring at struts that are almost perpendicular to the flow and downstream of strut vertices increase as Reynolds increases as illustrated in Figure 3.22. Some regions that do not exhibit flow reversal at Re = 160 do so at Re = 1600.

In the case of Bxvelocity, the size of the flow reversal regions that occur at the ribbon-like connectors and downstream of the proximal row of strut vertices are nearly the same when compared with the low Reynolds number flow as shown in Figure 3.23. Also, the row of under-deployed cells does not show significant increase of the reversal regions at high Reynolds number.

A major focus of this investigation is on flow recirculation zones with low or negative WSS near the struts. In addition to the potential physiological importance of these zones, they are also useful in demonstrating the level of hemodynamic detail that can be obtained using the microCT based CHD approach proposed in this work. The basic hemodynamics for the well apposed cells of different stents are similar and are in good qualitative agreement with previous studies based on CHD simulations utilizing idealized, symmetric, three-dimensionally modeled stent deployment [110, 116, 117]. Since the open cells of the NF stents are less constrained, the cell to cell variations due to natural deployment asymmetries can be dramatically greater than predicted by computer generated models.

The present results reinforce the importance of three-dimensionality in the development of recirculation zones near the struts. Seo *et al.* [124] observed the formation of helical vortices distal to such struts, while He *et al.* [115] have studied a model of a curved strut and concluded that recirculation zones can be reduced by orienting struts as much as possible in the flow direction. The current results indicate that recirculation zones occur near strut vertices or markers, at positions

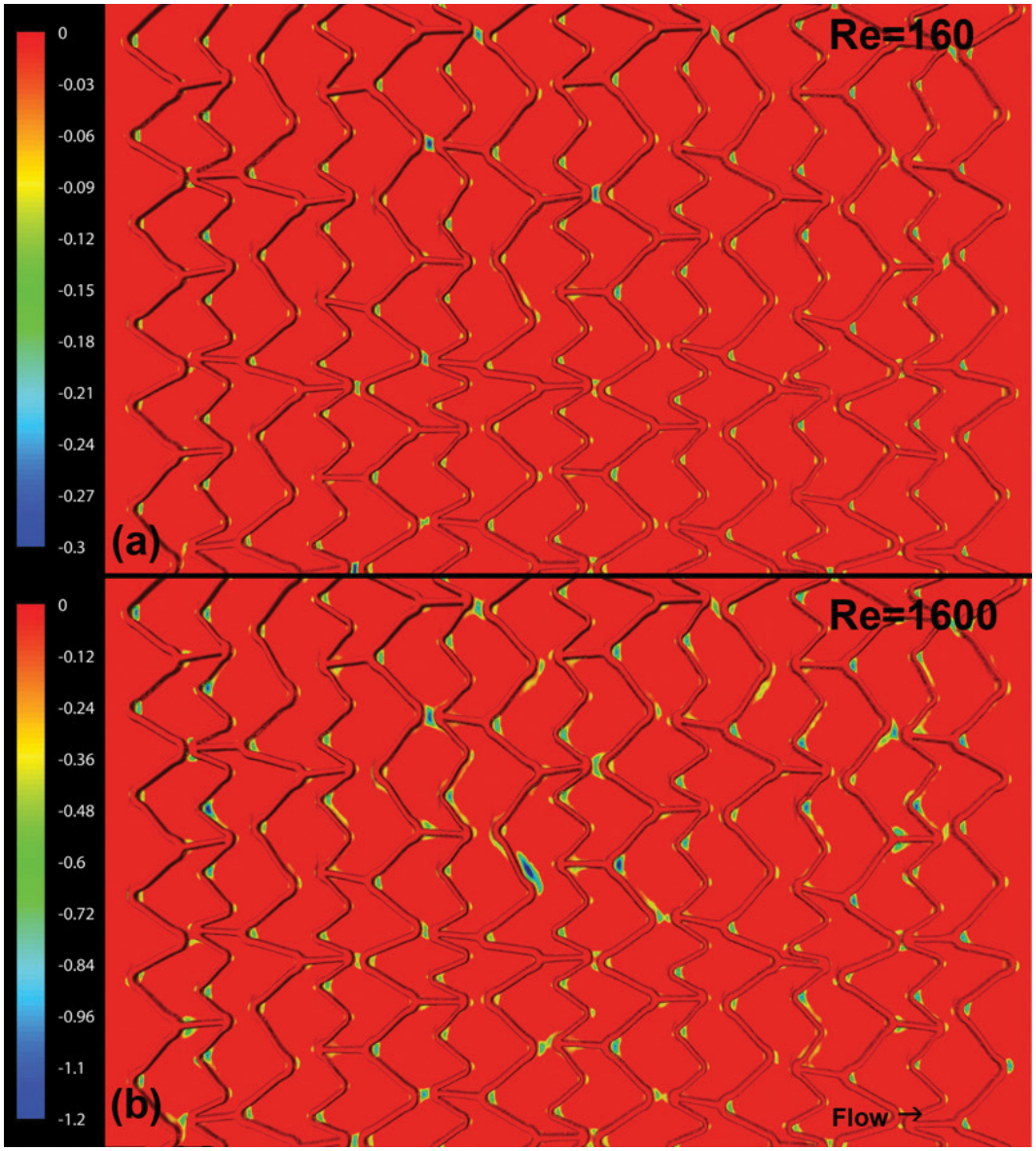

Figure 3.22. Wall shear stress (axial-component) contours (Pa) for the Taxus stent at Re = 160 (a) and at Re = 1600 (b). The contours are clipped to show regions of negative WSS

where the struts or markers have a perpendicular projection to the flow direction. This is also consistent with the three-dimensional strut model of Rajamohan *et al.* [125], although their larger recirculation zones may have been caused by the higher profile of their stents (400 μm diameter struts) with 200 μm projection into the

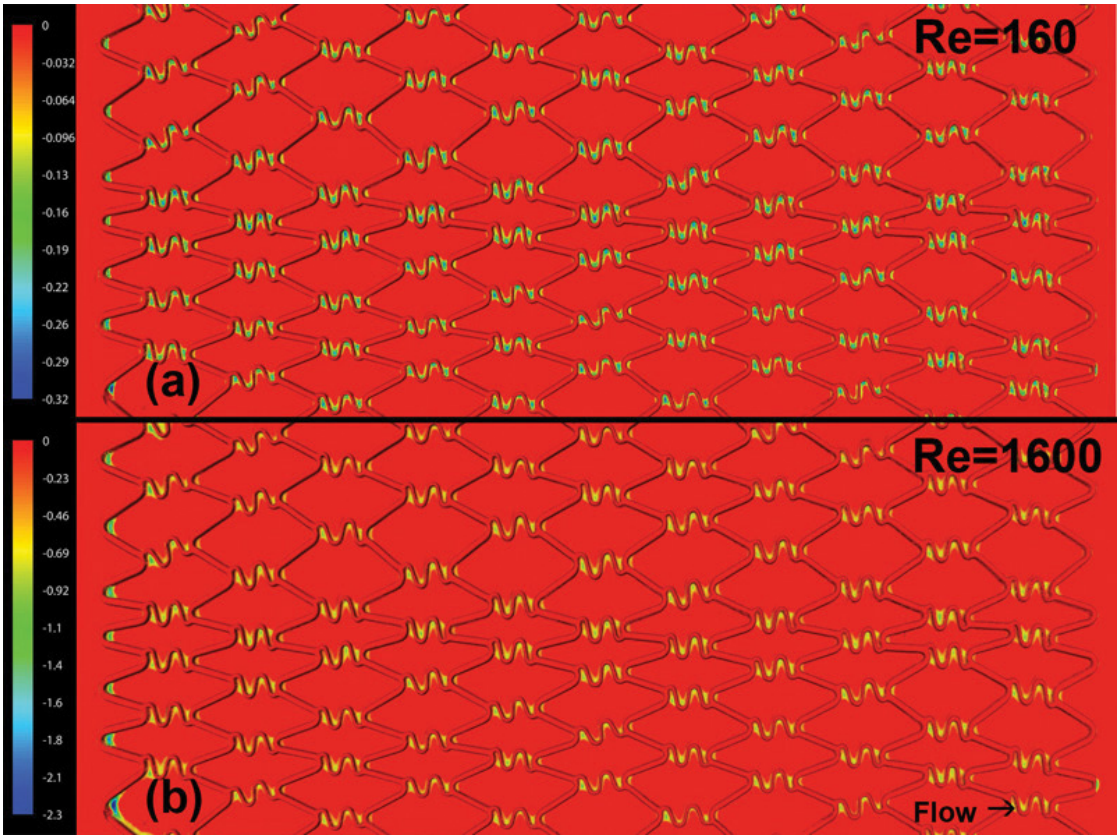

Figure 3.23. Wall shear stress (axial-component) contours (Pa) for the Velocity stent at Re = 160 (a) and at Re = 1600 (b). The contours are clipped to show regions of negative WSS

arterial lumen.

3.5 Pulsatile flow

Steady flow CHD simulations offer invaluable information regarding flow characteristics in stented vessels at a relatively low computational cost as the numerical solution is obtained for only one constant flow condition. However, time-dependent flow variations, especially for highly pulsatile flows, affect the velocity profile and therefore the WSS and should not be neglected when modeling physiological flows. In this section, the NF3 and the Taxus stents are used for unsteady flow CHD simu-

lations due to the variety of non-uniform deployment characteristics such as strut prolapse, vertex misalignment, strut orientation that are associated with these stents.

3.5.1 Boundary conditions

The boundary conditions imposed at the wall surface and the outlet face for the computational domains representing the NF3 and Taxus stents are the same as in the case of steady flow, i.e., no-slip and zero pressure, respectively. For the inlet face, a mass-flux boundary condition that is changing in time is imposed in FLUENT as the mass-flow type of boundary conditions is not available for unsteady flow simulations. Two flow rate waveforms measured in the common carotid artery by Ku *et al.* [58] and Holdsworth *et al.* [126] and shown in Figure 3.24 are used to define time-dependent flow at the inlet face of the stent domains. The simulation results are investigated at peak systole (T1), at the end of the first deceleration interval (T2), and at the end of the second deceleration interval (T3) which are indicated in Figure 3.24. The choice of these locations along the waveform is made to capture transient effects due to flow acceleration and deceleration that is typical of systole.

The corresponding Reynolds numbers for the quasi-steady diastolic flow is about 160 for both waveforms while the Reynolds number for peak systolic for the Ku waveform is about 550 and for the Holdsworth waveform is about 860. The Womersley number for the Ku and Holdsworth waveforms is 4.6 and 5, respectively. To ensure the Reynolds number is the same for the CHD simulations in both stents—NF3 has a diameter of 4.5 mm while Taxus has 3.0 mm—the flow waveforms are scaled. Note that the waveforms have similar diastolic flow rates while the Holdsworth waveform has a much higher peak systolic flow. Also, during

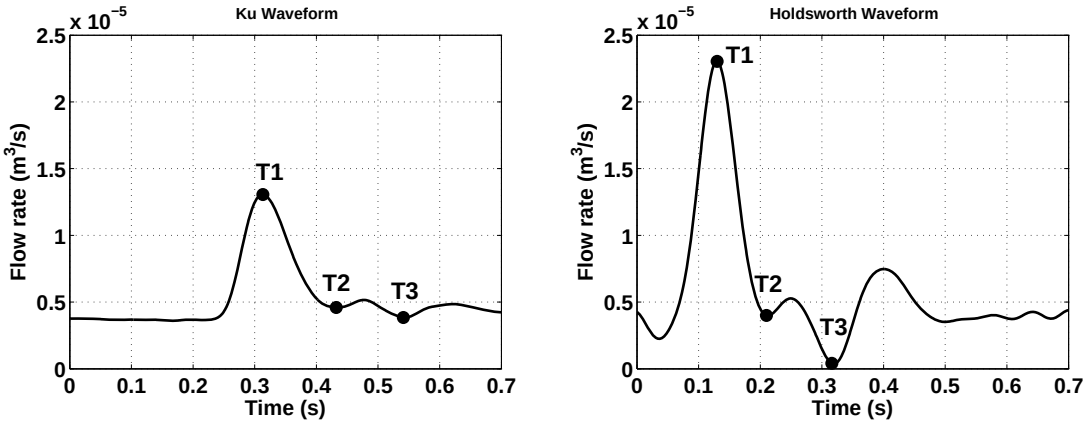

(a) (b)

Figure 3.24. Common carotid flow waveforms

systolic flow deceleration, the minimum flow (T3) in the case of the Holdsworth waveform is positive; however, it is much smaller than the minimum flow specific to the Ku waveform.

3.5.2 Unsteady flow results

The distribution of WSS is examined in a similar fashion as in the steady flow simulations. The axial-component of the WSS on the stent and wall surface for the NF3 stent at T1, T2, and T3 along the Ku waveform are shown in Figure 3.25. The maximum contour values for each WSS plot are clipped by the mean WSS value found on the luminal face of stent struts. This normalization provides a convenient way to visualize changes in WSS distribution at different points in time. The regions showing only red contours signify that the WSS value might be larger than the value indicated by the colormap. Also notice the change of the axial WSS magnitude in Figure 3.25a, 3.25b, and 3.25c as the flow velocity decreases during T2 and T3. The axial-component WSS distribution remains unchanged during peak flow (Figure 3.25a) and during the two deceleration intervals (Figure 3.25a

and 3.25b) while only the magnitude of the WSS component varies as the flow velocity increases and decreases. The WSS distribution is similar to the distribution that occurs during steady flow. This indicates that the flow driven by the Ku waveform is not highly pulsatile and the shape of the velocity profile is not significantly affected by flow transients.

The axial-component WSS distribution for the NF3 stent during flow driven by the Holdsworth waveform is presented in Figure 3.26. The contours look similar (if ignoring the change in axial WSS magnitude) for T1 and T2 (Figure 3.26a and 3.26b) with the latter point in time showing lower WSS values in some regions of the NF3 stented segment. During the flow following the second deceleration (T3) the axial WSS direction is reversed almost everywhere indicating flow reversal at the wall (Figure 3.26c). Positive axial-component WSS values occur at aligned vertex gaps indicating flow reversal—this time in the direction of mean flow. The WSS distribution is markedly different than the distribution at the other two points along the waveform. The WSS is uniformly distributed inside the stent cells while on the luminal face of struts the WSS is non-uniform. Referring back to the waveform plots shown in Figure 3.24 the Holdsworth waveform at time T3 exhibits positive net flow rate. This means that the velocity in the middle of the vessel and for the most part of the lumen must be positive and only in the region adjacent to the wall is the velocity reversed.

In Figure 3.27 and Figure 3.28, the contours of axial-component WSS are shown for the Taxus stent from flow simulations using the Ku and Holdsworth waveforms, respectively. Similar to the NF3 case, the WSS distribution does not change significantly at peak flow and following the two deceleration intervals, indicating that the pulsatility and the amount of flow acceleration and deceleration typical of the Ku waveform do not influence the WSS distribution (Figure 3.27).

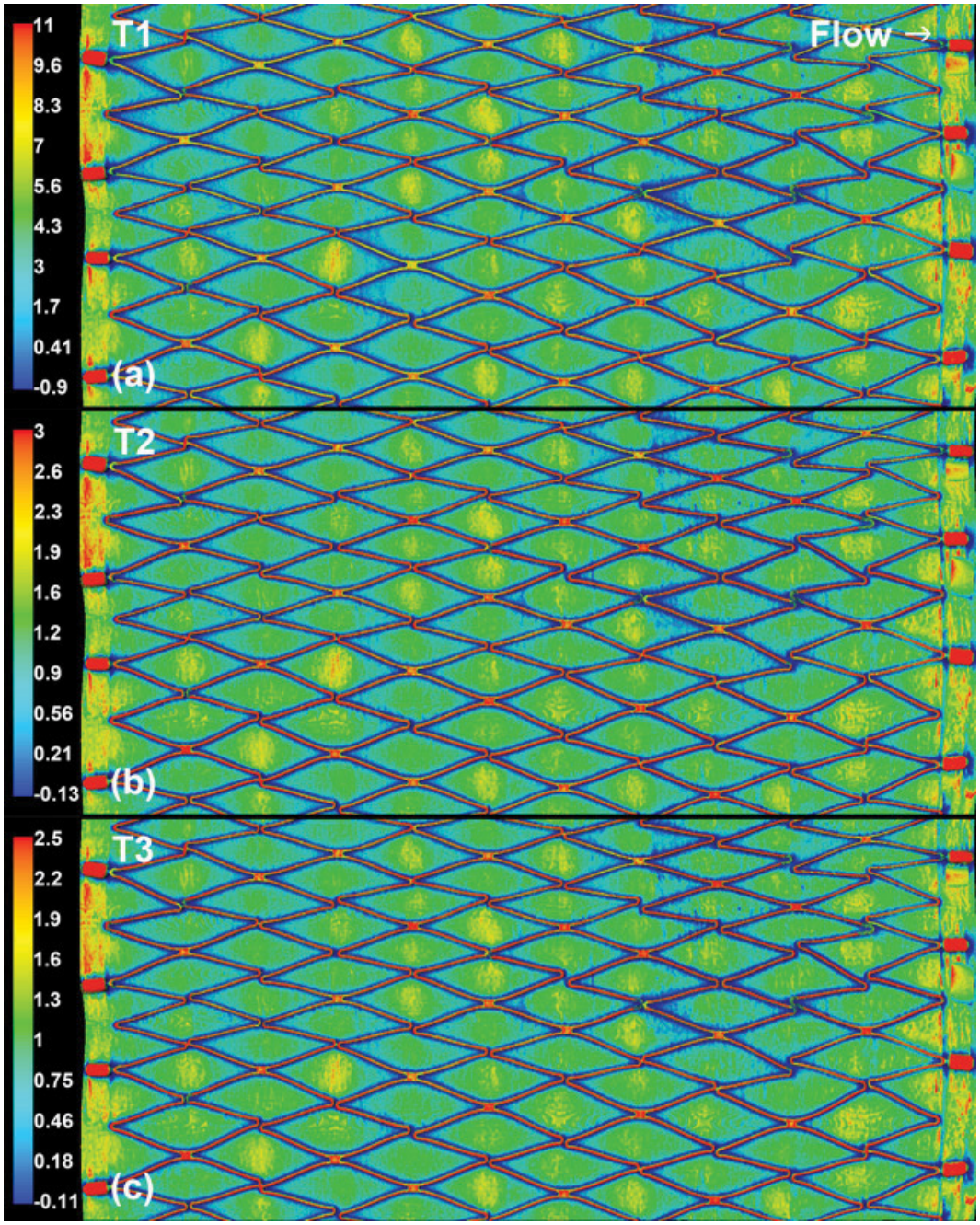

Figure 3.25. Wall shear stress (axial-component) contours (Pa) for the NF3 during peak flow (a), after the first deceleration (b), and after the second deceleration (c) using the Ku waveform

The Holdsworth waveform has a more significant impact on the flow and WSS distribution than the Ku waveform as shown in Figure 3.28b and 3.28c. During

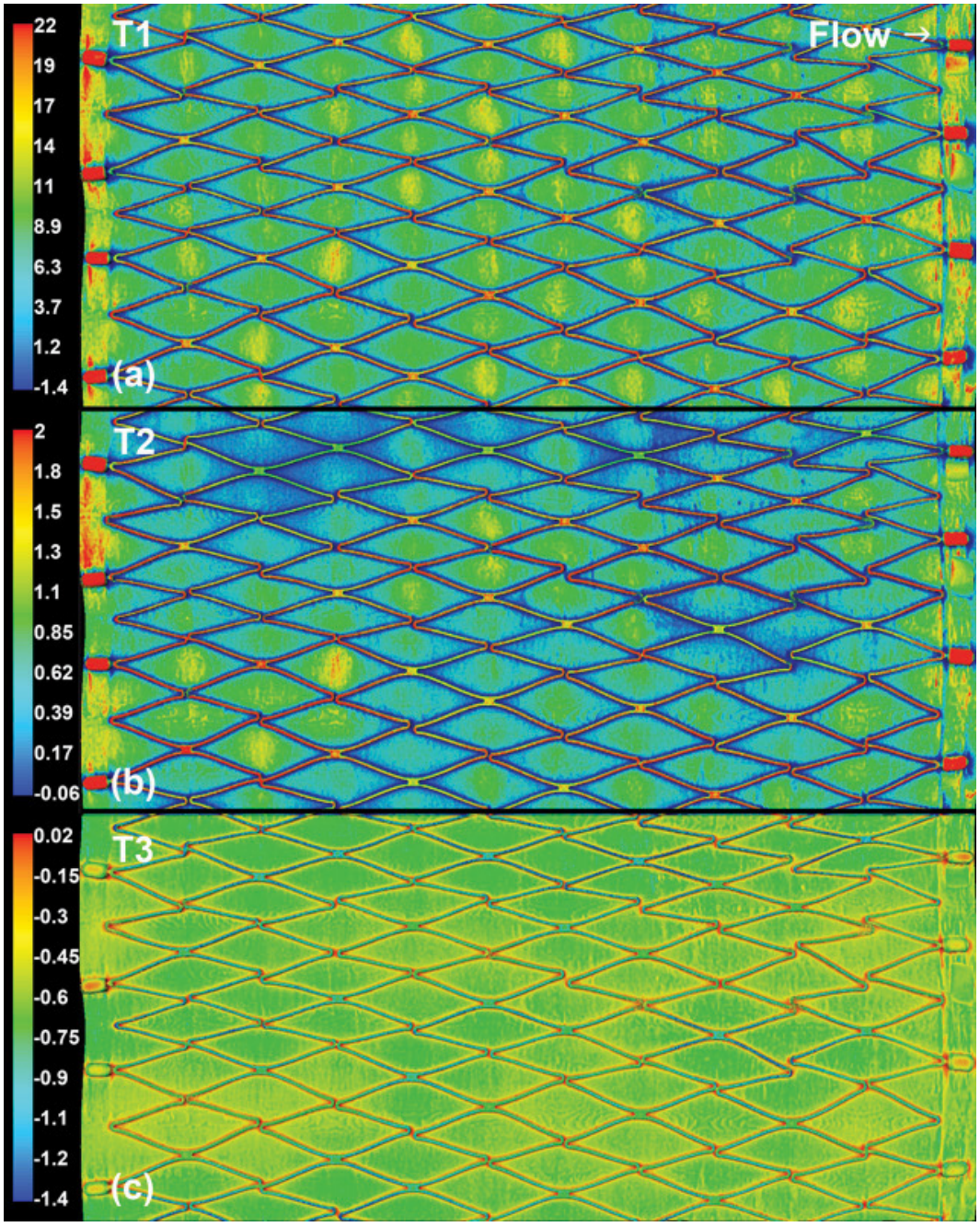

Figure 3.26. Wall shear stress (axial-component) contours (Pa) for the NF3 during peak flow (a), after the first deceleration (b), and after the second deceleration (c) using the Holdsworth waveform

the second deceleration (T3) the flow at the wall reverses in the Taxus stent case just as it reverses in the NF3 case. Similarly, stents and even the luminal face of

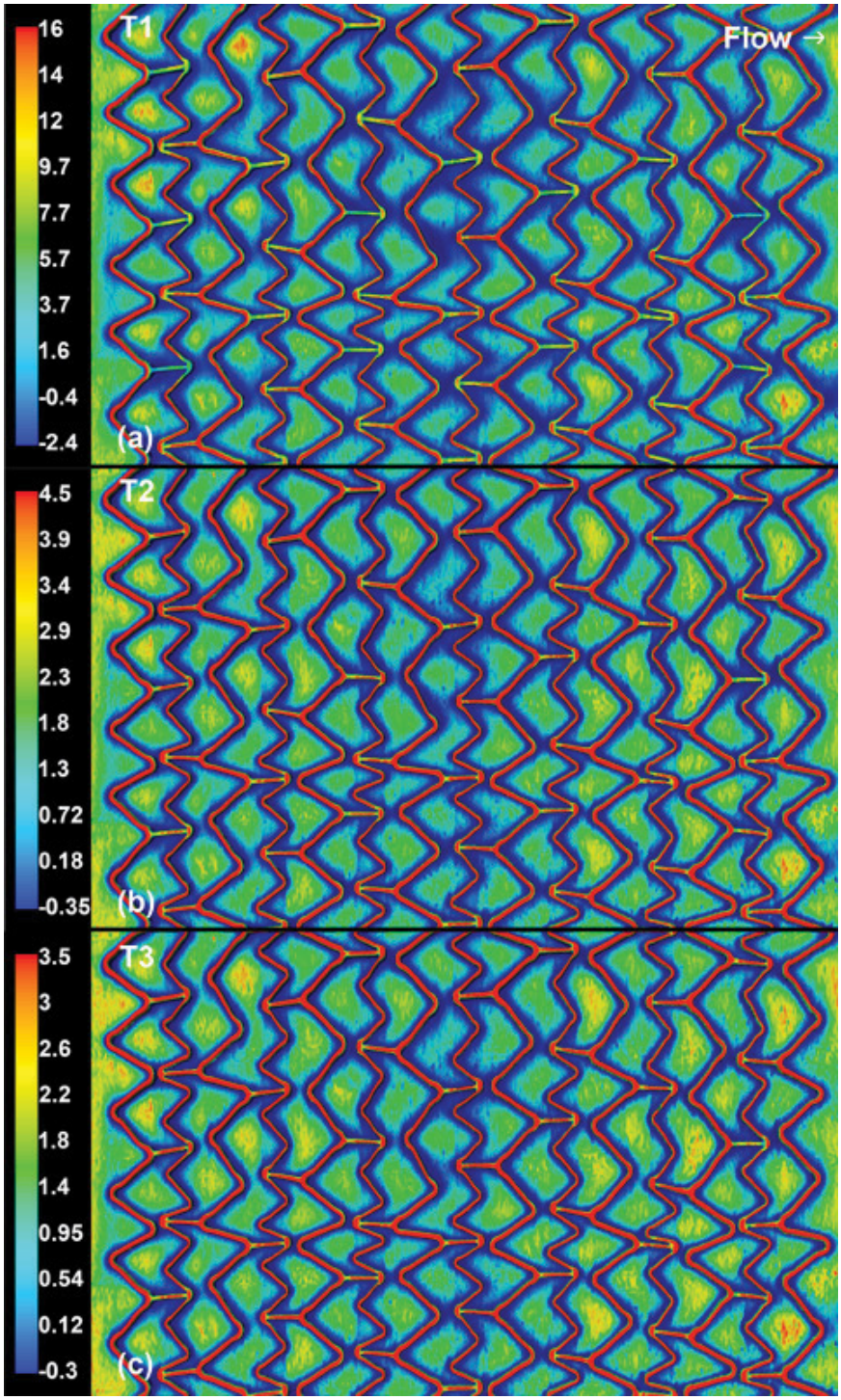

Figure 3.27. Wall shear stress (axial-component) contours (Pa) for the Taxus during peak flow (a), after the first deceleration (b), and after the second deceleration (c) using the Ku waveform

struts experiences reversed WSS. Again, the WSS is uniformly distributed in most stent cells—as opposed to being non-uniform in the steady flow case. A stent strut located at the proximal end of the stent (upper-left corner of Figure 3.28c) and protruding more into the lumen experiences positive WSS indicating that positive flow occurs away from the wall.

3.6 Summary

The CHD simulations of flow in real stents deployed in PTFE arterial grafts and canine artery demonstrate the feasibility of using high-resolution microCT datasets for accurate flow studies and calculations of WSS. This provides an enhanced capability for evaluating in detail the hemodynamic consequences of specific stent designs and has the potential to become a means for directly comparing their effects on flow in realistically deployed configurations.

Steady flow simulations are used to provide information about flow around struts that are prolapsed into the lumen or misaligned strut vertices. For the two types of intracranial stents, the closed-cell design NF3 and the open-cell design Enterprise, the basic hemodynamics are similar with some differences of potential significance. The WSS within the regularly apposed cells is lower for the Enterprise than for the NF3. Throughout the main stent body there are no recirculation zones or WSS reversal for the Enterprise and some very small reversal zones for the NF3, generated by strut vertex misalignment and strut prolapse. Due to their larger dimensions, significant reversal zones develop near the stent markers. These finding suggest that a lower profile stent (smaller strut dimension) may cause less potentially deleterious zones of low and oscillating WSS, which have been found to be associated with neointimal growth.

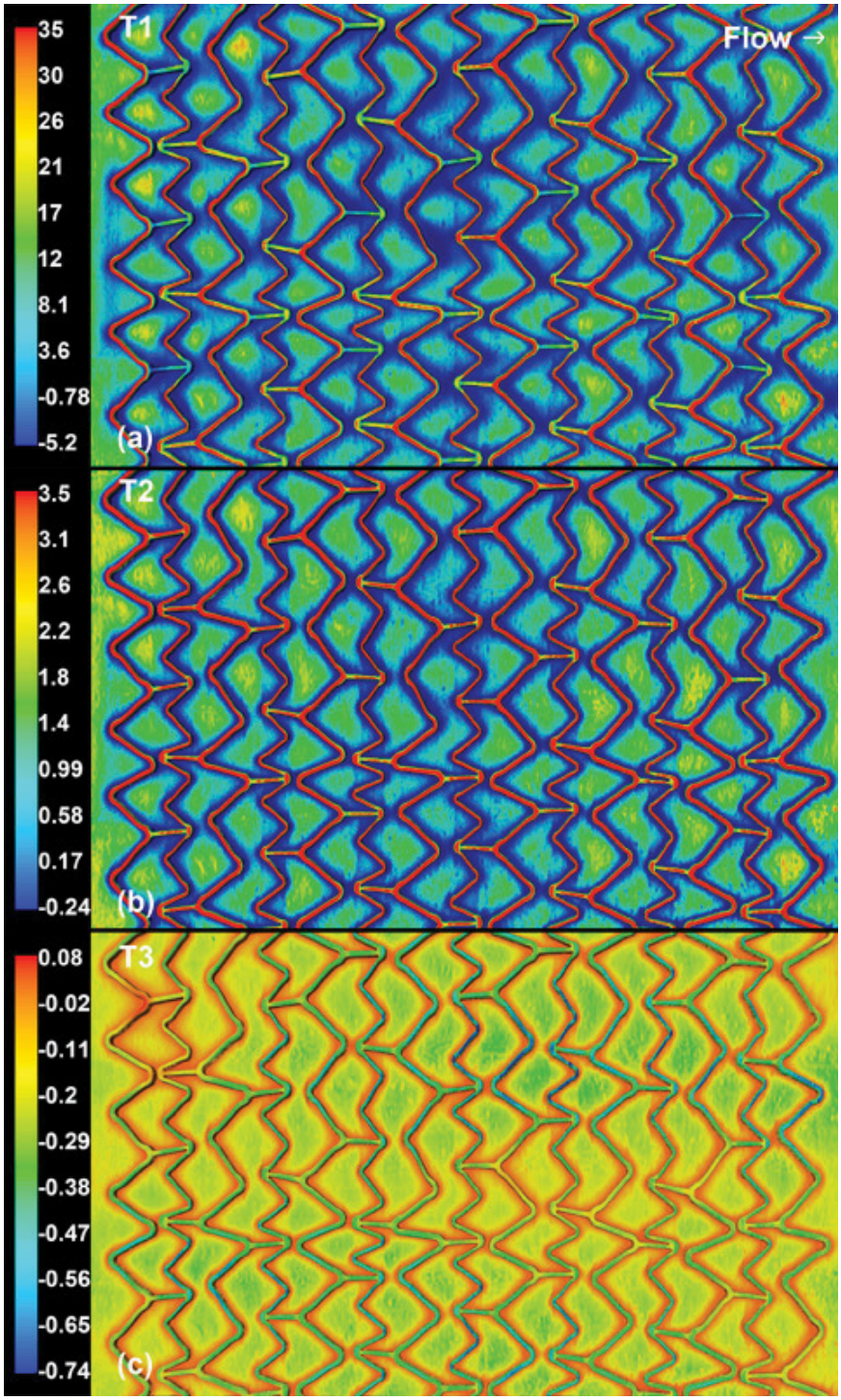

Figure 3.28. Wall shear stress (axial-component) contours (Pa) for the Taxus during peak flow (a), after the first deceleration (b), and after the second deceleration (c) using the Holdsworth waveform

The WSS distribution inside the stented region is in agreement with results from previous studies. Low WSS is present in the vicinity of struts and cell vertices while increased WSS is located on the luminal face of the struts which projects further into the higher velocity fluid stream away from the wall. While the Enterprise struts carrying the radiopaque markers exhibit significant prolapse, no recirculation zones or WSS reversal occurs within the middle segment cells, although zones of comparably low WSS develop near the strut vertices. Stent and wall surface reconstructions obtained from C-arm CT scans and used in CHD simulations yield erroneous flow results due to significant geometric non-uniformities and strut oversizing and cannot be used to study in-stent hemodynamics.

For the two coronary stents used in this work, the open-cell design Taxus stent exhibits non-uniform vertex gaps and some vertex misalignment, while the closed-cell design BxVelocity stent exhibits a more uniform deployment except for the misalignment of some connectors with respect to the mean flow direction and the row of under-deployed stent cells. The main effects of these anomalies are an increase in the WSS near the misaligned gaps for the Taxus stent and reduced WSS inside under-deployed cells for the BxVelocity stent. In addition, flow reversal regions are observed in both stents: the Taxus reversal zones develop distal to the strut vertices at small vertex gaps and at some struts oriented almost perpendicularly to the flow directions while the BxVelocity reversal zones develop near the ribbon-like connectors.

Unsteady flow also has a direct impact on stent hemodynamics as illustrated by the two waveforms typical of human common carotid artery that are used in this work. The normalized contour plots of the axial-component WSS show insignificant changes in WSS distribution between peak flow and decelerating flow for the Ku waveform. Although the Holdsworth waveform exhibits positive net flow rates,

negative flow at the wall develops during the systolic deceleration unlike the Ku waveform that does not induce wall flow reversal. While the two waveforms have similar Womersley numbers, the magnitude of flow acceleration and deceleration is higher for the Holdsworth waveform indicating that the deceleration rate along with the frequency of flow deceleration determine the occurrence of flow reversal. This aspect is investigated in the next chapters.

This work confirms the efficacy of the high-resolution microCT based stent reconstructions for accurate prediction of in-stent hemodynamic effects using CHD simulations. Key features that can potentially impact restenosis, such as significantly altered WSS patterns and the development of reversed flow regions can be predicted in detail. These methods should be of great value when comparing stent hemodynamic performance.

Chapter 4

Waveform parameterization

Arterial blood flow is in general laminar and unidirectional (i.e., no flow reversal occurs) throughout the cardiac cycle but flow perturbations can be induced by either arterial geometric features or by time variations of the blood flow waveform. These perturbations can result in flow oscillations (flow changing direction) and, thus, oscillatory wall shear stress (WSS) at the arterial wall, a condition which, as discussed earlier, has been correlated with the development of atherosclerosis. Analyzing the time-dependent aspect of blood flow in arteries as captured by the volumetric flow rate or the pressure waveform and identifying the waveform features or properties that can induce oscillatory WSS represents an important initial step in studying the possible role of the blood flow waveform in the development of atherosclerosis. This chapter is devoted to the parameterization of pulsatile flow waveforms with the aim of identifying waveform features that influence flow transients. Specifically, its application to physiological flow waveforms is demonstrated by using data available from literature.

4.1 Introduction

Blood flow in arteries is characterized by periodic pressure and flow waveforms that change with age, health level, and the degree of physical activity. The shape of both waveforms is determined by the activity of the heart (cardiac output and aortic valve activity) and by the geometric and viscoelastic properties of the vascu-

lar wall [1]. The latter two factors affect the shape of waveforms by influencing the pulse wave propagation through the arterial network and have been the subject of numerous studies which are summarized in [1]. The behavior of the arterial pressure and flow velocity as the flow pulse travels away from the heart is depicted in Figure 4.1 which is adapted from [1]. The mean pressure decreases slowly but the pressure amplitude variation increases while the oscillation decreases. While the pressure pulse waveform has long been used in clinical diagnosis, the flow waveform has received less attention. This may be due in part to the relative ease of recording pressure pulse waves and with arterial flow measurement becoming more viable and less invasive after technological advancements in flow imaging techniques such as phase-contrast magnetic resonance imaging (PC-MRI) and ultrasound (US).

While the *in vivo* pressure waveform at a single location along an artery provides valuable data for the clinician about blood flow, for experimental or computational hemodynamics studies the pressure at a single location is not enough to define the flow. It is the pressure difference between two locations, or the pressure gradient waveform, along the artery that is needed to drive the blood flow. However, the *in vivo* pressure gradient waveform is difficult to measure as the pressure difference between two points along straight arterial segments is very small [1]. Therefore, the *in vivo* volumetric flow rate waveform is used in most arterial hemodynamics studies.

In general, the healthy arterial blood flow waveform is characterized by a rapid acceleration phase during systole followed by a deceleration phase and then by a much smaller acceleration phase during diastole followed by a phase of nearly steady flow at end diastole [1]. A typical flow velocity waveform measured by Doppler US in the middle of the common carotid artery under rest conditions is shown in Figure 4.2. The flow rapidly accelerates to peak value during systole

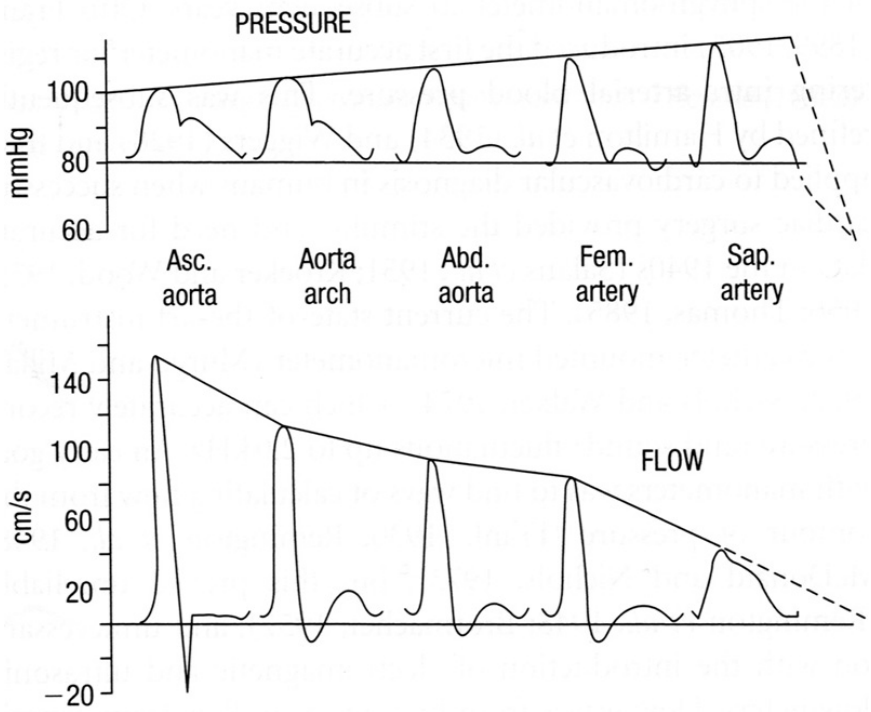

Figure 4.1. The pulsatile pressure variation increases while the arterial flow velocity variation decreases as the flow pulses travel away from the heart

while reaching a lower, quasi-steady value during diastole.

The periodicity of the flow is given by the cardiac cycle which, for resting conditions in a healthy adult, is about 0.8 s which corresponds to approximately 70 heart beats per minute [1]. During physical exercise or strenuous activity the blood flow velocity increases. The pulse rate also increases to more than 120 heart beats per minute resulting in a shorter waveform period. Also, successive cardiac cycles can exhibit variations as depicted in Figure 4.2 (acquired by Dr. Craig Hartley at the Baylor College of Medicine) in which the peak velocity of the last six cycles is greater than in previous cycles. During the systolic deceleration phase, blood velocity decreases rapidly and can result in low velocity or even flow reversal at the wall which can potentially translate into low and oscillatory WSS. Therefore, it is essential to analyze the effects of flow or velocity waveform time transients on the

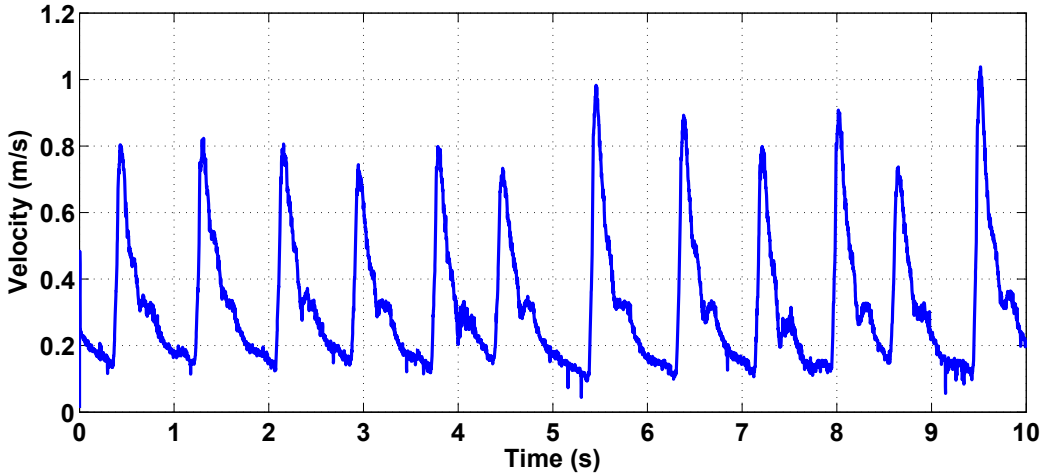

Figure 4.2. Blood velocity measured over several cardiac cycles by ultrasound in the author's common carotid artery showing inter-cycle variability

flow field and in particular on the shape of the velocity profile—and consequently WSS—in order to predict which waveforms may induce oscillatory WSS.

An important role in the investigation of physiological flow waveforms is represented by the measurement techniques used to acquire the blood flow rate or velocity. Measurement of arterial blood flow is usually performed using non-invasive methods such as PC-MRI and US. In the following section a brief overview of each acquisition method is given along with examples of *in vivo* measured flow waveforms in human systemic arteries available in the literature and used in computational hemodynamic (CHD) studies.

4.2 Flow waveform measurement

Time-dependent arterial flow rates can be acquired directly from PC-MRI measurements or indirectly, based on blood velocity, from Doppler US measurements. Both methods offer advantages and disadvantages over the other and are currently used in clinical practice to assess blood flow as well as vascular imaging.

4.2.1 PC-MRI flow measurement

The PC-MRI is a method for flow visualization and measurement derived from the MRI medical imaging method that is used to visualize internal structures of the body and provides an alternative to x-ray imaging such as computed tomography (CT). The basic principle underlying PC-MRI uses the basic property of spin that is characteristic of all elementary particles. As such, the hydrogen protons also exhibit spin (the proton rotates like a spinning top) and are used for MRI visualization. The magnetic moment developed by the hydrogen proton is influenced by magnetic fields and electromagnetic waves. Therefore, the strong magnetic field induced by an MRI transmitter will alter the spin thereby aligning it along the strong magnetic field direction. This change in spin motion acts as a tiny electric generator and induces an alternating voltage in the MRI receiver. Sensitive detectors are used for the MR imaging process.

The velocity measurement is performed by inducing a gradient along the magnetic field that causes all spins to have a phase shift which is position dependent. By comparing two MR images, one with and one without the gradient, it is possible to compute the phase shift which is directly proportional to the velocity of the moving protons. Thus, the blood velocity can be measured directly from phase-contrast MR images as the image voxels are velocity encoded and their intensity is proportional to the blood flow velocity. The method has a series of advantages such as high sensitivity and good vessel-tissue contrast even at low blood velocities. Problems with this method consist of relatively long measuring times associated with acquiring two images (with and without velocity encoding)—especially for three-dimensional measurements in which several magnetic field gradients are used—and the acquisition of one velocity component (i.e., the velocity component

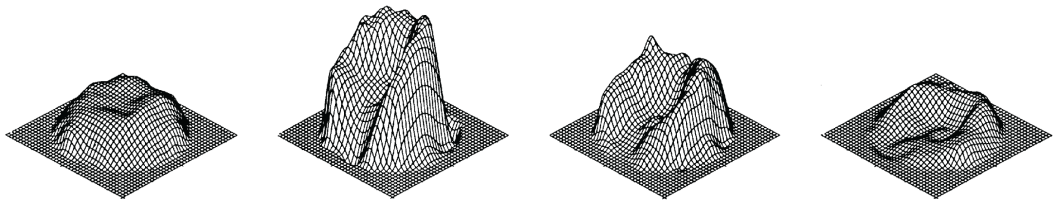

Figure 4.3. Three-dimensional velocity profiles acquired by PC-MRI in the human internal carotid artery at various times during the cardiac cycle

normal to the imaging plane).

Blood flow rate measurements can be readily obtained from three-dimensional PC-MRI acquisition of arterial cross-sections. As the entire image of the lumen is velocity encoded, the three-dimensional velocity profile is extracted and the volumetric flow rate can be found by integrating the velocity profile. Using multiple measurements synchronized with the cardiac cycle phases, the blood flow inside an artery as a function of time can be determined. The velocity profiles shown in Figure 4.3 were acquired, from left to right, during early systolic acceleration, mid-systolic peak flow, late systolic deceleration, and end-systolic flow, respectively, in the human internal carotid artery immediately distal to the carotid bifurcation [127]. The three-dimensional velocity profile also provides useful information about flow complexity in real arteries as illustrated by the skewed velocity profiles during peak- and late-systole (Figure 4.3) which may be influenced by the carotid bifurcation topology and secondary flow effects. For relatively straight arterial segments the velocity profiles are more regular, approaching the parabolic shape typical of fully developed flow in cylindrical pipes.

Most of the PC-MRI blood flow measurements have been performed in arteries prone to atherosclerosis development and as such both healthy and diseased conditions have been investigated [128–135]. Relevant to the current work are PC-MRI studies that measure the time-dependent blood flow waveform in arteries such as

the carotid, brachial, or coronary. The flow in the carotid arteries, which supply blood to the head and are prone to developing atherosclerotic plaque at the carotid bifurcation, has received much attention and several studies have characterized its waveform [127, 136–140].

The flow waveform in the carotid arteries, as shown in Figure 4.4 from PC-MRI measurements published in [137–140], is characterized by high pulsatility and high flow in the common carotid artery (CCA) while in the internal carotid artery (ICA) and external carotid artery (ECA), the two arteries that branch from the carotid bifurcation, the flow pulsatility decreases. Further distal into the arterial network the flow pulsatility and magnitude decreases more as illustrated by the flow waveform specific to the vertebral artery (VA). Individual variability as well as age, degree of physical fitness, and cardiovascular health result in differences between waveform shapes and flow magnitude. This adds to the difficulty in identifying hemodynamics phenotypes that negatively impact the cardiovascular system and promote arterial diseases.

4.2.2 Ultrasound flow measurement

Flow waveforms in the common carotid artery recorded with Doppler US and shown in Figure 4.5 are indirectly derived from the blood velocity assuming certain flow conditions. The US transducer, placed on the skin above an artery, sends high frequency sound waves that bounce off solid objects such as the red blood cells. The reflected sound waves from the moving red blood cells have a frequency shift due to the velocity of the moving cells. The reflected sound waves are then processed and compared with the input sound waves and a frequency spectrum that is directly proportional to the velocity of the moving cells is obtained. The velocity measurement thus obtained represents the velocity at one spatial loca-

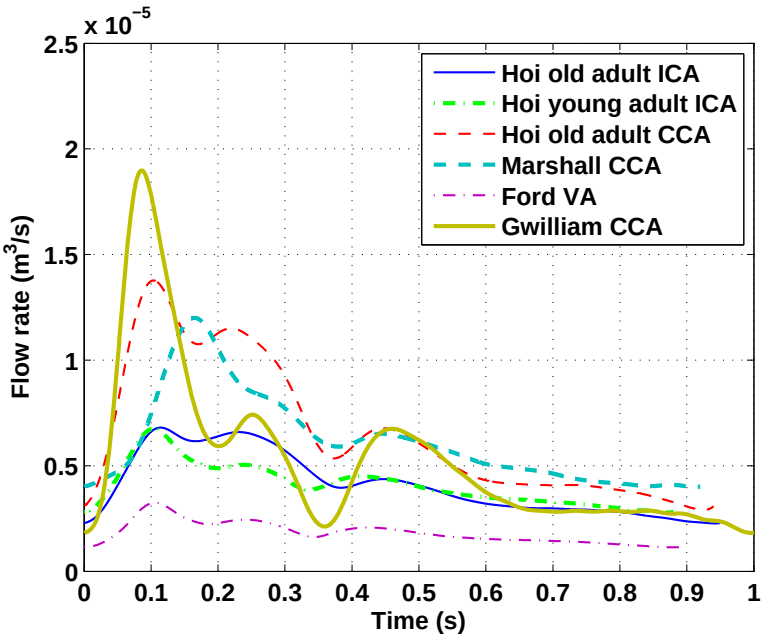

Figure 4.4. Arterial blood flow waveform acquired by phase-contrast magnetic resonance imaging

tion. The sound beams sent by the US probe form an interrogation region inside the sampled artery and an average velocity of the red blood cells passing through the interrogation region is obtained. Reducing the size of this region can provide velocity values that are characteristic of a point location rather than of a region [141]. To determine the arterial blood flow rate, the US transducer position is adjusted such that the highest blood velocity is recorded [142]. From the fluid dynamics theory of developed flow in a round pipe, the highest velocity value occurs in the center; therefore, it is assumed that the highest velocity value obtained with the US measurement represents the centerline blood velocity. Knowing the centerline velocity and assuming that the blood velocity profile is parabolic, the flow rate can be calculated. These assumptions are reasonable for low pulastility blood flows in relatively straight arterial segments. As shown in Figure 4.3, the velocity profile departs from the parabolic shape due to bifurcations, flow pulsatility, and

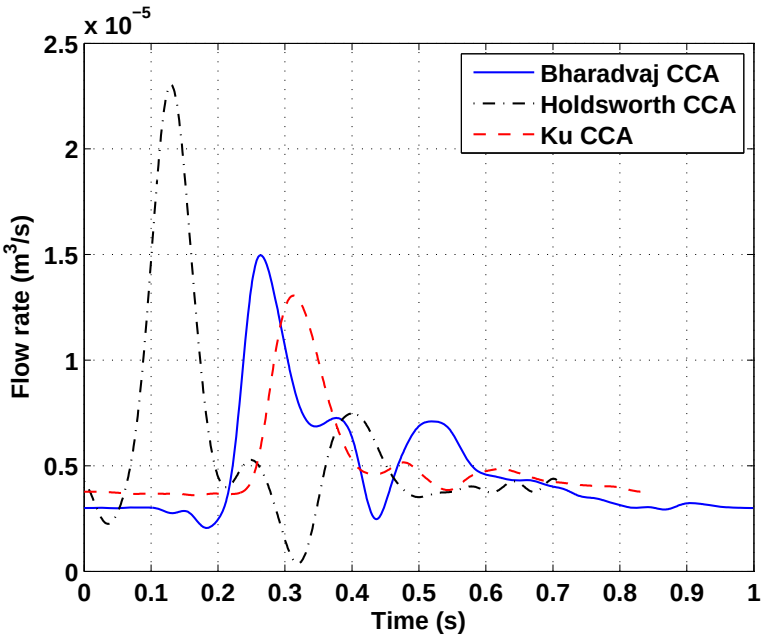

Figure 4.5. Common carotid artery flow waveform acquired by Doppler ultrasound

secondary flows.

Improvements in flow rate estimates can be obtained by assuming pulsatile velocity profiles (known as Womersley type profiles) instead of parabolic [143]. Another option is to measure the blood velocity at different locations along the arterial lumen by reducing the interrogation volume and employing multigate US transducers, thus reconstructing the velocity profile. This strategy ensures that flow rate measurements are based on actual blood velocity profiles and have been shown to be in good agreement with MRI flow rate measurements [130, 141, 144–146]. A detailed discussion of advancements in US blood flow measurement can be found in the review by Hoskins [147].

As most clinical data on blood flow consists of either arterial blood pressure or flow rate, experimental and computational hemodynamics studies rely on the accurate measurement of blood flow rate to determine other flow parameters such

as the velocity profile and the WSS in arterial districts that are subject to cardiovascular diseases. The shape of the blood flow waveform and its influence on velocity profiles has received little attention in CHD studies so far.

4.3 Previous work

While there is a wealth of physiologic data on blood flow rates and waveforms in different parts of the cardiovascular system, most of the data contains flow magnitude values with little information on the characteristics of the waveform shape [1]. The literature on blood flow waveform measurement or hemodynamics studies using patient-specific flow waveforms have not taken into consideration the effect of waveform shape and features such as acceleration and deceleration phases on the flow velocity. Some studies, as discussed below, have defined feature points along the waveform for comparison purposes among different waveforms but without relevance to hemodynamic effects.

The flow rate waveform in the common carotid artery was measured in 17 healthy volunteers and over 3000 cardiac cycles were analyzed in a Doppler US study aimed at defining an archetypal blood flow waveform [126]. Waveform feature points included minimum diastolic velocity, peak systolic velocity, minimum dicrotic notch velocity (at end systole), velocity at the point of maximum acceleration, time cycle phase of maximum acceleration, etc. The mean peak systolic velocity was 108.2 ± 3.8 cm/s while the cycle-to-cycle variability was $\pm 3.9\%$, the mean diastolic velocity was 20.9 ± 2.0 cm/s. However, there were no parameters describing the systolic deceleration phase of the waveform.

Using a similar waveform analysis, the flow in the common, internal, and external carotid arteries was measured and characterized by Hoi *et al.* [140]. The

waveform, measured by PC-MRI, and the feature points are shown in Figure 4.6 (adapted from Hoi *et al.* [140]) and are somewhat similar to the feature points defined in [126]. Feature points such as P1, the peak systolic volumetric flow rate, P2, the flow rate at mi-systolic flow, and D4, the end-diastolic flow rate, are used to define the pulsatility index, $\mathrm{PI} = (\mathrm{VFR_{P1}} - \mathrm{VFR_{D4}})/\mathrm{VFR_{avg}}$, the resistance index, $\mathrm{RI} = (\mathrm{VFR_{P1}} - \mathrm{VFR_{D4}})/\mathrm{VFR_{P1}}$, and the flow augmentation index, $\mathrm{FAI} = (\mathrm{VFR_{P2}} - \mathrm{VFR_{D4}})/(\mathrm{VFR_{P1}} - \mathrm{VFR_{D4}})$, where VFR is the volumetric flow rate. These indices were used to characterize the flow waveform and compare the waveforms measured in young (28 ± 7 years) and old adults (68 ± 8 years). It was found that the ICA waveforms have lower PI and RI and higher FAI than the ECA and CCA waveforms. Also, the time to peak flow for the ICA waveforms was, on average, about 12 ms less than that for the ECA and CCA which had similar time to peak flow. The old adult ICA waveforms showed higher FAI and RI than young adult ICA which can be explained from the observation that older adult waveforms had slightly higher late systolic peak (P2) and lower diastolic minimum (D4). The time to peak (H0 to P1, Figure 4.6) was slightly longer for old adult waveforms while the flow amplitudes at points H1, M1, P2, and H2 (Figure 4.6) were relatively higher for old adult waveforms when compared with young adult waveforms.

The waveform characterization provided by Hoi *et al.* [140] is useful to compare flow rate magnitudes and waveform shape and has been used in similar studies on arterial flow [138, 139]. However, this type of characterization does not account for the different acceleration and deceleration flow phases that occur during the cardiac cycle especially during systole and late systole when flow reversal at the wall has been observed [145]. A new method of flow waveform characterization in which the waveform is divided into intervals of flow acceleration and deceleration

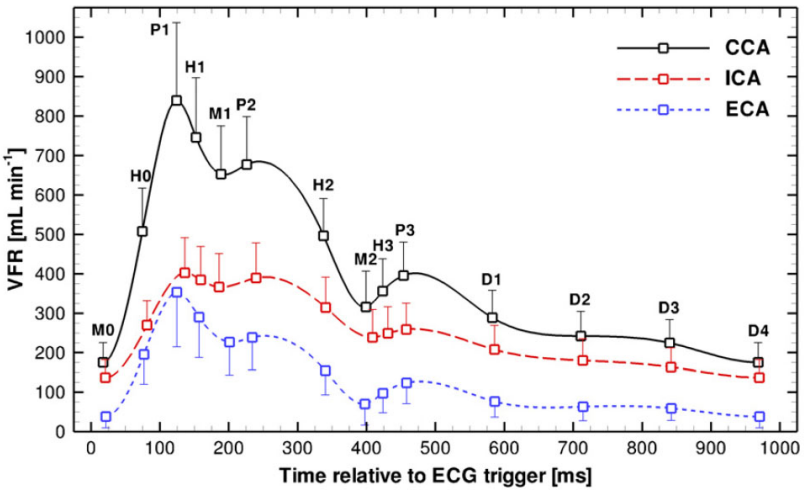

Figure 4.6. The volumetric flow rate waveforms in the common, internal, and external carotid artery of old adults

is proposed in the next section.

4.4 Waveform parameterization

The cardiac cycle is characterized by two phases: systole, when the left ventricle contracts and sends a burst of blood flow though the aortic valve into the aorta, and diastole, when the aortic valve closes, the left ventricle relaxes and fills with blood coming from the lungs through the left atrium. Although, during diastole, there is no pumping action from the heart, the blood does not reverse or stop but continues to flow at a lower rate. This is due to the elasticity of the aorta which acts as an accumulator or capacitor during systole and forces blood to flow during diastole. As the pressure wave developed by the ejection of blood from the left ventricle travels through the network of elastic arteries it suffers wave reflections that, in turn, affect the flow rate. These effects are dampened in small arteries and arterioles where flow becomes quasi-steady but are significant in major arteries.

The flow waveform typical of the common carotid artery, shown as an example

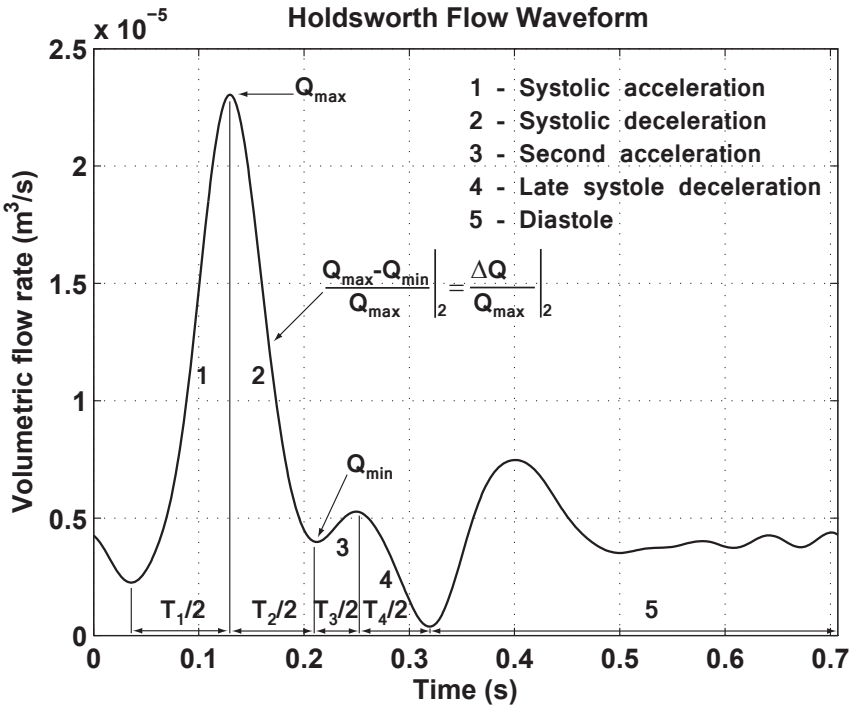

Figure 4.7. The common carotid flow rate waveform can be divided into intervals of accelerating (1 and 3), decelerating (2 and 4), and steady (5) flow

in Figure 4.7 and adapted from Holdsworth *et al.* [126], is characterized by strong flow acceleration during early systole, flow deceleration during mid-systole as reflected pressure waves traveling backwards from the upper body circulation affects the flow followed by another short flow acceleration during late systole from pressure waves reflected by the lower body circulation. Then, another flow deceleration occurs due to the closing of the aortic valve which corresponds to the dicrotic notch from the pressure pulse waveform. The small acceleration following the dicrotic notch flow represents the early diastolic phase when the flow is again accelerated by the contraction of the aorta which is then followed by a phase of quasi-steady flow [1].

The shape of the waveform, as determined by the cardiac cycle and vascular properties (through wave reflections) and as discussed previously, can vary

from one individual to another and even in the same individual between rest and physical activity conditions. The impact of the different phases (i.e., acceleration, deceleration) of the waveform on the flow depends on the time interval and the amount of flow variation during that particular waveform phase. Therefore, dividing the waveform into intervals of acceleration, deceleration, and steady flow and identifying parameters that define those intervals will allow for the systematic investigation of transient effects on the flow and, in particular, on WSS as determined by waveform features.

In Figure 4.7, the waveform has been divided into five distinct flow intervals. The first interval, T_1, corresponds to the systolic acceleration phase, the second interval, T_2, to the deceleration caused by the flow wave reflection from the upper body, the third interval, T_3, to the small acceleration caused by the wave reflection from the lower body, and the fourth interval, T_4, to the deceleration caused by the closure of the aortic valve at the end of systole. The fifth interval, T_5 is the diastolic flow which is characterized by an acceleration phase and a small deceleration phase that is followed by another phase of near steady flow. The diastolic flow phase is not parameterized as the amplitude of the pulsation during this phase of flow is small and cannot result in wall flow reversal and, therefore, is considered as an interval of quasi-steady flow. Each interval can be described by its time period, T_i, which is defined as twice the time from local peak to local trough or vice versa, and by its amplitude ratio,

$$\frac{\Delta Q}{Q_{\max}} = \frac{Q_{\max} - Q_{\min}}{Q_{\max}}, \tag{4.1}$$

where $Q_{\max}$ is the local maximum flow rate and $Q_{\min}$ is the local minimum flow rate for that particular interval. Therefore, a normalized amplitude ratio such as $\Delta Q/Q_{\max}$ that depends only on the local variation of flow amplitude for a

particular interval is more suitable to describe the effects of the acceleration and deceleration phases on the flow field as discussed in greater detail later. The definition of T_i ensures that, for sinusoidal waveforms, the time period of the waveform coincides with the time period of the deceleration interval. The choice of non-dimensionalization by $Q_{\max}$ is made such that the amplitude ratio will vary from 0 (no flow amplitude change) to 1 (infinite flow amplitude change). Also, the ratio can take values higher than 1 if $Q_{\min}$ is negative, that is, if the flow waveform has negative net flow rate values.

The flow waveform parameterization proposed in this work can be applied to any physiologic waveform. Using waveform data available in the literature for arterial flow, typical values for $\Delta Q/Q_{\max}|_i$ and T_i are summarized in Table 4.1. The values for the amplitude ratio of the systolic acceleration, $\Delta Q/Q_{\max}|_1$ range from 0.60 to about 0.90 with lower values for smaller arteries (ICA, ECA, VA) where the pulsatility decreases. The $\Delta Q/Q_{\max}|_2$ and $\Delta Q/Q_{\max}|_4$ values are smaller than $\Delta Q/Q_{\max}|_1$. Also, $\Delta Q/Q_{\max}|_2$ values tend to be smaller than $\Delta Q/Q_{\max}|_4$ values. The interval of small acceleration due to reflected waves, interval 3, has a low amplitude ratio when compared with the other intervals. The negative value of $\Delta Q/Q_{\max}|_3$ for the CCA waveform from Marshall *et al.* [137] indicates that there is no flow acceleration but rather a change in the deceleration rate as a result of weak pressure wave reflection which is illustrated in Figure 4.8. Also, notice the small difference between the time periods of the deceleration phases, T_2 and T_4.

Using the two parameters defined earlier, $\Delta Q/Q_{\max}$ and T, generic waveforms can be constructed by defining half-period sine waves that describe each acceleration and deceleration interval. Then, the sine waves can be assembled, one after another, by matching the magnitudes at their beginning and ending interval points and shifting them on the time axis. The application of this method in cre-

Table 4.1. Parameters from measured waveforms typical of the common carotid artery (CCA), internal carotid artery (ICA), and vertebral artery (VA)

Waveform	$\frac{\Delta Q}{Q_{\max}}\Big\vert_1$	$\frac{\Delta Q}{Q_{\max}}\Big\vert_2$	$\frac{\Delta Q}{Q_{\max}}\Big\vert_3$	$\frac{\Delta Q}{Q_{\max}}\Big\vert_4$	T_1 (s)	T_2 (s)	T_3 (s)	T_4 (s)
CCA [148]	0.86	0.54	0.06	0.66	0.16	0.16	0.06	0.12
CCA old [140]	0.78	0.22	0.07	0.54	0.21	0.13	0.10	0.31
CCA [126]	0.90	0.83	0.24	0.93	0.19	0.16	0.07	0.14
CCA [58]	0.72	0.65	0.11	0.25	0.19	0.24	0.09	0.13
CCA [139]	0.90	0.70	0.20	0.72	0.17	0.22	0.11	0.21
CCA [137]	0.67	0.27	−0.06	0.29	0.33	0.15	0.13	0.23
ICA old [140]	0.66	0.10	0.07	0.40	0.23	0.10	0.13	0.31
ICA young [140]	0.58	0.28	0.03	0.23	0.21	0.19	0.08	0.19
ICA [138]	0.60	0.29	0.03	0.24	0.23	0.18	0.07	0.21
VA [138]	0.65	0.31	0.08	0.34	0.21	0.16	0.11	0.21

ating waveforms that replicate physiologic waveforms is illustrated in Figure 4.8. The magnitude of each sine wave is defined by $\Delta Q/Q_{\max}$ and $Q_{\min}$ (if it represents the first acceleration interval) and the period by T. Only the first half-wave (i.e., the rising part) is used to model the acceleration interval while the second half-wave (i.e., the declining part) is used to model the deceleration interval. The sine wave curves, in some cases, match the waveform curve while in others there is a mismatch between their slopes due to the irregular shape of the physiologic waveform.

Parameterizing the waveform using this strategy allows for the systematic investigation of waveform features such as the magnitude and time period of the acceleration and deceleration phases and their effect on the flow patterns, in particular on the velocity profiles. The method of constructing generic waveforms described in this section is later used to study the effect of different waveform features on WSS reversal occurrence for waveforms that resemble blood flow waveforms specific to human systemic arteries.

The time-dependent nature of the blood flow rate plays an important role in

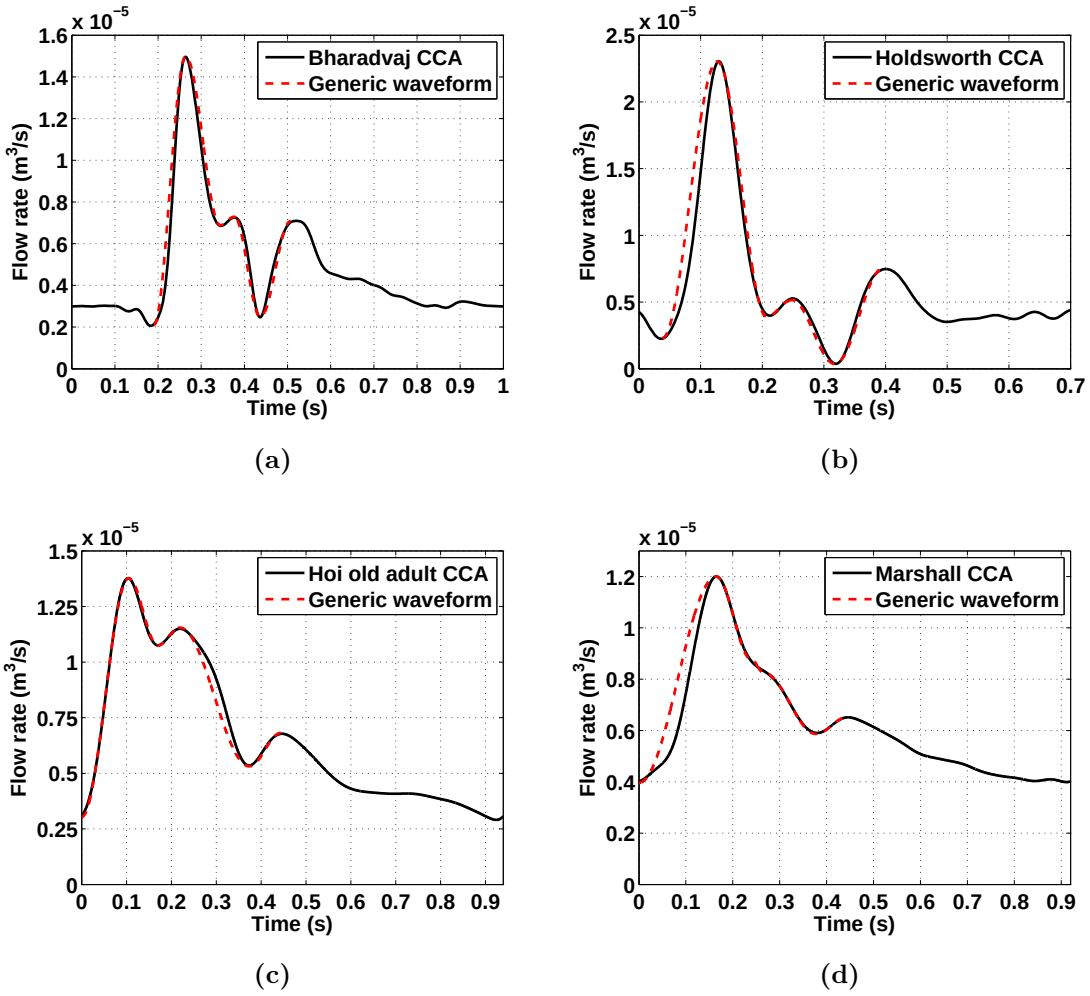

Figure 4.8. Generic waveforms that replicate physiologic flow waveforms can be constructed from half-period sine waves

determining the velocity profile in arteries where pulsatility effects are dominant. The departure of pulsatile velocity profiles from the parabolic shape that is characteristic of steady flows must not be neglected when investigating WSS distribution and flow patterns in time-dependent blood flows. Pulsatile flow theory is discussed next with an emphasis on the velocity profile shape during pulsatile flow deceleration.

4.5 Pulsatile flows

The investigation of the pressure-flow relation in the arterial system was the motivation behind one of the first theoretical studies on laminar, fully developed, incompressible flows driven by a periodic pressure gradient in rigid pipes of circular cross-section. The analytical solution for the velocity field and the flow rate as determined by an arbitrary periodic pressure gradient waveform was derived by Womersley [122]. Application of the pulsatile flow solution to investigate the velocity profiles and flow rates in physiologic flows of human and canine arteries soon followed [149]. Other early theoretical studies of unsteady pipe flows were conducted by Sexl *et al.* [150], Szymanski [151], Lambossy [152], Uchida [153] and more information on the state of research on pulsatile and oscillating flows can be found in the the review by Gundogdu and Carpinlioglu [154].

Relatively recent studies by Unsal *et al.* [155] and Haddad *et al.* [156] on flows driven by a sinusoidal mass flux waveform have identified two non-dimensional parameters that describe the flow amplitude variation and the flow pulsatily and used them to quantify flow reversal conditions in a straight tube. This will be discussed in greater detail in the next chapter. The theoretical basis for investigating pulsatile flows and some examples of pulsatile flows and their effect on the velocity profile are discussed for the remainder of this section.

4.5.1 Equations of flow

The theory of pulsatile flow in a cylindrical pipe is of interest in the current work as the flow conditions for the occurrence of WSS reversal due to waveform-induced flow transients are investigated. The incompressible flow of a Newtonian, homogeneous fluid in a cylindrical pipe is considered. From the general equations

describing the motion of a fluid, the continuity equation,

$$\frac{\partial \rho}{\partial t} + \rho \boldsymbol{\nabla} \cdot \boldsymbol{v} + \boldsymbol{v} \cdot \boldsymbol{\nabla} \rho = 0, \tag{4.2}$$

and the momentum equation,

$$\rho \left[\frac{\partial \boldsymbol{v}}{\partial t} + (\boldsymbol{v} \cdot \boldsymbol{\nabla}) \boldsymbol{v} \right] = -\boldsymbol{\nabla} p + \boldsymbol{\nabla} \cdot \boldsymbol{\tau} + \rho \boldsymbol{F}, \tag{4.3}$$

where ρ is the fluid density, $\boldsymbol{v}$ is the velocity, p is the pressure, $\boldsymbol{\tau}$, is the stress tensor, and $\boldsymbol{F}$ is the body force, the equations describing flow in cylindrical pipes are determined. Applying the assumptions about the flow and the fluid mentioned above, considering the flow to be axially symmetric and using cylindrical coordinates, the continuity equation reduces to

$$\frac{\partial v_z}{\partial z} = 0, \tag{4.4}$$

while the momentum equation in the z-direction becomes

$$\rho \frac{\partial v_z}{\partial t} = \mu \left(\frac{\partial^2 v_z}{\partial r^2} + \frac{1}{r} \frac{\partial v_z}{\partial r} \right) - \frac{\partial p}{\partial z}, \tag{4.5}$$

where v_z is the axial velocity component, r is the radial distance from the pipe axis, and μ is the fluid viscosity.

The driving pressure gradient, $\partial p/\partial z$, can be constant or vary in time. If $\partial p/\partial z(t) = A_0$, where A_0 is constant in time, then the velocity is given by the well known Poiseuille formula,

$$v_z(y) = -\frac{R^2}{4\mu} A_0 (1 - y^2), \tag{4.6}$$

where $y = r/R$, which corresponds to a parabola. If the pressure gradient is time-dependent,

$$\frac{\partial p}{\partial z}(t) = A e^{i\omega t}, \tag{4.7}$$

with frequency $f = \omega/2\pi$, then, inserting (4.7) into (4.5) and separating the velocity into functions of space and time, $v_z(r,t) = u(r)e^{i\omega t}$, the momentum equation becomes

$$\frac{\partial^2 u}{\partial r^2} + \frac{1}{r}\frac{\partial u}{\partial r} - \frac{i\omega}{\nu}u = -\frac{A}{\mu}, \tag{4.8}$$

which similar to the Bessel equation and where $\nu = \mu/\rho$ is the kinematic viscosity. The solution to (4.8) is

$$u(r) = \frac{A}{i\omega\rho}\left[1 - \frac{J_0\left(r\sqrt{\frac{\omega}{\nu}i^{\frac{3}{2}}}\right)}{J_0\left(R\sqrt{\frac{\omega}{\nu}i^{\frac{3}{2}}}\right)}\right]. \tag{4.9}$$

Converting back to the axial velocity, $v_z(y,t)$, the solution is the real part of

$$v_z(y,t) = \frac{1}{i\omega\rho}\left[1 - \frac{J_0(\alpha y i^{\frac{3}{2}})}{J_0(\alpha i^{\frac{3}{2}})}\right]\left[-\frac{\partial p}{\partial z}(t)\right], \tag{4.10}$$

where J_0 is the zero$^{\text{th}}$ order Bessel function of the first kind and α is the Womersley number as defined in (1.1).

The flow rate, $\dot{Q}(t)$, is given by

$$\dot{Q}(t) = 2\pi\int_0^R v_z(r,t)r\,dr = 2\pi R^2\int_0^1 v_z(y,t)y\,dy, \tag{4.11}$$

which, upon integration, becomes

$$\dot{Q}(t) = \frac{\pi R^2}{i\omega\rho}\left[1 - \frac{2\alpha i^{\frac{3}{2}}}{i^3\alpha^2}\frac{J_1(\alpha i^{\frac{3}{2}})}{J_0(\alpha i^{\frac{3}{2}})}\right]\left[-\frac{\partial p}{\partial z}(t)\right], \tag{4.12}$$

where J_1 is the 1$^{\text{st}}$ order Bessel function of the first kind. In a similar manner, the WSS, τ_w, which, for a Newtonian fluid is defined as

$$\tau_w = -\mu\frac{\partial v}{\partial r}\Big|_{r=R} = -\frac{\mu}{R}\frac{\partial v}{\partial y}\Big|_{y=1}, \tag{4.13}$$

becomes

$$\tau_w(t) = \frac{\mu\alpha i^{\frac{3}{2}}}{\rho R}\left[\frac{J_1(\alpha i^{\frac{3}{2}})}{J_0(\alpha i^{\frac{3}{2}})}\right]\left[-\frac{\partial p}{\partial z}(t)\right], \tag{4.14}$$

while considering only the real part.

Flow problems where the pressure gradient is not known and only the flow rate is given as a periodic function are usually described by a Fourier series,

$$\dot{Q}(t) = \dot{Q}_0 + \text{real}\left(\sum_k \dot{Q}_k e^{i\omega t}\right), \quad k \neq 0, \tag{4.15}$$

where $\dot{Q}_0$ is the steady flow rate component and $\dot{Q}_k$ is the magnitude of the k^{th} harmonic. The velocity, in terms of $\dot{Q}(t)$, is

$$u(y,t) = \dot{Q}(t)\left[\frac{\alpha i^{\frac{3}{2}} J_0(\alpha i^{\frac{3}{2}}) - \alpha i^{\frac{3}{2}} J_0(\alpha i^{\frac{3}{2}} y)}{\alpha i^{\frac{3}{2}} J_0(\alpha i^{\frac{3}{2}}) - 2J_1(\alpha i^{\frac{3}{2}})}\right], \tag{4.16}$$

and the WSS is

$$\tau_w(t) = -\frac{\mu}{\pi R^3}\dot{Q}(t)\left[\frac{\alpha^2 i^3 J_1(\alpha i^{\frac{3}{2}})}{\alpha i^{\frac{3}{2}} J_0(\alpha i^{\frac{3}{2}}) - 2J_1(\alpha i^{\frac{3}{2}})}\right], \tag{4.17}$$

again, considering only the real part.

The velocity field for flow in a canine femoral artery from the arterial pressure gradient was determined by Hale *et al.* [149]. The velocity calculated using the equations presented above at different radial locations is shown in Figure 4.9 along with the pressure gradient. The flow is pulsatile with $\alpha = 3.34$ and results in the occurrence of a phase lag (maximum at the centerline and minimum near the wall) between the velocity field and the pressure gradient. The flow also reverses, first at the wall (indicated by the curve for $y/R = 0.95$, where y is the distance from the vessel's centerline) and then in the center of the vessel (indicated by the curve for $y/R = 0$).

When the flow decelerates in response to time variations in the driving pressure gradient, the fluid near the wall will first reverse because of its small inertia while the higher momentum fluid in the middle of the pipe will take longer to respond to flow changes. This effect, discussed in early studies on pulsatile flows by Hale *et al.* [149] and by Womersley [122], is due to inertial effects and results in the

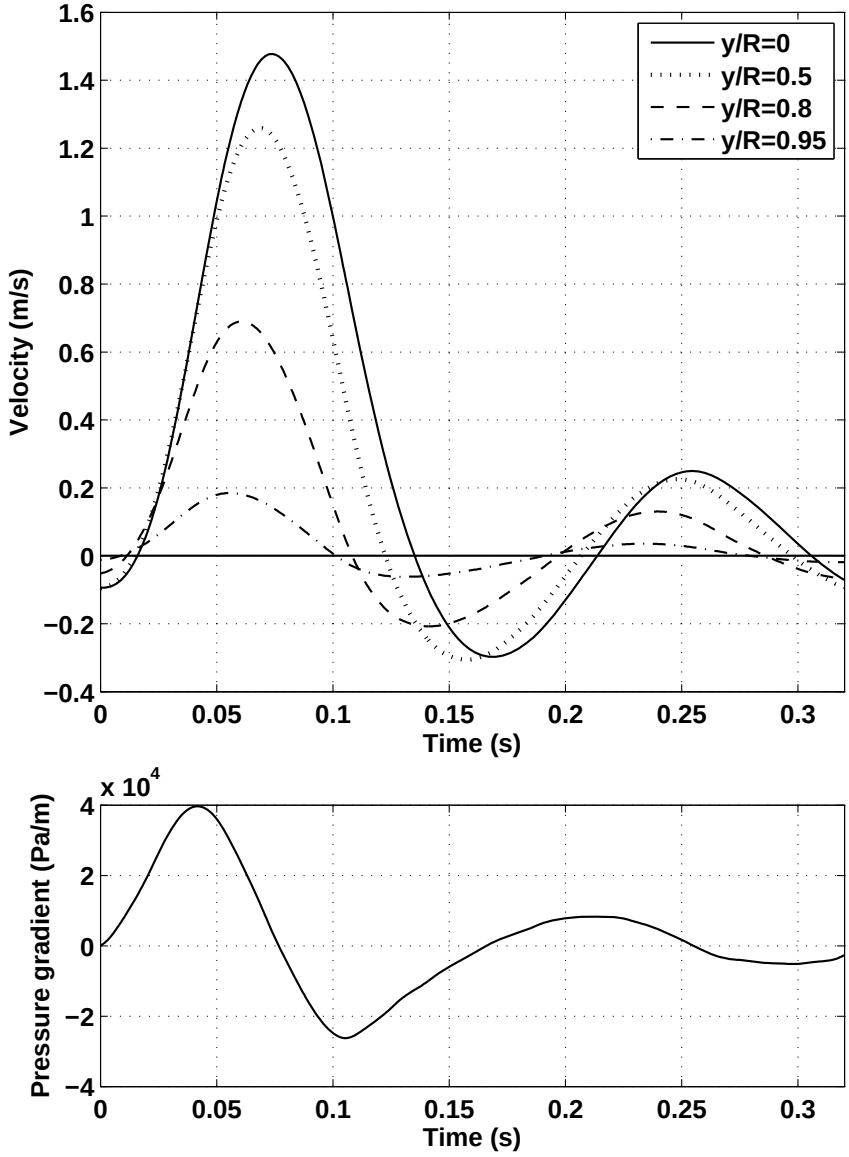

Figure 4.9. Velocity at different locations across the radial direction (top) and the pressure gradient driving the flow (bottom)

development of a phase lag between the pressure gradient oscillations and flow velocity oscillations. Due to the no-slip boundary condition at the wall, the fluid velocity is small near at the wall (hence low momentum) and the flow responds

almost in phase to pressure gradient oscillations, thus more easily reversing during a large change in pressure gradient. As illustrated in Figure 4.9, the phase lag between the pressure gradient and the flow velocity is minimal near the wall and maximal at the center of the pipe.

Uchida [153] also studied the behavior of oscillatory flows driven by a time dependent sinusoidal pressure gradient with zero mean and found that the flow velocity in the middle of the pipe always lagged flow velocity near the wall. However, for flows with positive net flow rates in round tubes, the velocity profiles for oscillatory flows differ from the velocity profiles of pulsatile flows with negative net flow rates. In the latter flow case, the entire velocity profile reverses and exhibits negative velocity values whereas in the former flow case, the velocity profile can contain negative values in the vicinity of the wall but positive values toward the center of the tube. Also, for pulsatile flows with no net flow reversal, there is a second flow reversal region developing away from the wall at higher α values after the flow first reverses at the wall as demonstrated by Haddad *et al.* [156].

The simplifying assumptions used in deriving the Womersley solution need to be considered when modeling blood flow as these simplifications can have an impact on the accuracy of the results. The flow obtained using the Womersley solution for a given time-varying flow rate has been compared with the flow obtained from a numerical model which accounts for arterial tapering and a compliant vessel wall [157]. The results show that the rigid, non-tapered vessel assumption specific to the Womersley solution tends to overestimate WSS by 2–7% when compared with the solution obtained with a compliant wall model or with a tapered vessel model. These findings indicate that using the Womersley solution to model blood flow in arteries with a high wall compliance wall such as the aorta is not adequate; however, for systemic arteries, in which the compliance rate is much lower, the effects

are negligible and the Womersley analytic solution provides reasonable results [2].

4.6 Summary

The flow rate waveform that characterizes systemic arterial blood blow can induce flow reversal at the wall even in straight arterial sections. In this chapter, the waveform is parameterized by taking into consideration the frequency and flow amplitude changes that characterize the acceleration and deceleration phases. Sine waves are used to model the acceleration and deceleration curves and can be assembled together to construct generic waveforms that can be used to systematically study the effects of the flow waveform shape on the velocity field. Also, this method has the potential to model and replicate real arterial blood flow waveforms.

Chapter 5

Flow reversal during pulsatile flow

The time transient aspects of blood flow are influenced by the flow waveform and the viscoelastic properties of the major arteries (which have a direct impact on the propagation of pressure pulse waves). The pulsatile arterial flow waveform is characterized by positive net values with the exception of a few arteries such as the coronary, brachial, and femoral [1]. The arterial geometry and blood flow waveform transients can induce perturbations that result in flow reversal at the vessel wall. While most hemodynamics studies have focused on the effects of arterial geometric features on the flow and endothelium, as discussed in previous chapters, little attention has been given to the effects of the flow waveform on the velocity profile, particularly on the the occurrence of wall flow reversal or wall shear stress reversal (WSSR). As this flow condition might occur near the vessel wall due to the fast flow deceleration phase present during late systole, low and oscillatory wall shear stress (WSS) develops. Therefore, it is of interest to quantify the waveform characteristics that result in this type of flow conditions that have been correlated with endothelial dysfunction and development of atherosclerosis as discussed earlier in this work.

In this chapter, the conditions for WSSR occurrence are investigated for pulsatile flows in cylindrical, rigid tubes with simple (sinusoidal) and complex waveforms (resembling physiologic flows) that define the volumetric flow rate. The critical conditions that indicate WSSR occurrence are defined in terms of non-dimensional parameters that quantify the time and magnitude variations of the

flow deceleration phase.

5.1 Introduction

Periodic, time-varying flows can be divided into oscillatory and pulsatile flows. While the former category includes flows with zero mean flow rate and reversing velocity profiles (Figure 5.1a), the latter includes flows with positive mean flow rates which may or may not contain negative net flow values and whose velocity profile may or may not exhibit negative values (Figure 5.1b). As the blood flow in healthy arteries is pulsatile with positive net flow rates, the focus of this work is on these types of flow while oscillatory flows are neglected as they already exhibit flow reversal.

Early theoretical studies on oscillatory and pulsatile flows in pipes and channels date from the early and middle twentieth century and investigated the relationship between pulsatile or oscillatory pressure gradient, flow rate, and velocity profile [122, 150–153]. The non-dimensional parameter that quantifies the pulsatile or oscillatory flow effects versus viscous effects is α, defined in equation (1.1) and known as the Womersley number [122]. In the definition of α, the flow pulsatility or oscillation is quantified by the frequency of the wave, which, for a sinusoidal waveform also coincides with the frequency of the waveform while for more complex waveforms it corresponds to the period of the fundamental harmonic. Time-dependent flows with α less than unity are considered to be quasi-steady flows with parabolic velocity profiles that are characteristic of steady flows. As an example, in Figure 5.1 the velocity profiles for oscillatory and pulsatile flows with $\alpha = 1$ are shown. The velocity magnitude has been non-dimensionalized by the mean velocity corresponding to the maximum flow rate. For oscillatory flows, the shape

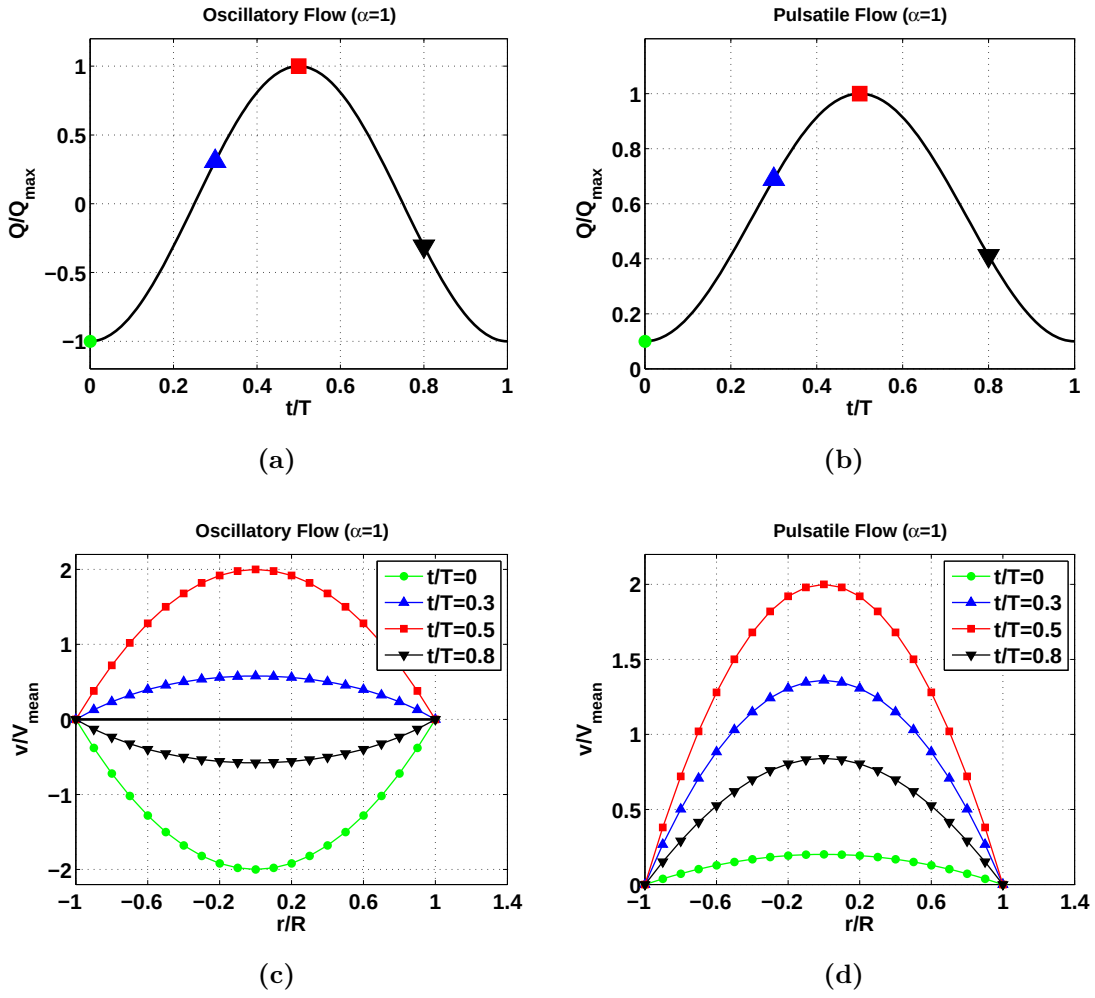

Figure 5.1. Generic waveforms that replicate physiologic flow waveforms can be constructed from half-period sine waves

of the velocity profile is parabolic at minimum, mid-acceleration, peak, and mid-deceleration flows (Figure 5.1c) with negative values during net flow reversal. The same can be said about the shape of the velocity profiles for the pulsatile flow as depicted in Figure 5.1d. The parabolic shape of the velocity profile is maintained throughout the entire waveform cycle even during the acceleration and deceleration phases. As no flow reversal is present for this particular pulsatile waveform the profiles exhibit only positive velocity values.

For flows with $\alpha > 1$, the effect of time-dependent flow transients becomes significant and the velocity profile departs from the parabolic shape as exemplified in Figure 5.2. Oscillatory flows with $\alpha = 8$ will exhibit velocity profiles similar to those shown in Figure 5.2a. As α increases, the location of peak velocity moves from the center of the pipe toward the wall and the profile exhibits a more blunt shape as the flow in the middle responds much slower to velocity oscillations. The velocity profiles for pulsatile flows at the same α value do not show such dramatic shape changes as those for oscillatory flows. The shape of the profiles also differs from parabolic, as shown in Figure 5.2b, with the acceleration and peak velocity profiles being somewhat blunt while the velocity profiles during deceleration and minimum flow exhibit negative values near the wall, thus, indicating wall flow reversal. Also, during deceleration and minimum flow, the velocity profiles indicate positive net flow rates as only a small fraction of the flow reverses. Higher α values will result in increased wall flow reversal during flow deceleration and blunter profiles during peak flow while lower values will result in the reduction and eventual disappearance of reversed flow at the wall.

During transition from negative to positive flow and vice-versa for oscillatory flows or during deceleration for pulsatile flows, the near-wall flow reverses first in response to pressure gradient variations. The flow velocity in the center of the pipe lags these pressure gradient changes. This phenomenon becomes more apparent as α increases as discussed in early studies on pulsatile flows by Hale *et al.* [149] and Womersley [122], on oscillatory flows by Uchida [153] and also reviewed in chapter 4, subsection 4.5.1.

The influence of the blood flow waveform on arterial hemodynamics and in particular on the flow conditions that favor the development of atherosclerosis is still under investigation but several studies indicate that different types of waveforms

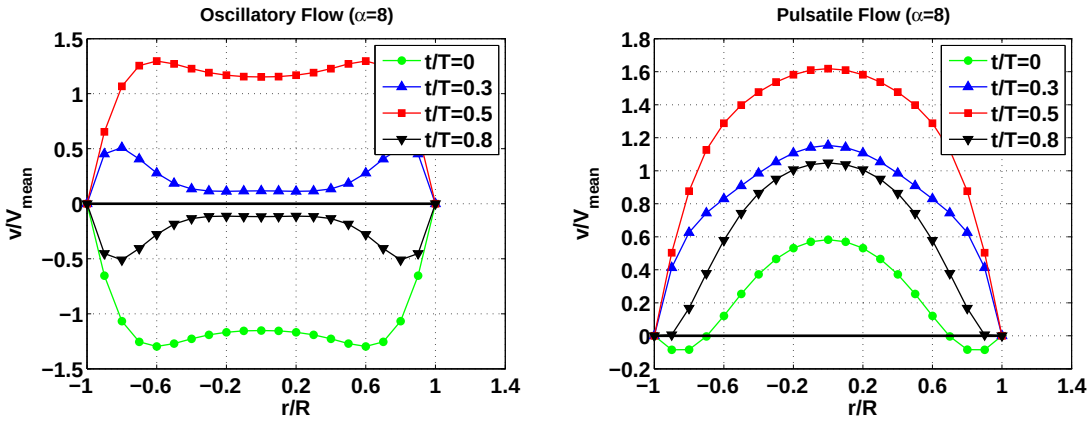

Figure 5.2. Flow in the carotid bifurcation obtained from an experimental model (a) and from a three-dimensional computational hemodynamics model (b)

have differing effects on the endothelium [20, 22, 158]. In the work by Dai *et al.* [20], endothelial cells were exposed *in vitro* to vascular flow patterns that reproduce *in vivo* region-specific WSS. The flow inside the human carotid bifurcation was measured and CHD simulations were performed to determine the time-dependent WSS distribution at two locations—the carotid sinus, which is susceptible to atherosclerotic plaque development and on the lateral wall of the internal carotid distal to the bifurcation where no adverse vascular events occur. The WSS patterns at these two locations illustrated in Figure 5.3 (adapted from [20]) show low (< 0.5 Pa) and negative WSS values (or WSSR) at the carotid sinus and relatively high and positive values on the internal carotid wall. Cultured endothelial cells exposed to these two distinct WSS yielded inflammatory and athero-prone responses for WSS waveform typical of the carotid sinus while athero-protective and normal endothelial cell function for the WSS patterns measured in the internal carotid. These results reinforce the role of time-dependent WSS patterns on endothelial function and atherosclerosis development.

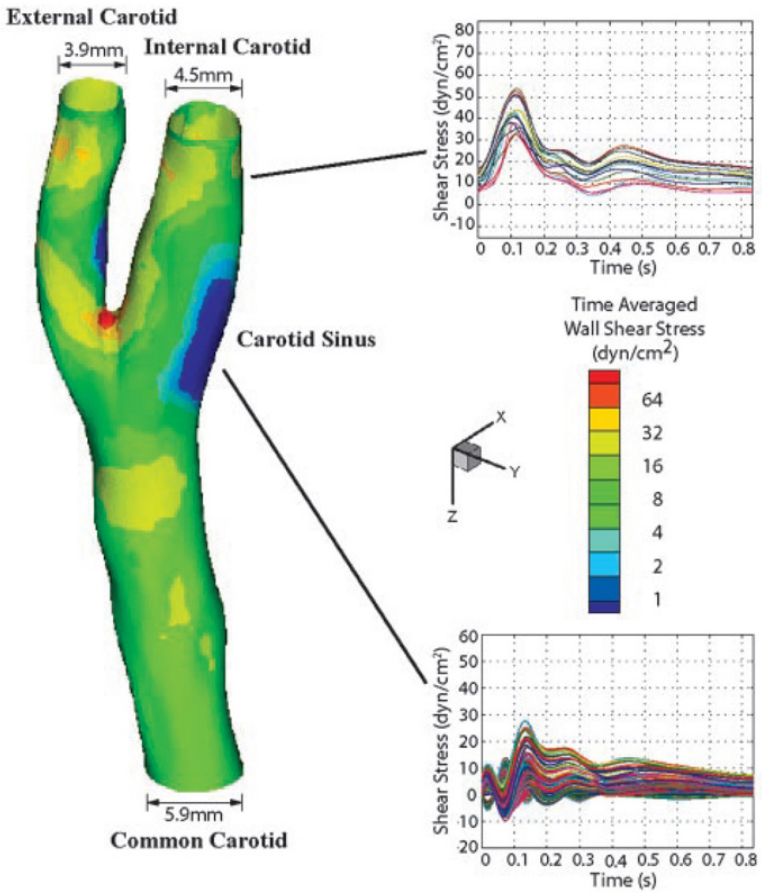

Figure 5.3. Time-averaged wall shear stress (WSS) in the human carotid bifurcation and time-dependent WSS waveforms at the carotid sinus and on the internal carotid lateral wall

Flow reversal and consequently WSSR are the result of flow transients that occur during the deceleration phase of a flow waveform. Investigating the waveform parameters that induce WSSR for waveforms with negative net flow rate values is meaningless as they already exhibit WSSR. For flow waveforms with positive net flow values such as human arterial waveforms, WSSR may or may not be present depending on the artery dimension, waveform shape, and the time period of the cardiac cycle. Non-dimensional parameters that quantify the change in magnitude and the time rate of change of the flow rate can be used to establish the conditions that determine WSSR. For flows characterized by sinusoidal waveforms

(shown in Figure 5.1b) it is obvious that the properties of the waveform and those of the deceleration phase are the same; however, for more complex waveforms with multiple acceleration and deceleration phases, as in the case of physiologic waveforms, this is no longer true; therefore, a new approach must be taken.

5.2 Previous work

Early investigations of pulsatile flows, as mentioned in the previous section, were analytical and sought to describe the relation between pressure and flow pulsations. Subsequent studies also consisted of experimental work in which measured velocity profiles and flow pulsations were compared with analytical solutions. Ohmi *et al.* [159] performed analytical and experimental work on both pulsatile and oscillating flows and offered approximate solutions in non-dimensional form but their analytical results on velocity profiles did not match the experimental measurements. Das and Arakeri [160] analytically investigated the pressure gradient and velocity distribution for laminar flows in circular tubes in both fully developed and starting flow cases. The flow rate was defined by a trapezoidal waveform and by sinusoidal oscillating waveforms. Reversed flow at the wall was observed for high pulsatility flows during the deceleration phase of the flow and during sudden flow stop. The analytical solution presented in their work is applicable to starting or stopping flows when the flow rate waveform is known; however, no comparison between theoretical and experimental data was given to validate the results.

Pulsatile flow waveform analysis has been performed on simple, sinusoidal waveforms with the aim of quantifying and describing the properties of pulsatile flows and near-wall reversed flow by Unsal *et al.* [155]. The study included both analytical and experimental investigations of flow behavior and velocity profiles for

sinusoidal flow waveforms with positive net flow rates. The amplitude of flow pulsation, $\dot{m}_A^* = \dot{m}_A/\dot{m}_M$, was non-dimensionalized by the time-averaged mass flow rate, $\dot{m}_M$, where $\dot{m}_A$ is the amplitude of the mass flow pulsation. In this dimensionless form, the mass-flow rate was defined as $\dot{m}^* = 1 + \dot{m}_A^* sin(2\pi ft)$, where f is the frequency of the mass flow rate. The velocity was normalized by $U_{AV} = \dot{m}_M/(\rho\pi R^2)$ while the time was normalized by $t_c = R^2/\nu$, the viscous diffusion of momentum time scale. From this, a new parameter representing the non-dimensional frequency, $F = fR^2/\nu$, was derived. This parameter is directly proportional to α^2, $F = \pi\alpha^2/2$, and was used along with $\dot{m}_A^*$ to describe the properties of pulsatile flows and the reversed flow regime. Flows with $\dot{m}_A^*$ ranging from 0.6 to 1 (zero minimum flow) and F ranging from 0.1 (quasi-steady) to 7 were investigated both analytically and experimentally. The amplitude ratios of the mass flow rate to the pressure gradient and velocity as well as the phase lag were computed as a function increasing pulsation frequency, F. Plots of the velocity profiles were presented and there was good agreement between analytical and experimental velocity data. The velocity profiles also indicated flow reversal at the wall as F was increased. A map of the flow conditions ($\dot{m}_A^*$ versus F) that result in flow reversal was also given.

A similar investigation representing an extension to the work of Unsal *et al.* [155] was conducted by Haddad *et al.* [156] for the same type of laminar flows in channels and circular pipes with known mass flow rates defined by sinusoidal waveforms. Following the same analytical approach and parameters, $\dot{m}_A^*$ and F, the time-dependent behavior of the velocity profile, WSS, and amount of reversed flow was investigated. A second type of flow reversal was observed away from the wall for higher flow pulsation frequency than for wall flow reversal and a flow reversal map similar to the one from the preceding study [155] was presented.

Also, the study showed that for a given flow pulsation amplitude there is a critical frequency at which the total reversed flow rate reaches a maximum value.

The analysis presented by Unsal *et al.* [155] and Haddad *et al.* [156] is well suited to describe flows with sinusoidal waveforms. However, using $\dot{m}_A^*$ to describe the flow amplitude pulsation for waveforms other than sinusoidal can be misleading. Both $\dot{m}_A^*$ and F are defined in terms of the overall waveform properties and do not account for phases of steady, accelerating, or decelerating flow that are found in more complex waveforms. This is of particular importance to physiologic waveforms typical of blood flow in which two deceleration phases are present during systole and a phase of quasi-steady flow is present during diastole.

The limitation of $\dot{m}_A^*$ and F to sinusoidal waveforms is illustrated by a simple example shown in Figure 5.4. Two flow waveforms are constructed such that both have the same time period and pulsation amplitude during flow acceleration and deceleration phases. The sine wave shown in Figure 5.4a has a time period of 0.28 s with $\dot{m}_A^* = 0.66$ and $\Delta Q/Q_{\max} = 0.70$. The corresponding critical value for WSSR is $F = 6.27$. The flow waveform in Figure 5.4b is characterized by a similar sinusoidal acceleration and deceleration followed by a phase of steady flow. The time period of the entire waveform is 0.42 s while the time period of the sinusoidal acceleration and deceleration is 0.28 s and $\Delta Q/Q_{\max} = 0.70$. Due to the addition of the steady flow phase following the deceleration phase, the time-mean flow rate is lower than the one corresponding to the sinusoidal waveform while the peak flow amplitude is the same. Therefore, the value of $\dot{m}_A^*$ is lower, $\dot{m}_A^* = 0.54$. The corresponding critical value for $\dot{m}_A^* = 0.54$ is $F = 3.71$. However, this value is lower than the correct critical value of 6.27, listed earlier for the sinusoidal wave. Designing an experiment with a flow waveform as depicted in Figure 5.4b and flow conditions corresponding to $F = 3.71$ will not result in WSSR as F is lower than

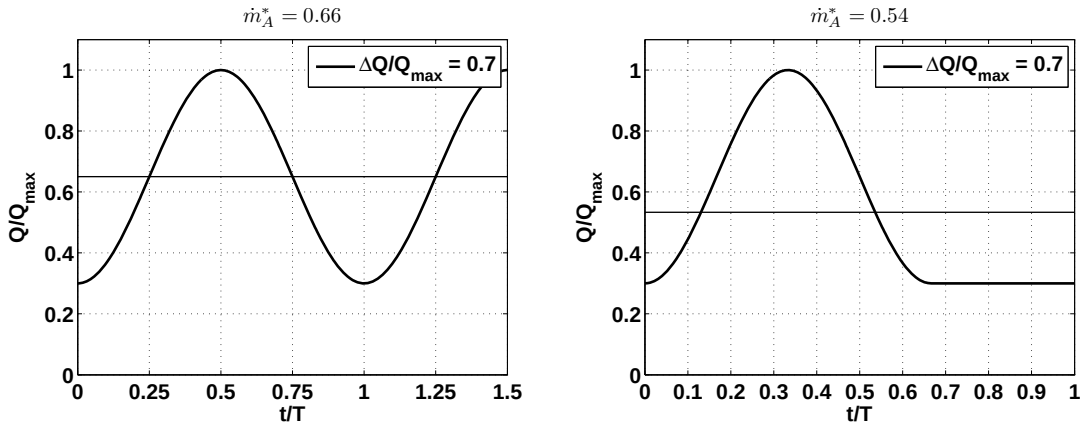

Figure 5.4. Sinusoidal flow waveform (a) and waveform with minimum steady flow (b). Both have similar $\Delta Q/Q_{\max}$ and F values but different time-averaged flow values

the true critical value. Thus, $\dot{m}_A^*$ is not suited to quantify the amplitude pulsation of complex waveforms with the purpose of determining WSSR occurrence. The same can be concluded about F as well as it is defined in terms of the overall waveform properties.

Flow reversal occurs during the deceleration phase of a waveform; therefore, a new set of parameters that describe the properties of the deceleration phase alone are needed to quantify the flow conditions for WSSR occurrence. As already discussed in chapter 4 the waveform can be divided into individual acceleration, deceleration, and steady flow intervals and $\Delta Q/Q_{\max}$ can be used to quantify the flow pulsation amplitude for a particular interval. The pulsation of a deceleration interval could also be described by $\dot{m}_A^*$ by computing the time-averaged flow during the deceleration phase alone. However, determining $\Delta Q/Q_{\max}$ is more convenient than $\dot{m}_A^*$ for an acceleration or deceleration interval as only $Q_{\max}$ and $Q_{\min}$ are needed and they are readily available from the measured waveform.

5.3 Computational methods

Flow reversal occurrence for waveforms with positive net flow rates depends on the time-change of flow amplitude during the deceleration phase of the waveform. Parameters such as α (or F) and $\dot{m}_A^*$ that quantify the pulsatility and flow amplitude variation of a waveform, respectively, do not capture the properties of complex waveforms that consist of multiple deceleration phases. As this part of the study is focused on quantifying the conditions under which wall flow reversal and, consequently, WSSR occurs during the deceleration phase of a complex waveform, a modified Womersley number is proposed to quantify the pulsatility of the deceleration phase only and will be referred to as the deceleration Womersley number,

$$\alpha_d = R\sqrt{\frac{2\pi\rho}{T_d\mu}}, \tag{5.1}$$

where T_d is the time period of the deceleration phase defined as twice the time from peak to trough (c.f. Figure 4.7). The definition of T_d was chosen such that $\alpha_d = \alpha$ for sinusoidal waveforms. The set of two parameters, α_d and the $\Delta Q/Q_{\max}$ ratio, is used to quantify the conditions under which the flow at the wall reverses for general pulsatile flow waveforms with positive net flow rates. For sinusoidal waveforms, the two parameters are analogous to the non-dimensional numbers, F and $\dot{m}_A^*$, used previously [155, 156]. Referring back to the simple example shown in Figure 5.4, the use of $\Delta Q/Q_{\max}$ will yield a unique α_d for the deceleration phase.

5.3.1 Generic waveforms assembly

The investigation of flows defined by complex waveforms to quantify the conditions for WSSR occurrence consists of systematic construction of waveforms with

different properties. In this work, waveforms that resemble physiologic cases of arterial blood flow are of interest. These waveforms, as discussed in previous chapters, typically consists of a systolic acceleration phase followed by a deceleration phase due to reflected waves that might contain a short flow acceleration phase and then followed by a phase of low pulsatility flow corresponding to diastolic flow. Generic waveforms can be constructed as described in chapter 4, section 4.4, by using sine waves to model the acceleration and deceleration intervals. These intervals can then be added together to form a set of discrete data points that describe the flow waveform as a function of time. To illustrate this concept, a generic waveform is shown in Figure 5.5 consisting of three acceleration and deceleration intervals and one interval of steady flow corresponding to diastole. Note that the data point values at the beginning and the end of the set are the same to ensure periodicity.

The waveform described by the set of discrete data points can be modeled by fitting a Fourier series to the data points. As the time period of the waveform is known by adding the time periods of each interval, the Fourier coefficients must be computed to determine the series and the analytical description of the waveform. This is achieved by the method proposed by Abuelma'atti [161], which requires no integration operations, no information about the derivatives of the function being approximated or sampled, and no limitations on the number of data points. The method is based on the determination of the Fourier coefficients in terms of the jumps of the sampled function and its derivatives and that the function is represented by polynomials. The set of n data points is divided into $n-1$ intervals and on each interval a first degree polynomial is defined between the two endpoints. The formulas for the Fourier coefficients are obtained from integration on each segment. This method can be used to compute the Fourier series without

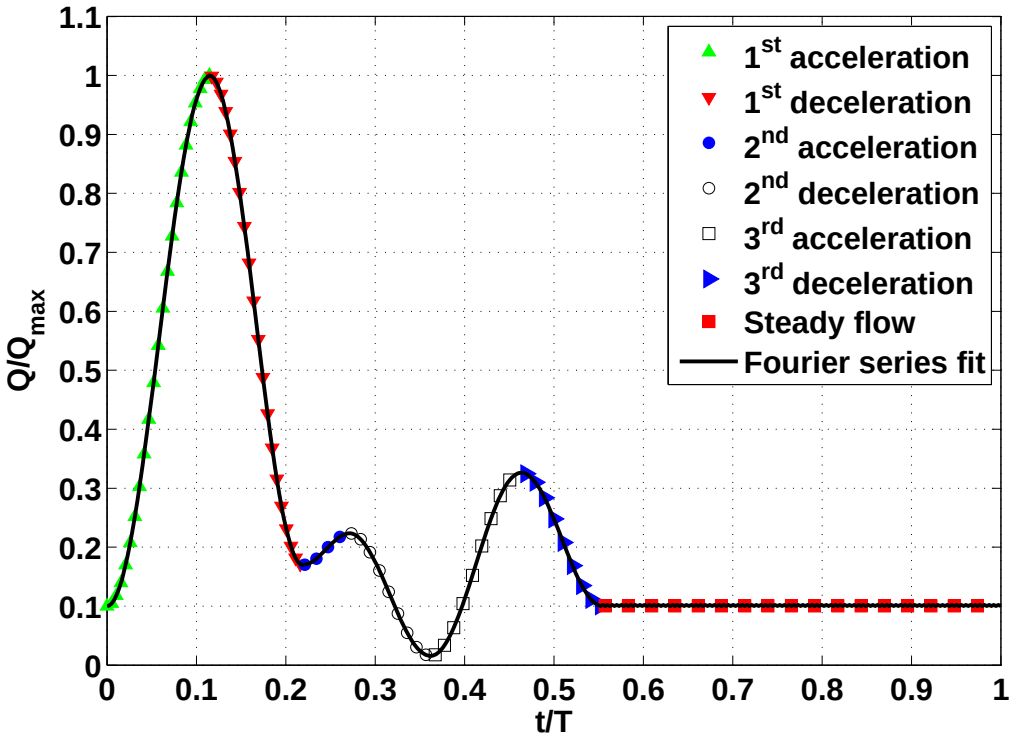

Figure 5.5. The common carotid flow rate waveform can be divided into intervals of accelerating, decelerating, and steady flow

limitations on the number of harmonics and to any desired level of accuracy [161].

The method described above is implemented in MATLAB 7.9 (MathWorks, Natick, MA) and the Fourier series representation for any arbitrary waveform defined by a set of discrete data points is obtained. In Figure 5.5, a ten harmonics Fourier series is fitted to the set of data points representing the generic waveform and an analytic expression for the waveform is obtained. Defining each phase of a waveform using $\Delta Q/Q_{\max}$ and T and then finding the analytical expression to describe the entire waveform by fitting a Fourier series to all the data points allows for systematic studies on waveform shape and their effect on the WSSR occurrence.

5.3.2 Determination of wall shear stress reversal

The generic waveforms resembling arterial blood flow waveforms can be systematically generated and defined by Fourier series as described above. These waveforms are then used with the analytical formulas derived from the Womersley solution [122] for flows with a known flow rate to compute the velocity profiles, pressure gradient, and WSS.

Flow reversal occurs during flow deceleration as the velocity in the vicinity of the wall is relatively small compared with the velocity in the center of the pipe while at the wall the velocity is zero due to the no-slip assumption. The near-wall velocity becomes negative and a small amount of flow reverses while the net flow remains positive. At the time instant when the velocity changes sign, the near wall velocity becomes zero. Therefore, the velocity gradient in the immediate vicinity of the wall is zero, resulting in zero WSS. Also, at the onset of reversed flow, an inflection point occurs in the velocity profile. The criteria for determining flow reversal occurrence can be set at the instant in time when WSS or $\tau_w \leq 0$. This means that finding the flow conditions for WSSR occurrence is equivalent to finding the zero of (4.17), which is a transcendental function requiring the use of numerical methods to find its zeros. The method proposed by Boyd [162] in which a function is represented by Chebyshev polynomials and evaluated at Chebyshev points on the canonical interval $[-1, 1]$ is used. This method is implemented in the `chebfun` function in MATLAB 7.9 and described in [163].

Generic waveforms with different $\Delta Q/Q_{\max}$ and T values are generated to investigate the effect of waveform properties on flow conditions for WSSR occurrence. Finding WSSR conditions for a waveform with known $\Delta Q/Q_{\max}$ during the deceleration phase is equivalent to finding the critical α_d, referred to as α_{dc}, that will

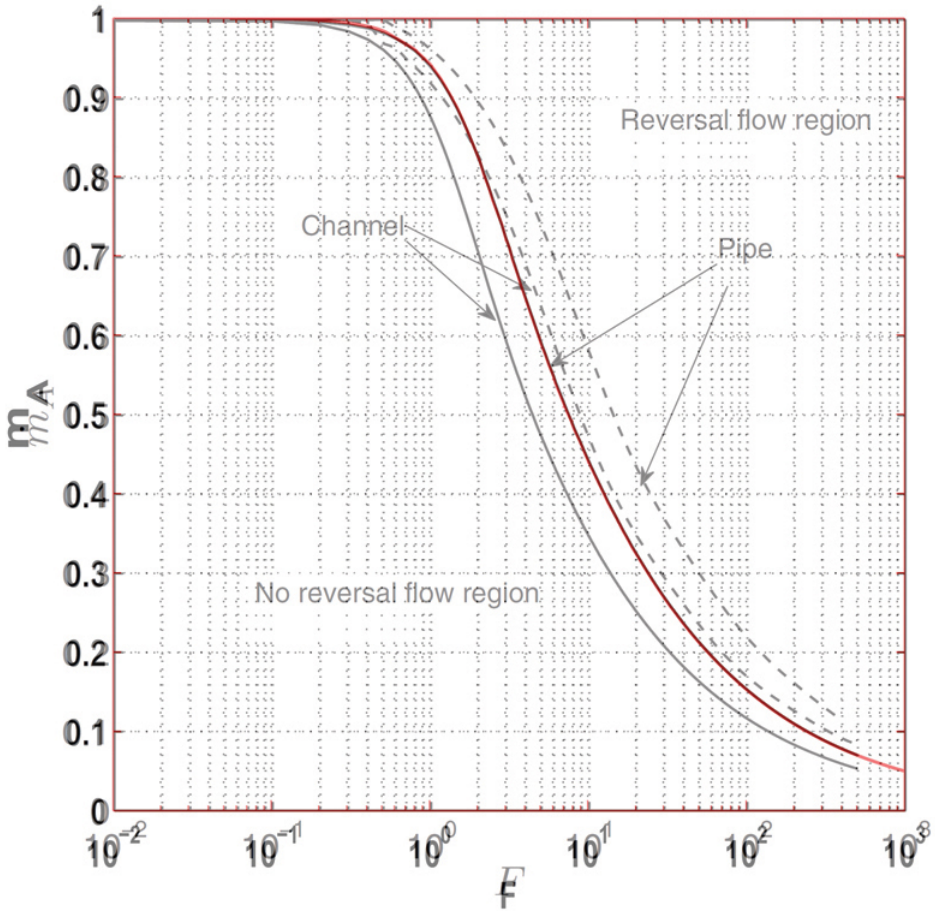

Figure 5.6. Comparison of critical F values computed for sinusoidal waveforms with data from [156]. The red plot represents data from current work

result in $\tau_w \leq 0$. An iterative process is started with an initial value for α_d and the zero of (4.17) is found inside a short time interval defined near the minimum flow value of the waveform's deceleration phase. If $\tau_w \leq 0$, then the value of α_{dc} is stored, if not, the value of α_d is incrementally increased until $\tau_w \leq 0$.

To validate the method described above, in Figure 5.6, the WSSR conditions for sinusoidal waveforms are compared against those determined in earlier work [155, 156]. The $\Delta Q/Q_{\max}$ and α_d are transformed into their $\dot{m}_A^*$ and F equivalents, respectively. Excellent agreement is found between the two curves of critical flow conditions for WSSR.

5.4 Flow reversal conditions for sinusoidal waveforms

The WSSR conditions, which, as mentioned earlier depend on the flow pulsatility and its amplitude, are first investigated for periodic flows defined by sinusoidal waveforms as shown in Figure 5.7a. The amplitude of the flow pulsation during the deceleration phase, as quantified by $\Delta Q/Q_{\max}$, is varied while the maximum flow rate, $Q_{\max}$, is kept constant. Waveforms are generated with $\Delta Q/Q_{\max}$ ranging from 0.02 to 0.99. For each value of $\Delta Q/Q_{\max}$ the corresponding critical deceleration Womersley number, α_{dc}, at which WSSR starts to occur is computed as described in section 5.3. The conditions for which WSSR occurs can be visualized by plotting α_{dc} against $\Delta Q/Q_{\max}$ as in Figure 5.7b. The region above the α_{dc} curve indicates flow conditions with increasing WSSR when moving away from the curve while the region below the curve indicates flow conditions with no WSSR. For $\Delta Q/Q_{\max} < 0.30$, α_{dc} values change rapidly as shown in Figure 5.7b in which the curve of α_{dc} values is plotted on a logarithmic scale. For $\Delta Q/Q_{\max} \geq 1.00$, WSSR is guaranteed as the net flow reverses ($Q_{\min}$ is negative). For flow waveforms with $\alpha_d > \alpha_{dc}$ the amount of WSSR increases while for $\alpha_d < \alpha_{dc}$ no WSSR occurs. As the pulsation amplitude decreases, much higher pulsation frequencies are required to generate WSSR, thus, resulting in higher α_{dc} as confirmed by earlier studies, which also investigated pulsatile flows driven by periodic, sinusoidal mass flow waveforms [155, 156]. As a reminder, for sinusoidal waveforms, $\alpha = \alpha_d$, but for waveforms other than simple sinusoids, the two parameters are different.

Next, the effect of the acceleration phase on wall flow reversal conditions is studied by varying the time period of the acceleration phase, T_1, with respect to

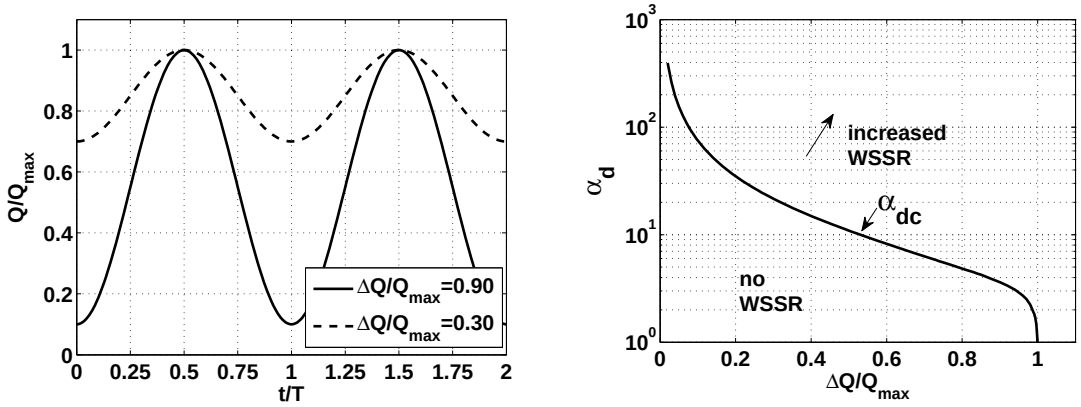

(a) (b)

Figure 5.7. Periodic sinusoidal flow waveforms (a) with different $\Delta Q/Q_{\max}$ values and wall shear stress reversal conditions (b) defined by the α_{dc} curve

the time period of the deceleration phase, T_2, as shown in Figure 5.8a for different $\Delta Q/Q_{\max}$values. The α_{dc} for waveforms with $T_1 < T_2$ does not differ significantly from the case of $T_1 = T_2$ for $\Delta Q/Q_{\max} > 0.2$ as illustrated in Figure 5.8b. Although the acceleration slope is increased when compared with the waveform with $T_1 = T_2$, there is only slight increase in α_{dc} as illustrated by the zoom-in picture shown in Figure 5.8b. An explanation for this insignificant increase might be the small inertia increase in the fluid layers near the wall while most of the inertia increase due to the higher acceleration rate occurs in the fluid near the center of the pipe. For sinusoidal flow waveforms with $T_1 > T_2$ and using the same T_1/T_2 ratios as before, the α_{dc} values do not differ significantly from the values for sinusoidal waveforms with $T_1 = T_2$ as well. Therefore, the difference between the acceleration and deceleration time periods for simple sinusoidal waveforms does not result in significant changes in α_{dc} values. A waveform with shorter acceleration time period results in slightly higher α_{dc} values for WSSR resulting in an upward shift of the critical curve corresponding to decreased WSSR while a waveform with longer acceleration time period results in slightly lower α_{dc} values.

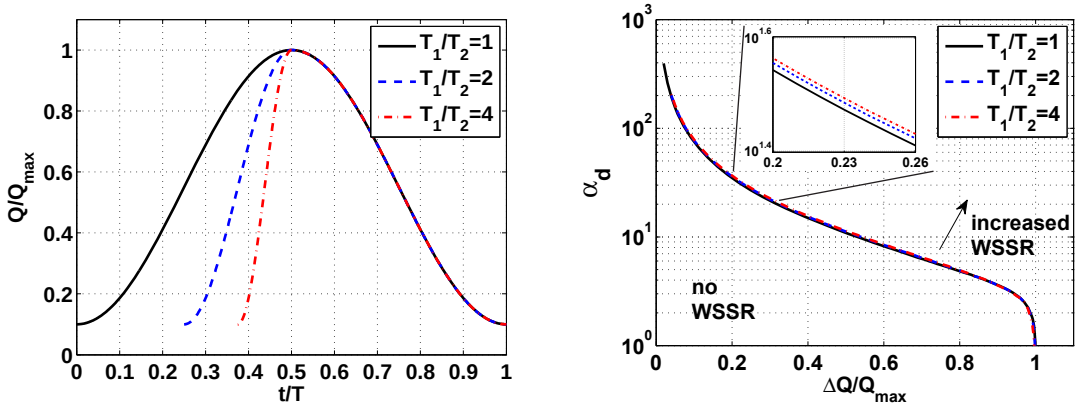

(a) (b)

Figure 5.8. Conditions for wall shear stress reversal (WSSR) are shown in (b) for asymmetric sinusoidal waveforms (a)

High pulsatility flows ($\alpha > 5$) exhibit velocity profiles that differ from the parabolic profile typical of steady flow as is the case with the periodic flows considered in this work. The effect of the velocity profile shape on WSSR conditions is investigated by generating waveforms with steady flow phases. This ensures that a parabolic velocity profile is established before the flow begins to accelerate or decelerate. Two types of waveforms are considered, as shown in Figure 5.9a, one with a sinusoidal flow acceleration and deceleration followed by steady flow phase and another one with a phase of steady minimum flow followed by a sinusoidal acceleration, then, a phase of steady maximum flow followed by a sinusoidal deceleration. The waveforms are defined with $\Delta Q/Q_{\max}$ values in the same range and with the same acceleration and deceleration time periods. The value of α_{dc}, when the flow waveform is accelerating from a steady minimum value and with $\Delta Q/Q_{\max} < 0.60$, is between 3% to 16% higher than the value of α_{dc} for the case of a sinusoidal flow waveform, thus, resulting in decreased WSSR as shown in Figure 5.9b. This means that a flow with a sinusoidal waveform can experience WSSR while a flow with a waveform that accelerates and then decelerates to a steady flow

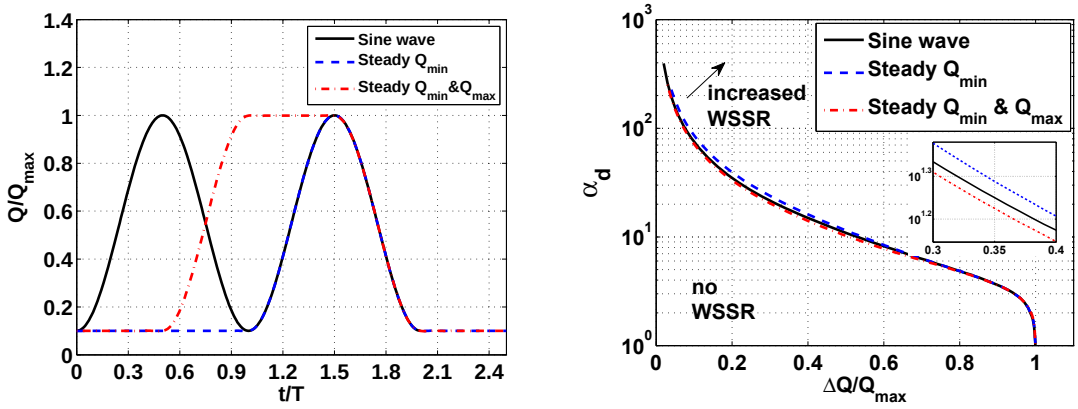

(a) (b)

Figure 5.9. Comparison of reversal conditions (b), between sinusoidal waveforms and waveforms with parabolic velocity profiles at the start of the acceleration and deceleration phases (a)

phase will not experience WSSR under similar flow conditions. If, on the other hand, the flow is allowed to attain a parabolic velocity profile during the phase of maximum flow and then decelerate to a phase of steady minimum, for waveforms with $\Delta Q/Q_{\max} < 0.70$, the value of α_{dc} is about 5% lower than the value of α_{dc} for sinusoidal waveforms. This means that a flow with the former type of waveform can experience WSSR while a flow with the latter waveform (sinusoidal) will not exhibit WSSR under similar flow conditions. The curves showing the critical values for WSSR occurrence under these types of flow waveforms are plotted in Figure 5.9b with a zoom-in window showing the difference—which becomes larger as $\Delta Q/Q_{\max}$ decreases—between α_{dc} for the three waveforms. Note that for waveforms with $\Delta Q/Q_{\max} > 0.70$, the effects of an initial parabolic velocity profile before flow acceleration or deceleration become negligible and the α_{dc} values are the same as the values for sinusoidal waveforms.

For flow waveforms with different pulsatility amplitudes during the acceleration and deceleration phases, as in cardiovascular flows, the WSSR conditions might

deviate from those for sinusoidal waves. To test such a hypothesis, flow waveforms with acceleration amplitude ratios, $\Delta Q/Q_{\max}|_1$, different than deceleration amplitude ratios, $\Delta Q/Q_{\max}|_2$, are generated. The flow following the initial deceleration phase is allowed to briefly accelerate and then to more slowly decelerate again and maintain a steady flow rate value such that the deceleration effects would decay before the next waveform cycle starts. This type of flow waveform, called the pulsatile post-deceleration waveform, is illustrated in Figure 5.10a along with a sinusoidal waveform of similar deceleration phase. The critical values, $\alpha_{dc}|_2$, for WSSR during the initial deceleration phase (considered the second interval of the waveform) are higher than α_{dc} values for sinusoidal flow waveforms with similar $\Delta Q/Q_{\max}|_2$ by as much as ten times when $\Delta Q/Q_{\max}|_1 = 0.90$ and $\Delta Q/Q_{\max}|_2 = 0.34$ but approach the α_{dc} values as $\Delta Q/Q_{\max}|_1 = \Delta Q/Q_{\max}|_2$. The relatively low amplitude change during the deceleration phase requires a higher pulsation frequency for WSSR to occur, thus, resulting in higher critical α_d values. The $\alpha_{dc}|_2$ curves for different values of $\Delta Q/Q_{\max}|_1$ are plotted against $\Delta Q/Q_{\max}|_2$ in Figure 5.10b. For waveforms with $0.20 < \Delta Q/Q_{\max}|_1 \leq 0.50$ and $\Delta Q/Q_{\max}|_2 \leq 0.70$, the $\alpha_{dc}|_2$ are lower than the α_{dc} values of the sinusoidal waveform as shown in the zoom-in window in Figure 5.10b. For waveforms with $\Delta Q/Q_{\max}|_1 > 0.50$ and $\Delta Q/Q_{\max}|_2 \leq 0.70$, the $\alpha_{dc}|_2$ are higher than the α_{dc} values for the sinusoidal waveform. Another important observation: waveforms with $\Delta Q/Q_{\max}|_2 > 0.70$ have $\alpha_{dc}|_2$ values similar with α_{dc} values for sinusoidal waveforms regardless of $\Delta Q/Q_{\max}|_1$.

The influence of a steady flow phase (instead of an acceleration phase) immediately following the initial deceleration is also investigated by constructing a steady post-deceleration flow waveform as illustrated in Figure 5.10a. The $\alpha_{dc}|_2$ values are similar to the values for the pulsatile post-deceleration waveforms; however, for $\Delta Q/Q_{\max}|_2 < 0.45$, there is a difference between the two critical values. This

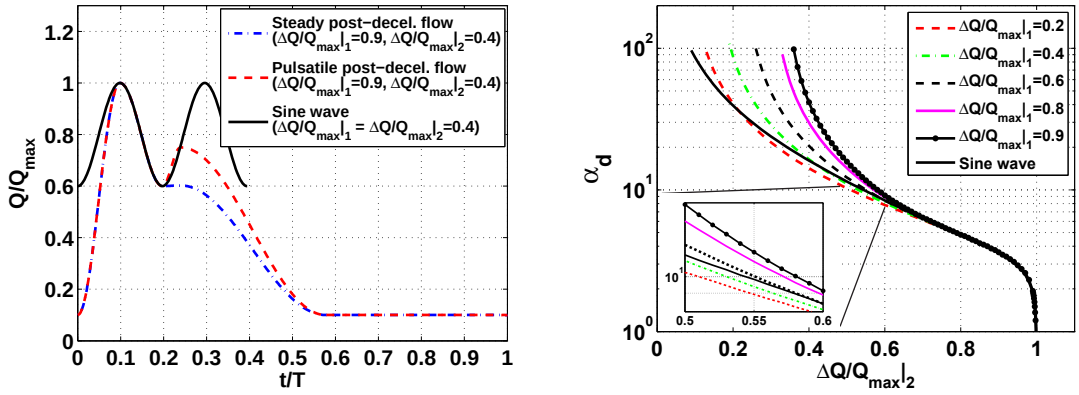

(a) **(b)**

Figure 5.10. Reversal at the end of the initial deceleration for waveforms with higher amplitudes during the acceleration than during deceleration is compared with reversal for sinusoidal waves

difference is dependent on the $\Delta Q/Q_{\max}|_1$ values and is most pronounced at the lower end of the $\Delta Q/Q_{\max}|_2$ range: a maximum of 10% for $\Delta Q/Q_{\max}|_1 = 0.20$ and $\Delta Q/Q_{\max}|_2 = 0.10$ while a maximum of 65% for $\Delta Q/Q_{\max}|_1 = 0.90$ and $\Delta Q/Q_{\max}|_2 = 0.35$. This difference quickly becomes negligible as $\Delta Q/Q_{\max}|_2$ increases for a fixed value of $\Delta Q/Q_{\max}|_1$. As the critical α_d values for these two types of waveforms are similar, only the $\alpha_{dc}|_2$ values for the pulsatile post-deceleration waveform are plotted in Figure 5.10b.

The waveforms considered so far resemble sinusoidal waves consisting of single acceleration and deceleration phases. The waveforms presented in Figure 5.10a, although consisting of multiple acceleration and deceleration phases, are used to investigate WSSR during the first deceleration phase and the other phases are used to ensure that the flow rate value at the end point of the waveform matches the value at the start point and that flow transients from the second deceleration phase are minimized. More complex waveforms are investigated in the next section.

5.5 Flow reversal conditions for complex waveforms

The typical blood flow waveform in major human arteries is characterized by increased flow during systole followed by a lower flow rate during diastole. The flow is unidirectional in relatively straight arterial segments and brief net flow reversal is observed in only few arteries such as the coronary, brachial, and femoral. This section is concerned only with flow waveforms that are typical of major systemic arteries such as cerebral arteries.

It is common practice in computational fluid dynamics studies on arterial blood flow to use archetypal flow waveforms that are available in the literature. As mentioned earlier, the volumetric flow rate can be divided into multiple intervals. In Figure 4.7, the first interval corresponds to the systolic acceleration phase, the second interval to the deceleration caused by the flow wave reflection from the upper body, the third interval to the small acceleration caused by the wave reflection from the lower body and the fourth interval to the deceleration caused by the closure of the aortic valve at the end of systole [1]. The fifth interval is the diastolic flow which is characterized by an acceleration phase and a small deceleration phase that is followed by another phase of nearly steady flow. The diastolic flow phase is not parameterized as the amplitude of the pulsation during this phase of flow is small and cannot result in wall flow reversal.

Generic waveforms are constructed with two acceleration and deceleration phases of interest and additional phases of relatively steady flow are added as well to account for the diastolic and pre-systolic flow. The phases are numbered starting with the acceleration, which is interval 1, the first deceleration, interval 2, second

acceleration due to wave reflections, interval 3, and second deceleration, interval 4. For these complex waveforms the WSSR conditions during the first deceleration phase (interval 2) are similar to the reversal conditions presented in the previous section on simple waveforms. This part of the study is focused on the occurrence of WSSR during the second deceleration phase, namely, interval 4 in Figure 4.7. As such, the effects of $\Delta Q/Q_{\max}|_1$, $\Delta Q/Q_{\max}|_2$, $\Delta Q/Q_{\max}|_3$, $\Delta Q/Q_{\max}|_4$, T_2, and T_4 on WSSR are quantified by finding $\alpha_{dc}|_4$, the critical α_d for WSSR during the second deceleration. All other parameters are kept constant. Examples of waveforms with different $\Delta Q/Q_{\max}|_1$ values are shown in Figure 5.11a. The value of $\Delta Q/Q_{\max}|_3$ is fixed at 0.06. For waveforms with relatively small $\Delta Q/Q_{\max}|_1$ and large $\Delta Q/Q_{\max}|_2$ and $\Delta Q/Q_{\max}|_4$, the minimum flow occurs at the end of the second deceleration phase. While this type of waveform is not representative of physiologic flows, it is useful for finding α_d for a wide range of waveform parameters. In Figure 5.11b waveforms with $\Delta Q/Q_{\max}|_1 = 0.90$ and $\Delta Q/Q_{\max}|_3 = 0.06$ and varying $\Delta Q/Q_{\max}|_2$ and $\Delta Q/Q_{\max}|_4$ are shown. Note that $\Delta Q/Q_{\max}$ is defined locally for each flow phase and, for example, two phases with the same $\Delta Q/Q_{\max}$ but defined by different flow magnitudes may look as having different $\Delta Q/Q_{\max}$ when plotted. Flow waveforms with $\Delta Q/Q_{\max}|_1 = 0.90$ and $\Delta Q/Q_{\max}|_2 = 0.60$ and varying $\Delta Q/Q_{\max}|_3$ and $\Delta Q/Q_{\max}|_4$ are shown in Figure 5.11c. Note how negative $\Delta Q/Q_{\max}|_3$ values result in flow deceleration occurring during the interval 3 of the waveform. For blood flow this interval usually corresponds to flow acceleration due to reflected waves; however, in some cases the reflected waves travel much slower and the flow does not accelerate but rather decelerates at a lower rate.

The WSSR conditions during the second deceleration phase are investigated for different values of $\Delta Q/Q_{\max}|_1$. The values of $\Delta Q/Q_{\max}|_2$ and $\Delta Q/Q_{\max}|_4$ are varied as well while the $\alpha_{dc}|_4$ values are computed for each combination of these

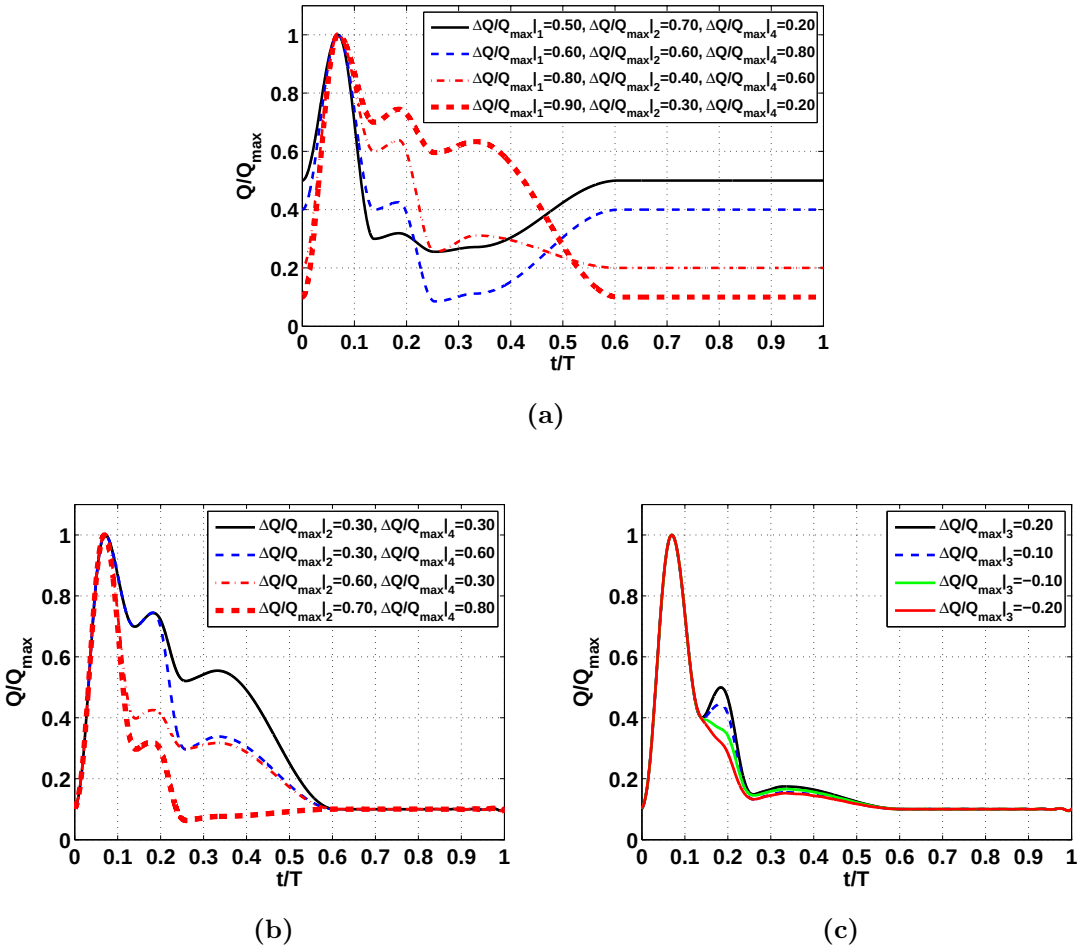

Figure 5.11. Flow waveforms used in the analysis of wall shear stress reversal conditions during the second deceleration phase

amplitude ratios. The values of $\Delta Q/Q_{\max}|_1$ vary from 0.50 to 0.90, the typical range found in physiologic waveforms. The results, represented by the plots of $\alpha_{dc}|_4$ against $\Delta Q/Q_{\max}|_4$ and shown in Figure 5.12, are compared against the α_{dc} values for the sinusoidal waveforms. For flow waveforms with $\Delta Q/Q_{\max}|_4 > 0.60$ the values of $\alpha_{dc}|_4$ and, consequently, WSSR do not depend on $\Delta Q/Q_{\max}|_1$ or on $\Delta Q/Q_{\max}|_2$ (Figure 5.12a) and are similar to α_{dc} values for sinusoidal waveforms. The results for $\Delta Q/Q_{\max}|_4 > 0.90$ are not plotted as they are similar to the results from sinusoidal waveforms. Also, as $\Delta Q/Q_{\max}|_2$ decreases, the effect of

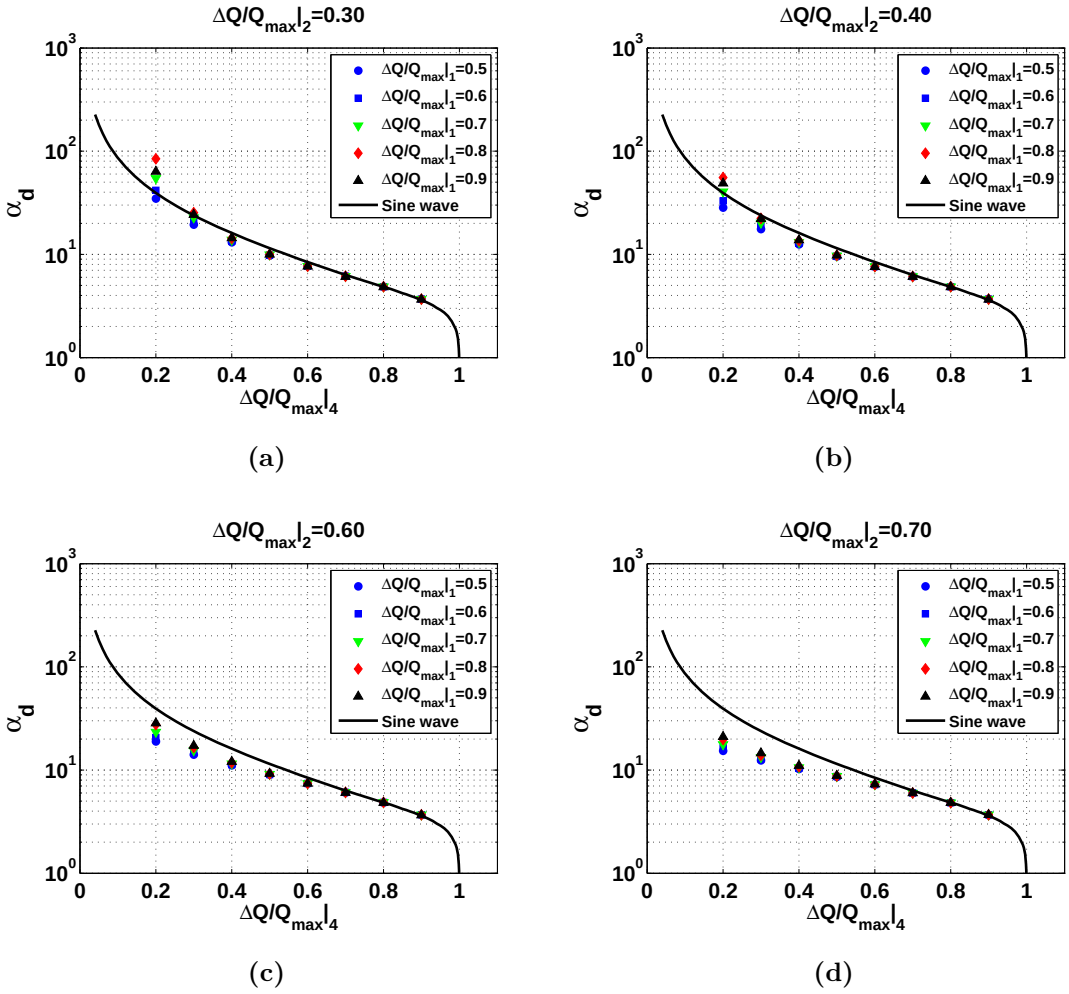

Figure 5.12. Critical values for wall shear stress reversal conditions during the second deceleration phase are the same for $\Delta Q/Q_{\max}|_4 > 0.60$ regardless of $\Delta Q/Q_{\max}|_1$

$\Delta Q/Q_{\max}|_1$ on $\alpha_{dc}|_4$ is more pronounced. For example, for $\Delta Q/Q_{\max}|_2 = 0.30$, the difference between $\Delta Q/Q_{\max}|_1 = 0.50$ and $\Delta Q/Q_{\max}|_1 = 0.90$ in the values of $\alpha_{dc}|_4$ is about 140% (Figure 5.12a). For $\Delta Q/Q_{\max}|_2 = 0.70$ and all the other parameters as before, this difference reduces to only 20% (Figure 5.12b). Under similar flow conditions, with no WSSR present for sinusoidal waveforms, for complex waveforms WSSR can occur during the second deceleration phase at lower α_{dc} if $\Delta Q/Q_{\max}|_2 > 0.50$ and $\Delta Q/Q_{\max}|_4 < 0.60$ regardless of $\Delta Q/Q_{\max}|_1$ values.

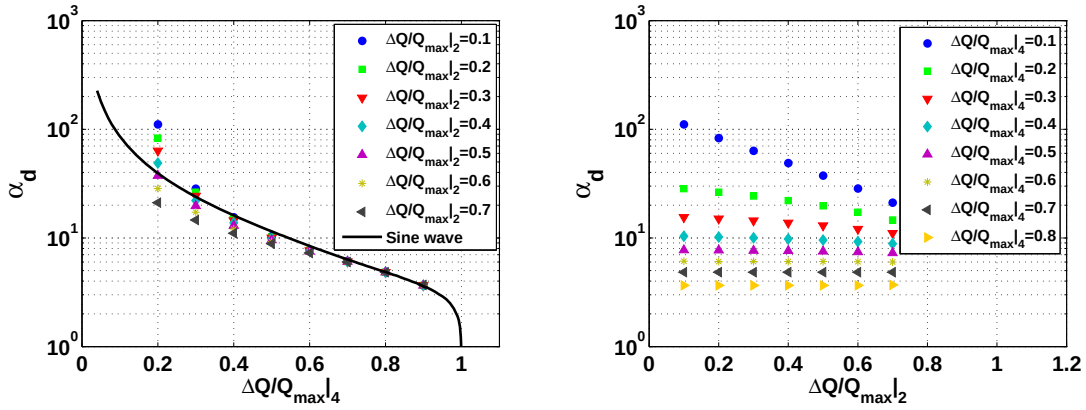

(a) **(b)**

Figure 5.13. Critical values for wall shear stress reversal (WSSR) conditions during the second deceleration phase do not depend on $\Delta Q/Q_{\max}|_2$ values if $\Delta Q/Q_{\max}|_4 > 0.5$

The effect of the pulsatility amplitude of the first deceleration phase (interval 2) on WSSR conditions during the second deceleration phase is investigated by varying $\Delta Q/Q_{\max}|_2$ and $\Delta Q/Q_{\max}|_4$, with $\Delta Q/Q_{\max}|_1 = 0.90$, $T_2 = T_4$, and keeping the other parameters constant. Examples of some of the flow waveforms used in the analysis are given in Figure 5.11b. The deceleration Womersley number for the second deceleration interval, α_d, is plotted against the pulsatility amplitude of the second deceleration interval, $\Delta Q/Q_{\max}|_4$, in Figure 5.13. The data points representing the critical $\alpha_{dc}|_4$ values are compared against α_{dc} values for sinusoidal waveforms. The $\alpha_{dc}|_4$ values and, therefore, WSSR conditions are the same regardless of $\Delta Q/Q_{\max}|_2$ values if $\Delta Q/Q_{\max}|_4 > 0.60$ (Figure 5.13b). Also, the $\alpha_{dc}|_4$ values for complex waveforms with $\Delta Q/Q_{\max}|_4 > 0.70$ are similar with α_{dc} values for the sinusoidal waveform. In Figure 5.13b the $\alpha_{dc}|_4$ is plotted against $\Delta Q/Q_{\max}|_2$ for different $\Delta Q/Q_{\max}|_4$ to show that for waveforms with $\Delta Q/Q_{\max}|_4 > 0.60$ the $\alpha_{dc}|_4$ do not depend on $\Delta Q/Q_{\max}|_2$, the change in flow amplitude during the first deceleration.

The amplitude of flow acceleration due to wave reflection (interval 3) is varied by changing $\Delta Q/Q_{\max}|_3$ from -0.20 to 0.20 to study the effect on WSSR during the second deceleration phase (interval 4). The choice of $\Delta Q/Q_{\max}|_3$ values is made with regard to typical values found in physiologic waveforms as discussed later in this section. Again, the reversal conditions are computed for different sets of $\Delta Q/Q_{\max}|_2$ and $\Delta Q/Q_{\max}|_4$ with $\Delta Q/Q_{\max}|_1$ being fixed at 0.90. Examples of some complex flow waveforms with $\Delta Q/Q_{\max}|_2 = 0.60$, $\Delta Q/Q_{\max}|_4 = 0.70$, and different $\Delta Q/Q_{\max}|_3$ values are shown in Figure 5.11c. The $\alpha_{dc}|_4$ for the second deceleration phase is independent of $\Delta Q/Q_{\max}|_3$ if $\Delta Q/Q_{\max}|_4 > 0.60$, as evident from the datasets plotted in Figure 5.14. However, there is an exception for waveforms with $\Delta Q/Q_{\max}|_2 \geq 0.70$ and negative values of $\Delta Q/Q_{\max}|_3$ as the $\alpha_{dc}|_4$ values decrease with decreasing $\Delta Q/Q_{\max}|_3$. For complex waveforms with $\Delta Q/Q_{\max}|_4 \leq 0.60$ the $\alpha_{dc}|_4$ increases with decreasing $\Delta Q/Q_{\max}|_3$ for positive values of $\Delta Q/Q_{\max}|_3$. Note that for waveforms with $\Delta Q/Q_{\max}|_4 > 0.70$ and any $\Delta Q/Q_{\max}|_2$ and $\Delta Q/Q_{\max}|_3$ values, the $\alpha_{dc}|_4$ is similar to α_{dc} for sinusoidal waveforms.

The results presented so far have assumed equal values for T_1, T_2, and T_4, the time periods for the acceleration, first deceleration, and the second deceleration phase, respectively. The effect of T_1 on WSSR was shown in the previous section on simple waveforms to be negligible. Therefore the time period, T_2 is allowed to vary with respect to the time period, T_4. Again, WSSR conditions are computed for flow waveforms with different values of $\Delta Q/Q_{\max}|_2$ and $\Delta Q/Q_{\max}|_4$ while keeping $\Delta Q/Q_{\max}|_1 = 0.90$. Another set of results is obtained by varying T_4 while T_2 is kept constant and keeping the same ratios of T_2/T_4 as before. As the values of $\alpha_{dc}|_4$ are similar between these two sets of results only the results from the first set are shown in Figure 5.15. In Figure 5.15a, 5.15b, and 5.15c, for waveforms with $T_2 < T_4$,

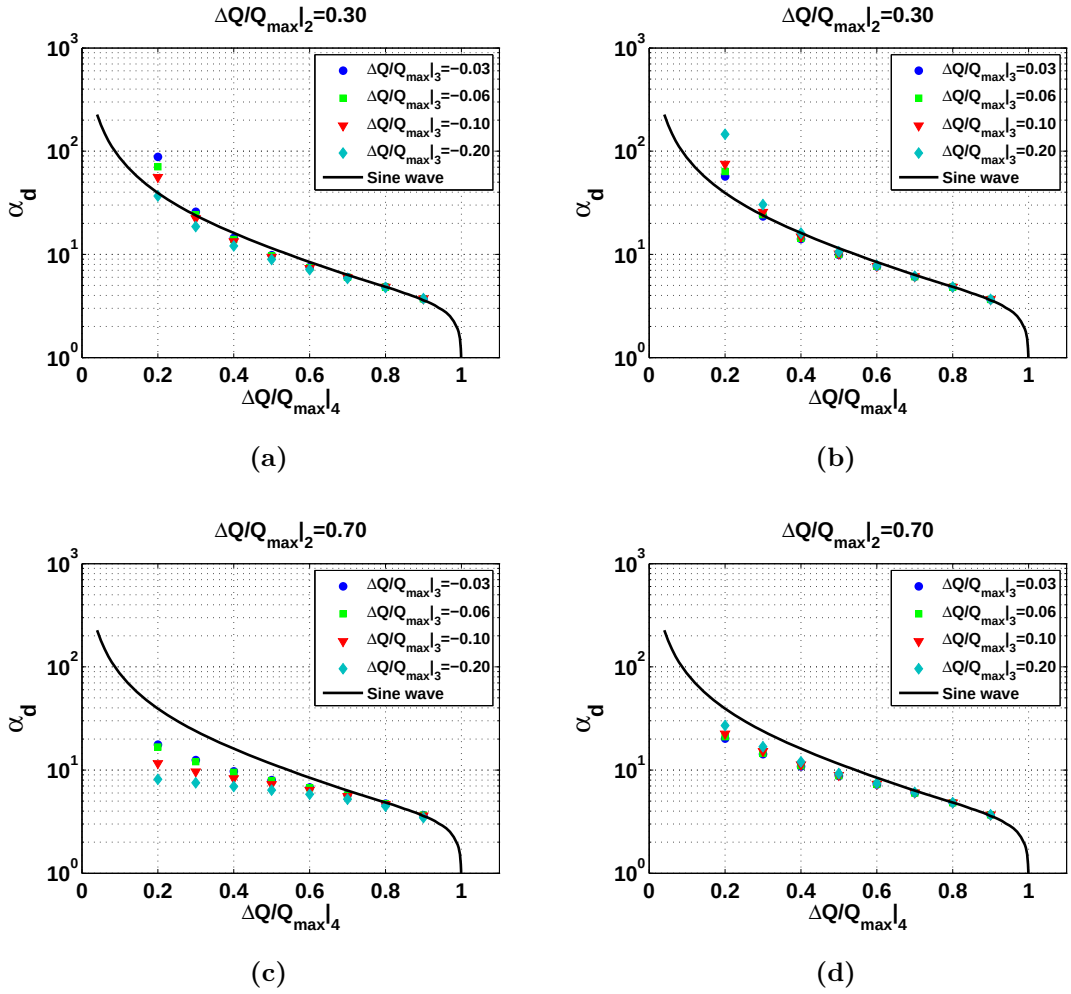

Figure 5.14. The critical deceleration Womersley number, $\alpha_{dc}|_4$, for waveforms with different $\Delta Q/Q_{\max}|_3$ values

and small values for $\Delta Q/Q_{\max}|_2$ and $\Delta Q/Q_{\max}|_4$ ($0.20 < \Delta Q/Q_{\max}|_2 < 0.60$ and $\Delta Q/Q_{\max}|_4 = 0.20$), the $\alpha_{dc}|_4$ values increase very rapidly (in the range of thousands) as $\Delta Q/Q_{\max}|_4$ decreases. Such huge flow variations in time are not physically possible and are relevant only from a theoretical perspective, hence they are omitted. For waveforms with $\Delta Q/Q_{\max}|_4 > 0.50$ the $\alpha_{dc}|_4$ values do not depend on $\Delta Q/Q_{\max}|_2$ and T_2 while waveforms with $\Delta Q/Q_{\max}|_4 > 0.60$ have similar WSSR conditions with those for sinusoidal waveforms. For complex wave-

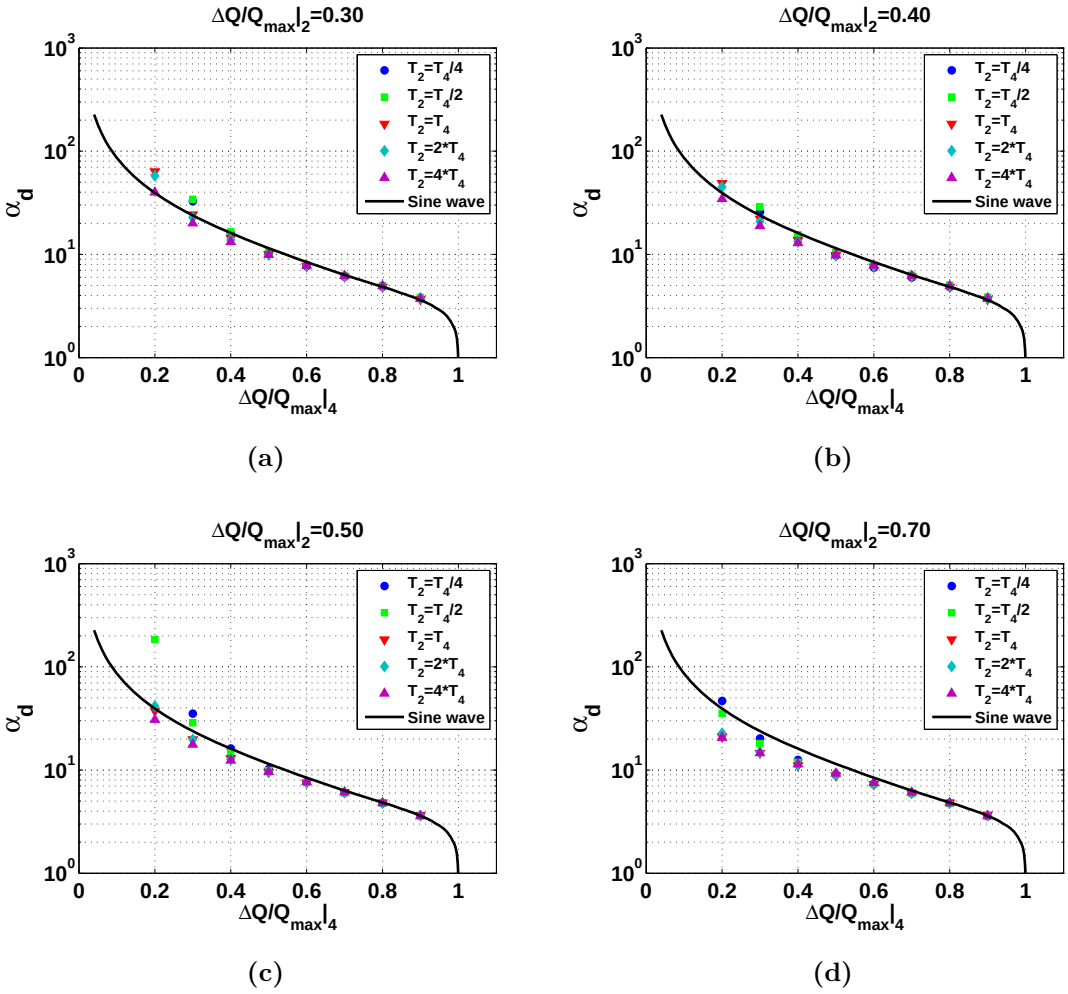

Figure 5.15. The critical deceleration Womersley number for different ratios of the first and second deceleration phase time periods

forms with $\Delta Q/Q_{\max}|_4 \leq 0.40$ the values of $\alpha_{dc}|_4$ increase significantly, especially when $\Delta Q/Q_{\max}|_2 < 0.30$ (c.f. Figure 5.15a). As an example, for waveforms with $\Delta Q/Q_{\max}|_2 = 0.50$, $\Delta Q/Q_{\max}|_4 = 0.20$ and $T_2 = T_4/2$ the $\alpha_{dc}|_4$ value is 50% higher than the value for waveforms with the same amplitude ratios but with $T_2 = 2T_4$.

In summary, the conditions at which WSSR occurs for sinusoidal and complex flow waveforms depend on the amplitude ratio and the time period of the flow deceleration phase. The effect of these waveform properties on WSSR, as quantified

by $\Delta Q/Q_{\max}$ and α_d, are summarized in Table 5.1. For simple flow waveforms with only one deceleration phase but with different acceleration and deceleration amplitudes the flow phase following the initial deceleration phase has an effect on WSSR and is therefore included in the table as well. For complex waveforms with two deceleration phases, the WSSR during the first deceleration phase occurs at similar $\alpha_{dc}|_2$ as for waveforms with one deceleration phase but with different acceleration and deceleration amplitude ratios (Figure 5.10). The conclusion that can be drawn from these results is that flow waveforms with two deceleration phases and with relatively low deceleration amplitude ratios have higher α_{dc} values and less tendency for WSSR than waveforms with one or two deceleration phases but with relatively high deceleration amplitude ratios. Also, for relatively high second deceleration phase amplitude ratios, $\Delta Q/Q_{\max}|_4 > 0.7$, the values of $\alpha_{dc}|_4$ are not affected by the waveform features and are similar to the values of α_{dc} for flows with sinusoidal waveforms.

The waveform characterization method and the results presented in this work are not restricted to waveforms constructed from sine waves and can be applied to real flow waveforms as well. Several volumetric flow waveforms typical of the human systemic arteries (common carotid artery—CCA, internal carotid artery—ICA, and vertebral artery—VA) and available in the literature are parameterized as described in chapter 4, section 4.4. The values of $\Delta Q/Q_{\max}|_i$ and T_i for each relevant flow phase as well as α for the waveform and $\alpha_d|_i$ for the deceleration phases are shown in Table 5.2, where D_i correspond to the amplitude ratios of the different flow phases, $\Delta Q/Q_{\max}|_i$. Typical amplitude ratio values for the systolic acceleration range from about 0.60 to 0.90, for the first and second deceleration vary from 0.20 to 0.90, while for the acceleration due to wave reflections vary from -0.06 to 0.2. The time periods of the deceleration intervals have similar values in

Table 5.1. Summary of results for $\alpha_{dc}|_2$ and $\alpha_{dc}|_4$. For $\Delta Q/Q_{\max}|_4$ greater than 0.70 $\alpha_{dc}|_4$ are similar to α_{dc} for sinusoidal waveforms

Waveform parameter	**First deceleration phase wall flow reversal**	**Second deceleration phase wall flow reversal**
$\Delta Q/Q_{\max}\|_1$	As $\Delta Q/Q_{\max}\|_1 > \Delta Q/Q_{\max}\|_2$ and $\Delta Q/Q_{\max}\|_2 < 0.70$, then $\alpha_{dc}\|_2$ increases	As $\Delta Q/Q_{\max}\|_1$ decreases and if $\Delta Q/Q_{\max}\|_4 < 0.50$, then $\alpha_{dc}\|_4$ increases
$\Delta Q/Q_{\max}\|_2$	As $\Delta Q/Q_{\max}\|_2$ increases, then $\alpha_{dc}\|_2$ decreases	As $\Delta Q/Q_{\max}\|_2$ decreases and if $\Delta Q/Q_{\max}\|_4 < 0.60$, then $\alpha_{dc}\|_4$ increases
$\Delta Q/Q_{\max}\|_3$	If $\Delta Q/Q_{\max}\|_3 = 0$, $\alpha_{dc}\|_2$ is higher than if $\Delta Q/Q_{\max}\|_3 > 0$	Increasing $\Delta Q/Q_{\max}\|_3$ and if $\Delta Q/Q_{\max}\|_4 < 0.60$, then $\alpha_{dc}\|_4$ decreases
$\Delta Q/Q_{\max}\|_4$	Not applicable	As $\Delta Q/Q_{\max}\|_4$ increases $\alpha_{dc}\|_4$ decreases
T_1	No effect	No effect
T_2	Defines $\alpha_{dc}\|_2$	If $T_2 < T_4$ and $\Delta Q/Q_{\max}\|_4 < 0.5$, then $\alpha_{dc}\|_4$ increases
T_3	Not applicable	No effect
T_4	Not applicable	Defines $\alpha_{dc}\|_4$

the rage of 0.10 s to 0.30 s. The corresponding $\alpha_d|_2$ and $\alpha_d|_4$ values for the first and second deceleration phase, respectively, are in the range from 4 to 12 with an assumed arterial radius of 3.3 mm for the common carotid, 2.5 mm for the internal carotid, and 1.7 mm for the vertebral artery [142, 164, 165]. The values of α, based on the fundamental harmonic and on the typical arterial radius, are also shown. Notice that the α_d values differ between the first and second deceleration phase and are, on average, almost two times greater than the α values. This supports the relevance of α_d rather than α in quantifying the local time rate of change of flow during the deceleration phase.

For each waveform, the condition for WSSR during the second deceleration phase, namely $\alpha_{dc}|_4$, can be found from the analytical solution to the laminar, pulsatile flow in circular pipes. These values of the actual $\alpha_{dc}|_4$ are compared in Table 5.2 with the estimated $\alpha_{dc}|_4$ values obtained from the plots presented

Table 5.2. Parameters for waveforms typical of systemic arteries. The values of $\alpha_d|_2$ and $\alpha_d|_4$, are based on T_2 and T_4 and on typical arterial radii

	D_1	D_2	D_3	D_4	T_2 (s)	T_4 (s)	α	$\alpha_d\|_2$	$\alpha_d\|_4$	Est. $\alpha_{dc}\|_4$	Actl. $\alpha_{dc}\|_4$
CCA[1]	0.86	0.54	0.06	0.66	0.16	0.12	4.2	12.1	10.5	6.5	6.0
CCA[2]	0.78	0.22	0.07	0.54	0.13	0.31	4.3	7.5	11.6	8.1	8.4
CCA[3]	0.90	0.83	0.24	0.93	0.16	0.14	5.0	11.2	10.5	3.2	3.0
CCA[4]	0.72	0.65	0.11	0.25	0.24	0.13	4.6	8.9	8.6	18.5	19.3
CCA[5]	0.90	0.70	0.20	0.72	0.22	0.21	4.2	9.2	8.9	6.0	5.6
CCA[6]	0.67	0.27	−0.06	0.29	0.15	0.23	4.4	8.7	10.8	18.6	11.0
ICA[7]	0.66	0.10	0.07	0.40	0.10	0.31	3.3	5.8	10.2	15.1	14.7
ICA[8]	0.58	0.28	0.03	0.23	0.19	0.19	3.4	7.4	7.4	26.5	26.3
ICA[9]	0.60	0.29	0.03	0.24	0.18	0.21	3.4	7.0	7.6	26.5	23.6
VA[9]	0.65	0.31	0.08	0.34	0.16	0.21	2.3	3.9	4.5	18.2	16.4

[1] Bharadvaj *et al.* [148] [2] Old adult—Hoi *et al.* [140]
[3] Holdsworth *et al.* [126] [4] Ku *et al.* [58] [5] Gwilliam *et al.* [139] [6] Marshall *et al.* [137]
[7] Old adult—Hoi *et al.* [140] [8] Young adult—Hoi *et al.* [140] [9] Ford *et al.* [138]

in Figures 5.7–5.15. While there is good agreement between the actual and estimated $\alpha_{dc}|_4$ values, the slight difference between them could be caused by the acceleration and deceleration slope or real flow waveforms being different than the slope of the sinusoidal wave used to model the archetypal flow waveforms. In the case of the common carotid waveform measured by Marshall *et al.* [137], the value of $\Delta Q/Q_{\max}|_4$, shown in Table 5.2, is debatable as the shape of the waveform makes it difficult to define the beginning of the second deceleration phase. A comparison between the $\alpha_d|_4$ and actual $\alpha_{dc}|_4$ values (computed with typical arterial radius values) indicates that some waveforms exhibit WSSR when $\alpha_d|_4 > \alpha_{dc}|_4$. This is the case for the common carotid artery waveforms from the studies of Bharadvaj *et al.* [148], Hoi *et al.* [140], Holdsworth *et al.* [126], and Gwilliam *et al.* [139]; however, while the average arterial diameter taken from published data and considered here results in WSSR, a patient-specific artery whose diameter might be smaller will not necessarily result in WSSR. This observation reinforces the need for using patient-specific data for both the arterial geometry and flow con-

ditions as many computational hemodynamics studies use archetypal waveforms with patient-specific arterial geometry.

The plots of α_{dc} curves can be used to indicate whether the combination of $\Delta Q/Q_{\max}$ and α_d values specific to a flow waveform will result in WSSR occurrence in a straight pipe. To illustrate this, data from real flow waveforms typical of the human carotid and vertebral arteries is compared in Figure 5.16 against the corresponding curves of $\alpha_{dc}|_4$ determined earlier from generic waveforms. As mentioned before, the region above the $\alpha_{dc}|_4$ curve indicates WSSR while the region below it no WSSR. The parameters describing the waveform ($\Delta Q/Q_{\max}|_i$ and T_i), which are measured for some published waveforms and shown in Table 5.2, are used to determine which $\alpha_{dc}|_4$ curve characterizes the critical conditions for WSSR occurrence for that particular waveform. Then, the waveform parameters that describe the second deceleration, $\Delta Q/Q_{\max}|_4$ and $\alpha_d|_4$, are compared against the critical values described by the $\alpha_{dc}|_4$ curve. To determine the value of $\alpha_d|_4$, the diameter of the artery for each waveform must be known. This is a difficult task as most of the studies on blood flow measurement include multiple measurements on groups of individuals and provide only an average value for the arterial diameter. Therefore, diameters typical of the carotid and vertebral artery which are available in literature are used to compute $\alpha_d|_4$. As an example, the combination of $\Delta Q/Q_{\max}|_4$ and $\alpha_d|_4$ for the waveform measured by Bharadvaj *et al.* [148] indicates that WSSR is present whereas for the waveform measured by Ku *et al.* [58] there is no WSSR (Figure 5.16a). It should be noted that by changing the diameter, the value of $\alpha_d|_4$, which is strongly influenced by it, will increase or decrease and so the data point will move across the curve of $\alpha_{dc}|_4$ from WSSR conditions to no WSSR conditions. Thus, if the flow waveform from Bharadvaj *et al.* [148] drives the flow in an artery with a diameter smaller than the critical value, then WSSR

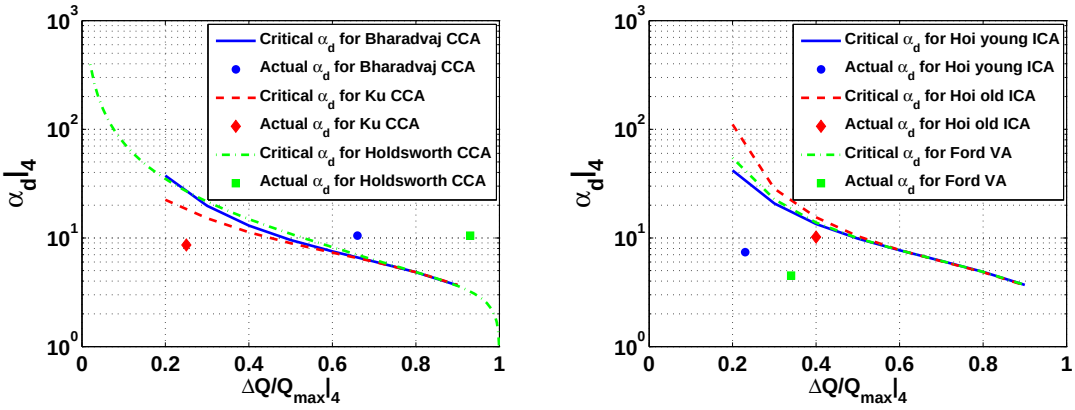

(a) (b)

Figure 5.16. Flow reversal as indicated by wall shear stress reversal regions for arterial flow waveforms. CCA—common carotid artery, ICA—internal carotid artery, VA—vertebral artery

is not present. Flow waveforms typical of the internal carotid and vertebral artery have lower pulsatility, therefore, lower $\Delta Q/Q_{\max}|_4$ for the deceleration phase, and do not exhibit WSSR as shown in Figure 5.16b.

Also worth investigating is the effect of the relatively brief acceleration phase (i.e., interval 3) in delaying WSSR occurrence for blood flow waveforms. The typical waveform contains a short phase of flow acceleration due to reflected waves that splits the systolic deceleration into two phases. Assuming two flow waveforms with identical peak flow magnitude and minimum flow magnitude but different deceleration phases (one with continuous deceleration, the other with split deceleration), the resulting WSS evolution in time can be compared to detect WSSR occurrence.

Two flow waveforms are constructed as shown in Figure 5.17a: one waveform with a continuous deceleration phase (type 1 waveform, Figure 5.17a) and another waveform with the deceleration interrupted by a small acceleration phase followed by a second deceleration phase (type 2 waveform, Figure 5.17a). The initial rate of flow deceleration for both waveforms is similar. The amplitude ratio of the

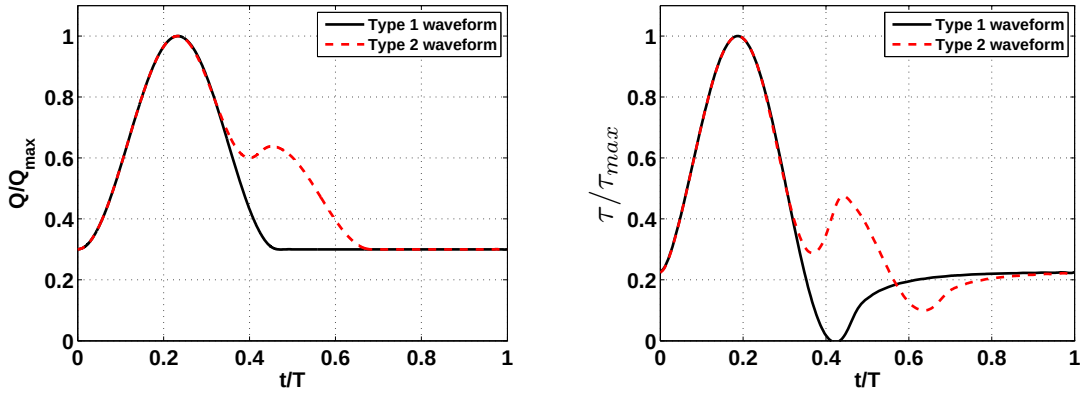

Figure 5.17. Flow reversal is not present if the deceleration is briefly interrupted by an interval of small flow acceleration

deceleration phases of type 2 waveform must be lower than the amplitude ratio of the deceleration phase from the type 1 waveform due to the requirement of similar minimum flow rates for both waveforms. The flow conditions are chosen such that type 1 waveform will experience WSSR. The same conditions are used for type 2 waveform and the WSS distribution in time is computed and compared with the one obtained from type 1 waveform.

It is evident from Figure 5.17b that the short acceleration phase results in WSS increase and prevents the occurrence of WSSR. As the amplitude ratio of the second deceleration phase of type 2 waveform is always smaller than the amplitude ratio of the deceleration phase of type 1 waveform, the corresponding α_{dc} value for type 2 waveform is smaller than the α_{dc} value for type 1 waveform, thus, ensuring that no WSSR occurs for type 2 waveform. If the brief acceleration phase occurs early in the deceleration, the amplitude ratio of the second deceleration for type 2 waveform will have to increase and, as its value approaches that of the amplitude ratio of type 1 waveform, the effect of the small acceleration phase in delaying WSSR will be minimal. If the brief acceleration phase occurs halfway through

the deceleration, no WSSR occurs for type 2 waveform under flow conditions that result in WSSR for the type 1.

Another factor that can influence the deceleration rate besides the amplitude ratio is the time period of deceleration. For type 2 waveform to exhibit WSSR and, hence, for α_d to approach the critical value, the deceleration time periods must be much shorter than the deceleration time periods for type 1 waveform. This becomes apparent by considering at the definition of either α or α_d in which the time period appears under the square root and, hence, has a weak influence on the values of α and α_d. However, for physiologic waveforms, the time periods of the deceleration phases and, thus, α_d have similar values as shown in Table 5.2. Therefore, assuming similar time periods for the deceleration phases of type 1 and type 2 waveforms is reasonable if modeling physiologic flow. In conclusion, for flow waveforms with parameters in the range of physiologic flows, the brief acceleration phase that occurs during deceleration, as exemplified by type 2 waveform, will not exhibit WSSR under flow conditions that result in WSSR for flow waveforms with continuous deceleration.

The analysis proposed in this work can be applied to predict or quantify the possibility of WSSR during the systolic deceleration for flow rate waveforms typical of the major systemic arteries. By identifying feature points along the waveform that indicate local maximum and minimum flow rates and splitting the waveform into intervals of acceleration and deceleration, the amplitude ratios, $\Delta Q/Q_{\max}$, and the time periods, T, of each interval can be obtained. Then, the value of α_d for the deceleration phase can be computed and if α_d is larger than α_{dc}, there exists the possibility of WSSR for that particular flow waveform and arterial radius as exemplified in Table 5.2 and in Figure 5.16.

Investigation of blood flow waveform chronic changes due to different factors

such as the level of physical activity or aging would be of interest and the method presented in this work has the potential to be used on such studies. Age related changes in arterial wall properties result in arterial stiffening which has a direct impact on the blood pressure and flow waveforms [1]. The most common effects associated with the aging of systemic arteries are decreased systolic and diastolic blood flow and increased pressure pulse velocity as well as wave reflections. As a consequence, the waveform shapes appear flattened when compared with waveforms typical of young adults [1, 166]. Because the wave reflections travel much faster in stiff arteries, the small acceleration phase (interval 3 in Figure 4.7), which is due to reflected waves, occurs much earlier following the peak systolic flow. In terms of the parameters used to characterize the flow waveforms, blood flow waveform changes due to aging can be described by a decrease in the acceleration amplitude ratio, $\Delta Q/Q_{\max}|_1$, as well as $\Delta Q/Q_{\max}|_2$ and an increase of $\Delta Q/Q_{\max}|_4$. This contrasts with the typical flow waveform shape for young adults which is illustrated in the waveform measured by Holdsworth *et al.* [126] and presented in Figure 4.7. The carotid flow measurements by Hoi *et al.* [140] show that old adult waveforms tend to have a faster flow deceleration phase than young adult waveforms suggesting that in the former case there is a greater chance of WSSR. This is also apparent from the critical values, $\alpha_{dc}|_4$, presented in Table 5.2, which, for the old adult internal carotid artery waveform are much lower than those for the young adult waveform. Azhim *et al.* [166] measured blood velocity waveforms in common carotids of young and old adults, active and sedentary, and found that with age, for sedentary adults, the waveform flattens but the second deceleration is not faster than that of the young adult waveform suggesting that the old adult waveforms are not more susceptible to WSSR than the waveforms typical of young adults. These contradictory findings warrant the need for dedicated studies to in-

vestigate aging effects on the shape of flow waveforms in the systemic arteries as no clear conclusion can be drawn at the moment on whether the waveform typical of old arteries is more prone to WSSR than the waveform specific to young arteries.

The analysis of physiologic flows presented in this work is limited by several assumptions and factors. The shape of the acceleration and deceleration curves in a real flow waveform might not resemble the sinusoidal curves used to build generic waveforms and this can have an impact on the value of α_{dc} as the deceleration rate would be different. Also, the variability of the physiologic waveform between cardiac cycles can have an effect on wall flow reversal as one waveform period might indicate conditions favorable for wall flow reversal while another waveform period might not. The physiologic flow waveform is assumed to be an accurate representation of the flow rate change in time. However, the accuracy of the *in vivo* arterial blood flow rate measurement is still debatable as discussed in chapter 4, section 4.2. Improvements in velocity profile measurements are expected to provide more accurate descriptions of the blood flow rate waveforms in the future [133, 144, 167].

The assumptions used in deriving the Womersley solution to the pulsatile flow problem include straight pipe with rigid wall, no taper, and Newtonian fluid. The Newtonian fluid behavior of blood in the large systemic arteries is accepted as an adequate assumption with no significant effects on the results of blood flow simulations [2]. The flow obtained from the Womersley solution for a given time-varying flow rate has been compared with the flow obtained from a numerical model which accounts for arterial tapering and compliant vessel wall [157]. The results show that the rigid, non tapered vessel assumption specific to the Womersley solution tends to overestimate the WSS by 2–7% when compared with the solution obtained with a compliant wall model or with a tapered vessel model. These findings

indicate that the α_{dc} values might be lower for arteries with highly compliant walls such as the aorta but for systemic arteries the compliance rate is much lower and the effects are negligible [2].

5.6 Summary

The properties of the flow waveform can induce wall flow reversal and consequently WSSR that might have deleterious effects on the arterial wall and initiate arterial disease. The occurrence of WSSR for different types of flow rate waveforms such as simple sinusoids with one deceleration phase or more complex waveforms with multiple deceleration phases can be predicted by using the analysis and the results described in this chapter. The analysis has the potential to predict WSSR for physiologic flow waveforms found in the systemic arteries of the cardiovascular system.

A new set of parameters consisting of the flow deceleration amplitude ratio, $\Delta Q/Q_{\max}$, and the Womersley deceleration number, α_d, is proposed to describe WSSR for periodic, pulsatile flow waveforms inside a rigid, circular pipe. For sinusoidal flow waveforms, the reversal conditions are in agreement with previous findings while for complex waveforms that resemble the blood flow typical of the systemic arteries the results presented in this work are new. Waveforms with an amplitude ratio of the acceleration phase greater than the deceleration one have a higher α_{dc} value than waveforms with equal acceleration and deceleration amplitudes. The WSSR conditions for complex waveforms are affected by the amplitude ratios of the flow acceleration and deceleration phases while the time periods of these phases have a lesser effect. For complex waveforms with deceleration amplitude ratios, $\Delta Q/Q_{\max}$, greater than 0.7, the α_{dc} values are similar to those found

for sinusoidal waveforms. The method of characterizing flow waveforms and quantifying the waveform features that lead to WSSR can be applied to the analysis of blood flow waveforms of the systemic arteries to predict which waveforms induce potential blood flow reversal at the arterial wall.

Chapter 6

Conclusions

Computational hemodynamics (CHD) represents a powerful tool for investigating the cardiovascular system and the role of vascular flow conditions in the development of diseases such as atherosclerosis or in-stent restenosis and thrombosis. Accurate geometric representations of patient-specific vascular districts and acquisition of blood flow data (e.g., flow rate, velocity) combined with CHD simulations can potentially be used as a virtual test-bed for non-invasive evaluation of cardiovascular function and blood flow in particular vascular districts and investigation of different vascular treatment options. In this work, the influence of realistic stent geometry, stent-wall interaction, and time-dependent flow conditions on arterial flow are investigated by employing CHD simulations.

Advancements in clinical imaging modalities such as x-ray, magnetic resonance imaging (MRI) and ultrasound (US) have made feasible the use of representations of real vascular districts in CHD studies. In this work stent reconstructions by different computed tomography (CT) techniques are evaluated to assess stent deployment characteristics and possible use of real deployed stent imaging in CHD studies on flow in stented arteries. High-resolution microCT reconstructions of real intracranial and coronary stents deployed in graft tubes are used to investigate the impact of non-uniform stent deployment on the flow. In the second part of this work, the influence of time-dependent arterial flow conditions on the possibility of wall flow reversal and oscillatory wall shear stress (WSS) occurrence in straight cylindrical tubes are investigated. The main results as well as an overview

of possible future directions are discussed in the following sections.

6.1 Stent imaging

The impact of the spatial resolution of current clinical CT angiography on the quality of three-dimensional stent reconstructions is evaluated in this work by imaging a Cypher stent deployed in a straight polytetrafluoroethylene (PTFE) graft tube. The stent reconstructions obtained with 64-slice multi-detector CT (MS-CT), C-arm CT, and flat panel CT (FP-CT) are compared with high-resolution stent reconstruction by high-resolution pre-clinical microCT. Due to spatial resolution limitations MS-CT, C-arm CT, and FP-CT images may introduce false gaps in stent struts and incorrectly remove real strut gaps by merging adjacent strut vertices. Quality of stent visualization using MS-CT appears significantly inferior to C-arm CT and FP-CT. Overestimation of stent thickness hampers stent lumen visibility and early detection of in-stent restenosis. Stent geometry reconstructions obtained from MS-CT, C-arm CT, and FP-CT at current spatial resolutions cannot be used for accurate CHD studies due to imaging artifacts that greatly compromise the reconstruction of small stent structures.

Visualization by microCT of intracranial stents (Neuroform 3 (NF3), Enterprise, and Pharos) and coronary stents (Taxus, BxVelocity) deployed in straight graft tubes and in a short canine femoral artery segment (NF3) can accurately reveal non-uniform deployment characteristics and stent-wall interaction. Open-cell design stents such as the NF3, Pharos, and Taxus are prone to strut vertex misalignment, strut prolapse into the lument, non-uniform strut orientation, and non-uniform vertex gaps. Closed-cell design stents such as the Enterprise and BxVelocity show fewer non-uniformities than open-cell design stents—the BxVe-

locity used in this work shows a row of under-deployed stent cells. Wall prolapse at stent cell centers and strut impingement on the wall are present in open-cell design stents especially with the NF3 deployed *ex vivo* inside a canine artery segment. This work demonstrates the potential of microCT imaging to capture minute stent deployment details and stent-wall interaction which are essential for accurate CHD simulations.

6.2 Flow in stented vessels

Datasets of real deployed stents in which both the stent and the wall geometries are captured by high-resolution microCT and employed for the first time in CHD studies. Steady flow simulations for thin strut intracranial stents (NF3, Enterprise) show that no recirculation zones or WSS reversal occur for the Enterprise. In the case of the NF3 stent small reversal zones are generated by strut vertex misalignment and vertex gaps. Significant reversal zones are found near the stent markers due to their large dimension. The flow recirculation regions for the NF3 do not significantly increase as the Reynolds (Re) number increases by an order of magnitude. Flow simulations based on the NF3 stent reconstructions from C-arm CT scans reveal large differences in flow patterns as illustrated by the WSS distribution and magnitude when compared with flow results obtained from microCT reconstructions of the identical stent. Strut size overestimation, wall roughness, and the inability to reconstruct stent markers are some of the direct effects of the resolution limitations associated with C-arm CT imaging. Strut vertex gaps are fused and strut prolapse into the lumen is not captured resulting in the occurrence of high WSS in these regions which are typically subjected to low WSS as indicated by CHD simulations based on the NF3 microCT reconstruction. Stent and wall

surface reconstructions obtained from C-arm CT scans and used in CHD simulations yield erroneous flow results due to significant geometric non-uniformities and strut oversizing and cannot be used to study in-stent hemodynamics.

In the case of coronary stents (Taxus, BxVelocity) the low WSS and flow recirculation regions are larger than in the case of intracranial stents due to thicker struts. These regions occur downstream of struts oriented at high angles with respect to the flow direction, struts vertex gaps, and ribbon-like connectors. Small wall creases formed at the downstream side of strut vertices due to strut impingement are characterized by flow recirculation as well. Also, these flow recirculation regions increase as the Reynolds number increases. The WSS is non-uniform inside stent cells with lower magnitude near the struts and strut vertices and higher magnitude in the center.

Unsteady flow simulations, which included two physiological waveforms characteristic of human common carotid arteries, show that the WSS distribution remains unchanged throughout the cardiac cycle—for both intracranial and coronary stents—with the exception of a brief flow reversal moment occurring during the deceleration phase of the Holdsworth waveform. During the phase of flow reversal near the wall, the WSS distribution inside stent cells is uniform with low WSS magnitude along the stent struts near the wall.

This work demonstrates an enhanced capability for evaluating in great detail the hemodynamic consequences of specific stent designs and may become a means for directly comparing their effects in a realistically deployed state on a patient-specific basis. Key features that can potentially impact restenosis, such as significantly modified WSS patterns and the development of reversed blood flow zones can be predicted in detail. These methods should be of great value when comparing stent hemodynamic performance and for the development and

evaluation of new, more effective stent designs.

6.3 Flow waveform characterization and reversal conditions

Transient flow effects due to variations of blood flow throughout the cardiac cycle play an important role in cardiovascular physiology. The properties of the flow waveform, especially during deceleration phases, can induce wall flow reversal and consequently WSS reversal which might stimulate deleterious effects on the endothelium. In this work, the arterial volumetric flow waveform is divided into intervals and parameterized by the properties of each interval—the amplitude change and the time period.

A new set of parameters consisting of the Womersley deceleration number, α_d, and the amplitude ratio, $\Delta Q/Q_{\max}$, is proposed to describe the conditions under which periodic, pulsatile flow rate waveforms exhibit wall flow reversal. Waveforms with an amplitude ratio of the acceleration phase greater than the deceleration one have a higher critical α_d value than waveforms with equal acceleration and deceleration amplitudes. The reversal conditions for complex waveforms that resemble physiological flow are affected by the amplitude ratios of the flow acceleration and deceleration phases while the time periods of these phases have a lesser effect. For flow waveforms with deceleration amplitude ratios, $\Delta Q/Q_{\max}$, greater than 0.7, the critical α_d values are similar to those found for sinusoidal waveforms. The method presented in this work can be applied to the analysis of blood flow waveforms of the systemic arteries to predict which waveforms induce blood flow reversal near the arterial wall.

6.4 Future work

The potential offered by CHD simulations when combined with realistic, patient-specific vascular geometry and flow conditions is significant. As this work has shown, high-resolution reconstructions of deployed stents by microCT imaging provide detailed deployment characteristics such as strut prolapse, vertex misalignment, and wall creases. Spatial resolution limits of current clinical CT technologies do not allow the accurate visualization and reconstruction of such features yet. It is possible that in the future, improvements in spatial and temporal resolutions combined with better CT reconstruction algorithms will allow for accurate *in vivo* stent imaging and reconstruction which could be used with CHD simulations to provide post-stenting evaluation of blood flow changes due to stent implants. Improvements in microCT technology could also allow for imaging of larger arterial specimens that include curvature, bifurcations, or aneurysms.

The complex interaction between blood flow and the arterial wall cannot be modeled at once and many assumptions and simplification are used in current blood flow models in order to obtain initial results that capture essential flow features. As blood flow models become more complex, additional aspects of arterial blood flow can be added to CHD simulations such as wall compliance, mass transport to the wall, non-Newtonian behavior, etc. Investigation of various stent designs in different deployment configurations and their impact on the flow could be investigated through combined microCT imaging and CHD simulations as this method is capable of capturing accurate images of real stents without relying on virtual stent deployment which cannot guarantee accurate modeling of non-uniform deployment and anomalies.

Wall flow reversal (or wall shear stress reversal) conditions for flow waveforms

have been investigated in this work for flows in straight, cylindrical pipes. It would also be of interest to investigate reversal conditions for flows in curved pipes by analyzing the axial-component velocity profile. For time-dependent flows in curved pipes with finite curvature there is no analytical flow solution and either experimental or numerical methods must be employed to find flow reversal conditions. Also, the flow conditions will depend, besides $\Delta Q/Q_{\max}$ and α_d, on two more non-dimensional parameters: the curvature ratio, $\delta = a/R$, where a is the pipe radius and R is the curvature radius, and the Dean number, $D = 2\mathrm{Re}\sqrt{\delta}$. Parametric flow waveforms can potentially be used in *in vitro* studies on endothelial cell function and response to changing flow conditions to better understand which flow transients have deleterious effects.

Bibliography

[1] Nichols, W.W. and O'Rourke, M.F., 2005, *McDonald's Blood Flow in Arteries: Theoretical, Experimental and Clinical Principles*, Oxford University Press, New York.

[2] Pedley, T.J., 2003, "Mathematical Modelling of Arterial Fluid Dynamics," Journal of Engineering Mathematics, **47**(3–4), pp. 419–444.

[3] Ku, D., 1997, "Blood Flow in Arteries," Annual Reviews of Fluid Mechanics, **29**, pp. 399–434.

[4] Zhang, J.F., Johnson, P.C., and Popel, A.S., 2009, "Effects of Erythrocyte Deformability and Aggregation on the Cell Free Layer and Apparent Viscosity of Microscopic Blood Flows," Microvascular Research, **77**(3), pp. 265–272.

[5] Lasheras, J.C., 2007, "The Biomechanics of Arterial Aneurysms," Annual Review of Fluid Mechanics, **39**, pp. 293–319.

[6] Kamiya, A. and Togawa, T., 1980, "Adaptive Regulation of Wall Shear Stress to Flow Change in the Canine Carotid Artery," American Journal of Physiology, **239**(1), pp. H14–H21.

[7] Langille, B.L. and Odonnell, F., 1986, "Reductions in Arterial Diameter Produced by Chronic Decreases in Blood Flow Are Endothelium Dependent," Science, **231**(4736), pp. 405–407.

[8] Zarins, C.K., Zatina, M.A., Giddens, D.P., Ku, D.N., and Glagov, S., 1987,

"Shear Stress Regulation of Artery Lumen Diameter in Experimental Atherogenesis," Journal of Vascular Surgery, **5**(3), pp. 413–420.

[9] Girerd, X., London, G., Boutouyrie, P., Mourad, J.J., Safar, M., and Laurent, S., 1996, "Remodeling of the Radial Artery in Response to a Chronic Increase in Shear Stress," Hypertension, **27**(3), pp. 799–803.

[10] Malek, A.M., Alper, S.L., and Izumo, S., 1999, "Hemodynamic Shear Stress and Its Role in Atherosclerosis," JAMA—Journal of the American Medical Association, **282**(21), pp. 2035–2042.

[11] Davies, P.F., 1995, "Flow-Mediated Endothelial Mechanotrasduction," Physiological Reviews, **75**(3), pp. 519–560.

[12] Chiu, J.J. and Chien, S., 2011, "Effects of Disturbed Flow on Vascular Endothelium: Pathophysiological Basis and Clinical Perspectives," Physiological Reviews, **91**(1), pp. 327–387.

[13] Nerem, R.M., Levesque, M.J., and Cornhill, J.F., 1981, "Vascular Endothelial Morphology as an Indicator of the Pattern of Blood Flow," Journal of Biomechanical Engineering—Transactions of the ASME, **103**(3), pp. 172–176.

[14] Dewey, C.F., Bussolari, S.R., Gimbrone, M.A., and Davies, P.F., 1981, "The Dynamic Response of Vascular Endothelial Cells to Fluid Shear Stress," Journal of Biomechanical Engineering—Transactions of the ASME, **103**(3), pp. 177–185.

[15] Davies, P.F., 2009, "Hemodynamic Shear Stress and the Endothelium in Cardiovascular Pathophysiology," Nature Clinical Practice Cardiovascular Medicine, **6**(1), pp. 16–26.

[16] Fry, D.L., 1968, "Acute Vascular Endothelial Changes Associated with Increased Blood Velocity Gradients," Circulation Research, **22**(2), pp. 165–197.

[17] Caro, C.G., Fitzgerald, J.M., and Schroter, R.C., 1971, "Atheroma and Arterial Wall Shear: Observations, Correlation and Proposal of a Shear Dependent Mass Transfer Mechanism for Ahterogenesis," Proceedings of the Royal Society, **B117**, pp. 109–159.

[18] Ku, D.N., Giddens, D.P., Zarins, C.K., and Glagov, S., 1985, "Pulsatile Flow and Atherosclerosis in the Human Carotid Bifurcation—Positive Correlation between Plaque Location and Low and Oscillating Shear Stress," Arteriosclerosis, **5**(3), pp. 293–302.

[19] Libby, P., 2002, "Atherosclerosis: The New View," Scientific American, **286**(5), pp. 47–55.

[20] Dai, G.H., Kaazempur-Mofrad, M.R., Natarajan, S., Zhang, Y.Z., Vaughn, S., Blackman, B.R., Kamm, R.D., Garcia-Cardena, G., and Gimbrone, M.A., 2004, "Distinct Endothelial Phenotypes Evoked by Arterial Waveforms Derived from Atherosclerosis-Susceptible and -Resistant Regions of Human Vasculature," Proceedings of the National Academy of Sciences of the United States of America, **101**(41), pp. 14871–14876.

[21] Thijssen, D.H.J., Dawson, E.A., Tinken, T.M., Cable, N.T., and Green, D.J., 2009, "Retrograde Flow and Shear Rate Acutely Impair Endothelial Function in Humans," Hypertension, **53**(6), pp. 986–992.

[22] Eberth, J.F., Popovic, N., Gresham, V.C., Wilson, E., and Humphrey, J.D., 2010, "Time Course of Carotid Artery Growth and Remodeling in Response

to Altered Pulsatility," American Journal of Physiology—Heart and Circulatory Physiology, **299**(6), pp. H1875–H1883.

[23] Nigro, P., Abe, J.I., and Berk, B.C., 2011, "Flow Shear Stress and Atherosclerosis: A Matter of Site Specificity," Antioxidants and Redox Signaling, **15**(5), pp. 1405–1414.

[24] Samady, H., Eshtehardi, P., McDaniel, M.C., Suo, J., Dhawan, S.S., Maynard, C., Timmins, L.H., Quyyumi, A.A., and Giddens, D.P., 2011, "Coronary Artery Wall Shear Stress Is Associated with Progression and Transformation of Atherosclerotic Plaque and Arterial Remodeling in Patients with Coronary Artery Disease," Circulation, **124**(7), pp. 779–788.

[25] Berger, S.A. and Jou, L.D., 2000, "Flows in Stenotic Vessels," Annual Review of Fluid Mechanics, **32**, pp. 347–382.

[26] Ross, R., 1999, "Atherosclerosis—an Inflammatory Disease," New England Journal of Medicine, **340**(2), pp. 115–126.

[27] Naghavi, M., Libby, P., Falk, E., Casscells, S.W., Litovsky, S., Rumberger, J., Badimon, J.J., Stefanadis, C., Moreno, P., Pasterkamp, G., Fayad, Z., Stone, P.H., Waxman, S., Raggi, P., Madjid, M., Zarrabi, A., Burke, A., Yuan, C., Fitzgerald, P.J., Siscovick, D.S., de Korte, C.L., Aikawa, M., Airaksinen, K.E.J., Assmann, G., Becker, C.R., Chesebro, J.H., Farb, A., Galis, Z.S., Jackson, C., Jang, I.K., Koenig, W., Lodder, R.A., March, K., Demirovic, J., Navab, M., Priori, S.G., Rekhter, M.D., Bahr, R., Grundy, S.M., Mehran, R., Colombo, A., Boerwinkle, E., Ballantyne, C., Insull, W., Schwartz, R.S., Vogel, R., Serruys, P.W., Hansson, G.K., Faxon, D.P., Kaul, S., Drexler, H., Greenland, P., Muller, J.E., Virmani, R., Ridker, P.M., Zipes, D.P., Shah,

P.K., and Willerson, J.T., 2003, "From Vulnerable Plaque to Vulnerable Patient—a Call for New Definitions and Risk Assessment Strategies: Part I," Circulation, **108**(14), pp. 1664–1672.

[28] Garasic, J.M., Edelman, E.R., Squire, J.C., Seifert, P., Williams, M.S., and Rogers, C., 2000, "Stent and Artery Geometry Determine Intimal Thickening Independent of Arterial Injury," Circulation, **101**(7), pp. 812–818.

[29] Farooq, V., Gogas, B.D., and Serruys, P.W., 2011, "Restenosis Delineating the Numerous Causes of Drug-Eluting Stent Restenosis," Circulation—Cardiovascular Interventions, **4**(2), pp. 195–205.

[30] Kolandaivelu, K., Swaminathan, R., Gibson, W.J., Kolachalama, V.B., Nguyen-Ehrenreich, K.L., Giddings, V.L., Coleman, L., Wong, G.K., and Edelman, E.R., 2011, "Stent Thrombogenicity Early in High-Risk Interventional Settings Is Driven by Stent Design and Deployment and Protected by Polymer-Drug Coatings," Circulation, **123**(13), pp. 1400–1409.

[31] Brown, P.M., Zelt, D.T., and Sobolev, B., 2003, "The Risk of Rupture in Untreated Aneurysms: The Impact of Size, Gender, and Expansion Rate," Journal of Vascular Surgery, **37**(2), pp. 280–283.

[32] Canton, G., Levy, D.I., and Lasheras, J.C., 2005, "Hemodynamic Changes Due to Stent Placement in Bifurcating Intracranial Aneurysms," Journal of Neurosurgery, **103**(1), pp. 146–155.

[33] Canton, G., Levy, D.I., Lasheras, J.C., and Nelson, P.K., 2005, "Flow Changes Caused by the Sequential Placement of Stents Across the Neck of Sidewall Cerebral Aneurysms," Journal of Neurosurgery, **103**(5), pp. 891–902.

[34] Cebral, J. and Lohner, R., 2005, "Efficient Simulation of Blood Flow Past Complex Endovascular Devices Using an Adaptive Embedding Technique," IEEE Transactions on Medical Imaging, **24**(4), pp. 468–476.

[35] Benard, N., Perrault, R., and Coisne, D., 2006, "Computational Approach to Estimating the Effects of Blood Properties on Changes in Intra-Stent Flow," Annals of Biomedical Engineering, **34**(8), pp. 1259–1271.

[36] Radaelli, A.G., Augsburger, L., Cebral, J.R., Ohta, M., Rufenacht, D.A., Balossino, R., Benndorf, G., Hose, D.R., Marzo, A., Metcalfe, R., Mortier, P., Mut, F., Reymond, P., Socci, L., Verhegghe, B., and Frangi, A.F., 2008, "Reproducibility of Haemodynamical Simulations in a Subject-Specific Stented Aneurysm Model—a Report on the Virtual Intracranial Stenting Challenge 2007," Journal of Biomechanics, **41**(10), pp. 2069–2081.

[37] Mantha, A., Karmonik, C., Benndorf, G., Strother, C., and Metcalfe, R., 2006, "Hemodynamics in a Cerebral Artery Before and After the Formation of an Aneurysm," AJNR Am J Neuroradiol, **27**(5), pp. 1113–1118.

[38] Shimogonya, Y., Ishikawa, T., Imai, Y., Matsuki, N., and Yamaguchi, T., 2009, "Can Temporal Fluctuation in Spatial Wall Shear Stress Gradient Initiate a Cerebral Aneurysm? A Proposed Novel Hemodynamic Index, the Gradient Oscillatory Number (GON)," Journal of Biomechanics, **42**(4), pp. 550–554.

[39] Westerhof, N., Lankhaar, J.W., and Westerhof, B.E., 2009, "The Arterial Windkessel," Medical and Biological Engineering and Computing, **47**(2), pp. 131–141.

[40] Westerhof, N., Elzinga, G., and Sipkema, P., 1971, "An Artificial Arterial

System for Pumping Hearts," Journal of Applied Physiology, **31**(5), pp. 776–781.

[41] Lambermont, B., D'Orio, V., Gerard, P., Kolh, P., Detry, O., and Marcelle, R., 1998, "Time Domain Method to Identify Simultaneously Parameters of the Windkessel Model Applied to the Pulmonary Circulation," Archives of Physiology and Biochemistry, **106**(3), pp. 245–252.

[42] Stergiopulos, N., Segers, P., and Westerhof, N., 1999, "Use of Pulse Pressure Method for Estimating Total Arterial Compliance in Vivo," American Journal of Physiology, **276**, pp. H424–H428.

[43] Segers, P., Stergiopulos, N., Westerhof, N., Wouters, P., Kolh, P., and Verdonck, P., 2003, "Systemic and Pulmonary Hemodynamics Assessed with a Lumped-Parameter Heart-Arterial Interaction Model," Journal of Engineering Mathematics, **47**(3-4), pp. 185–199.

[44] Vandenberghe, S., Segers, P., Meyns, B., and Verdonck, P., 2001, "Hydrodynamic Characterisation of Ventricular Assist Devices," International Journal of Artificial Organs, **24**(7), pp. 470–477.

[45] Pantalos, G.M., Koenig, S.C., Gillars, K.J., Giridharan, G.A., and Ewert, D.L., 2004, "Characterization of an Adult Mock Circulation for Testing Cardiac Support Devices," ASAIO Journal, **50**(1), pp. 37–46.

[46] Khalil, H.A., Kerr, D.T., Franchek, M.A., Metcalfe, R.W., Benkowski, R.J., Cohn, W.E., Tuzun, E., Radovancevic, B., Frazier, O.H., and Kadipasaoglu, K.A., 2008, "Continuous Flow Total Artificial Heart: Modeling and Feedback Control in a Mock Circulatory System," ASAIO Journal, **54**(3), pp. 249–255.

[47] Formaggia, L., Nobile, F., Quarteroni, A., and Veneziani, A., 1999, "Multiscale Modelling of the Circulatory System: A Preliminary Analysis," Computing and Visualization in Science, **2**, pp. 75–83.

[48] Formaggia, L., Gerbeau, J.F., Nobile, F., and Quarteroni, A., 2001, "On the Coupling of 3D and 1D Navier-Stokes Equations for Flow Problems in Compliant Vessels," Computer Methods in Applied Mechanics and Engineering, **191**(6–7), pp. 561–582.

[49] Urquiza, S.A., Blanco, P.J., Venere, M.J., and Feijoo, R.A., 2006, "Multidimensional Modelling for the Carotid Artery Blood Flow," Computer Methods in Applied Mechanics and Engineering, **195**(33–36), pp. 4002–4017.

[50] Dong, S.C., Insley, J., T Karonis, N., Papka, M.E., Binns, J., and Karniadakis, G., 2006, "Simulating and Visualizing the Human Arterial System on the Teragrid," Future Generation Computer Systems—The International Journal of Grid Computing Theory Methods and Applications, **22**(8), pp. 1011–1017.

[51] Grinberg, L. and Karniadakis, G.E., 2008, "Outflow Boundary Conditions for Arterial Networks with Multiple Outlets," Annals of Biomedical Engineering, **36**(9), pp. 1496–1514.

[52] Grinberg, L., Anor, T., Cheever, E., Madsen, J.R., and Karniadakis, G.E., 2009, "Simulation of the Human Intracranial Arterial Tree," Philosophical Transactions of the Royal Society A—Mathematical Physical and Engineering Sciences, **367**(1896), pp. 2371–2386.

[53] Grinberg, L., Anor, T., Madsen, J.R., Yakhot, A., and Karniadakis, G.E.,

2009, "Large Scale Simulation of the Human Arterial Tree," Clinical and Experimental Pharmacology and Physiology, **36**(2), pp. 194–205.

[54] Spilker, R.L., Feinstein, J.A., Parker, D.W., Reddy, V.M., and Taylor, C.A., 2007, "Morphometry-Based Impedance Boundary Conditions for Patient-Specific Modeling of Blood Flow in Pulmonary Arteries," Annals of Biomedical Engineering, **35**(4), pp. 546–559.

[55] Taylor, C.A. and Steinman, D.A., 2010, "Image-Based Modeling of Blood Flow and Vessel Wall Dynamics: Applications, Methods and Future Directions," Annals of Biomedical Engineering, **38**(3), pp. 1188–1203.

[56] Zarins, C.K., Giddens, D.P., Bharadvaj, B.K., Sottiurai, V.S., Mabon, R.F., and Glagov, S., 1983, "Carotid Bifurcation Atherosclerosis. Quantitative Correlation of Plaque Localization with Flow Velocity Profiles and Wall Shear Stress," Circulation Research, **53**(4), pp. 502–514.

[57] Hoskins, P.R. and Hardman, D., 2009, "Three-Dimensional Imaging and Computational Modelling for Estimation of Wall Stresses in Arteries," British Journal of Radiology, **82**, pp. S3–S17.

[58] Ku, D.N., Giddens, D.P., Phillips, D.J., and Strandness, D.E., 1985, "Hemodynamics of the Normal Human Carotid Bifurcation—in Vitro and in Vivo Studies," Ultrasound in Medicine and Biology, **11**(1), pp. 13–26.

[59] Ionescu, M., Metcalfe, R.W., Cody, D., Alvarado, M.V.Y., Hipp, J., and Benndorf, G., 2011, "Spatial Resolution Limits of Multislice Computed Tomography (MS-CT), C-arm CT, and Flat Panel-CT (FP-CT) Compared to MicroCT for Visualization of a Small Metallic Stent," Academic Radiology, **18**(7), pp. 866–875.

[60] Auricchio, A., Faletra, F., and Moccetti, T., 2009, "Acute Coronary Syndrome Following a Recent Bentall-De Bono Procedure," European Heart Journal, **30**(5), pp. 627–627.

[61] Benndorf, G., Campi, A., Schneider, G.H., Wellnhofer, E., and Unterberg, A., 2001, "Overlapping Stents for Treatment of a Dissecting Carotid Artery Aneurysm," Journal of Endovascular Therapy, **8**(6), pp. 566–570.

[62] Doerfler, A., Wanke, I., Egelhof, T., Stolke, D., and Forsting, M., 2004, "Double-Stent Method: Therapeutic Alternative for Small Wide-Necked Aneurysms. Technical Note," Journal of Neurosurgery, **100**(1), pp. 150–154.

[63] Sani, S. and Lopes, D.K., 2005, "Treatment of a Middle Cerebral Artery Bifurcation Aneurysm Using a Double Neuroform Stent "Y" Configuration and Coil Embolization: Technical Case Report," Neurosurgery, **57**, p. E209.

[64] Kim, M., Levy, E.I., Meng, H., and Hopkins, L., 2007, "Quantification of Hemodynamic Changes Induced by Virtual Placement of Multiple Stents across a Wide-Necked Basilar Trunk Aneurysm," Neurosurgery, **61**(6), pp. 1305–1313.

[65] Pugliese, F., Weustink, A.C., Van Mieghem, C., Alberghina, F., Otsuka, M., Meijboom, W.B., van Pelt, N., Mollet, N.R., Cademartiri, F., Krestin, G.P., Hunink, M.G.M., and de Feyter, P.J., 2008, "Dual Source Coronary Computed Tomography Angiography for Detecting in-Stent Restenosis," Heart, **94**(7), pp. 848–854.

[66] Otsuka, M., Tanimoto, S., Sianos, G., Kukreja, N., Weustink, A.C., Serruys, P.W., and De Feyter, P.J., 2009, ""Radio-Lucent" and "Radio-Opaque"

Coronary Stents Characterized by Multislice Computed Tomography," International Journal of Cardiology, **132**(1), pp. E8–E10.

[67] Meijboom, W.B., Meijs, M.F.L., Schuijf, J.D., Cramer, M.J., Mollet, N.R., van Mieghem, C.A.G., Nieman, K., van Werkhoven, J.M., Pundziute, G., Weustink, A.C., de Vos, A.M., Pugliese, F., Rensing, B., Jukema, J.W., Bax, J.J., Prokop, M., Doevendans, P.A., Hunink, M.G.M., Krestin, G.P., and de Feyter, P.J., 2008, "Diagnostic Accuracy of 64-Slice Computed Tomography Coronary Angiography," Journal of the American College of Cardiology, **52**(25), pp. 2135–2144.

[68] Cademartiri, F., Palumbo, A.A., Maffei, E., La Grutta, L., Casolo, G., Aldrovandi, A., Reverberi, C., Brambilla, V., Coruzzi, P., Beghi, C., Ardissino, D., Crisi, G., and Zompatori, M., 2007, "Non Invasive Imaging of Coronary Arteries with 64-Slice CT and 1.5T MRI: Challenging Invasive Techniques," Acta Biomedica, **78**(1), pp. 6–15.

[69] Barrett, J.F. and Keat, N., 2004, "Artifacts in CT: Recognition and Avoidance," Radiographics, **24**(6), pp. 1679–1691.

[70] Kume, T., Akasaka, T., Kawamoto, T., Watanabe, N., Toyota, E., Sukmawan, R., Sadahira, Y., and Yoshida, K., 2005, "Visualization of Neointima Formation by Optical Coherence Tomography," International Heart Journal, **46**(6), pp. 1133–1136.

[71] de Ribamar Costa, J., J., Mintz, G.S., Carlier, S.G., Fujii, K., Sano, K., Kimura, M., Tanaka, K., Costa, R.A., Lui, J., Na, Y., Castellanos, C., Biro, S., Moussa, I., Stone, G.W., Moses, J.W., and Leon, M.B., 2007,

"Intravascular Ultrasound Assessment of Drug-Eluting Stent Expansion," American Heart Journal, **153**(2), pp. 297–303.

[72] Okamura, T., Serruys, P.W., and Regar, E., 2010, "Three-Dimensional Visualization of Intracoronary Thrombus During Stent Implantation Using the Second Generation, Fourier Domain Optical Coherence Tomography," European Heart Journal, **31**(5), pp. 625–625.

[73] Okamura, T. and Matsuzaki, M., 2012, "Sirolimus-Eluting Stent Fracture Detection by Three-Dimensional Optical Coherence Tomography," Catheterization and Cardiovascular Interventions, **79**(4), pp. 628–632.

[74] Levy, E.I., Turk, A.S., Albuquerque, F.C., Niemann, D.B., Aagaard-Kienitz, B., Pride, L., Purdy, P., Welch, B., Woo, H., Rasmussen, P.A., Hopkins, L.N., Masaryk, T., McDougall, C.G., and Fiorella, D.J., 2007, "Wingspan in-Stent Restenosis and Thrombosis: Incidence, Clinical Presentation, and Management," Neurosurgery, **61**(3), pp. 644–650.

[75] Benndorf, G., Ionescu, M., MV, Y.A., Hipp, J., and Metcalfe, R., 2009, "Wall Shear Stress in Intracranial Self-Expanding Stents Studied Using Ultra-High-Resolution 3D Reconstructions," AJNR Am J Neuroradiol, **30**(3), pp. 479–486.

[76] Benndorf, G., Strother, C.M., Claus, B., Naeini, R., Morsi, H., Klucznik, R., and Mawad, M.E., 2005, "Angiographic CT in Cerebrovascular Stenting," AJNR Am J Neuroradiol, **26**(7), pp. 1813–1818.

[77] Ebrahimi, N., Claus, B., Lee, C.Y., Biondi, A., and Benndorf, G., 2007, "Stent Conformity in Curved Vascular Models with Simulated Aneurysm

Necks Using Flat-Panel CT: An in Vitro Study," AJNR Am J Neuroradiol, **28**(5), pp. 823–829.

[78] Mahnken, A.H., Seyfarth, T., Flohr, T., Herzog, C., Stahl, J., Stanzel, S., Kuettner, A., Wildberger, J.E., and Gunther, R.W., 2005, "Flat-Panel Detector Computed Tomography for the Assessment of Coronary Artery Stents—Phantom Study in Comparison with 16-Slice Spiral Computed Tomography," Investigative Radiology, **40**(1), pp. 8–13.

[79] Steinman, D.A., 2002, "Image-Based Computational Fluid Dynamics Modeling in Realistic Arterial Geometries," Annals of Biomedical Engineering, **30**(4), pp. 483–497.

[80] Ritman, E.L., 2004, "Micro-Computed Tomography—Current Status and Developments," Annual Review of Biomedical Engineering, **6**, pp. 185–208.

[81] Ross, W., Cody, D.D., and Hazle, J.D., 2006, "Design and Performance Characteristics of a Digital Flat-Panel Computed Tomography System," Medical Physics, **33**(6), pp. 1888–1901.

[82] Benndorf, G., Ionescu, M., Alvarado, M.V.Y., Biondi, A., Hipp, J., and Metcalfe, R., 2010, "Anomalous Hemodynamic Effects of a Self-Expanding Intracranial Stent: Comparing in-Vitro and Ex-Vivo Models Using Ultra-High Resolution MicroCT Based CFD," Journal of Biomechanics, **43**(4), pp. 740–748.

[83] Maintz, D., Seifarth, H., Flohr, T., Kramer, S., Wichter, T., Heindel, W., and Fischbach, R., 2003, "Improved Coronary Artery Stent Visualization and in-Stent Stenosis Detection Using 16-Slice Computed-Tomography and Ded-

icated Image Reconstruction Technique," Investigative Radiology, **38**(12), pp. 790–795.

[84] Suzuki, S., Furui, S., Kaminaga, T., Yamauchi, T., Kuwahara, S., Yokoyama, N., Suzuki, M., and Isshiki, T., 2005, "Evaluation of Coronary Stents in Vitro with CT Angiography—Effect of Stent Diameter, Convolution Kernel, and Vessel Orientation to the Z-Axis," Circulation Journal, **69**(9), pp. 1124–1131.

[85] van Werkum, J.W., Heestermans, A.A., Zomer, A.C., Kelder, J.C., Suttorp, M.J., Rensing, B.J., Koolen, J.J., Brueren, B.R.G., Dambrink, J.H.E., Hautvast, R.W., Verheugt, F.W., and ten Berg, J.M., 2009, "Predictors of Coronary Stent Thrombosis the Dutch Stent Thrombosis Registry," Journal of the American College of Cardiology, **53**(16), pp. 1399–1409.

[86] Boll, D.T., Merkle, E.M., Paulson, E.K., and Fleiter, T.R., 2008, "Coronary Stent Patency: Dual-Energy Multidetector CT Assessment in a Pilot Study with Anthropomorphic Phantom," Radiology, **247**(3), pp. 687–695.

[87] Halpern, E.J., Halpern, D.J., Yanof, J.H., Amin-Spector, S., Fischman, D., Aviram, G., and Sosna, J., 2009, "Is Coronary Stent Assessment Improved with Spectral Analysis of Dual Energy CT?" Academic Radiology, **16**(10), pp. 1241–1250.

[88] Schepis, T., Koepfli, P., Leschka, S., Desbiolles, L., Husmann, L., Gaemperli, O., Eberli, F.R., Wildermuth, S., Marincek, B., Luscher, T.F., Alkadhi, H., and Kaufmann, P.A., 2007, "Coronary Artery Stent Geometry and in-Stent Contrast Attenuation with 64-Slice Computed Tomography," European Radiology, **17**(6), pp. 1464–1473.

[89] Buhk, J.H., Lingor, P., and Knauth, M., 2008, "Angiographic CT with Intravenous Administration of Contrast Medium Is a Noninvasive Option for Follow-up After Intracranial Stenting," Neuroradiology, **50**(4), pp. 349–354.

[90] Alvarado, M.V.Y., Ebrahimi, N., and Benndorf, G., 2009, "Study of Conformability of the New Leo Plus Stent to a Curved Vascular Model Using Flat-Panel Detector Computed Tomography (DynaCT)," Neurosurgery, **64**(3), pp. S130–S134.

[91] Connolley, T., Nash, D., Buffiere, J.Y., Sharif, F., and McHugh, P.E., 2007, "X-Ray Micro-Tomography of a Coronary Stent Deployed in a Model Artery," Medical Engineering and Physics, **29**(10), pp. 1132–1141.

[92] Morlacchi, S., Keller, B., Arcangeli, P., Balzan, M., Migliavacca, F., Dubini, G., Gunn, J., Arnold, N., Narracott, A., Evans, D., and Lawford, P., 2011, "Hemodynamics and in-Stent Restenosis: Micro-CT Images, Histology, and Computer Simulations," Annals of Biomedical Engineering, **39**(10), pp. 2615–2626.

[93] Lingamfelter, M., 2010, *Unwrapping of Stented Coronary Artery Geometries and Novel Three-Dimensional Imaging Techniques Applied to Intracranial Aneurysms*, B.S. Thesis, University of Houston, Houston, TX.

[94] Benndorf, G., Claus, B., Strother, C.M., Chang, L., and Klucznik, R.P., 2006, "Increased Cell Opening and Prolapse of Struts of a Neuroform Stent in Curved Vasculature: Value of Angiographic Computed Tomography: Technical Case Report," Neurosurgery, **58**(4 Suppl 2), pp. ONS–E380; discussion ONS–E380.

[95] Valdivia y Alvarado, M., Ebrahimi, N., and Benndorf, G., 2009, "Study of

Conformability of the New Leo Plus Stent to a Curved Vascular Model Using Flat-Panel Detector Computed Tomography (DynaCT)," Neurosurgery, **64**(3 Suppl), pp. 130–134.

[96] Krischek, O., Miloslavski, E., Fischer, S., Shrivastava, S., and Henkes, H., 2011, "A Comparison of Functional and Physical Properties of Self-Expanding Intracranial Stents [Neuroform3, Wingspan, Solitaire, Leo(+), Enterprise]," Minimally Invasive Neurosurgery, **54**(1), pp. 21–28.

[97] Garg, S. and Serruys, P.W., 2010, "Coronary Stents Current Status," Journal of the American College of Cardiology, **56**(10), pp. S1–S42.

[98] Nakazawa, G., Yazdani, S.K., Finn, A.V., Vorpahl, M., Kolodgie, F.D., and Virmani, R., 2010, "Pathological Findings at Bifurcation Lesions—The Impact of Flow Distribution on Atherosclerosis and Arterial Healing after Stent Implantation," Journal of the American College of Cardiology, **55**(16), pp. 1679–1687.

[99] Metcalfe, R.W., 2003, "The Promise of Computational Fluid Dynamics as a Tool for Delineating Therapeutic Options in the Treatment of Aneurysms," AJNR Am J Neuroradiol, **24**(4), pp. 553–554.

[100] Pache, J., Kastrati, A., Mehilli, J., Schuhlen, H., Dotzer, F., Hausleiter, J., Fleckenstein, M., Neumann, F.J., Sattelberger, U., Schmitt, C., Muller, M., Dirschinger, J., and Schomig, A., 2003, "Intracoronary Stenting and Angiographic Results: Strut Thickness Effect on Restenosis Outcome (Isar-Stereo-2) Trial," Journal of the American College of Cardiology, **41**(8), pp. 1283–1288.

[101] Rolland, P.H., Mekkaoui, C., Vidal, V., Berry, J.L., Moore, J.E., Moreno,

M., Amabile, P., and Bartoli, J.M., 2004, "Compliance Matching Stent Placement in the Carotid Artery of the Swine Promotes Optimal Blood Flow and Attenuates Restenosis," European Journal of Vascular and Endovascular Surgery, **28**(4), pp. 431–438.

[102] Takebayashi, H., Mintz, G.S., Carlier, S.G., Kobayashi, Y., Fujii, K., Yasuda, T., Costa, R.A., Moussa, I., Dangas, G.D., Mehran, R., Lansky, A.J., Kreps, E., Collins, M.B., Colombo, A., Stone, G.W., Leon, M.B., and Moses, J.W., 2004, "Nonuniform Strut Distribution Correlates with More Neointimal Hyperplasia after Sirolimus-Eluting Stent Implantation," Circulation, **110**(22), pp. 3430–3434.

[103] Papafaklis, M.I., Bourantas, C.V., Theodorakis, P.E., Katsouras, C.S., Naka, K.K., Fotiadis, D.I., and Michalis, L.K., 2010, "The Effect of Shear Stress on Neointimal Response Following Sirolimus- and Paclitaxel-Eluting Stent Implantation Compared with Bare-Metal Stents in Humans," Journal of the American College of Cardiology—Cardiovascular Interventions, **3**(11), pp. 1181–1189.

[104] Chen, H.Y., Sinha, A.K., Choy, J.S., Zheng, H., Sturek, M., Bigelow, B., Bhatt, D.L., and Kassab, G.S., 2011, "Mis-Sizing of Stent Promotes Intimal Hyperplasia: Impact of Endothelial Shear and Intramural Stress," American Journal of Physiology—Heart and Circulatory Physiology, **301**(6), pp. H2254–H2263.

[105] Tahir, H., Hoekstra, A.G., Lorenz, E., Lawford, P.V., Hose, D.R., Gunn, J., and Evans, D.J.W., 2011, "Multi-Scale Simulations of the Dynamics of in-Stent Restenosis: Impact of Stent Deployment and Design," Interface Focus, **1**(3), pp. 365–373.

[106] Cook, S., Wenaweser, P., Togni, M., Billinger, M., Morger, C., Seiler, C., Vogel, R., Hess, O., Meier, B., and Windecker, S., 2007, "Incomplete Stent Apposition and Very Late Stent Thrombosis after Drug-Eluting Stent Implantation," Circulation, **115**(18), pp. 2426–2434.

[107] Berry, J.L., Santamarina, A., Moore, J.E., Roychowdhury, S., and Routh, W.D., 2000, "Experimental and Computational Flow Evaluation of Coronary Stents," Annals of Biomedical Engineering, **28**(4), pp. 386–398.

[108] Balakrishnan, B., Tzafriri, A.R., Seifert, P., Groothuis, A., Rogers, C., and Edelman, E.R., 2005, "Strut Position, Blood Flow, and Drug Deposition—Implications for Single and Overlapping Drug-Eluting Stents," Circulation, **111**(22), pp. 2958–2965.

[109] LaDisa, J. F., J., Olson, L.E., Hettrick, D.A., Warltier, D.C., Kersten, J.R., and Pagel, P.S., 2005, "Axial Stent Strut Angle Influences Wall Shear Stress after Stent Implantation: Analysis Using 3D Computational Fluid Dynamics Models of Stent Foreshortening," Biomedical Engineering Online, **4**, p. 59.

[110] LaDisa, J. F., J., Guler, I., Olson, L.E., Hettrick, D.A., Kersten, J.R., Warltier, D.C., and Pagel, P.S., 2003, "Three-Dimensional Computational Fluid Dynamics Modeling of Alterations in Coronary Wall Shear Stress Produced by Stent Implantation," Annals of Biomedical Engineering, **31**(8), pp. 972–980.

[111] LaDisa, J.F., Olson, L.E., Guler, I., Hettrick, D.A., Audi, S.H., Kersten, J.R., Warltier, D.C., and Pagel, P.S., 2004, "Stent Design Properties and Deployment Ratio Influence Indexes of Wall Shear Stress: A Three-Dimensional

Computational Fluid Dynamics Investigation within a Normal Artery," Journal of Applied Physiology, **97**(1), pp. 424–430.

[112] Faik, I., Mongrain, R., Leask, R.L., Rodes-Cabau, J., Larose, E., and Bertrand, O., 2007, "Time-Dependent 3D Simulations of the Hemodynamics in a Stented Coronary Artery," Iop Publishing Ltd, pp. S28–S37.

[113] Balossino, R., Gervaso, F., Migliavacca, F., and Dubini, G., 2008, "Effects of Different Stent Designs on Local Hemodynamics in Stented Arteries," Journal of Biomechanics, **41**(5), pp. 1053–1061.

[114] Pant, S., Bressloff, N.W., Forrester, A.I.J., and Curzen, N., 2010, "The Influence of Strut-Connectors in Stented Vessels: A Comparison of Pulsatile Flow through Five Coronary Stents," Annals of Biomedical Engineering, **38**(5), pp. 1893–1907.

[115] He, Y., Duraiswamy, N., Frank, A.O., and Moore, J.E., 2005, "Blood Flow in Stented Arteries: A Parametric Comparison of Strut Design Patterns in Three Dimensions," Journal of Biomechanical Engineering—Transactions of the ASME, **127**(4), pp. 637–647.

[116] LaDisa, J. F., J., Olson, L.E., Molthen, R.C., Hettrick, D.A., Pratt, P.F., Hardel, M.D., Kersten, J.R., Warltier, D.C., and Pagel, P.S., 2005, "Alterations in Wall Shear Stress Predict Sites of Neointimal Hyperplasia after Stent Implantation in Rabbit Iliac Arteries," American Journal of Physiology—Heart and Circulatory Physiology, **288**(5), pp. H2465–H2475.

[117] LaDisa, J. F., J., Olson, L.E., Guler, I., Hettrick, D.A., Kersten, J.R., Warltier, D.C., and Pagel, P.S., 2005, "Circumferential Vascular Deformation after Stent Implantation Alters Wall Shear Stress Evaluated with Time-

Dependent 3D Computational Fluid Dynamics Models," Journal of Applied Physiology, **98**(3), pp. 947–957.

[118] Gundert, T.J., Shadden, S.C., Williams, A.R., Koo, B.K., Feinstein, J.A., and LaDisa, J.F., 2011, "A Rapid and Computationally Inexpensive Method to Virtually Implant Current and Next-Generation Stents into Subject-Specific Computational Fluid Dynamics Models," Annals of Biomedical Engineering, **39**(5), pp. 1423–1437.

[119] Fluent, 2006, *Fluent 6.3 User's Guide*, Lebanon, NH.

[120] Rolland, P.H., Charifi, A.B., Verrier, C., Bodard, H., Friggi, A., Piquet, P., Moulin, G., and Bartoli, J.M., 1999, "Hemodynamics and Wall Mechanics after Stent Placement in Swine Iliac Arteries: Comparative Results from Six Stent Designs," Radiology, **213**(1), pp. 229–246.

[121] Stuhne, G.R. and Steinman, D.A., 2004, "Finite-Element Modeling of the Hemodynamics of Stented Aneurysms," Journal of Biomechanical Engineering—Transactions of the ASME, **126**(3), pp. 382–387.

[122] Womersley, J.R., 1955, "Method for the Calculation of Velocity, Rate of Flow and Viscous Drag in Arteries When the Pressure Gradient Is Known," Journal of Physiology—London, **127**(3), pp. 553–563.

[123] Tritton, D.J., 1988, *Physical Fluid Dynamics*, Oxford Science Publications, Oxford.

[124] Seo, T.L., Schchter, L.G., and Barakat, A.I., 2005, "Computational Study of Fluid Mechanical Disturbance Induced by Endovascular Stents," Annals of Biomedical Engineering, **33**, pp. 444–4577.

[125] Rajamohan, D., Banerjee, R.K., Back, L.H., Ibrahim, A.A., and Jog, M.A., 2006, "Developing Pulsatile Flow in a Deployed Coronary Stent," Journal of Biomechanical Engineering—Transactions of the ASME, **128**(3), pp. 347–359.

[126] Holdsworth, D.W., Norley, C.J.D., Frayne, R., Steinman, D.A., and Rutt, B.K., 1999, "Characterization of Common Carotid Artery Blood-Flow Waveforms in Normal Human Subjects," Physiological Measurement, **20**(3), pp. 219–240.

[127] Botnar, R., Rappitsch, G., Scheidegger, M.B., Liepsch, D., Perktold, K., and Boesiger, P., 2000, "Hemodynamics in the Carotid Artery Bifurcation: A Comparison between Numerical Simulations and in Vitro MRI Measurements," Journal of Biomechanics, **33**(2), pp. 137–144.

[128] Glor, F.P., Ariff, B., Hughes, A.D., Crowe, L.A., Verdonck, P.R., Barratt, D.C., Thom, S.A.M., Firmin, D.N., and Xu, X.Y., 2004, "Image-Based Carotid Flow Reconstruction: A Comparison between MRI and Ultrasound," Physiological Measurement, **25**(6), pp. 1495–1509.

[129] Kaazempur-Mofrad, M.R., Isasi, A.G., Younis, H.F., Chan, R.C., Hinton, D.P., Sukhova, G., LaMuraglia, G.M., Lee, R.T., and Kamm, R.D., 2004, "Characterization of the Atherosclerotic Carotid Bifurcation Using MRI, Finite Element Modeling, and Histology," Annals of Biomedical Engineering, **32**(7), pp. 932–946.

[130] Oktar, S.O., Yucel, C., Karaosmanoglu, D., Akkan, K., Ozdemir, H., Tokgoz, N., and Tali, T., 2006, "Blood-Flow Volume Quantification in Internal Carotid and Vertebral Arteries: Comparison of 3 Different Ultrasound Tech-

niques with Phase-Contrast MR Imaging," AJNR Am J Neuroradiol, **27**(2), pp. 363–369.

[131] Bammer, R., Hope, T.A., Aksoy, M., and Alley, M.T., 2007, "Time-Resolved 3D Quantitative Flow MRI of the Major Intracranial Vessels: Initial Experience and Comparative Evaluation at 1.5T and 3.0T in Combination with Parallel Imaging," Magnetic Resonance in Medicine, **57**(1), pp. 127–140.

[132] Hansen, K.L., Udesen, J., Oddershede, N., Henze, L., Thomsen, C., Jensen, J.A., and Nielsen, M.B., 2009, "In Vivo Comparison of Three Ultrasound Vector Velocity Techniques to MR Phase Contrast Angiography," Ultrasonics, **49**(8), pp. 659–667.

[133] Hollnagel, D.I., Summers, P.E., Poulikakos, D., and Kollias, S.S., 2009, "Comparative Velocity Investigations in Cerebral Arteries and Aneurysms: 3D Phase-Contrast MR Angiography, Laser Doppler Velocimetry and Computational Fluid Dynamics," NMR in Biomedicine, **22**(8), pp. 795–808.

[134] Hoi, Y.M., Wasserman, B.A., Lakatta, E.G., and Steinman, D.A., 2010, "Effect of Common Carotid Artery Inlet Length on Normal Carotid Bifurcation Hemodynamics," Journal of Biomechanical Engineering-Transactions of the ASME, **132**(12).

[135] Suh, G.Y., Les, A.S., Tenforde, A.S., Shadden, S.C., Spilker, R.L., Yeung, J.J., Cheng, C.P., Herfkens, R.J., Dalman, R.L., and Taylor, C.A., 2011, "Hemodynamic Changes Quantified in Abdominal Aortic Aneurysms with Increasing Exercise Intensity Using MR Exercise Imaging and Image-Based Computational Fluid Dynamics," Annals of Biomedical Engineering, **39**(8), pp. 2186–2202.

[136] Milner, J.S., Moore, J.A., Rutt, B.K., and Steinman, D.A., 1998, "Hemodynamics of Human Carotid Artery Bifurcations: Computational Studies with Models Reconstructed from Magnetic Resonance Imaging of Normal Subjects," Journal of Vascular Surgery, **28**(1), pp. 143–156.

[137] Marshall, I., Papathanasopoulou, P., and Wartolowska, K., 2004, "Carotid Flow Rates and Flow Division at the Bifurcation in Healthy Volunteers," Physiological Measurement, **25**(3), pp. 691–697.

[138] Ford, M.D., Alperin, N., Lee, S.H., Holdsworth, D.W., and Steinman, D.A., 2005, "Characterization of Volumetric Flow Rate Waveforms in the Normal Internal Carotid and Vertebral Arteries," Physiological Measurement, **26**(4), pp. 477–488.

[139] Gwilliam, M.N., Hoggard, N., Capener, D., Singh, P., Marzo, A., Verma, P.K., and Wilkinson, I.D., 2009, "MR Derived Volumetric Flow Rate Waveforms at Locations within the Common Carotid, Internal Carotid, and Basilar Arteries," Journal of Cerebral Blood Flow and Metabolism, **29**(12), pp. 1975–1982.

[140] Hoi, Y., Wasserman, B.A., Xie, Y.Y.J., Najjar, S.S., Ferruci, L., Lakatta, E.G., Gerstenblith, G., and Steinman, D.A., 2010, "Characterization of Volumetric Flow Rate Waveforms at the Carotid Bifurcations of Older Adults," Physiological Measurement, **31**(3), pp. 291–302.

[141] Tortoli, P., Guidi, F., Guidi, G., and Atzeni, C., 1996, "Spectral Velocity Profiles for Detailed Ultrasound Flow Analysis," IEEE Transactions on Ultrasonics Ferroelectrics and Frequency Control, **43**(4), pp. 654–659.

[142] Tortoli, P., Morganti, T., Bambi, G., Palombo, C., and Ramnarine, K.V.,

2006, "Noninvasive Simultaneous Assessment of Wall Shear Rate and Wall Distension in Carotid Arteries," Ultrasound in Medicine and Biology, **32**(11), pp. 1661–1670.

[143] Ponzini, R., Vergara, C., Rizzo, G., Veneziani, A., Roghi, A., Vanzulli, A., Parodi, O., and Redaelli, A., 2010, "Womersley Number-Based Estimates of Blood Flow Rate in Doppler Analysis: In Vivo Validation by Means of Phase-Contrast MRI," IEEE Transactions on Biomedical Engineering, **57**(7), pp. 1807–1815.

[144] Tortoli, P., Bambi, G., Guidi, F., and Muchada, R., 2002, "Toward a Better Quantitative Measurement of Aortic Flow," Ultrasound in Medicine and Biology, **28**(2), pp. 249–257.

[145] Tortoli, P., Michelassi, V., Bambi, G., Guidi, F., and Righi, D., 2003, "Interaction between Secondary Velocities, Flow Pulsation and Vessel Morphology in the Common Carotid Artery," Ultrasound in Medicine and Biology, **29**(3), pp. 407–415.

[146] Leguy, C.A.D., Bosboom, E.M.H., Hoeks, A.P.G., and van de Vosse, F.N., 2009, "Assessment of Blood Volume Flow in Slightly Curved Arteries from a Single Velocity Profile," Journal of Biomechanics, **42**(11), pp. 1664–1672.

[147] Hoskins, P.R., 2010, "Haemodynamics and Blood Flow Measured Using Ultrasound Imaging," Proceedings of the Institution of Mechanical Engineers Part H—Journal of Engineering in Medicine, **224**(H2), pp. 255–271.

[148] Bharadvaj, B.K., Mabon, R.F., and Giddens, D.P., 1982, "Steady Flow in a Model of the Human Carotid Bifurcation. 1. Flow Visualization," Journal of Biomechanics, **15**(5), pp. 349–362.

[149] Hale, J.F., McDonald, D.A., and Womersley, J.R., 1955, "Velocity Profiles of Oscillating Arterial Flow with Some Calculations of Viscous Drag and the Reynolds Number," Journal of Physiology—London, **128**(3), pp. 629–640.

[150] Sexl, T., den von, U., and Richardson, E.G., 1930, "Annulareffekt," Zeitschrift für Physik, **61**, pp. 349–362.

[151] Szymanski, P., 1932, "Some Exact Solutions of the Hydrodynamic Equations of a Viscous Fluid in the Case of a Cylindrical Tube," Journal de Mathématiques Pures et Appliquées, **11**, pp. 67–107.

[152] Lambossy, P., 1952, "Oscillations Forcées D'un Liquide Incompressible Et Visqueux Dans Un Tube Rigide Et Horizontal. Calcul De La Force Frottement," Helvetica Physica Acta, **25**, pp. 371–386.

[153] Uchida, S., 1956, "The Pulsating Viscous Flow Superposed on the Steady Laminar Motion of Incompressible Fluid in a Circular Pipe," Journal of Applied Mathematics and Physics (ZAMP), **7**, pp. 403–422.

[154] Gundogdu, M.Y. and Carpinlioglu, M.O., 1999, "Present State of Art on Pulsatile Flow Theory—(Part 1: Laminar and Transitional Flow Regimes)," JSME International Journal Series B—Fluids and Thermal Engineering, **42**(3), pp. 384–397.

[155] Unsal, B., Ray, S., Durst, F., and Ertunc, O., 2005, "Pulsating Laminar Pipe Flows with Sinusoidal Mass Flux Variations," Fluid Dynamics Research, **37**(5), pp. 317–333.

[156] Haddad, K., Ertunc, O., Mishra, M., and Delgado, A., 2010, "Pulsating Laminar Fully Developed Channel and Pipe Flows," Physical Review E, **81**(1).

[157] Cezeaux, J.L. and VanGrondelle, A., 1997, "Accuracy of the Inverse Womersley Method for the Calculation of Hemodynamic Variables," Annals of Biomedical Engineering, **25**(3), pp. 536–546.

[158] Coppola, G. and Caro, C., 2009, "Arterial Geometry, Flow Pattern, Wall Shear and Mass Transport: Potential Physiological Significance," Journal of the Royal Society Interface, **6**(35), pp. 519–528.

[159] Ohmi, M., Usui, T., Fukawa, M., and Hirasaki, S., 1976, "Pressure and Velocity Distributions in Pulsating Laminar Pipe Flow," Bulletin of the JSME—Japan Society of Mechanical Engineers, **19**(129), pp. 298–306.

[160] Das, D. and Arakeri, J.H., 2000, "Unsteady Laminar Duct Flow with a Given Volume Flow Rate Variation," Journal of Applied Mechanics—Transactions of the ASME, **67**(2), pp. 274–281.

[161] Abuelma'atti, M.T., 1999, "A Simple Algorithm for Computing the Fourier Spectrum of Experimentally Obtained Signals," Applied Mathematics and Computation, **98**(2–3), pp. 229–239.

[162] Boyd, J.P., 2006, "Computing the Zeros, Maxima and Inflection Points of Chebyshev, Legendre and Fourier Series: Solving Transcendental Equations by Spectral Interpolation and Polynomial Rootfinding," Journal of Engineering Mathematics, **56**(3), pp. 203–219.

[163] Trefethen, L., 2007, "Computing Numerically with Functions Instead of Numbers," Mathematics in Computer Science, **1**(1), pp. 9–19.

[164] Scheel, P., Ruge, C., and Schoning, M., 2000, "Flow Velocity and Flow Volume Measurements in the Extracranial Carotid and Vertebral Arteries

in Healthy Adults: Reference Data and the Effects of Age," Ultrasound in Medicine and Biology, **26**(8), pp. 1261–1266.

[165] Studinger, P., Lenard, Z., Kovats, Z., Kocsis, L., and Kollai, M., 2003, "Static and Dynamic Changes in Carotid Artery Diameter in Humans During and after Strenuous Exercise," Journal of Physiology—London, **550**(2), pp. 575–583.

[166] Azhim, A., Katai, M., Akutagawa, M., Hirao, Y., Yoshizaki, K., Obara, S., Nomura, M., Tanaka, H., Yamaguchi, H., and Kinouchi, Y., 2006, *Blood Flow Velocities in Common Carotid Artery Changes with Age and Exercise*, 2006 International Conference on Biomedical and Pharmaceutical Engineering.

[167] Tortoli, P., Bambi, G., and Ricci, S., 2006, "Accurate Doppler Angle Estimation for Vector Flow Measurements," IEEE Transactions on Ultrasonics Ferroelectrics and Frequency Control, **53**(8), pp. 1425–1431.